



University  
of Glasgow

MICROSTRUCTURE CHARACTERIZING AND  
MECHANICAL PROPERTIES OF SELECTIVE LASER  
MELTED TI-6AL-4V ALLOYS

DANG KHOA DO

JAMES WATT SCHOOL OF ENGINEERING

2021

**MICROSTRUCTURE CHARACTERIZING AND  
MECHANICAL PROPERTIES OF SELECTIVE LASER  
MELTED TI-6AL-4V ALLOYS**

**DANG KHOA DO**

James Watt School of Engineering

A thesis submitted to University of Glasgow in  
fulfilment of the requirement for the degree of  
Doctor of Philosophy

2021

## Abstract

Selective laser melting (SLM) is an additive manufacturing technique that can produce complex functional metal parts of high relative density and near-net shape. Due to the complete melting of metal powders in a layer-by-layer approach during the SLM process, heterogeneity in the as-produced microstructure is a big hindrance in the application of SLM parts. The formation progress of such heterogeneous microstructure in SLM built Ti-6Al-4V and how it behaves under different working conditions are not yet fully understood.

This study thus aims to better understand the evolution of microstructure within Ti-6Al-4V's as-fabricated and heat-treated conditions for the microstructural regulation. Furthermore, this research also paves the way for identifying microstructure behaviours under high strain rate conditions that are important for the successful implementation of SLM-built Ti-6Al-4V in many industries.

Firstly, the effect of SLM processing parameters on the part quality and macrostructure are investigated to obtain the optimised processing window based on the optimal relative density and surface roughness achieved. Secondly, the resulting microstructure of Ti-6Al-4V parts is examined and analysed quantitatively using microstructural characterisation techniques and numerical simulations to promote the interpretation of the SLM forming process. Thirdly, the mechanical testing of SLM Ti-6Al-4V parts manufactured by a wide range of laser energy densities is conducted under quasi-static (e.g. tensile tests and Vickers microhardness tests) and high strain rate (e.g. Split-Hopkinson pressure bar tests) conditions. The dynamic behaviours of SLM Ti-6Al-4V is benchmarked against that of Ti-6Al-4V produced by traditional methods to investigate the microstructure features and dynamic recrystallization in the SLM-built material. Lastly, the influence of the heat treatment on the SLM Ti-6Al-4V microstructure is studied with a view to improving mechanical properties. Annealing strategies are designed to decompose and spheroidise the  $\alpha'$  martensitic microstructure into a bimodal to balance mechanical strength and ductility. A Phase Field model is developed to validate the experimental observation and facilitate the findings in this section.

The conclusions are drawn that the heterogeneity in the microstructure and mechanical properties is indeed established during the fabrication process. The phase transformation during the cyclic thermal loading process of SLM is also shown. Differences in thermo-plasticity and auto-tempering influenced by laser energy densities lead to heterogeneity in the microstructure behaviours and mechanical properties. Additionally, the kinetic pathways of  $\alpha'$  decomposition is revealed by the Phase Field

model, which facilitates understanding of microstructure evolution in isothermal heat treatment of SLM Ti-6Al-4V.

The key contributions in this study further enrich the scientific knowledge regarding microstructure evolution occurring during SLM process and under different loading conditions. The findings of this thesis are a valuable reference for both microstructure regulation and employing the SLM components for industrial application.



# Acknowledgement

The work presented in this thesis would not have been possible without the support of many individuals for whom I would like to extend my heartfelt gratitude. First and foremost, I would like to send my greatest appreciation to my supervisor, Dr Peifeng Li, for his invaluable advices, kindness, and patience throughout my candidature. His support and commitment to the research encouraged me to push forward through difficult times. Appreciation is also extended to Dr Zhiyong Wang, Dr Ruoxuan Huang, Dr Ge Liu, Dr Ngoc Vu Nguyen for being an excellent team and their willingness to always lend a helping hand whenever I needed.

Next, I would also like to thank Professor Chee Kai Chua and Professor David Cumming for the opportunity in conducting the research in both Singapore Centre for 3D Printing (SC3DP) and James Watt School of Engineering – University of Glasgow. I also acknowledge the research funding received from these institutions. I am also grateful to all my colleagues and friends, whom I came to know in SC3DP and the Materials and Manufacturing Research Group. I thank them for all the enjoyable and delightful experiences we shared throughout the time of this research. Particularly, I would like to sincerely thank Dr Cher Fu Tey for not only a wonderful friend, but also a great teacher in all matters, from research's work, professional career to social life. Additionally, I would like to send my appreciation to all the laboratory personnel for their technical assistance and making my research experience a smooth and a pleasant one.

Lastly, but certainly not the least, I would like to express my sincere gratitude to my family and friends for always being there to support my decisions. More importantly, I am thankful to my mother and my wife, the two most important women of my life: one gave me the motivation to start my PhD, the other one gave me the strength to finish.

# Contents

<b>Abstract</b> .....	<b><i>i</i></b>
<b>Acknowledgement</b> .....	<b><i>iii</i></b>
<b>List of Figures</b> .....	<b><i>vii</i></b>
<b>List of Tables</b> .....	<b><i>xv</i></b>
<b>List of Abbreviations</b> .....	<b><i>xvi</i></b>
<b>Chapter 1 – Introduction</b> .....	<b>1</b>
<b>1.1 – Background</b> .....	<b>2</b>
<b>1.2 – Motivation</b> .....	<b>4</b>
<b>1.3 – Objectives</b> .....	<b>5</b>
<b>1.4 – Scope</b> .....	<b>5</b>
<b>1.5 – Thesis organisation</b> .....	<b>6</b>
<b>Chapter 2 – Literature review</b> .....	<b>7</b>
<b>2.1 – Selective laser melting</b> .....	<b>8</b>
2.1.1 – Working principle .....	8
2.1.2 – Processing parameters .....	10
<b>2.2 – Defects in selective laser melting of Ti-6Al-4V</b> .....	<b>12</b>
2.2.1 – Porosity.....	12
2.2.2 – Surface quality .....	14
<b>2.3 – Phase transformation in Ti-6Al-4V</b> .....	<b>16</b>
2.3.1 – The diffusion-controlled transformation.....	16
2.3.2 – Diffusionless transformation .....	19
<b>2.4 – Microstructure of SLM Ti-6Al-4V</b> .....	<b>20</b>
2.4.1 – Prior $\beta$ columnar grains .....	20
2.4.2 – $\alpha'$ martensite grains .....	22
<b>2.5 – Microstructure change under dynamic conditions</b> .....	<b>23</b>
<b>2.6 – Mechanical properties of SLM Ti-6Al-4V</b> .....	<b>26</b>
2.6.1 – Quasi-static tensile properties .....	26

---

2.6.2 – Dynamic compressive properties .....	29
<b>2.7 – Chapter summary.....</b>	<b>30</b>
<b><i>Chapter 3 – Research methodology .....</i></b>	<b><i>32</i></b>
<b>3.1 – Materials .....</b>	<b>33</b>
<b>3.2 – Fabrication process .....</b>	<b>33</b>
<b>3.3 – Metrological characterization .....</b>	<b>35</b>
<b>3.4 – Mechanical testing .....</b>	<b>36</b>
3.4.1 – Quasi-static tensile testing .....	36
3.4.2 – Micro-hardness testing .....	37
3.4.3 – Dynamic compression testing .....	37
<b>3.5 – Metallographic characterization .....</b>	<b>39</b>
<b>3.6 – Crystallographic representation.....</b>	<b>39</b>
<b><i>Chapter 4 – Effect of processing parameters on the as-built properties .....</i></b>	<b><i>41</i></b>
<b>4.1 – Optimal processing parameters .....</b>	<b>42</b>
<b>4.2 – Thermal simulation of the SLM process.....</b>	<b>47</b>
4.2.1 – Thermal model .....	47
4.2.2 – Predicted melt pool profile and solidification condition.....	50
4.2.3 – Heat history .....	53
<b>4.3 – Microstructure and texture evolution .....</b>	<b>54</b>
4.3.1 – Columnar $\beta$ .....	54
4.3.2 – $\alpha'$ martensite.....	56
<b>4.4 – Effect of the laser energy density on the microstructure evolution .....</b>	<b>58</b>
<b>4.5 – Effect of the laser energy density on mechanical properties .....</b>	<b>62</b>
4.5.1 – The hardness and quasi-static tensile properties.....	62
4.5.2 – Fracture behaviours .....	65
4.5.3 – The relationship of the $\alpha'$ martensite and the mechanical properties .....	68
<b>4.6 – Chapter summary.....</b>	<b>70</b>
<b><i>Chapter 5 – Dynamic behaviours of SLM Ti-6Al-4V .....</i></b>	<b><i>72</i></b>
<b>5.1 – Dynamic compression properties.....</b>	<b>73</b>
<b>5.2 – Adiabatic shear bands .....</b>	<b>76</b>

---

<b>5.3 – The role of deformation twins .....</b>	<b>81</b>
<b>5.4 – Dynamic recrystallized grains.....</b>	<b>89</b>
<b>5.5 – Mechanisms of the dynamic recrystallization in SLM built Ti-6Al-4V .....</b>	<b>98</b>
5.5.1 – The early stage of DRX.....	98
5.5.2 – The final stage of DRX.....	103
<b>5.6 – Chapter summary.....</b>	<b>104</b>
<b><i>Chapter 6 – Heat treatment of SLM Ti-6Al-4V .....</i></b>	<b><i>106</i></b>
<b>6.1 – Heat treatment design.....</b>	<b>107</b>
<b>6.2 – Microstructure evolution.....</b>	<b>108</b>
<b>6.3 – The decomposition of <math>\alpha'</math> martensite .....</b>	<b>116</b>
<b>6.4 – The kinetic pathways of the <math>\alpha'</math> decomposition .....</b>	<b>121</b>
<b>6.5 – The static globularization process. ....</b>	<b>124</b>
<b>6.6 – Mechanical properties.....</b>	<b>128</b>
<b>6.7 – Chapter summary.....</b>	<b>131</b>
<b><i>Chapter 7 – Conclusions and Future work .....</i></b>	<b><i>133</i></b>
<b>7.1 – Conclusions and contributions of the thesis .....</b>	<b>134</b>
7.1.1 – Evolution of SLM Ti-6Al-4V microstructures as subject to laser energy density .....	134
7.1.2 – Decomposition and globularization of $\alpha'$ martensite in SLM Ti-6Al-4V .....	135
<b>7.2 – Future work .....</b>	<b>136</b>
7.2.1 – Controlling the heterogeneity of SLM Ti-6Al-4V microstructure for superior properties.....	136
7.2.2 – Phase Field modelling on martensite evolution during Selective Laser Melting .....	136
7.2.3 – Study on machinability of SLM Ti-6Al-4V .....	137
<b>7.3 – Journal publication.....</b>	<b>137</b>
<b><i>References .....</i></b>	<b><i>138</i></b>

## List of Figures

Figure 1. Schematic illustration of a) Selective Laser Melting, b) Directed Energy Deposition and c) Electron Beam Melting (25).....	9
Figure 2. Schematic illustration of scanning strategies (28).....	12
Figure 3. Optical micrographs of a) lack-of-fusion porosity and b) gas-entrapment porosity (46).....	14
Figure 4. Morphology on the surface of a) an SLM specimen constructed vertically, b) an SLM specimen constructed horizontally, c) an EBM specimen built vertically, and d) an EBM specimen constructed in horizontal (the arrow indicates the build direction) (61).....	15
Figure 5. Schematic of phase transformation during solidification process: a) $\beta$ phase grain, b) $\alpha_{GB}$ starts nucleating, c) $\alpha_{GB}$ finishes covering on the grain boundary, d) $\alpha$ colony precipitates from the grain boundary and e) $\alpha$ basketweave is formed inside the grain (67).....	17
Figure 6. Distribution of $\alpha$ variants in presentation as a) colony structures observed by SEM (71) , b) basketweave structures observed by SEM (72), c, d) colony structures observed by EBSD indicating preferred $\alpha$ variants inside prior $\beta$ grains (73) and e, f) basketweave structures observed by SEM and EBSD with associated pole figure indicating a presence of 12 $\alpha$ variants (74).....	18
Figure 7. Diagram of phase transformation of a) iTi-6Al-4V and b) as a function of cooling rate (77) .	19
Figure 8. Schematic of martensitic transformation mechanism (62).....	19
Figure 9. Optical micrograph showing microstructure on a) 3D Ti-6Al-4V built sample, b) xz plane and c) yz plane with the arrow showing the growth direction of columnar grains (14).....	21
Figure 10. a) The Ti6Al4V single-track front view shows the development of prior $\beta$ -grains that are perpendicular to the edge of the molten pool (red line). Simulated free surface borders (yellow line) and heat-affected zone borders (green and blue line) are defined. b) Modelled front-view temperature. c) Modelled side-view temperature. d) Ti6Al4V displays two laser scanning directions (89). And e) Schematic of $\beta$ -growth direction along thermal gradient (90).....	22
Figure 11. Martensitic microstructure as highlighted by circle and arrows observed in a, b) Optical Microscope and c, d) Scanning Electron Microscope (93).....	23

---

Figure 12. Optical micrographs of a) adiabatic shear band and b) its microstructure developed in Ti-5Al-5Mo-5V-1Cr-1Fe alloy (107) .....	24
Figure 13. EBSD map of a) shear zone and b) microstructure inside ASB (111).....	25
Figure 14. Dynamic behaviours of SLM Ti-6Al-4V at different strain rates (135).....	30
Figure 15. a) SEM image of ELI argon atomised Ti-6Al-4V and b) powder size distribution .....	33
Figure 16. The ‘stripes’ scanning strategy in the SLM process .....	34
Figure 17. a) As-built rods and 20 x 10 x 10 mm solid blocks inside the working chamber, b) 10 x 10 x 10 mm solid blocks samples, c) dog-bone tensile samples machined from as-built rods and d) vertically built dog-bone tensile samples.....	36
Figure 18. Schematic illustration of a) compressive specimens machined from a horizontally built rod and b) a SHPB system .....	38
Figure 19. a) The orientation unit triangle based on the Euler angle colouring and the corresponding crystallographic planes of b) (10-10), c) (2-1-10) and d) (0001) .....	40
Figure 20. Diagram showing relationship between the relative density and the laser energy density	44
Figure 21. SEM images showing porosity at different energy density regions .....	44
Figure 22. Diagram showing the relationship between surface roughness and laser energy density..	45
Figure 23. OM images showing the top and side surface profiles in SLM Ti-6Al-4V specimens at a) insufficient, b) optimal and c) excessive energy density.....	46
Figure 24. Schematic of the simulation model of a) the one-layer scan and b) the five-layer scan .....	48
Figure 25. Heat point source as laser beam on mesh .....	48
Figure 26. The predicted isotherm profile in the a) XY plane, b) XZ plane, c) YZ plane and d) the experimental melt pool profile on the substrate plate for comparison .....	50
Figure 27. Isotherm profiles during cool down (Unit: °C).....	51
Figure 28. Solidification map showing predicted the thermal gradient G and the growth rate R along the centre line of the melt pool.....	52

---

Figure 29. Diagram of the predicted heat history in the SLM process of Ti-6Al-4V .....	54
Figure 30. EBSD orientation map of a) the $\alpha'$ martensite grains and b) the reconstructed $\beta$ grains....	54
Figure 31. Illustration of columnar $\beta$ microstructure in a) schematic graph of the sample, OM images in the b) top left corner, c) central and d) bottom right areas of the sample .....	56
Figure 32. SEM images showing the hierarchical structure of $\alpha'$ martensite at a) lower magnification: primary and secondary $\alpha'$ and b) at higher magnification: tertiary $\alpha'$ .....	57
Figure 33. Schematic illustration of the martensite evolution during the heat history of SLM process	58
Figure 34. SEM images showing the $\alpha'$ martensite grains in different conditions.....	59
Figure 35. Relationship between processing parameters and a) columnar $\beta$ grain size and b) $\alpha'$ martensite grain size.....	60
Figure 36. Grain density of the tertiary $\alpha'$ martensites in different processing conditions .....	61
Figure 37. Diagram of heat history in SLM process of Ti-6Al-4V using high laser energy density condition (2E-P-0.5V) .....	61
Figure 38. The predicted temperature isotherms in different processing conditions in the a) XY plane and b) XZ plane .....	62
Figure 39. Relationship between hardness and laser energy density .....	63
Figure 40. Tensile curves of SLM Ti-6Al-4V in different processing conditions.....	64
Figure 41. Relationship between tensile strength and laser energy density .....	64
Figure 42. Relationship between elongation and laser energy density .....	65
Figure 43. SEM images of fracture surfaces in different processing conditions .....	66
Figure 44. SEM images of fracture surfaces revealing lack of consolidation in the conditions a) 0.5E-P-2V and b) 0.5E-0.5P-V .....	66
Figure 45. SEM images showing a) micro cracks and b) stairs on the fracture surfaces of the E-P-V condition.....	67

---

Figure 46. SEM images showing a) slip sign and b) stairs on the fracture surfaces of the 2E-P-0.5V condition.....	67
Figure 47. SEM images showing a) stairs and b) stairs and pores on the fractures surfaces of the 2E-2P-V condition.....	67
Figure 48. The dynamic mechanical response of SLM Ti-6Al-4V .....	73
Figure 49. Dynamic stress and strain curves of 0.5E-P-2V samples .....	75
Figure 50. Dynamic stress and strain curves of E-P-V samples .....	75
Figure 51. Dynamic stress and strain curves of 2E-2P-V samples .....	75
Figure 52. Dynamic stress and strain curves of 2E-P-0.5V samples .....	76
Figure 53. Dynamic stress and strain curves of 4E-2P-0.5V samples .....	76
Figure 54. SEM images showing a) the 0.5E-P-2V compressed specimen and b) the local region of ASB .....	77
Figure 55. SEM images showing a) the E-P-V compressed specimen and b) the local region of ASB...	77
Figure 56. SEM images showing a) the 2E-P-0.5V compressed specimen and b) the local region of ASB .....	78
Figure 57. SEM images showing a) the 2E-2P-V compressed specimen and b) the local region of ASB	78
Figure 58. SEM images showing a) the 4E-2P-0.5V compressed specimen and b) the local region of ASB .....	78
Figure 59. Dynamic mechanical responses of the reference Ti-6Al-4V with images of interrupting tested samples at different strains .....	79
Figure 60. OM images showing the reference Ti-6Al-4V tested specimen at a) 0.17 strain, b) 0.33 strain and c) 0.5 strain .....	80
Figure 61. OM image showing the bifurcation of ASB at 0.5 strain .....	80
Figure 62. Crystallography of key deformation modes in Ti-6Al-4V.....	82
Figure 63. EBSD map of the reference Ti-6Al-4V at a) 0.17 strain, b) 0.33 strain and c) 0.5 strain.....	84



---

Figure 64. EBSD map showing secondary twins in the reference Ti-6Al-4V specimen .....	84
Figure 65. EBSD map showing a) the scanned area and b) deformation twins in 0.5E-P-2V condition	85
Figure 66. EBSD map showing a) the scanned area and b) deformation twins in E-P-V condition .....	85
Figure 67. EBSD map showing a) the scanned area and b) deformation twins in 2E-P-0.5V condition	86
Figure 68. EBSD map showing a) the scanned area and b) deformation twins in 2E-2P-V condition...	86
Figure 69. EBSD map showing a) the scanned area and b) deformation twins in 4E-2P-0.5V condition .....	87
Figure 70. ODF of the SLM Ti-6Al-4V dynamic specimen showing high intensity at $\phi = 57.2^\circ$ (marked as arrows) in the a) 0.5E-P-2V, b) E-P-V, c) 2E-P-0.5V, d) 2E-2P-V and e) 4E-2P-0.5V condition.....	88
Figure 71. EBSD map of the ASB region and b) high- magnification of DRXed grains with misorientation angle boundary in the reference Ti-6Al-4V at 0.33 strain .....	90
Figure 72. a) EBSD map of the ASB region and b) high- magnification of DRXed grains with misorientation angle boundary in the reference Ti-6Al-4V at 0.5 strain .....	90
Figure 73. a) EBSD map of the ASB regions and b) Pole figure of the DRXed grains in 0.5E-P-2V condition .....	91
Figure 74. a) EBSD map of the ASB regions and b) Pole figure of the DRXed grains in E-P-V condition	91
Figure 75. a) EBSD map of the ASB regions and b) Pole figure of the DRXed grains in 2E-P-0.5V condition .....	92
Figure 76. a) EBSD map of the ASB regions and b) Pole figure of the DRXed grains in 2E-2P-V condition .....	92
Figure 77. a) EBSD map of the ASB regions and b) Pole figure of the DRXed grains in 4E-2P-0.5V condition.....	92
Figure 78. ODF figures of the DRXed grains in the condition a) 0.5E-P-2V, b) E-P-V, c) 2E-P-0.5V, d) 2E-2P-V, and d) 4E-2P-0.5V.....	93
Figure 79. KAM map showing thermal dislocations in the as-built condition of 0.5E-P-2V at a) lower and b) higher magnification.....	94

---

Figure 80. KAM map showing thermal dislocations in the as-built condition of E-P-V at a) lower and b) higher magnification.....	95
Figure 81. KAM map showing thermal dislocations in the as-built condition of 2E-P-0.5V at a) lower and b) higher magnification.....	95
Figure 82. KAM map showing dislocations in a) the ASB region and b) high magnification inside the ASB of the 0.5E-P-2V condition.....	96
Figure 83. KAM map showing dislocations in a) the ASB region and b) high magnification inside the ASB of the E-P-V condition.....	96
Figure 84. KAM map showing dislocations in a) the ASB region and b) high magnification inside the ASB of the 2E-P-0.5V condition.....	97
Figure 85. KAM map showing dislocations in a) the ASB region and b) high magnification inside the ASB of the 2E-2P-V condition.....	97
Figure 86. KAM map showing dislocations in a) the ASB region and b) high magnification inside the ASB of the 4E-2P-0.5V condition.....	97
Figure 87. EBSD and KAM maps showing the DRXed grains at the early stage (in the transition zones) at a) 0.5E-P-2V, b) 2E-P-0.5V and c)2E-2P-V condition.....	101
Figure 88. Misorientation angle distribution the DRXed grains in different conditions .....	102
Figure 89. Diagram showing the heat treatment strategies.....	108
Figure 90. OM images of the microstructure after heat treated at a) 850 °C – 4h showing columnar grains and b) 950 °C – 4h showing $\alpha_{GB}$ and globular grains .....	109
Figure 91. EBSD maps showing the microstructure in the annealing conditions of a) 850 oC – 2h, b) 950 oC – 2h, c) 950 oC – 4h and d) 950 oC – 8h .....	109
Figure 92. EBSD maps showing the microstructure in the annealing conditions of a) 850 °C – 4h, b) 950 °C – 2h and c) 950 °C – 6h.....	110
Figure 93. EBSD map showing the hierarchical structures at 850 °C – 4h.....	110
Figure 94. Diagram showing the coarsening effect in the hierarchical structure by heat treatment.	113

---

Figure 95. Schematics definition of grain aspect ratio and shape factor .....	114
Figure 96. Diagram showing grain aspect ratio in the as built and heat treatment conditions.....	114
Figure 97. Diagram showing grain shape factor in the as built and heat treatment conditions.....	115
Figure 98. Diagram showing the globularized fraction in the as built and heat treatment conditions .....	115
Figure 99. Illustration of the total free energy of the Ti-Al-V system on the $\eta - xV$ space.....	116
Figure 100. The total free energy diagram showing (a) phase stability and (b) transformation pathway of SLM Ti-6Al-4V .....	118
Figure 101. Diagram showing the evolution of $\eta$ over simulation iteration at different temperatures .....	119
Figure 102. The Phase Field simulated microstructure at a) 850 °C and b) 950 °C .....	119
Figure 103. SEM images showing solute-rich and solute-lean phases with the appearance of anneal twins marked by arrows in a) 950 °C – 4 hours and b) – 8 hours .....	120
Figure 104. The evolution of $\eta$ in the free energy diagram at a) 850 °C and b) 950 °C.....	120
Figure 105. SEM image showing the $\alpha_s$ laths in the equiaxed $\beta$ grain in 950 °C – 6h.....	122
Figure 106. Thermodynamic diagrams and schematic illustrations showing the kinetic pathway of SLM Ti-6Al-4V from a) initial $\alpha'$ martensites, b,c) spinodal decomposition into hcp solute-lean and hcp solute-rich phases and d,e) precipitation into equilibrium $\alpha+\beta$ .....	123
Figure 107. Thermodynamic diagrams and schematic illustrations showing the kinetic pathway of SLM Ti-6Al-4V from a) initial $\alpha'$ martensites, b,c) spinodal decomposition into hcp solute-lean and bcc solute-rich phases and d,e) precipitation into equilibrium $\alpha+\beta$ .....	123
Figure 108. Schematic of the globularization process: a) initial morphology of solute-rich and solute-lean phases, b) initial solute-lean $\alpha$ grain with anneal twins, c) boundary splitting mechanism at the triple points, d) termination migration mechanism on fragmented grains and e) final globular grains .....	124
Figure 109. a) EBSD map the globularized microstructure showing fragmented grains, b) anneal twins and c) thermal grooving process in the solute-lean $\alpha$ grain at 950 °C.....	125

---

Figure 111. Diagram showing the stress-strain curves of the as built and exemplary annealing conditions .....	129
Figure 112. Diagram showing the strength and elongation of the as built and annealing conditions	129
Figure 113. Diagram showing dynamic stress-strain curves of the three annealing conditions .....	130
Figure 114. Dynamic mechanical properties of the as built and three annealing conditions .....	131

---

## List of Tables

Table 1. Classification of AM processes.....	8
Table 2. Processing parameters in the SLM process .....	10
Table 3. Processing conditions and resulted porosity in Selective Laser Melting of Ti-6Al-4V .....	13
Table 4. Quasi-static tensile properties of Ti-6Al-4V manufactured by SLM and traditional methods	26
Table 5. Heat treatment results on quasi-static tensile properties of SLM Ti-6Al-4V.....	27
Table 6. The chemical composition of ELI argon atomised Ti-6Al-4V grade 23 .....	33
Table 7. Design table of processing parameters and responses on relative density and surface roughness .....	42
Table 8. Analysis of Variance on the relative density response .....	43
Table 9. Analysis of Variance on the top surface roughness response .....	43
Table 10. Analysis of Variance on the top surface roughness response .....	43
Table 11. Optimal processing window for SLM Ti-6Al-4V .....	46
Table 12. Standard parameters for thermal modelling of SLM Ti-6Al-4V .....	49
Table 13. Groups of processing parameters to analyse the effect of laser energy density .....	59
Table 14. Processing conditions of SLM Ti-6Al-4V for dynamic properties analysis .....	73
Table 15. The mechanical properties under dynamic conditions of SLM Ti-6Al-4V.....	74
Table 16. Deformation twinning modes in titanium and its alloys.....	82
Table 17. Twinning fraction in the reference material at different strains (Unit: %).....	82
Table 18. Twinning fraction in SLM Ti-6Al-4V samples in different processing conditions (Unit: %)....	83
Table 19. SEM images and the phase fraction analysis in each annealing condition.....	111

## List of Abbreviations

3D	Three-dimensional
AC	Air cooling
AM	Additive manufacturing
ASB	Adiabatic shear band
ASL	Adiabatic shear localization
BCC	Body centred cubic
BMD	Bound metal deposition
CAD	Computer aided designed
CALPHAD	Calculation of phase diagrams
CDRX	Continuous dynamic recrystallization
CRSS	Critically resolved shear stress
DDRX	Discontinuous dynamic recrystallization
DED	Directed energy deposition
DMLS	Direct metal laser sintering
DRX	Dynamic recrystallization
EBF	Electron beam free form fabrication
EBM	Electron beam melting
EBSD	Electron backscattered diffraction
EDM	Electrical discharge machining
EDS	Energy dispersive X-ray spectroscopy
FC	Furnace cooling
FCC	Face centred cubic
FDM	Finite difference method
FESEM	Field emission scanning electron microscopy
GND	Geometrically necessary dislocation
HAZ	Heat affected zone
HCP	Hexagonal close packed
IPF	Inverse pole figure
ISO	International organization for standardization
KAM	Kernel average misorientation
LENS	Laser engineered near net shape
ODF	Orientation distribution function

OM	Optical microscopy
PF	Pole figure
PriSM	Progressive subgrain misorientation
SEM	Scanning electron microscopy
SHPB	Split-Hopkinson pressure bar
SLM	Selective laser melting
SLS	Selective laser sintering
SMD	Shaped metal deposition
TDRX	Twinning-induced dynamic recrystallization
UTS	Ultimate tensile strength
WAALM	Wire arc additive layer manufacturing
WQ	Water quenching
XRD	X-ray diffraction
YS	Yield strength

# Chapter 1 – Introduction

In this chapter, the research background, motivation, objectives and scope are discussed. The background provides a brief description of the unique features of additive manufacturing (AM) and in production of metallic functional parts, especially the titanium alloys, for industrial applications. Understanding the metallurgy of AM-built titanium alloys thus motivates this research. The main objectives of this work, which are to characterise the microstructure evolution and mechanical properties of Ti-6Al-4V built by Selective Laser Melting, an AM process, will be further evaluated. At the end of this chapter, the thesis organisation is also presented as an overview of this thesis' content.



## **1.1 – Background**

AM, also commonly referred to as 3D printing, is defined by the successive fusion of material layers into a 3-dimensional (3D) component. AM processes deposit and fuse raw materials—which may be solid, liquid or suspension based—on the particular position inside the structure envelope to create the desired transverse profile. These cross-section layers are sequentially added to create a 3D structure, which is why they are called additive manufacturing.

Conversely, traditional processes are often subtractive as they rely on a set of computer-generated numerical controls (CNC) to cut, frame, drill and fit the object in net form. Although subtractive operations can produce complex external features with tight tolerances, they are not ideal for the production of internal features, which the cutting instruments cannot reach. Parts with complex internal structures may be created by casting, which involves the creation of an equally complex mould. Because the moulds can be costly and time-consuming to make, this method is also only justified when the casting volume is high enough to normalise the mould costs (1). However, in AM, where geometric complexity comes at little to no extra cost, this concern is not important. Simply put, AM has the ability to revolutionise the design and production of metallic products.

In addition, AM technologies are increasingly mature for industrial acceptance over the last few years, and the sales of metal AM systems have been growing significantly (2). Particularly during 2019–2020, the demand for AM has risen considerably and many companies have shifted their manufacturing chains to AM due to the fact that the Covid-19 pandemic has heavily affected both the global supply chain and the logistics sectors, while the most of the world's conventional production processes are located in China (3). Consequently, the interest in metal AM research has increased significantly in the last five years.

Metal AM components typically experience a complex cyclical thermal history involving directional heat extraction, repeated melting, and rapid solidification that would create heterogeneous microstructures which differ intrinsically from the material components created by conventional methods (4, 5). As a consequence, heterogeneous properties in metal AM components can occur. Besides, AM defects, for instance pores and rough surfaces, also contribute to metal AM parts' heterogeneous qualities (6).

No exception is the Selective Laser Melting (SLM), which is the AM powder bed fusion technique. SLM uses a laser beam to melt metal powder bed layers selectively. Because of its performance, high resolution, good surface finish and noble gas operating environment, SLM is a favourite AM technique for manufacturing Ti-6Al-4V components. The workhorse Ti-6Al-4V is the most common titanium alloy

and considered one of the most important engineering materials owing to its high strength-to-weight ratio, excellent resistance to corrosion and good biocompatibility, which are extremely useful in aerospace, maritime & offshore, medical and so on (7). Thus, Ti-6Al-4V is one of the most researched SLM AM content. However, there are limitations related to the microstructures of the Ti-6Al-4V parts produced by SLM.

Firstly, it still remains to be primitive stage which needs further established on how SLM influences the microstructure characteristics of the as-built Ti-6Al-4V parts. The SLM Ti-6Al-4V microstructure is generally made from columnar prior  $\beta$  and fine acicular  $\alpha'$  martensite as a result of high thermal gradient during fabrication process (8). However, few studies have examined the evolution mechanism of microstructures that control the growth of such columnar and acicular grains during the SLM manufacture of Ti-6Al-4V. A thorough understanding of the cyclic thermal microstructures development of the as-constructed Ti-6Al-4V parts will play a critical role and contribute to the universal microstructure regulation knowledge in SLM.

Secondly, the lack of knowledge of the evolution of microstructures under SLM Ti-6Al-4V's dynamical working conditions is a major concern. Conventional mechanical experiments are performed in almost quasi-static environments where strain rates are smaller than  $10^{-3} \text{ s}^{-1}$  (9). On the other hand, dynamic conditions are defined if the strain rate is large enough so that the dislocation speeds are the same or even bigger than the shear wave velocity, which are measured by most literatures to be  $10^2 - 10^4 \text{ s}^{-1}$  (10, 11). Deformation is significantly different in these strain rates than in quasi-static settings. High strain rates also impact thermally active mechanisms and can result in adiabatic heat microstructural changes (12). In fact, dynamic deformation can be found in industry application such as aircraft landing gears, bird strike, car crash or ballistic impact armours. Therefore, recognising SLM Ti-6Al-4V's reaction to a dynamic deformation plays a significant role in its applications and particularly in safety standards.

Another issue to be tackled for Ti-6Al-4V processed by SLM is how the mechanical properties correspond to conventional types. The rapid cooling speeds and layer build-up of the SLM technique in particular contribute to the non-equilibrium phase and anisotropic behaviours (6, 13, 14). The martensitic microstructure results in high hardness and high strength, but poor ductility, which requires the use of heat treatments in order to achieve the combination of properties close to those of bulk materials. Vrancken, Thijs (15) discovered that heat treatments on SLM Ti-6Al-4V as-built parts are required adjustments to enhance the mechanical properties due the difference in the starting microstructure. Standard heat treatments such as milling, duplexing, and beta annealing do not improve the efficiency of the SLM Ti-6Al-4V.

## **1.2 – Motivation**

The justification behind the application of AM processes instead of conventional fabrication methods is their ability to produce structures and topologies that are not feasible by traditional means. For that reason, in order to help the novel design process of AM parts by understanding the material properties of a specific design part based on its production and subsequent thermal treatment process, a thorough understanding of the metallurgical aspects of SLM is important.

Metal and alloy microstructures have a significant effect on the material's properties. Numerous mechanical properties of materials, such as strength, hardness and creep resistance, are dependent on the phase morphology, grain size and orientation, and dislocations resulted from processing. Thus, understanding grain microstructures and their modifications as a result of recrystallization and grain growth is critical, as a change in microstructure results in a change in material properties, which may render the material unsuitable for use in such applications. Additionally, the microstructures are critical for the design and application of enhanced-performance structures. Over the last few decades, considerable work has been directed toward developing novel materials with unique microstructures capable of exhibiting unconventional mechanical properties in both the static and dynamic regimes. In short, the values of investigating on microstructure evolution and regulation is undoubtedly important for the development and application of engineering structures and processing methods.

Ti-6Al-4V titanium alloy is focused on because of its use in a variety of top-value applications such as surgical devices, aircraft and maritime components, which are more likely to utilise the AM technology in manufacturing due to the currently high initial cost of AM systems. Also difficult is the manufacture of titanium alloy through traditional processing—e.g. machining—because of its high resistance and chemical reactivity, which reduces the tool life in machining processes significantly. For the first time in 2014, the commercial use of metal AM technology started with the launch of the Swedish supercar manufacturer Koenigsegg for the One:1 project. The Swedish supercar had titanium airducts, exhaust components and full AM-produced turbo-loaders (16). As such, the application of AM for replacing the traditionally manufacturing of titanium alloys is a matter of time, when the AM initial and running costs are lower thanks to the advancement of technology. However, understanding about the performance of AM manufactured materials and particularly SLM Ti-6Al-4V is severely lacking under dynamic conditions and is thus necessary to pay greater attention.

This thesis takes into account the dynamic behaviours of the SLM Ti-6Al-4V for safety purposes when using the material for industrial and commercial applications. On 15 April 1912, the British passenger liner RMS Titanic sank, following its colliding with an iceberg in the North Atlantic Ocean. As the Titanic clashed with the iceberg, the hull plates ripped open and began to crack as the ship filled with water.

Low water temperatures and high dynamic loading also contributed to the brittle failure of the rivets used to secure the hull plates to the main structure of the ship. Due to excessive loading, the rivets were sheared off or the heads popped off during impact, exposing riveted seams. Additionally, the rivets around the plates' perimeter elongated as a result of the pressures applied by the water, which ruptured the caulking and created another inlet for the water. The devastating accident resulted in the horrific deaths of nearly 1500 passengers and crew, making the Titanic the deadliest international maritime tragedy in modern history due to material failure. The accident is the turning point for the work in complex environments on material behaviour and failure. The subject has been more than 100 years since then, both in academic and in industrial studies, especially with the rise of the offshore, automotive and aerospace industry.

### **1.3 – Objectives**

The aims of this study are to obtain a detailed understanding for the microstructures and mechanical properties of SLM Ti-6Al-4V parts and to recognise issues of heterogeneity and defects throughout the process. The research will concentrate on the phase and microstructural evolution of Ti-6Al-4V during the fabrication, the heat treatment process and the conditions of impact loading. This research will be the first to explore the microstructure evolution of SLM Ti-6Al-4V under dynamic conditions that aids understanding the microstructural regulation of the metallic materials manufactured by SLM.

The objectives of the present research are listed as follows:

1. Parametric study on the microstructure development during SLM fabrication process and the resulted mechanical properties of SLM Ti-6Al-4V.
2. Investigation on the effect of processing parameters on the dynamic recrystallization of the as-built martensitic microstructure under high strain rate condition.
3. Evaluation on the decomposition mechanism of the initial martensitic microstructure and the static globularization process in the heat treatments of SLM Ti-6Al-4V alloy in order to improve the mechanical properties.

### **1.4 – Scope**

The scope of this thesis is listed as follows:

1. For investigating metallography and phase characterization, Optical microscope (OM), scanning electron microscopy (SEM), electron backscatter diffraction (EBSD) and energy dispersive spectroscopy (EDS) will be carried out.

2. Thermal simulation and Phase Field modelling will be done in MATLAB to understand the metallurgical aspects in SLM fabrication and heat treatment processes.
3. Mechanical properties characterization of SLM built and traditionally built parts for comparison will follow ASTM standards.

### **1.5 – Thesis organisation**

This thesis consists of 7 chapters.

Chapter 1 introduces the research background, motivation as well as objectives and scope of this study.

Chapter 2 is dedicated to reviewing the current technology of the SLM process with details on the working principle and fundamental processing parameters, and the literature on the metallurgy of titanium alloys, especially Ti-6Al-4V. The critical aspects of SLM Ti-6Al-4V in the as-built conditions are discussed, which ranges from manufacturing defects, microstructure and phase transformation to mechanical properties in the as-built state and after subsequent heat treatments, in both quasi-static and dynamic conditions.

Chapter 3 describes the methodology and equipment used in this study

Chapter 4 devises optimum parameters by analysing the relative density and surface morphology of as-built components with a wide range of laser energy densities. Using thermal simulation, the phase transition and microstructure evolution during the SLM manufacturing process are investigated. SLM Ti-6Al-4V's microstructure and quasi-static mechanical properties are quantified in an attempt to monitor these characteristics through processing parameters.

Chapter 5 characterises SLM Ti-6Al-4V's dynamic compressive properties. In terms of texture evolution and dynamic recrystallization mechanisms, variance in microstructure shift within adiabatic shear bands as subject to laser energy densities is emphasised. The dynamic behaviours of traditionally built parts are also taken into examination to aid the analysis and to highlight the difference in microstructure evolution between the two manufacturing methods.

Chapter 6 designs heat treatment plans to achieve the mechanical properties of SLM Ti-6Al-4V parts as comparable to wrought products. In doing so, the decomposition of  $\alpha'$  martensite and the globularization process play an important role and are characterised by experiments and Phase Field modelling.

Chapter 7 summarises the thesis' main conclusions and highlights the research gaps not covered in this current work for future investigations.

## **Chapter 2 – Literature review**

This chapter presents a well-round perspective of Ti-6Al-4V manufactured by additive manufacturing (AM). The state-of-the-art technology of Selective Laser Melting (SLM) is then introduced and analysed, with advantages and challenges, compared to the conventional manufacturing methods. It provides a detailed overview on the manufacturing process, metallurgy, mechanical properties and heat treatment of SLM Ti-6Al-4V.

## **2.1 – Selective laser melting**

### **2.1.1 – Working principle**

Additive manufacturing (AM), which is commercially known as 3D Printing, is a modern near-net shape manufacturing technique to produce solid functional parts by consolidating partial or completely melted layers of material. By the definition of the Technical Committee of the ASTM F42, AM is the process for joining materials, as opposed to subtractive manufacturing, for the creation of solid parts from a 3D model data, typically from layer to layer (17). The deposited materials are melted by an electron beam or a laser focussed heat source. Each layer is a section of the final 3D part; that is, the final component's 3D geometry is created by building a stack of 2D profiles, layer-by-layer via locally melting.

In general, it is possible to classify metal additives based on the heat source and material feedstock, as shown in Table 1. Among these processes, selective laser melting (SLM), electron beam melting (EBM) and direct metal deposition (DED) are the most common processes to manufacture Ti-6Al-4V which have been widely used in aerospace industry. This study will focus on the SLM process due to the rising demand in the aerospace industry as well as the greater advantages on the printing resolution and surface quality as presented below (18).

*Table 1. Classification of AM processes*

Deposition method	Heating source			
	High power beam		Electric Arc	Resistance heater
	Electron beam	Laser beam		
Powder-bed	EBM	SLM		
		SLS (DMLS)		
Powder-blown		DED (LENS)		
Wire	EBF	SMD	WAALM	
Extrusion-based				BMD

\*EBM: electron beam melting, SLM: selective laser melting; SLS: selective laser sintering, DMLS: direct metal laser sintering, LENS: laser engineered near net shape, DED: directed energy deposition, EBF: electron beam free form fabrication, SMD: shaped metal deposition, WAALM: wire arc additive layer manufacturing, BMD: bound metal deposition.

SLM was introduced in 1995 at ILT Institute Fraunhofer (19). The system, as shown in a, comprises a process chamber, a laser source-connected optical unit and a control computer. The powder is put on the retractable platform and then spread through the use of a coating system. The optical unit

produces and directs the laser beam by scanner mirrors for melting the metal powder locally. By such sophisticated system, complex geometries can be generated fully automatically directly from the 3D CAD data.

The build chamber is filled with inert gases such as argon to maintain a low oxygen atmosphere to prevent oxidation during part production. The powder melts and forms a fluid melting pool when sufficient laser power is applied, which solidifies rapidly to the room temperature and forms the final dense part. After the scan fuses the cross sections of each layer, the build platform is reduced by an amount equivalent to the prefixed thickness of the layer, and a new powder layer is spread over the powder bed. This process is continued until the final part is fully fabricated (8, 20).

Generally, SLM works in the same principle as EBM, a powder bed deposition process, except that the heat source is a laser beam, as shown in Figure 1. And the main distinction between DED and SLM is the method in which powder materials are deposited. In SLM, metal powders are evenly spread by a rake on the substrate, rather than being blown out of a nozzle as in DED (see Figure 1b). Unmelted powders in SLM's powder bed can act as support materials to build the subsequent layers, enabling higher flexibility of SLM compared to DED. Additionally, The layer thickness of the SLM is tens of microns, much smaller than that of DED and EBM processes (21). Thus, this technique can produce high-precision parts with better resolution and surface quality than EBM and DED processes. References to the working principle of the SLM machine can be found in the references (22-24).

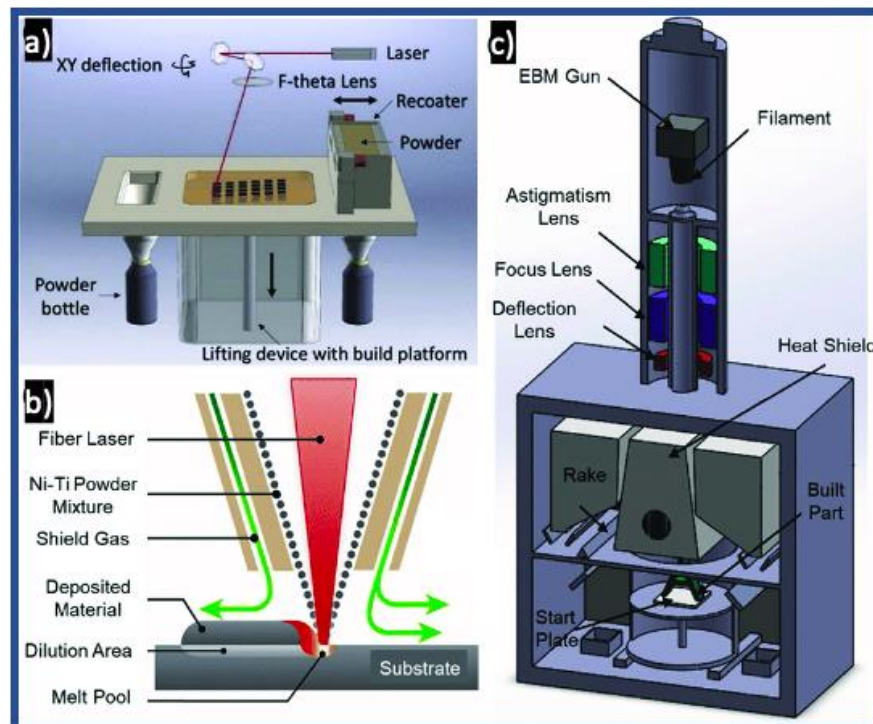


Figure 1. Schematic illustration of a) Selective Laser Melting, b) Directed Energy Deposition and c) Electron Beam Melting (25)



AM technology, including SLM, has many advantages over conventional manufacturing methods and is actively considered for manufacturing functional components for commercial and industrial applications. These benefits include:

- Manufacturing of complex parts with innovative shapes and structures which cannot be produced by traditional manufacturing methods.
- Creating functionally graded materials to change the properties of a single part in locations of strategic interest.
- Enabling multi-material manufacturing or joining two dissimilar materials together within a single part.

### **2.1.2 – Processing parameters**

SLM is an advanced process which involves many factors affecting the finishing quality of the printed products. These factors can be classified in four groups relating to the material, the laser source, the scanning process and the environment, as tabulated in Table 2.

*Table 2. Processing parameters in the SLM process*

<b>Materials</b>	<b>Laser</b>	<b>Scan</b>	<b>Environment</b>
Material composition	Laser scan mode	Scanning speed	Platform temperature
Powder relative density	Wavelength	Scan distance	Gas flow rate
Particle size distribution	Laser power	Hatch spacing	Type of inert gas
Particle shape	Offset point	Layer thickness	Part orientation
Thermal properties	Laser spot size	Scan sectors	Part placement
Powder flowability	Laser type	Scan pattern	Chamber pressure
		Border contours	

Taking into consideration so many material and processing parameters, careful monitoring of the relevant factors is required to produce printed parts with the highest standard. Among these, the SLM system specifies multiple laser parameters (such as laser wavelength, laser operating mode and spot size) which cannot be altered. Furthermore, several material parameters are set for a given powder, such as thermal properties. These define the limits of the SLM process.

Laser power, scan speed, hatch spacing and layer thickness have been extensively analysed as the primary processing parameters for SLM (8, 26). Such parameters specify the energy that the laser beam delivers to the raw powder in a volumetric unit known as energy density ( $E$ ):

$$E = \frac{P}{V \cdot h \cdot t} \quad (\text{Equation 1})$$

in which  $P$  is the laser power,  $V$  is the scanning speed,  $h$  is the hatch spacing and  $t$  is the layer thickness. The energy density affects the physical densification, and thus determines the physical and mechanical qualities of the SLM fabricated parts.

During the manufacturing process, the laser beam moves constantly, defined by the scanning speed, across the powder bed. The scanning speed regulates the time required for the production. Therefore, if a fast processing time is needed, higher scanning speed is required. The maximum scanning speed which can be employed is restricted by the laser's maximum power inside the SLM system since high scanning speed with low laser power may lead to an insufficient fusion and a failed printing job.

Layer thickness determines how much energy a powder layer needs to melt and consolidate completely. To be more specific, it is not possible to link well between layers unless previously processed layers are also partly remelted, which is controlled by the thickness of the powder layer. Production time is shortened by adding larger layer thickness, but at an expense of surface quality and dimensional precision. On the other hand, higher energy density is needed to melt and bond thicker layers of powder. In addition, the hatch spacing has been reported to impact the overlap and bonding of neighbouring melting tracks and hence affect the porosity and roughness of the manufactured parts in SLM (8, 27).

The scan pattern, also called the scan strategy, can be built in many respects. Usually, the scan pattern comprises of straight and parallel scan vectors which can be modified inside or between consecutive layers. And the configuration of the scanning techniques thus affects the quality of SLM components. Figure 2 shows some examples of the scanning strategies, including the 'meander', 'stripes' and 'chessboard'. The 'meander' comprises straight line vector path from each side of the border. This strategy is quick and efficient, which is ideal for parts with a small XY cross section, however it also comes with inconsistent heat distribution throughout each layer. In the 'stripes' strategy, the area within the border is split into strips, commonly 5-10 mm wide, and a meander technique is used within each strip. This method allows constant time between each successive track and therefore maintains a more consistent temperature throughout, which is ideal for parts with a large XY cross section but slower than the 'meander' as more laser jumps are required. The 'chessboard', is a further advancement on 'stripes' in which the area is split into squares like a chessboard. This strategy is applied in order to minimise the residual stress however is not advised when productivity is in favoured due to significantly slower scanning time.

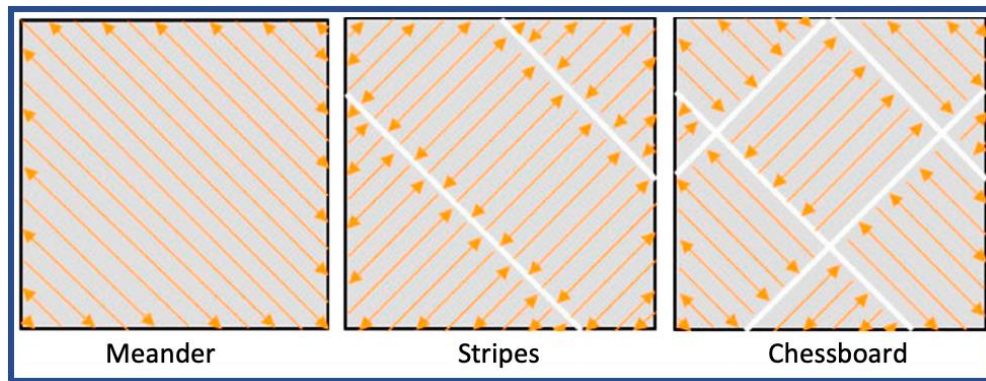


Figure 2. Schematic illustration of scanning strategies (28)

## **2.2 – Defects in selective laser melting of Ti-6Al-4V**

### **2.2.1 – Porosity**

Theoretically, AM techniques can achieve a completely dense structure, but non-optimal processing conditions may result in porosity. The root of porosity in SLM is directly related to the melt pool behaviour produced at each laser exposure and the quality of the raw powder. Therefore, porosity can be minimised in the final part by maintaining strict process control over essential process parameters such as various scanning strategies, laser energy density, powder density, layer thickness and hatch spacing. Many authors have stated that the EBM technique produces almost fully dense components, while the samples fabricated by the SLM method display an overall density of 98 to 99 %, which is lower.

Porosity forming in SLM parts is directly linked to the melting pool behaviours. The melt track during scanning has been reported to become inconsistent for inaccurate choices of laser power and scanning speed (29, 30). Besides, excessive overlap of the neighbouring scan tracks will contribute to local powder denudation and, therefore, porosity (31). The characteristics of the material powder, such as particles' shape and size distribution, strongly defines the degree to which powder particles are bundled during layer deposition. Therefore, it will influence the deposited layer's thickness and relative density, which in turn influence the relative density of the printed parts.

Indeed, unregulated porosity is unavoidable and very typical in SLM Ti-6Al-4V parts. Using X-ray tomography, Leuders, Thöne (32) reckoned 0.23% porosity in as-fabricated samples. Kasperovich and Hausmann (33) recorded that 0.08 % porosity could still stay under optimised SLM conditions, and small-sized pores hold a significant volume percentage. Besides, the unregulated pores of the Ti-6Al-4V produced by SLM will degrade its material properties. The shape and orientation of pores significantly affect the ductility of SLM Ti-6Al-4V, as observed by Vilaro, Colin (34). Macroscopic analysis and microstructure studies showed that pores could act as the nucleation sites for initiating

adiabatic shear bands and microcracks, which are critical in the mechanical strength of Ti-6Al-4V under dynamic and quasi-static conditions (35, 36). See Table 3 for more information on the porosity of SLM Ti-6Al-4V from the literature.

*Table 3. Processing conditions and resulted porosity in Selective Laser Melting of Ti-6Al-4V*

Ref.	Power (W)	Scan Speed (mm s <sup>-1</sup> )	Hatch (μm)	Layer (μm)	Porosity (%)	Technique/Resolution
(37)	42	200	75	30	1.42 ± 1.37	Archimedes (NA)
(8)						
(33)	200	1250	–	40	0.11 ± 0.04	Optical density (22 μm/voxel)
(32, 38)	400	–	–	30	0.23	Tomography (22 μm/voxel)
(14)	157	225	100	50	0.1 - 0.3	Optical density (22 μm/voxel)
(39)	195	225	–	–	0.3 ± 0.1	NA
(40)	120	960	100	30	0.45 ± 0.1	Archimedes (NA)
		540			1.37 ± 0.08	
		400			5.23 ± 0.1	
		1260			1.37 ± 0.07	
		1500			5.48 ± 0.11	
(34)	160	600	200	40	< 1.0	Archimedes (NA)
(41)	175	710	120	30	< 0.5	Optical density (NA)
(42)	–	–	–	–	< 0.5	Tomography (NA)
(43)	150-200	800-1500	75	20	< 0.1	Optical density (NA)
(44, 45)	375	686-1029	120	60	< 0.5	Tomography (NA)

NA: Not Applicable

The porosity in the SLM manufactured parts consists of two types of pores: pores by gas entrapment and pores by lack of fusion (36). The morphology of these two pores is shown in Figure 3. The spherical or elliptical form of the gas pores is usually approximately 1–100  $\mu\text{m}$  in diameter and is uniformly distributed in the material. The circular shapes indicate that these pores are created by the gas entrapment, meaning that the gas trapped in the melt pool hasn't escaped in time and has instead been caught in the solidified bead (46-48). Slower scan speed and increase laser power typically mitigate gas pores in some way but can hardly fully remove them (49).

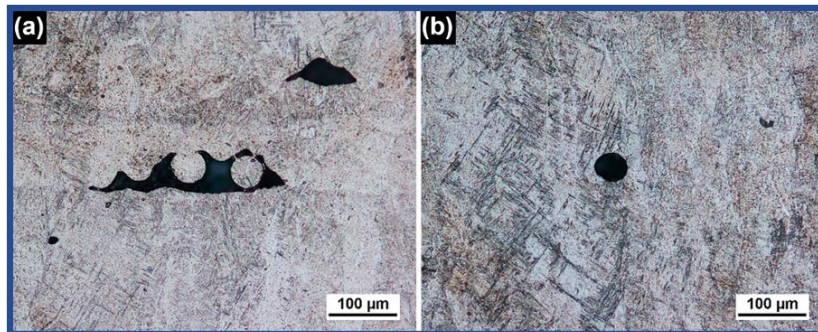


Figure 3. Optical micrographs of a) lack-of-fusion porosity and b) gas-entrapment porosity (46)

Unlike gas pores, lack-of-fusion pores are described to be bigger and have irregular shapes with sharp tips. Such pores are usually formed and spread in the joint region over two neighbouring layers. As described in the literature (34, 50), lack-of-fusion pores are created mainly due to deviations from optimal processing conditions, such as insufficient laser energy to try to fuse extremely large quantities of material, leading to inadequate melting and poor bonding. These pores' sharp tips are prone to extreme local stress and cause premature failure when exposed to loading (34, 36).

### **2.2.2 – Surface quality**

Achieving good surface finish on the functional parts is a very important requirement in aerospace industry to avoid surface related cracking and premature failure (18). In spite of substantial improvements in system, material capability and dimensional accuracy in recent years, SLM continues to suffer significant surface quality disadvantages. Generally, it comes to three factors contributing to surface roughness: (1) staircase effect (2) adherence of partially melted powders to the outer surface, and (3) existence of open pores and incompletely melted regions (51). Yet, all three factors share one similar thing: non-optimal processing conditions.

Granted, laser power, scanning speed, layer thickness and hatch spacing have been reported to be the key parameters influencing the SLM surface quality (52-54). Mumtaz and Hopkinson (53) confirmed that high powers tend to reduce the surface roughness as higher-energy recoil pressures smoothen the melting pool and increase the wettability to mitigate the balling effect. In addition, a relatively low

speed is normally selected because the extended time helps the melt pool to redistribute and obtain a smooth surface (53). Wang, Liu (55) have shown that the cumulative effects of scanning power and velocity define the scanning tracks' characteristics, such as track width and distance, which are essential to a good surface quality.

Similar conclusions have been drawn on the Ti-6Al-4V manufactured by SLM as well as other AM processes. Resch, Alexander (56) found that the surface quality of SLM Ti-6Al-4V improves directly with lower scanning speeds. In the same line, Zhai, Galarraga (57) have found that higher laser power ensures lower surface roughness of EBM and DED built Ti-6Al-4V products. More importantly, the experimental work of Mahamood and Akinlabi (58) showed that if the power is too high, powder spattering may occur due to the excessively high amount of energy density in the melting pool, leading to a poor surface finish. As seen by Kaplan and Groboth (59) and Mazumder, Dutta (60), a suitable range of hatch distance values would essentially flatten the surface.

Furthermore, Ti-6Al-4V built by SLM often has better surface finish than its counterparts built by EBM. Rafi, Karthik (61) suggested that difference between SLM and EBM processing conditions would account for different surface quality. Figure 4 shows the external surface morphologies of SLM and EBM Ti-6Al-4V specimens built vertically and horizontally. As being shown, the surface built by EBM has more partially melted powder, while the surface built by SLM is smoother. This is due to higher thermal radiation from the melt pool caused by a high energy electron beam. Besides, since the staircase effect is related to track width and hatch distance, SLM appears to produce a smaller melting pool that ensures better surface quality.

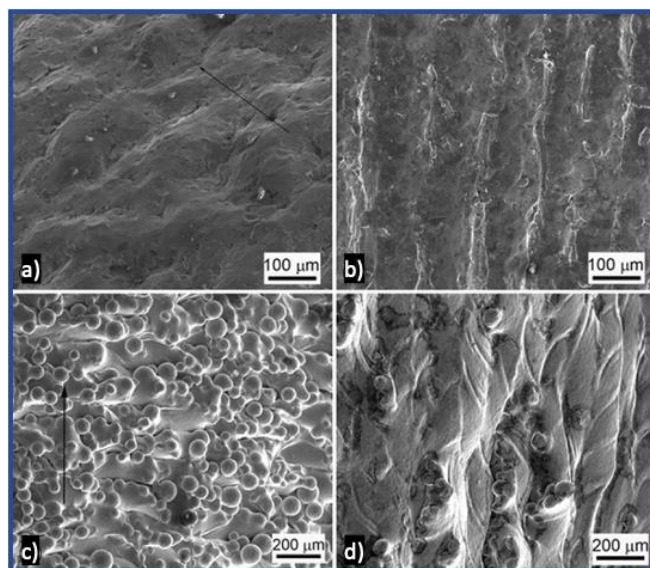


*Figure 4. Morphology on the surface of a) an SLM specimen constructed vertically, b) an SLM specimen constructed horizontally, c) an EBM specimen built vertically, and d) an EBM specimen constructed in horizontal (the arrow indicates the build direction) (61)*

Finally, it is worth noting that the surface finish of SLM Ti-6Al-4V can only be improved to some degree by the optimal processing parameters. To achieve a good surface quality, some kind of post-processing is therefore needed. In fact, post-processing is mandatory for almost all AM parts in aerospace industry, ranging from machining to chemical etching and vibrahoning as subject to structure complexity.

### **2.3 – Phase transformation in Ti-6Al-4V**

Titanium is a polycrystal element consisting of more than one crystal structure depending on temperature. At low temperatures, pure Ti transforms into an *hcp* form, known as  $\alpha$  phase (with lattice parameters  $a = 0.295$  nm and  $c = 0.468$  nm), whereas at high temperatures, when heated above 882 °C, Ti processes a *bcc* form, known as  $\beta$  phase (with lattice parameter  $a = 0.332$  nm), until the melting temperature reaches approximately 1670 °C (7).

Ti-6Al-4V is a titanium alloy that solves 6 wt.% Al and 4 wt.% V to pure Ti. Adding  $\alpha$  stabiliser (Al) and  $\beta$  stabiliser (V) lets Ti-6Al-4V retain dual-phase  $\alpha+\beta$  at room temperature. However, Ti-6Al-4V's phase transformation strongly depends on the temperature history and cooling rates induced by the manufacturing process (62). In the fabrication processes involving complete melting and solidification, Ti-6Al-4V may experience the liquid  $\rightarrow \beta \rightarrow (\alpha + \beta)$  or liquid  $\rightarrow \beta \rightarrow \alpha'$  phase transformation. The  $\alpha+\beta$  dual phase exists only in a slow solidification process in which the phase transformation is a diffusional process. By contrast, the  $\alpha'$  martensite phase formation is beneficially created by rapid cooling through diffusion-free transformation. More details on these two processes are reviewed as below.

#### **2.3.1 – The diffusion-controlled transformation**

A slow cooling process leads to the diffusional transformation of Ti-6Al-4V, which is greatly important in terms of morphology, orientation and distribution of the equilibrium  $\alpha + \beta$  phases. The Burger orientation relation between the two phases is determining characteristic of this transformation:  $\{110\}_{\beta} // (0001)_{\alpha}$  and  $\langle 111 \rangle_{\beta} // \langle 11-20 \rangle_{\alpha}$  (62-65). This relation of orientation results in twelve possible crystallographic  $\alpha$  variants in one parent  $\beta$  grain. When the nucleating  $\alpha$  phase forms as high aspect ratio laths and exhibits a crystallographic relationship to the prior  $\beta$  matrix, the result is the Widmanstätten morphology (62).

Figure 5 demonstrates the morphology development phases of Widmanstätten. At the onset of the transformation, the grain boundary  $\alpha$  ( $\alpha_{GB}$ ) begins nucleating on the prior  $\beta$ -phase boundaries, followed by the formation of the Widmanstätten  $\alpha$  plates. The Widmanstätten  $\alpha$  can nucleate in packets of similarly arranged platelets called colonies (see Figure 5d) or as basketweave structures (see Figure 5e). A basketweave morphology indicates a rapid cooling rate or a  $\beta$ -stabilizer enrichment during

the phase transformation. The number of Widmanstätten  $\alpha$  platelets in each colony will increase with increasing temperature and holding time in the  $\beta$  solution treatment, and decrease with higher  $\beta$ -stabilizing elements and faster cooling speeds (7, 66).

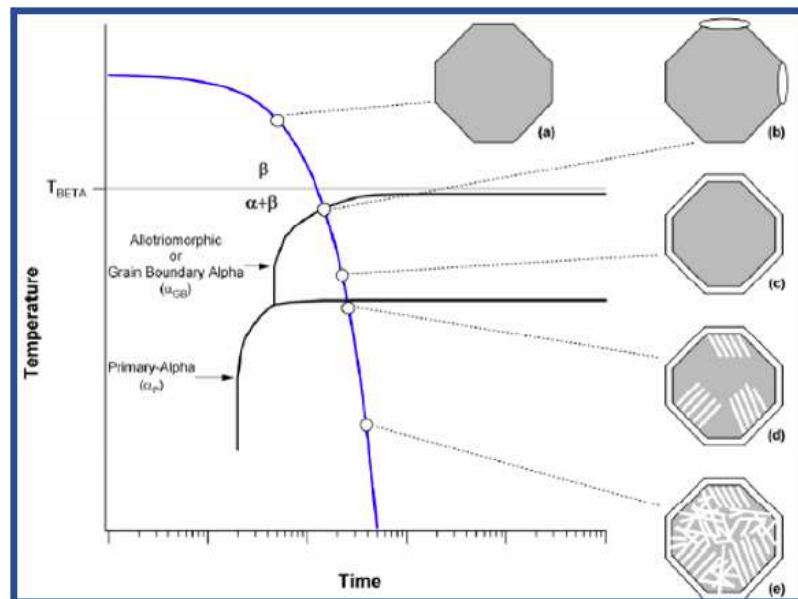


Figure 5. Schematic of phase transformation during solidification process: a)  $\beta$  phase grain, b)  $\alpha_{GB}$  starts nucleating, c)  $\alpha_{GB}$  finishes covering on the grain boundary, d)  $\alpha$  colony precipitates from the grain boundary and e)  $\alpha$  basketweave is formed inside the grain (67)

Figure 6 highlights the variety of  $\alpha$  variant distributions that can emerge from diffusional transformation. At fairly slow cooling rates from the  $\beta$  phase region, the  $\alpha$  phase forms in lath colonies, which are of the same Burgers orientation variant (Figure 6a, Figure 6c). Every  $\alpha$ -grain colony behaves as a single crystal or grain because the orientation variation between colonised  $\alpha$ -grains is very small (64). Hence, colony size is also used to describe mechanical properties such as fatigue life and crack production (65). By contrast, basketweave structure observes the total 12 potential variants distributed in the morphology, resulting from the quick cooling or isothermal heat treatment at  $\alpha+\beta$  temperatures (64). In low undercooling transformation, triangular configurations of individual variants are well observed, as shown in Figure 6e and Figure 6f. At higher the cooling speed, the basketweave structures possesses a more evenly distributed of 12 variants over the morphology as indicated in Figure 6f. However, whether these basketweave morphologies are examples of self-adapted distributions of variants regulated by elastic interactions (68, 69), or whether they are a statistical consequence of random nucleation of the 12 crystallographic variants (62, 70) is not fully understood in the literature.



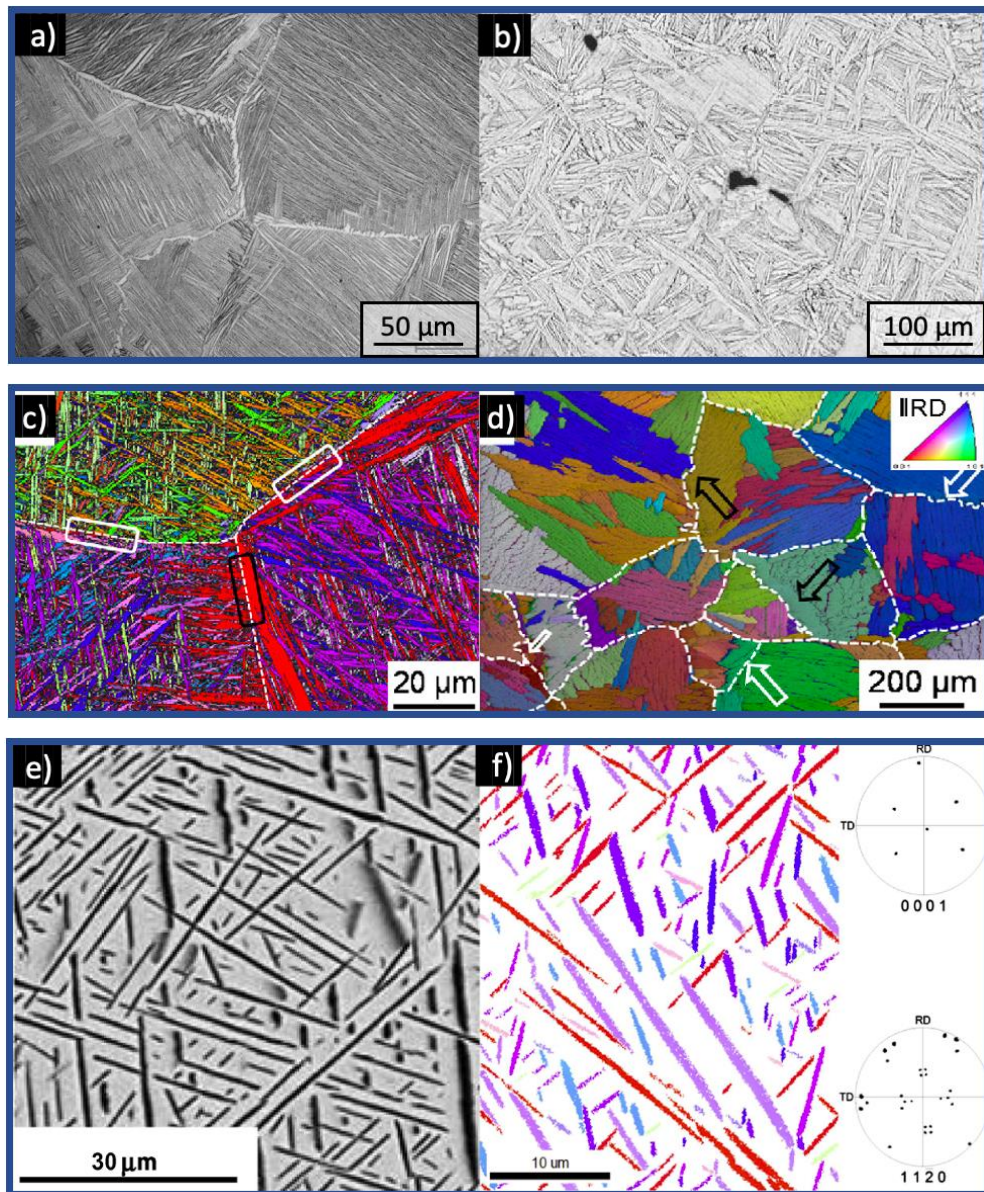


Figure 6. Distribution of  $\alpha$  variants in presentation as a) colony structures observed by SEM (71), b) basketweave structures observed by SEM (72), c, d) colony structures observed by EBSD indicating preferred  $\alpha$  variants inside prior  $\beta$  grains (73) and e, f) basketweave structures observed by SEM and EBSD with associated pole figure indicating a presence of 12  $\alpha$  variants (74)

The  $\alpha_{GB}$  is also connected to one of the grains on either side of the boundary with the Burgers relationship (75) or with two grains, in the case the corresponding parent  $\beta$  grains are directly correlated (76). Therefore, a complete option of 24 variants is available, one or two of which tend to dominate a given grain boundary. If the adjacent  $\beta$  grain boundaries share a  $\{110\}$  plane, the chosen variant always has the basal plane parallel to this common  $\{110\}$ . Furthermore, it has been proposed that the preferred variant would be the one with its most popular tight packed direction,  $\langle 111 \rangle \beta // \langle 11-20 \rangle \alpha$ , closest to the boundary plane (75).

### 2.3.2 – Diffusionless transformation

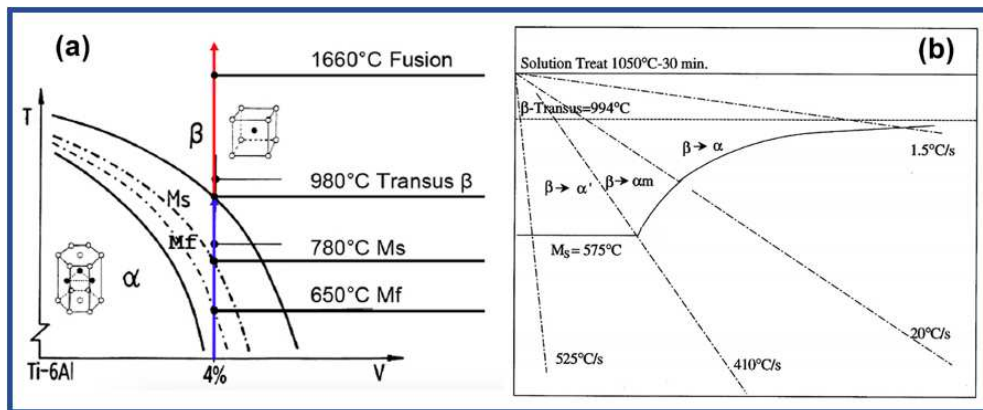


Figure 7. Diagram of phase transformation of a) Ti-6Al-4V and b) as a function of cooling rate (77)

The  $\beta \rightarrow \alpha'$  phase transformation is a displacive process requiring adequate fast cooling from temperatures above the martensitic start-temperature ( $M_s$ ) (Figure 7a). A wide range of  $M_s$  have been stated for Ti-6Al-4V, from 575 °C (78) to 800 °C (79), as subject to different initial microstructures, composition homogeneity and impurity elements (79, 80). Regarding the cooling rate, the completeness of  $\alpha'$  martensite formation depends on specific cooling rate ranges (see Figure 7b). Cooling rates above 410 °C s<sup>-1</sup> will create a full  $\alpha'$  martensite morphology, while cooling rates between 410 °C s<sup>-1</sup> and 20 °C s<sup>-1</sup> will lead to a partial  $\alpha'$  morphology, and cooling rates below 20 °C s<sup>-1</sup> will not develop  $\alpha'$  structures (78).

Banerjee and Williams (62) thoroughly studied the martensitic transformation and concluded that there are three different steps involving in the martensitic displacive mechanism as represented in Figure 8. The first one is the Bain distortion that turns the cubic lattice into orthorhombic or hexagonal. The second involves a lattice shear by either twinning or slip to recognise the invariant plane. The third is a shuffle that is carried out in [1-10] direction on the alternating (110) plane to carry the atoms to the proper hexagonal configuration of the martensite.

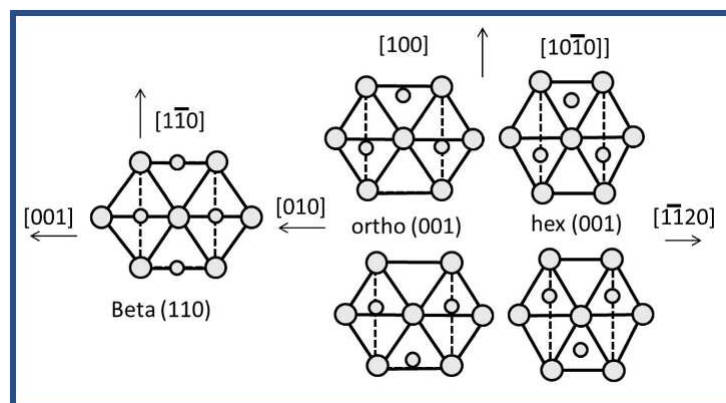


Figure 8. Schematic of martensitic transformation mechanism (62)

The martensitic phase transformation also follows the Burgers orientation relationship (76, 79, 80). However, since the shuffle can occur in alternative directions in a specific martensite plate, there will be a domain structure within each domain with a given shuffle path (62). In other words, one or two preferred variants are selected. If, on the other hand, the shuffle takes place without the Bain distortion, a total 12 variants of martensite can be generated from two opposite directions on each of the six {110} planes, as explained in the studies of Tahara, Kim (81) and Yano, Murakami (82).

## **2.4 – Microstructure of SLM Ti-6Al-4V**

In the SLM fabricated Ti-6Al-4V samples, the microstructure is dominated by columnar  $\beta$  grains and  $\alpha'$  martensite laths. During the manufacturing process, the molten pool solidifies via transformation into the  $\beta$  phase when it is cooled down to the solidus temperature. The solidification is followed by the formation of  $\alpha'$  phases within the (prior)  $\beta$  grains when the temperature falls further to the  $M_s$  at a high cooling rate, which has been reported to be  $10^4 - 10^6 \text{ }^\circ\text{C s}^{-1}$  in SLM process (8, 27, 61). Thus, the size, shape and arrangement of the parent  $\beta$  grains is certainly influencing both the morphology and properties of the  $\alpha'$  phase (34, 83).

### **2.4.1 – Prior $\beta$ columnar grains**

The typical morphology of the  $\beta$  prior columnar grains in Ti-6Al-4V components manufactured by SLM is shown in Figure 9, which appear as continuous multi-layered structures in all the reported microstructures. Obviously, these columnar grains are much higher than the layer thickness, with the size varies between 1 and 20 mm in length and between 0.2 and 4 mm in width (47, 84, 85). Thijs, Verhaeghe (8) stated that the average width of  $\beta$  grains is directly associated with the scan track width. Simonelli, Tse (86), however, disagreed, claiming that the average columnar grain width is equal to the hatch distance. It is widely agreed that columnar grain epitaxial growth occurs by re-melting and nucleating processes at the top of previous layers (85).

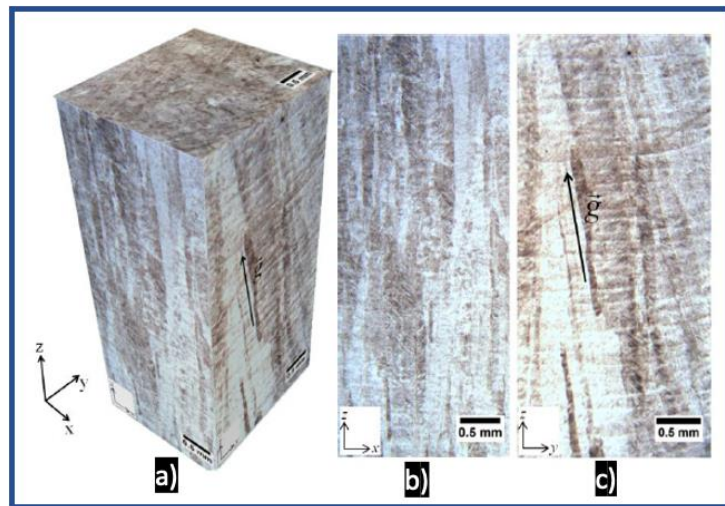


Figure 9. Optical micrograph showing microstructure on a) 3D Ti-6Al-4V built sample, b) xz plane and c) yz plane with the arrow showing the growth direction of columnar grains (14)

A number of comprehensive studies have been done to recreate the previous structures and texture, based on data from the electron back scatter diffraction (EBSD), for trying to define the growth mechanism of the prior  $\beta$  grains in SLM Ti-6Al-4V parts. Those studies display a solid  $\langle 001 \rangle$  fibre texture with the longitudinal axis of prior  $\beta$  grains parallel to the construction direction (14, 15, 86, 87). It is well known that a grain grows opposite the maximum heat gradient at the solidification front (88). And in SLM process, the overall direction of heat flow is perpendicular to and toward the substrate, which is caused by a downward conductive and an outward convective heat flow. The prior  $\beta$ , therefore, has a preferred growth direction of  $\langle 001 \rangle$ , parallel to the building direction.

The nature of the thermal activity in SLM process also substantially affects the growth behaviour of prior  $\beta$  grains. In the course of a rotating scan strategy, Simonelli, Tse (14) observed the columnar grains growing at an inclined angle of around  $20^\circ$  to the z-axis. Wavy grain boundaries observed by (8) are explained by the change in direction of scanning vectors. SLM is known as a cold powder-bed technique, and the heat release from a molten pool takes place through (i) the substrate, (ii) the previous layers and (iii) the surrounding environment (20). While the loss of heat through the substrate mainly dominates the heat dissipation, the latter pathways play a certain role as well. The thermal behaviour of the SLM process, therefore, should be extensively studied in order to understand the growth of  $\beta$  grains.

In addition, Figure 10 illustrates both the cross section of the single Ti-6Al-4V bead constructed by SLM, and the corresponding temperature field of the predicted molten pool by simulation. It is shown that the heat gradient appears to be perpendicular to the isotherm and dissipates down into the substrate at the bottom. Consequently, the primary  $\beta$  grains nucleate and subsequently grow perpendicular to the molten pool borders as validated by the microstructure in Figure 10a. Therefore, all the variables



affecting the geometry and motion path of the molten pool will affect the growing characteristics of the prior  $\beta$  grains.

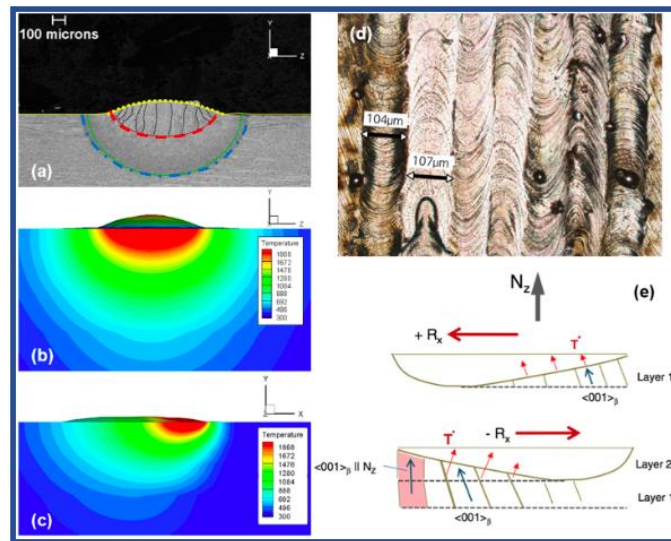


Figure 10. a) The Ti6Al4V single-track front view shows the development of prior  $\beta$ -grains that are perpendicular to the edge of the molten pool (red line). Simulated free surface borders (yellow line) and heat-affected zone borders (green and blue line) are defined. b) Modelled front-view temperature. c) Modelled side-view temperature. d) Ti6Al4V displays two laser scanning directions (89). And e) Schematic of  $\beta$ -growth direction along thermal gradient (90)

#### 2.4.2 – $\alpha'$ martensite grains

As being discussed, the thermal behaviours with extreme fast cooling rate in SLM process leads to the liquid  $\rightarrow \beta \rightarrow \alpha'$  phase transformation. At room temperature,  $\alpha'$  martensite phase dominates the as-built SLM Ti-6Al-4V microstructure, which appears as needle-shaped grains embedded within prior columnar  $\beta$  grains.

Morphology of  $\alpha'$  martensite can be easily detected by optical microscope and electron scanning microscopy which has been confirmed in several well-established studies (8, 15, 39, 47, 61, 79, 91). Figure 11 shows the final SLM Ti-6Al-4V morphological optical micrographs in various experiments. The microstructure of SLM Ti-6Al-4V built-up samples is certainly represented by the fine  $\alpha'$  martensite phase with a typical lath width of 0.2-1  $\mu\text{m}$  (47). The existence of  $\alpha'$  was also verified by the pattern of diffraction of the X-ray, showing the  $\alpha'$  hexagonal lattice of  $a = 0.293 \text{ nm}$  and  $c = 0.467 - 0.0468 \text{ nm}$  (92).

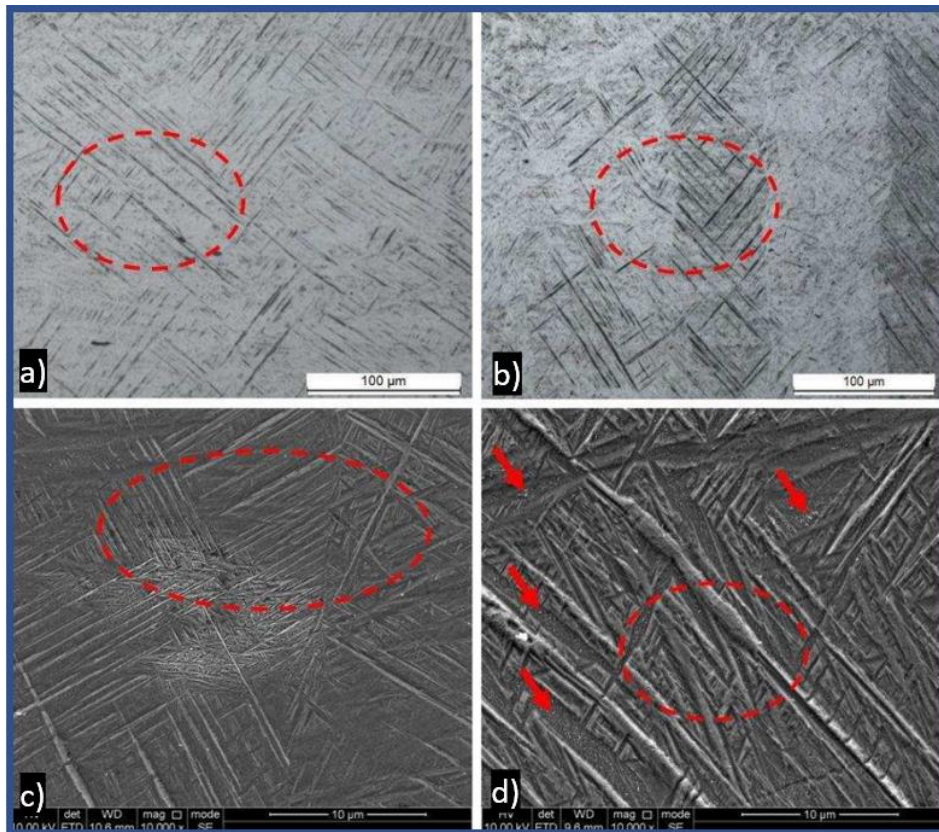


Figure 11. Martensitic microstructure as highlighted by circle and arrows observed in a, b) Optical Microscope and c, d) Scanning Electron Microscope (93)

More importantly,  $\alpha'$  martensite was recently documented to have a hierarchical structure in the study of Yang, Yu (94). They reported that the microstructure of SLM Ti-6Al-4V is composed of four martensites: primary, secondary, tertiary and quartic  $\alpha'$  martensites, containing a large number of dislocations. The size of such martensites may be regulated by changing SLM processing parameters, resulting as 1 to 3  $\mu\text{m}$  for primary and secondary  $\alpha'$  and up to 20 nm for quartic  $\alpha'$  (94, 95).

The grain size of  $\alpha'$  martensite typically increases with the increase in laser energy input. Do and Li (91) stated that increasing energy density contributes to a slower cooling rate and, therefore, to a higher  $\alpha'$  grain morphology. Besides, as Ti-6Al-4V has very low thermal conductivity at room temperature, a part of the heat obtained from subsequent scanning layers accumulates in the printed materials. This accumulated heat increases with increased number of build layers, resulting in higher temperatures and a lower cooling rate, particularly in the middle zone of the printed component, resulting in a coarser grain morphology (89).

## **2.5 – Microstructure change under dynamic conditions**

Ti-6Al-4V is used for industrial uses such as turbine blades, motor casing and sports gear where, in sudden situations, material can suffer from volatile charges such as ballistic impact, propagation of

cracks and crash (96). Adiabatic shear localization (ASL) is an important form of failure mode for materials under impact loading, usually related to a catastrophic system collapse with a complete loss of carrying capacity. Therefore, considerable attention was paid in different engineering fields to regulatory factors that form and produce ASL.

ASL, or generally referred to as adiabatic shear band (ASB) as seen in Figure 12, is the result of localization of plastic stress at high strain rates, where extreme plastic deformation is strongly concentrated in narrow zones. Zener and Hollomon (97) were the first to define ASB forming process as when plastic deformation happens in a component, a significant portion of the work performed is transferred into heat. When the strain rate is high enough, there might be insufficient time to dissipate heat from the deformation field. This is the thermal softening effect. When the thermal softening effect exceeds the rise in strength caused by strain hardening, the deformation becomes volatile and the homogenised plastic deformation can make room for the localised band deformation. ASBs have been observed and described as effects of this thermal softening effect in various metals and alloys, such as steel (98-100), Ta (101, 102), Al (103), Ti (104, 105) and Mg (106).

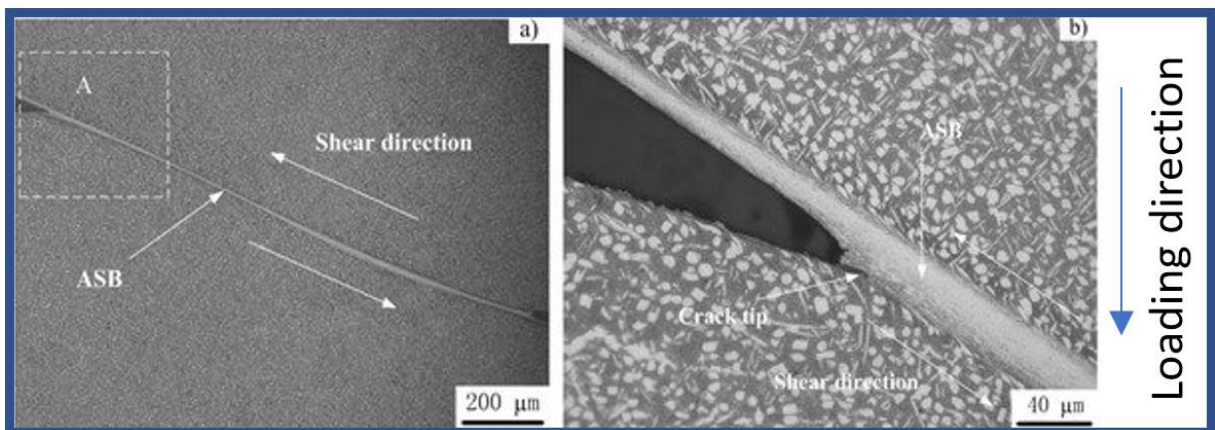


Figure 12. Optical micrographs of a) adiabatic shear band and b) its microstructure developed in Ti-5Al-5Mo-5V-1Cr-1Fe alloy (107)

Other studies have, however, suggested that dynamic recrystallization (DRX) is responsible for the initiation of ASBs rather than thermal softening. Rittel and Osovski (108) and Rittel, Landau (109) extensively studied microstructures using experiments and finite element approach. They developed a theory that ASBs were formed by other factors that soften the microstructure, i.e. DRX, rather than thermal softening effect. The microstructure within ASBs has been described by Xu, Zhang (110) as comprising ultra-fine grains, suggesting the occurrence of recrystallization within the shear bands. This finding was confirmed in electron backscatter diffraction (EBSD) in the study of Zhang, He (111) (see Figure 13). In the same way, Murr and Pizana (112) examined the Ti-6Al-4V ASBs, and verified the ultra-fine equiaxed grains in the microstructure of ASB using the technique of Transmission Electron



Microscopy. Yang and Wang (113) studied the evolution of ASB's microstructures in  $\alpha$  titanium alloy and reported that DRX determines the ultrafine structures.

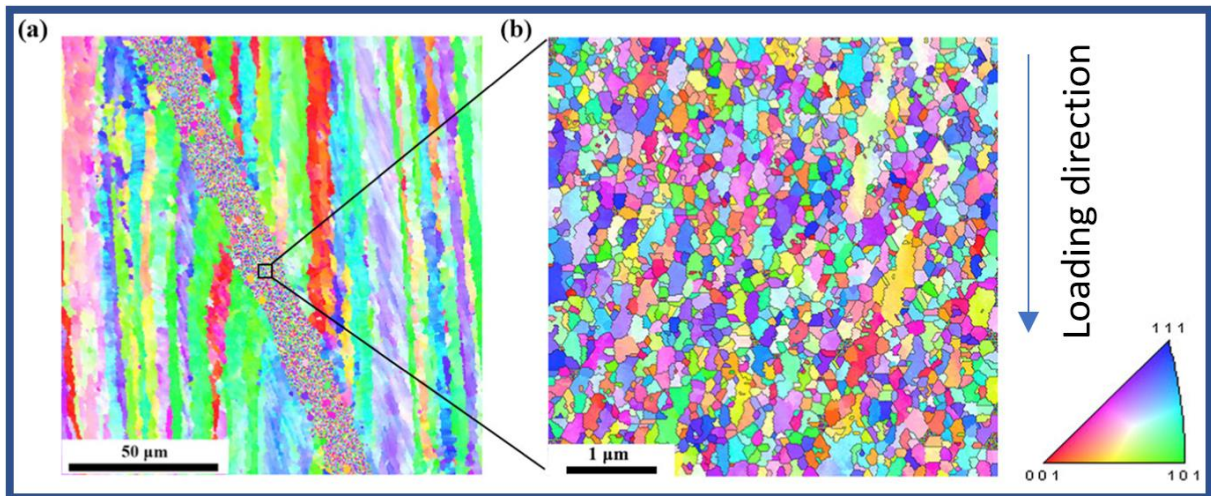


Figure 13. EBSD map of a) shear zone and b) microstructure inside ASB (111)

Many theoretical studies have been done to explain the DRX process within ASBs. Derby (113) developed the model representing the grain size relationship as a function of strain rate, which Meyers, Xu (98) translated as rotational DRX. This model enables recrystallization by rotating subgrains through plastic deformation. Similarly, Hines, Vecchio (114) proposed the progressive subgrain misorientation (PriSM) mechanism, based on a 'bi-crystal' approach with the crystal plasticity theory to explain the evolution of subgrain misorientation. In this mechanism, recrystallization is divided into three components: subgrain formation, subgrain rotation during dynamic deformation, and subgrain boundary refinement during shear band cooling.

More recent studies suggested a new category of DRX progression, known as continuous DRX (CDRX) (115-117), discontinuous DRX (DDRX) (115, 118, 119), and twinning-induced DRX (TDRX) (120, 121). The first mechanism increases the misorientation of grain boundaries from low angles into high angles within highly deformed grains before new grains are progressively formed, hence the name continuous (115). In comparison, DDRX shapes new grains by breaking down the low-angle grain boundaries which separate the new grains from the parent grains (122). The TDRX is the most recent mechanism proposed via activated twins for the nucleation and growth of the new grains (121). These processes have shown their ability accounting for the shear band microstructures of titanium and other metals (123). Yet it remains a topic for debate when considering the principal mechanisms for the initiation of ASBs.



## **2.6 – Mechanical properties of SLM Ti-6Al-4V**

In SLM or in any AM process, it is necessary to see how competitive or enhanced material properties in comparison to the components developed with conventional production techniques are obtained. Ti-6Al-4V is a workhorse material making up nearly 60% of all the titanium alloys in aerospace industry for its outstanding properties such as high strength-to-weight and corrosive resistance (124). For long Ti-6Al-4V have been employed for jet engine fan blades, low pressure compressors, wheels, wing joints, springs and airframe structures, whose working conditions are in both static and dynamic states (124, 125). In this section, quasi-static tensile and dynamic compressive properties, which are commonly used to analyse the performance of Ti-6Al-4V in aerospace industry, will be discussed.

### **2.6.1 – Quasi-static tensile properties**

Uniaxial tensile tests are typically performed using cylindrical bars or dog-bone specimens which are constructed in direct net forms or machined according to the requirements of ASTM E8. The tests are carried out in quasi-static state, which is approximately  $0.01 \text{ s}^{-1}$  at low stress rate. Table 4 summarises tensile test properties derived from SLM manufactured Ti-6Al-4V parts and compared to those developed using conventional methods.

*Table 4. Quasi-static tensile properties of Ti-6Al-4V manufactured by SLM and traditional methods*

<b>Build Orientation / Conventional method</b>	<b>Yield Strength (MPa)</b>	<b>Ultimate Strength (MPa)</b>	<b>Elongation (%)</b>	<b>Reference</b>
Horizontal	1100 ± 11	1211 ± 25	6.5 ± 0.53	(42)
Vertical	1150 ± 23	1246 ± 31	1.4 ± 0.76	(21)
Horizontal	1273 ± 35	1421 ± 27	3.2 ± 0.4	
Vertical	962 ± 51	1166 ± 32	1.7 ± 0.65	(34)
Horizontal	1137 ± 45	1206 ± 30	7.6 ± 1.25	
Horizontal	1110 ± 17	1267 ± 19	7.28 ± 0.21	(15)
Vertical	1143 ± 41	1219 ± 29	4.89 ± 0.83	(61)
Horizontal	1195 ± 35	1269 ± 62	5 ± 0.04	
Vertical (unmachined)	802 ± 71	1062 ± 62	12.7 ± 2.52	(33)
Vertical (machined)	988 ± 49	1157 ± 54	11.3 ± 1.77	
Vertical	967 ± 10	1117 ± 3	8.9 ± 0.42	(14)
Horizontal	1075 ± 25	1199 ± 49	7.6 ± 0.56	
Horizontal	910 ± 17	1035 ± 5	3.3 ± 0.08	(126)
Horizontal	1125 ± 21	1250 ± 31	6 ± 0.64	(26)

Vertical	1166 ± 19	1321 ± 17	2.0 ± 0.41	(41)
Vertical (unmachined)	990 ± 23	1095 ± 19	8.1 ± 1.01	(39)
Vertical (machined)	1040 ± 14	1140 ± 21	8.2 ± 0.42	
Horizontal	1008 ± 25	1080 ± 7	1.6 ± 0.06	(32)
Vertical	1330 ± 48	1400 ± 64	4.4 ± 0.91	(24)
Vertical	1070 ± 14	1250 ± 18	5.5 ± 0.38	(43)
Horizontal	1050 ± 19	1180 ± 20	8.5 ± 0.95	
Forged, mill annealed	970 ± 15	1030 ± 16	16 ± 0.91	(57)
Forged, mill annealed	960 ± 21	1006 ± 14	18.37 ± 1.23	(15)
Cast	865 ± 32	980 ± 26	13.5 ± 1.75	(34)
Cast	750 ± 16	875 ± 17	4.5 ± 0.94	(127)
ASTM F136	>795	>860	>10	(42)

The effect of microstructures on mechanical properties is evidently significant. The presence of a finely formed  $\alpha'$  martensite microstructure in SLM Ti-6Al-4V samples results in a high tensile strength, high yield stress and low elongation compared to conventionally manufactured components. The enhancement of tensile properties, and in particular ductility, requires some different post-SLM thermal treatments, which transform the  $\alpha'$  martensite into different morphologies of equilibrium ( $\alpha+\beta$ ) phase. The results of heat treatments on mechanical properties of SLM Ti-6Al-4V are summarised and presented in Table 5. In addition, it should be pointed out that the in-situ decomposition of  $\alpha'$  martensite is possible during SLM to create ultrafine ( $\alpha+\beta$ ) structures (45). The overall elongation has been increased to about 11.4% with a high yield strength above 1100 MPa, which is superior to both the typical SLM manufactured Ti-6Al-4V and traditionally mill-annealed Ti-6Al-4V, with a globular ( $\alpha+\beta$ ) microstructure.

Table 5. Heat treatment results on quasi-static tensile properties of SLM Ti-6Al-4V

Heat treatments	Build Orientation	Yield Strength (MPa)	Ultimate Strength (MPa)	Elongation (%)	Ref.
540°C, 5 h, WQ	Vertical	1118 ± 16	1223 ± 21	5.36 ± 0.71	(15)
640°C, 4 h	Vertical	1152 ± 19	1256 ± 14	3.9 ± 0.53	(41)
	Vertical	1140 ± 14	1214 ± 21	3.2 ± 0.64	
	Horizontal	1104 ± 22	1225 ± 32	7.4 ± 0.91	
700°C, 1 h, AC	Horizontal	1051 ± 11	1115 ± 13	11.3 ± 0.25	(33)
705°C, 3 h, AC	Vertical	1026 ± 23	1082 ± 31	9.04 ± 0.83	(15)

730°C, 2 h, AC	Vertical	900 ± 26	1000 ± 15	1.9 ± 0.31	(34)
	Horizontal	965 ± 11	1046 ± 19	9.5 ± 1.20	
800°C, 2 h	Horizontal	962 ± 17	1040 ± 23	5.0 ± 0.52	(32)
800°C, 2 h, argon	Horizontal	–	1228 ± 31	8.0 ± 0.91	(38)
850°C, 2 h, FC	Vertical	955 ± 16	1004 ± 11	12.84 ± 0.93	(15)
850°C, 5 h, FC	Vertical	909 ± 19	965 ± 26	11.25 ± 0.46	
900°C, 2 h; 700°C, 1 h, ACI	Horizontal	908 ± 23	988 ± 10	9.5 ± 0.68	(33)
940°C, 1 h, AC; 650°C, 2 h, AC	Vertical	899 ± 53	948 ± 63	13.59 ± 2.69	(15)
950°C, 0.5 h	Vertical	960 ± 42	1042 ± 27	13 ± 1.21	(42)
950°C, 1 h, WQ; 700°C, 2 h, AC	Vertical	925 ± 19	1040 ± 14	7.5 ± 0.69	(34)
	Horizontal	944 ± 8	1036 ± 12	8.5 ± 0.18	
1000°C, 1 h, FC (4 h)	–	826.87 ± 16	945.85 ± 18	12.67 ± 0.98	(128)
1000°C, 1 h, FC (34 h)	–	804.77 ± 7	908.63 ± 14	18.11 ± 0.62	
1020°C, 2 h, FC	Vertical	760 ± 26	840 ± 21	14.06 ± 1.26	(15)
1050°C, 2 h in vacuum	Horizontal	–	986 ± 9	13.8 ± 0.24	(38)
1050°C, 2 h	Horizontal	798 ± 16	945 ± 22	11.6 ± 1.16	(32)
1015°C, 0.5 h, AC; 730°C, 2 h, AC	Vertical	822 ± 11	902 ± 20	12.74 ± 1.20	(15)
1015°C, 0.5 h, AC; 843°C, 2 h, FC	Vertical	801 ± 15	874 ± 9	13.45 ± 0.71	
1050°C, 1 h, WQ; 820°C, 2 h, AC	Vertical	869 ± 9	951 ± 21	7.9 ± 0.23	(34)
	Horizontal	913 ± 12	1019 ± 19	8.9 ± 0.68	
900°C, 100 MPa, 2 h; 700°C, 1 h, AC	Horizontal	885 ± 17	973 ± 26	19 ± 1.67	(33)
920°C, 100 MPa, 2 h	Horizontal	912 ± 6	1005 ± 15	8.3 ± 0.58	(32)
920°C, 100 MPa, 2 h	Horizontal	–	1088.5 ± 34	13.8 ± 2.12	(38)
600–700°C, 2 h, FC; 920°C, 103 MPa, 4 h, FC	Vertical	1000 ± 16	1100 ± 8	12.5 ± 0.64	(43)
	Horizontal	930 ± 9	1020 ± 15	15.5 ± 0.81	
1050°C, 100 MPa, 2 h	Horizontal	–	1006.8 ± 14	13.5 ± 1.12	(38)

\*WQ: water quench; AC: air cooling; FC: furnace cooling.

The build orientation also plays a role in mechanical behaviours. Although it is still debated regarding the impact of build orientation on the tensile strength and yield stress (43), statistics, as shown in Table

4 and Table 5, proves that horizontally constructed parts have a higher elongation and strength than the vertically constructed counterparts. This disparity in elongation and tensile strength is due to the porosity orientation with respect to the direction of load (34, 129). As mentioned, lack-of-fusion pores are distributed within the joint regions of SLM layers. The pores in vertically built specimens that are perpendicular to the stress axis will open up and induce crack propagation at a relatively low stress. Horizontally built parts, by comparison, are tested with the pores parallel to the loading direction, which makes it more difficult for the opening of pores.

### **2.6.2 – Dynamic compressive properties**

Dynamic deformation is characterised by a high strain rate often reaching  $10^2 \text{ s}^{-1}$ . The value of understanding high strain rates is that the rate of impact is very fast in some applications such as landing gear or wing joint deformation. In order to develop improved impact-resistant systems, it is necessary to forecast the anticipated behaviours of material which is exposed to high strain rates.

Specific devices for high strain rates are needed in the dynamic deformation tests, and Ti-6Al-4V dynamic compression tests have been carried out using the Split Hopkinson Pressure Bar (SHBP) technique. The literature has been well established on the dynamic behaviours of deformation of traditionally produced Ti-6Al-4V (13, 130-133). In nearly all these experiments, heterogeneity of the flow stress with temperature and strain rate has been observed and compared with the corresponding microstructural characteristics. By contrast, little attention has been paid to investigation into the dynamic behaviours of Ti-6Al-4V produced by AM processes. Ti-6Al-4V samples fabricated by DED were tested at a varying strain rates from  $1000 \text{ s}^{-1}$  to  $8000 \text{ s}^{-1}$  and over a broad range of temperatures (35, 36). These studies suggest that for all conditions examined, the mechanical strengths of DED Ti-6Al-4V are less than those of conventionally processed Ti-6Al-4V. However, the dynamic compressive strength at  $2000 \text{ s}^{-1}$  and  $7000 \text{ s}^{-1}$  of the laser melted Ti-6Al-4V with regulated porosity is substantially higher than that of conventionally produced Ti-6Al-4V (134).

More importantly, according to the existing literature information, there are only two studies on dynamic compression properties of SLM Ti-6Al-4V by Ramezani, Flores-Johnson (135) and Pang, Liu (136). Figure 14 shows the SLM Ti-6Al-4V's stress flow, ultimate strength and yield stress, which indicates a heavy dependency on the strain rate as compared to that under quasi-static condition. It is shown that SLM Ti-6Al-4V's compressive strengths are lower than the forged Ti64's over the entire strain rate range. The main findings of the compression experiments are the ductility and compressive strengths of SLM Ti-6Al-4V evaluated under quasi-static compression are considerably higher than under dynamic conditions. Similar results were also published in the research of Mohammadhosseini,

Masood (137) on Ti-6Al-4V processed by EBM technique. This is presumably the consequence of various dislocation motion mechanisms in plastic deformation of SLM Ti-6Al-4V.

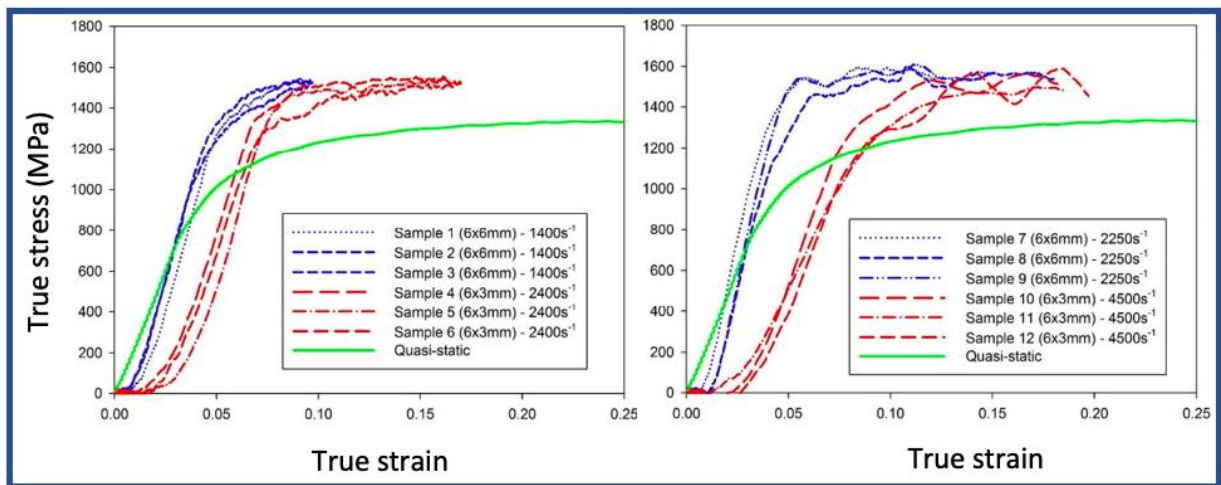


Figure 14. Dynamic behaviours of SLM Ti-6Al-4V at different strain rates (135)

Most of these above studies focussed on the influence of processing parameters on the dynamic behaviours of SLM and other AM processes built Ti-6Al-4V under particular high strain rates. Nevertheless, the thorough study of the deformation characteristics and the connexion between the evolution of the microstructure and mechanical properties are often restricted. It has been reported that due to low thermal conductivity, titanium alloys can easily form adiabatic shear bands during high strain rate operations (132). Most plastic works transform into heat during dynamic operations, and the Ti-6Al-4V's low thermal conductivity means that there is little time to disperse the heat produced, resulting in adiabatic shear formation. Moreover, the shear band is also dynamically recrystallized due to the locally excessive temperature (138, 139). In doing so, attention has been continually paid to microstructures and the micro-mechanisms of grain refining within the shear band in order to improve the operability of titanium alloys (140). Therefore, there exists a significant lack of understanding in the microstructure features in the dynamic behaviours of SLM Ti-6Al-4V and their impact on the mechanical strength, that is critical for many industry applications.

## **2.7 – Chapter summary**

With advancements in AM technology, it can now directly produce completely functional metallic components. In particular, SLM offers its capacity to produce parts with complicated designs for the aerospace industry. Recently, the emergence of SLM plays a more important role thanks to its independence from the global supply chain which has been disrupted by the Covid-19.

SLM method uses a laser source to melt metal powders in a layer-by-layer process. The molten pool consolidates with a quick cooling rate of around  $10^4 - 10^6 \text{ K s}^{-1}$  in fabrication of Ti-6Al-4V. The thermal

behaviours of SLM process results in a columnar  $\beta$  and acicular  $\alpha'$  martensitic microstructure via a diffusionless transformation.

It is necessary to recognise and conduct proper inspection of defects and mechanical properties before the parts are placed into operation. The literature review addressed multiple types of common defects, such as porosity and surface roughness. Porosity is recognised to be caused by lack of fusion and gas entrapment, and both types of porosity can be formed in on single SLM Ti-6Al-4V part. Although nearly fully dense parts can be achieved by optimising processing parameters, surface roughness is inevitable and can be enhanced only to some extent.

The applications of Ti-6Al-4V in aerospace industry involves in both static and dynamic operating conditions, which are commonly analysed by quasi-static tensile and dynamic compressive properties. The presence of  $\alpha'$  martensite in microstructure of SLM produced Ti-6Al-4V components significantly increases ultimate and yield strength, but it also results in low ductility due to high dislocations in the martensites.

## **Chapter 3 – Research methodology**

The experimental specifics for the study are discussed in this chapter. The raw materials and fabrication process in Selective Laser Melting of Ti-6Al-4V is detailed. The methods of testing, measurement and characterisation are then documented for physical qualities, metallography and mechanical properties. Finally, descriptions are established for post-treatment experiments.

### 3.1 – Materials

The samples employed in this research were manufactured using the extra low interstitial argon atomised Ti-6Al-4V (grade 23) powders supplied by TLS Technik GmbH & Co., Germany. The chemical composition of the powders is provided by the supplier as reported in Table 6. The powder was assessed under Scanning Electron Microscopy (SEM) to be nearly spherical with some smaller condensed particles attached to the main particle as shown in Figure 15. The powder size and distribution were determined in the range within 20-63  $\mu\text{m}$ .

Table 6. The chemical composition of ELI argon atomised Ti-6Al-4V grade 23

Element	Composition (wt. %)
Al	6.46
V	4.24
Fe	0.17
N	0.01
C	0.007
H	0.002
Ti	Balance

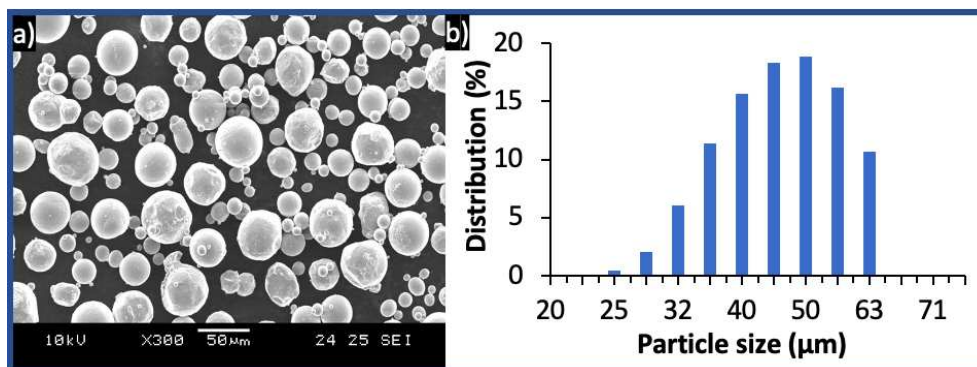


Figure 15. a) SEM image of ELI argon atomised Ti-6Al-4V and b) powder size distribution

### 3.2 – Fabrication process

The SLM 250 HL system from SLM Solutions GmbH, located at Singapore Centre for 3D Printing (SC3DP) was employed for the fabrication process. The system employs the ytterbium dual laser sources which operate a laser beam following the Gaussian distribution mode, with the maximum power of 400 W and 1000 W. The integrated software architecture from this system enables user to modify the system parameters according to the production needs. Therefore, this makes it a very versatile and perfect system for R&D environment as well as for small lot production areas. The SLM 250 HL system can



process most of the metals and compounds including stainless steel, tool steel, cobalt chromium, Inconel, aluminum, copper, titanium. The fundamental specification of the SLM 250 HL machine are listed as:

- *Operating chamber: 250 × 250 × 250 mm*
- *Laser source: Nd:YAG laser 400 W and 1000 W,*
- *Maximum scanning speed: 3000 m s<sup>-1</sup>*
- *Layer thickness: 20 – 75 μm*
- *Operational beam focus variable 70 – 130 μm*
- *Inert gas consumption in operation: 0.5 l min<sup>-1</sup>*

The workflow for pre-processing needed numerous phases and required many software packages. A 3D CAD model was first developed in Solidworks and then transformed into a triangulated model (STL file). Secondly, the Materialise Magics performed a printability check, adding supports and component arrangement on the build plate. Finally, the job ended with the part slicing and exporting into a 3D printer readable file format.

The ‘stripes’ scanning strategy was chosen as this study gives priority a consistent thermal behaviour during processing in order to minimise the heterogeneity occurring in the microstructures, and also a balanced scanning time. This scanning strategy, as shown in Figure 16, initially scanned the border contours which helped improve the surface finish and minimize the sub-surface defects of the printed parts. These border contours also formed an infill hatching area, also known as volume area, defined by offsetting 100 μm from the inner line. The volume area was then locally scanned by scanning vectors inside the columnar stripes. The direction of scanning vector was rotated by an angle of 67° every next layer in order to achieve the minimum residual stress, as reported in the reference (141).

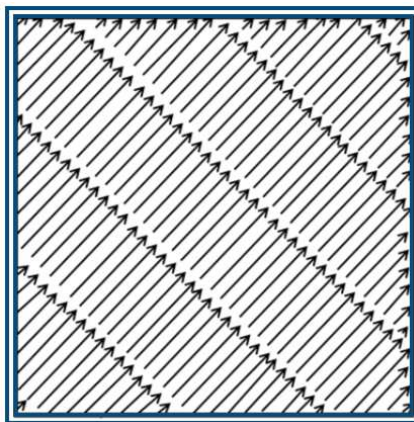


Figure 16. The ‘stripes’ scanning strategy in the SLM process

During production, the system's operating chamber was flushed into (> 99.99 % purity) argon gas to keep the oxygen level below 0.02% to avoid component oxidation. The substrate plate was preheated at 200 ° C and maintained during the process. When the print job completed, the whole build plate was lifted up and removed from the system for the printed parts to be cut by an EDM wire cutter. The unused powders were then extracted and sieved using a stainless-steel mesh to ensure that the generated powders were smaller than 63 µm for recycling.

### **3.3 – Metrological characterization**

The part density measurement were performed on the solid blocks with the size of 20 mm x 10 mm x 10 mm (see Figure 17a) in order to reduce the sensitivity of error caused by air bubbles when conducting experiment. Relative density of fabricated samples was determined in percentage of the bulk material (4.43g/cc (7)) using the Archimedes method via a XS 204 Mettler Toledo weighing scale machine with sensitivity of 0.001 g and repeatability of  $1 \times 10^{-4}$  g. Masses of solid block samples were measured in air and in ethanol independently at room temperature and denoted as  $m_a$  and  $m_e$  respectively. The difference in these two masses is the Archimedes force in ethanol, which linked to the actual volume of the part. The part density  $\rho_p$  was thus calculated by dividing the weight by the volume of the part, as obtained by inputting  $m_a$ ,  $m_e$  and the density of ethanol  $\rho_e$  into the following equation:

$$\rho_p = \frac{m_a}{m_a - m_e} \times \rho_e \quad (\text{Equation 2})$$

The surface quality examination was carried out using the 10 mm cube samples (see Figure 17b) by Optical Microscope (OM) via a ZEISS Axioskop 2 MAT microscope using x5 and x10 magnification lenses. These samples were also used for metallographic characterization as the cube specimens give more advantages for sample preparation (mounting, grinding, polishing...) and analysing microstructure on a consistent surface size on XY and Z planes, as compared to the 20 x 10 x 10 mm density cubes or cylindrical samples, as following ASTM F2921-11 standard.

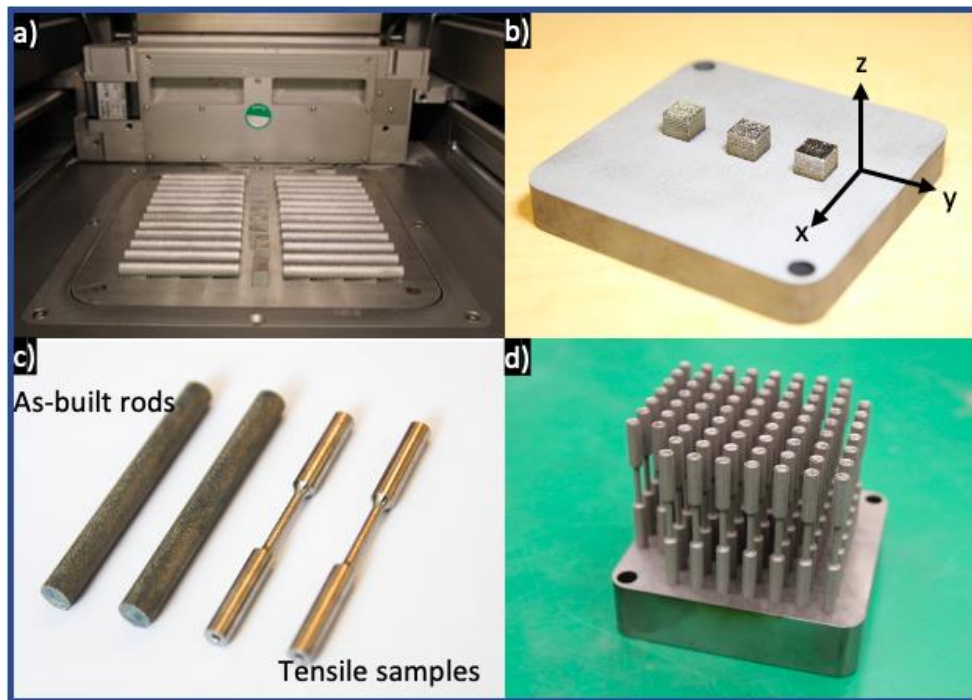


Figure 17. a) As-built rods and 20 x 10 x 10 mm solid blocks inside the working chamber, b) 10 x 10 x 10 mm solid blocks samples, c) dog-bone tensile samples machined from as-built rods and d) vertically built dog-bone tensile samples

### **3.4 – Mechanical testing**

#### **3.4.1 – Quasi-static tensile testing**

Two types of tensile samples were employed for investigation of quasi-static tensile properties of SLM Ti-6Al-4V as shown in Figure 17. The first type samples were initially manufactured from horizontally built cylindrical rods (diameter = 9 mm, length = 82 mm) and then machined into the final dog-bone shape with the gage length of 16 mm and the diameter of 3 mm according to ASTM E8/E8M standard. Samples of as-fabricated dog-bone shape samples (without machining) of the same gage length, which were vertically produced on a substrate plate.

The horizontally built samples, which were machined in order to cross out the influence of surface roughness, were tested used to analyse the effect of laser energy densities on the mechanical properties in the as-built (non-heat treated) conditions, whereas the vertically built dog-bone samples were employed without being machined due to the constrains of time and resources, and were heat treated before the tests in order to investigate the effect of heat treatment parameters on mechanical responses. It is noteworthy that due to many variables produced between horizontally and vertically built samples (different build plate size, sample arrangement, being machined, virgin vs old powders,...) it was not suitable to compare the effect of build direction in this study.

Tensile tests were conducted at the strain rate of  $0.001 \text{ s}^{-1}$  via a Universal Instron Testing Machine (Static tester series 5569) equipped with a 50 kN load cell and a clip-on  $10 \pm 1\text{mm}$  Instron extensometer. The loading direction was perpendicular to the build direction of horizontally fabricated samples and parallel to that of vertically produced samples. For tensile testing, when a load is applied to a material the degree of deformation depends on the applied stress. At lower loads, the stress ( $\sigma$ ) is directly proportional to the strain ( $\epsilon$ ) and, the deformation is elastic, obeying Hook's Law. The proportionality constant between ( $\sigma$ ) and ( $\epsilon$ ) is called as Young's modulus (E) which is a direct indication of how stiff a material is. After a critical stress level, the material starts to deform plastically. The stress level at which this transition from elastic to plastic deformation occurs is called the yield strength (YS). The maximum tensile stress a material can withstand before fracture is called its ultimate tensile strength (UTS) and ductility quantifies the amount of plastic deformation that has sustained before fracture.

#### **3.4.2 – Micro-hardness testing**

The microhardness of the SLM Ti-6Al-4V specimens was determined using digital microhardness tester (MATSUZAWA Co., Ltd. Model - MMT X7, Japan) with a Vickers elongated diamond pyramid indenter and a  $\times 20$  objective lens. A load of 500 kgf was applied to the surface for 10s. Six indentations were placed on the surface and the average value was considered. Precision microscopes of magnification of  $\times 50$  were used to measure the indentations. The diagonal length of the indentation was measured by built in scaled microscope and Vickers values were converted to microhardness values.

#### **3.4.3 – Dynamic compression testing**

Final cylindrical samples of 5 mm diameter and 5 mm length were machined from the horizontally built cylindrical rods for dynamic compression experiments (see Figure 18a). The flat ends of the samples were precisely polished to achieve exact right angle from the longitudinal axis. The surfaces of the specimens were inspected in an optical microscope, and only samples without surface defects were tested, as they could lead to premature failure during compression.

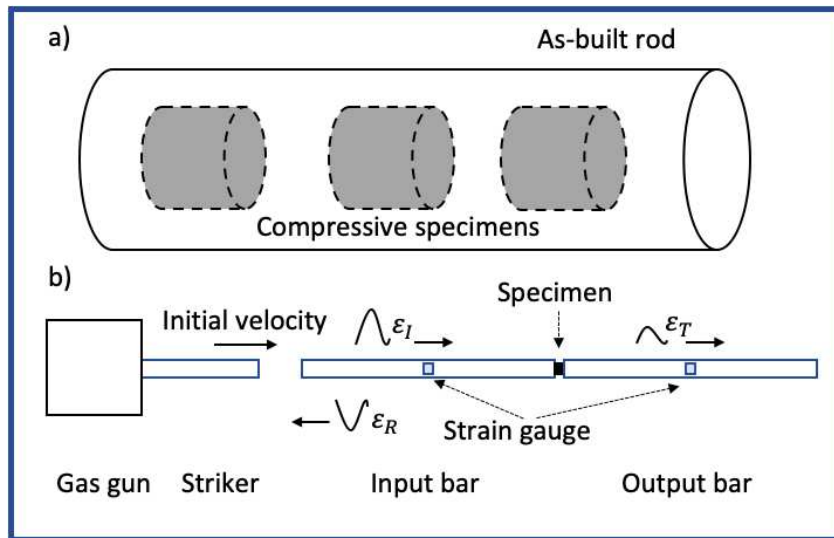


Figure 18. Schematic illustration of a) compressive specimens machined from a horizontally built rod and b) a SHPB system

The SLM Ti-6Al-4V dynamic compression experiments were performed in a Split Hopkinson Pressure Bar (SHPB) device. The setup consisted of two long cylindrical bars with the same diameter of 20 mm, known as the input and output bars. The specimen was placed in between the two bars, whereby a striker bar was propelled by a gas gun to hit incident bar, as schematically illustrated in Figure 18b. The striker, input and output bars were built from YAG300 maraging steel (Young's modulus = 184 GPa, Poisson's ratio = 0.3 and yield strength = 2000 MPa) with the length of 400 mm, 1200 mm and 1200 mm, respectively. Strain gauges are then placed on both rods in order to obtain the incident wave as well as the transmitted wave data from the two rods. The specimen will first be coated with a layer of grease that helps to reduce the frictional effect between the bars and the specimen. After that, the specimen will be placed between the two bars and be ready for the experiment. The pressure in the gas gun was then adjusted to 10 bar, after which the large difference in pressure causes the striker to hit the incident bar. After the incident bar is hit, it would then continue on to hit the specimen and causes it to be deformed.

In the interrupting experiments, stopper rings were designed to stop the compression when the height of the specimen becomes 2.5 mm, 2.0 mm and 1.5 mm respectively so that different strains could be examined for the dynamic compression. The specimen will then be placed in these stoppers and the whole process stated earlier will be repeated.

In the SHPB experiments, a high strain rate was achieved by regulating the gas chamber pressure and, thus, the initial striking speed. This impact created compression waves which travelled down the input bar and parts continued into the specimen. The waves then went through the specimen into the output

bar. Strain gauges were placed on the input and output bar to measure the incident ( $\varepsilon_I$ ), reflected ( $\varepsilon_R$ ) and transmitted ( $\varepsilon_T$ ) strain waves.

The SHPB follows the dynamic wave propagation theory and the engineering stress ( $\sigma$ ), the engineering strain ( $\varepsilon$ ) and the strain rate ( $\dot{\varepsilon}$ ) are given by the following equations:

$$\sigma = \frac{AE}{A_s} \varepsilon_T \quad (\text{Equation 3})$$

$$\varepsilon = \frac{2c_0}{l_s} \int_0^t \varepsilon_R dt \quad (\text{Equation 4})$$

$$\dot{\varepsilon} = \frac{2c_0}{l_s} \varepsilon_R \quad (\text{Equation 5})$$

In which  $A$ ,  $E$  and  $c_0$  are respectively the cross-sectional area, Young's modulus and the wave transmitting speed in the bar; and  $A_s$  and  $l_s$  are the initial cross-sectional area and the length of the specimen.

### **3.5 – Metallographic characterization**

The tested components were initially sectioned by the Struers Discotom 5 Cutting machine with a 25mm diameter silica carbide cutting blade, and then embedded into a cylinder resin mounts of 30mm diameter by the Simplimet 3 Mounting machine.

The standard metallographic preparation steps for SLM Ti-6Al-4V were followed as grinding with the 320-grit SiC papers until a flat surface was achieved, and then polishing by the diamond suspension of 9  $\mu\text{m}$  and consecutively by the colloidal silica suspension of 0.4  $\mu\text{m}$ . The samples were then subject for etching with the Kroll's reagent which consists of 10 ml of HF, 5 ml of HNO<sub>3</sub> and 85 ml of water for microstructure and crystallographic texture investigations. The etching of SLM Ti-6Al-4V was carried out by submerging the tested surface in the reagent in 8 – 12 s.

The microstructure characterization was conducted using JSM-7600 Schottky Field Emission Scanning Electron Microscopy (FESEM) integrated with a Nordlys Oxford Instruments electron back scattered diffraction (EBSD) system and a FEI Quanta SEM with an EDAX-TSL EBSD system.

### **3.6 – Crystallographic representation**

The grain and texture analysis were processed from the EBSD results using MATLAB and MTEX toolbox. In order to describe the grain orientation or crystallographic texture, the pole figure (PF) and the orientation distribution function (ODF) representation methods were employed. The PF is a two-dimensional stereographic projection of a unit sphere on the equatorial plane, which shows the

variation of pole density with pole orientation for a selected set of crystal planes with respect to a reference direction (142). By contrast, the ODF method describing the frequency of orientations in the three-dimensional (Euler) orientation space. It is worth pointing out the display of three-dimensional information on a two-dimensional projection plane further reduces texture information available in a pole figure. This 3D space in the ODF is defined by the three Euler angles ( $\phi_1$ ,  $\Phi$ ,  $\phi_2$ ), which represent a set of three successive rotations that bring the crystal axes into coincidence with the specimen axes (142). The Euler space forms a three-dimensional periodic lattice with unit cell  $\{2\pi, 2\pi, 2\pi\}$ . However, it is often restricted to the region  $\{2\pi, \pi, \pi/3\}$  when it comes to *hcp* metals due to a glide plane and the hexagonal symmetry (143).

In addition, in order to visualize the grain orientation maps, the MTEX assigned a colour to each possible orientation defined by its Euler angles ( $\phi_1$ ,  $\Phi$ ,  $\phi_2$ ) and took these as the RGB values of a colour, following the Euler angle colouring as in the commercial EBSD processing software (HKL CHANNEL5, Oxford Instruments). The reference unit of this Euler angle orientation is indicated in Figure 19, which was applied in all the orientation maps presented throughout the thesis.

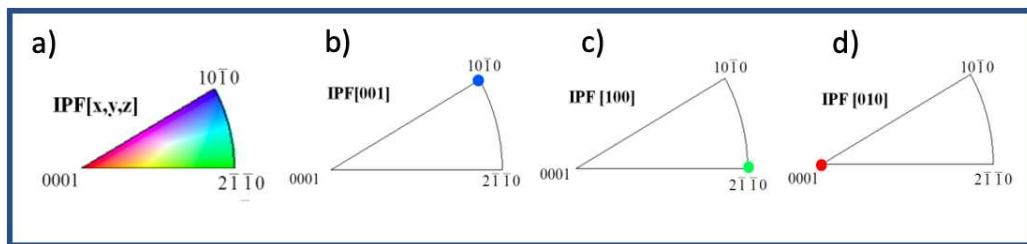


Figure 19. a) The orientation unit triangle based on the Euler angle colouring and the corresponding crystallographic planes of b) (10-10), c) (2-1-10) and d) (0001)

## **Chapter 4 – Effect of processing parameters on the as-built properties**

Selective Laser Melting is an advanced manufacturing process which can manipulate the microstructure evolution in order to achieve the desirable mechanical properties in the as-built products via processing parameters. This chapter studies the effect of processing parameters with a focus on the laser energy density on the Selective Laser Melted SLM Ti-6Al-4V, in terms of porosity, relative density, surface quality, microstructure evolution, mechanical properties and fracture behaviours. A thermal simulation was also developed and employed to analyse the heat history during the built process that can give important insights of the as-built properties of SLM Ti-6Al-4V.



#### 4.1 – Optimal processing parameters

In order to determine the optimal processing condition for the SLM process of Ti-6Al-4V, a series of experiments was designed and carried out in a wide range of laser energy density by varying the scanning speed whilst keeping other parameters as constants as shown in Table 7. The laser energy density (E) was calculated by the laser power (P), the scanning speed (V), the hatch spacing (h) and the layer thickness, as in the following equation:

$$E = \frac{P}{V \times h \times t} \quad (\text{Equation 6})$$

Although this method would not provide the global optimal parameters for SLM Ti-6Al-4V, the results were capable of achieving two main purposes of this study: (1) screening the optimal region of energy density which gives the relative density  $\geq 99\%$  and surface roughness  $\leq 10 \mu\text{m}$ , and (2) effectively and efficiently quantify the impact of laser energy density on relative density and surface roughness over a broad range with minimum number of experiments. The relative density was measured using the Archimedes principle. The surface quality was analysed under the optical microscope in order to quantify the average roughness parameters  $R_a$  from the top and side surfaces. The average roughness parameter is the arithmetical mean height along the sampling length.

The Analysis of Variance (ANOVA) and the regression models were calculated on the responses, as shown respectively in Table 8-Table 10 and (Equation 7)-(Equation 9). Finally, the optimal parameters were chosen based on the predicted values from response models and the validated results.

Table 7. Design table of processing parameters and responses on relative density and surface roughness

Power (W)	Speed (mm/s)	Hatch (mm)	Energy (J/mm <sup>3</sup> )	Relative density (%)			Side surface roughness ( $\mu\text{m}$ )	Top surface roughness ( $\mu\text{m}$ )
120	1714	0.08	17.50	93.62	93.78	94.06	26.2	65
120	1090	0.08	27.52	94.96	95.35	95.42	15.1	35.2
120	800	0.08	37.50	96.59	97.14	97.25	13.4	23.4
120	631	0.08	47.54	98.04	97.24	97.58	10.2	18.6
120	521	0.08	57.58	98.25	98.35	98.14	8.8	13.5
120	444	0.08	67.57	99.23	99.15	99.2	7.5	12.4
120	387	0.08	77.52	99.15	99.05	99.01	7.4	8.5
120	342	0.08	87.72	98.75	98.25	98.15	8.2	9.8
120	307	0.08	97.72	98.64	98.67	98.1	12.3	12.6
120	279	0.08	107.53	98.56	98.45	98.14	14.2	13.5
120	255	0.08	117.65	97.59	98.62	98.25	16.9	17.6
120	235	0.08	127.66	98.05	98.15	98.32	20.6	19.8
120	218	0.08	137.61	97.56	97.12	97.86	25.6	23.4
120	203	0.08	147.78	97.12	97.5	97.05	35.2	35.6

Table 8. Analysis of Variance on the relative density response

Source	DF	SS	MS	F-Value	P-Value
Regression	3	77.214	25.7379	232.46	0.000
E	1	20.145	20.1452	181.95	0.000
E <sup>2</sup>	1	9.478	9.4779	85.60	0.000
E <sup>3</sup>	1	4.577	4.5771	41.34	0.000
Error	35	3.875	0.1107		
Lack-of-Fit	10	1.664	0.1664	1.88	0.097
Pure Error	25	2.212	0.0885		
Total	38	81.089			

$R^2 = 92.55\%$ ;  $R^2\text{-adjusted} = 94.81\%$ ;  $R^2\text{-predicted} = 94.24\%$

Table 9. Analysis of Variance on the top surface roughness response

Source	DF	SS	MS	F-Value	P-Value
Regression	3	2735.5	911.82	54.13	0.000
E	1	795.6	795.58	47.22	0.000
E <sup>2</sup>	1	377.7	377.69	22.42	0.001
E <sup>3</sup>	1	168.8	168.80	10.02	0.010
Error	10	168.5	16.85		
Total	13	2903.9			

$R^2 = 94.20\%$ ;  $R^2\text{-adjusted} = 92.46\%$ ;  $R^2\text{-predicted} = 70.21\%$

Table 10. Analysis of Variance on the top surface roughness response

Source	DF	SS	MS	F-Value	P-Value
Regression	2	873.48	436.740	160.41	0.000
E	1	543.38	543.384	199.58	0.000
E <sup>2</sup>	1	709.33	709.333	260.53	0.000
Error	11	29.95	2.723		
Total	13	903.43			

$R^2 = 96.68\%$ ;  $R^2\text{-adjusted} = 96.08\%$ ;  $R^2\text{-predicted} = 91.96\%$

The regression models:

$$\text{Density} = 89.959 + 0.2588 E - 0.002378 E^2 + 0.000007 E^3 \quad (\text{Equation 7})$$

$$\text{Top surface roughness} = 99.66 - 2.775 E + 0.02583 E^2 - 0.000069 E^3 \quad (\text{Equation 8})$$

$$\text{Side surface roughness} = 34.36 - 0.7276 E + 0.004918 E^2 \quad (\text{Equation 9})$$

Porosity is the most observable defects which strongly affects the mechanical properties and the performances of as-built products. Achieving fully-dense products has long been a difficult goal for additive manufacturing as porosity still even exists in conventional manufactured components (144). It has been studied that relative density or porosity is highly influenced by powder characteristics (particle sizes and materials composition) so as to the fabricating processing parameters (145). Rombouts, Kruth (146) reported that highly porous defects appear in ferrous alloy due to the formation

of carbon monoxide/dioxide as a product of carbon and oxygen during SLM process. Campanelli, Angelastro (147) and Kruth, Badrossamay (148) also suggest that porosity may also resulted from gas entrapment of components during solidification process.

The trend of relative density is represented in Figure 20. In this study, the employed material was very low carbon in content, the particle was spherical, and the particle size range was within the layer thickness. The dominant factor affecting the porosity of as-built products was thus not associated to the powder, but the processing parameters. It is found that insufficient energy densities could not fully melt down the metal powders, consequently resulting in lack-of-fusion pores and discontinuous melt tracks. Besides, the depth of penetration of the melt pool formed by insufficient laser energy densities was not enough to create interlayer fusion, which led to delamination and cracks in the specimens as shown in Figure 21. Interlayer cracks and delamination are often resulted from the incomplete fusion between layers, and the built-up residual stress which is due to the rapid heating and cooling during the SLM process (89).

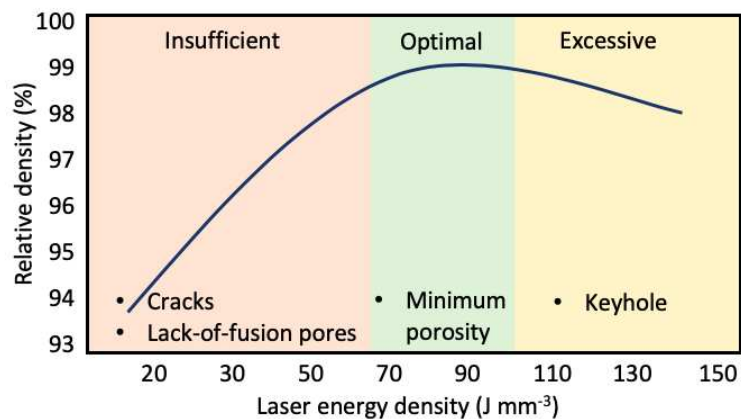


Figure 20. Diagram showing relationship between the relative density and the laser energy density

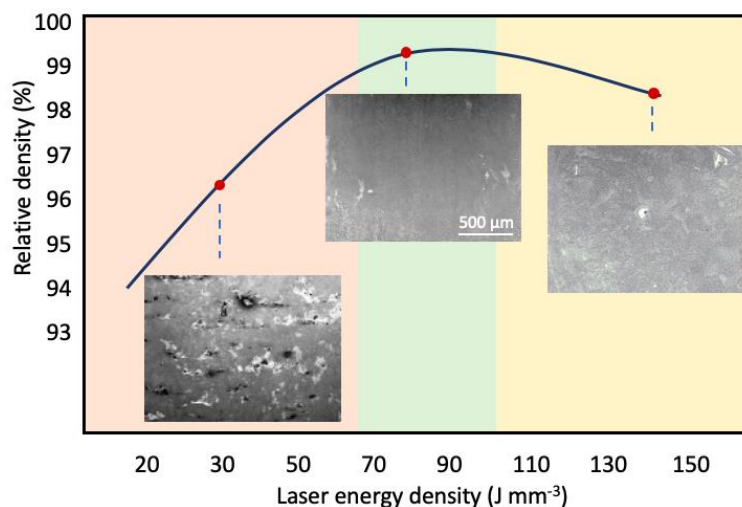


Figure 21. SEM images showing porosity at different energy density regions

By contrast, optimal laser energy densities provided sufficient energy to fully melt the powders and form good fusion between each layer, resulting in nearly fully dense specimens (above 99% relative density). Although other defects such as residual stress could not be totally avoided, high relative density in the parts is the most crucial influencing mechanical properties and fracture behaviour. Thus, optimal processing parameters are essential to manufacture high quality fully dense parts.

Exceeded the laser energy densities above the optimal values resulted in excessive melting which led to detrimental effects to the relative density and surface quality. It is reported that too much energy from the laser beam causes the Marangoni effect that influences the stability of the melt pool (149, 150). The Marangoni effect is the mass transfer along the interfaces of melt pool that have different surface tension. To be more specific, because a liquid with a high surface tension pulls more than a counterpart with a low surface tension, the Marangoni effect causes instability of the flow and the depth of the melt pool which leads to balling defects on the top surface, and keyhole defects at the bottom of the melt track. These balling and keyhole defects caused decreasing trend in relative density at excessive energy densities values.

The pattern of surface roughness on the top and the side surfaces of printed specimens, as well as OM images of surface qualities are represented in Figure 22 and Figure 23. It is evident that inadequate energy density resulted in high porosity, delamination and internal cracks reducing the surface quality. When increasing laser energy density, the temperature of exposed powders could exceed the melting temperature that the evaporation locally took hold and generated a recoil pressure on the melt pool's surface (91). Optimal laser energy densities created adequate recoil pressure to increase the flattening effect on the melt pool, thereby improving the surface quality (91, 145). Nevertheless, excessive melting from high energy densities resulted in undesirable effects, such as the intensive evaporation and balling effect, thus roughened the surfaces.

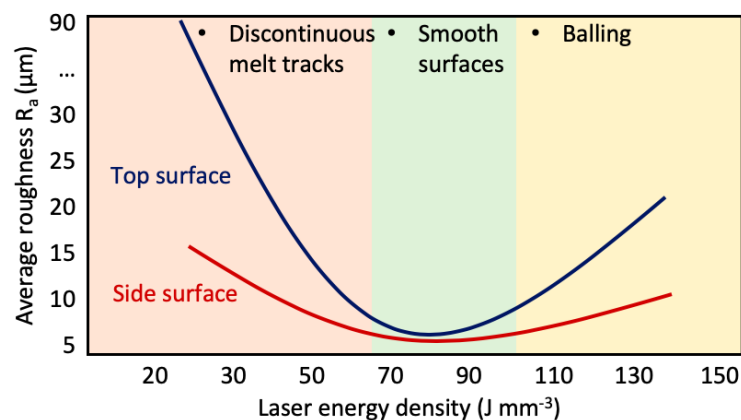


Figure 22. Diagram showing the relationship between surface roughness and laser energy density

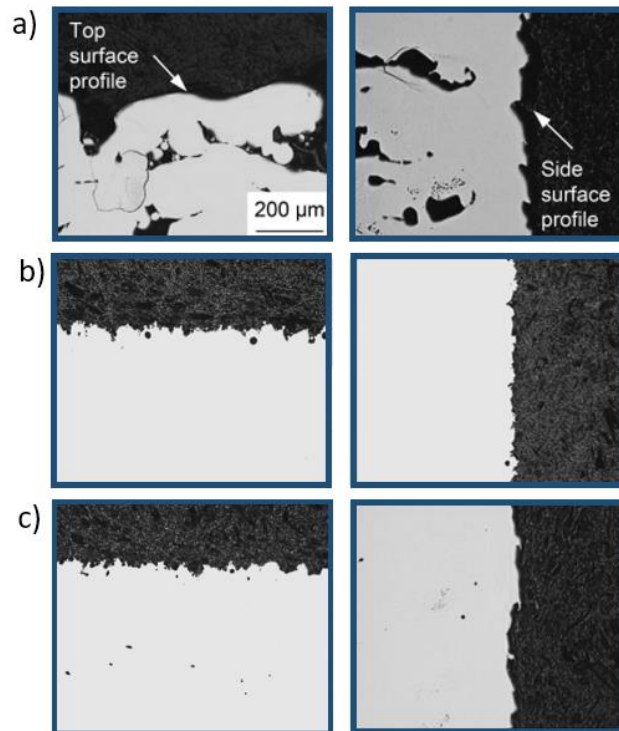


Figure 23. OM images showing the top and side surface profiles in SLM Ti-6Al-4V specimens at a) insufficient, b) optimal and c) excessive energy density

The side surface morphology technically characterises the repetitive melting layers that were successively built, while the top surface morphology represents the single pressure-free surface (151). Since the re-melting process helped strengthen the interlayer bonding, it is observable that the side surfaces have smoother morphology than that on the top surfaces. It is reported that re-melting scanning strategy could increase the surface quality (152). Yasa, Deckers (153) found that the surface morphology is greatly improved by re-melting the contour and applying lower laser power in the infill since it creates less edge effect.

Table 11. Optimal processing window for SLM Ti-6Al-4V

Processing parameters	
Laser power (W):	120
Scanning speed ( $\text{mm s}^{-1}$ ):	400
Hatch spacing ( $\mu\text{m}$ ):	80
Layer thickness ( $\mu\text{m}$ ):	50
Energy density ( $\text{J mm}^{-3}$ ):	75

Optimal processing parameters are crucial in the SLM process to produce high quality parts. Based on the relative density and surface quality analysis, the optimal set of processing parameters for SLM Ti-6Al-4V was chosen as shown in Table 11, which achieved near fully dense parts (99.2% relative density)

and the best surface quality ( $R_a = 7.0$  and  $8.6 \mu\text{m}$  on the side and top surface respectively). This optimal set of processing parameters will be taken as the baseline condition for further analysis in this thesis.

## **4.2 – Thermal simulation of the SLM process**

### **4.2.1 – Thermal model**

Thermal simulation has been well established an effective approach to predict the size of the melt pool and the thermal profiles during the SLM fabrication. Many studies applied the Rosenthal point source technique in their modelling to simulate the laser scanning of the SLM process (154, 155). More precisely, the Rosenthal point source facilitates a heat source of an infinite temperature under steady state condition to imitate the laser exposure point at the origin of the laser beam, and the movement of the heat source can be seen as the laser scanning process. The analytical solution of the Rosenthal point source is represented in the following equation:

$$T - T_0 = \frac{\lambda P}{2\pi k R} \exp\left(\frac{-V(x + R)}{2\alpha}\right) \quad (\text{Equation 10})$$

in which  $T_0$  is initial temperature,  $\lambda$  is the absorption rate,  $P$  is laser power,  $R$  is the geometry factor defined as  $R = \sqrt{x^2 + y^2 + z^2}$ ,  $k$  is thermal conductivity,  $V$  is scanning speed, and  $\alpha$  is thermal diffusivity.

The benefit of the Rosenthal equation is that it is very straightforward and has many applications. Another excellent feature of this simple formula has is the ability to predict temperature history as a function of time, temperature gradient, cooling rate, and solidification rate. The claims of the Rosenthal equation were based on the following assumptions:

- Thermophysical properties, such as thermal conductivity, density, and real heat, are not affected by changes in temperature. The latent heat resulting from phase shift is not taken into account.
- Consistent scanning speed and power input result in a quasi-stationary temperature distribution across the melt pool.
- The heat source is a point source.
- Heat losses due to convection and radiation at the surface are ignored, as is convection within the melt pool. As a result, heat transfer is solely controlled by diffusion.

To apply the Rosenthal theorem in a powder-bed system, an incremental assumption is made: that powder deposition has a negligible effect on the size of the melt pool. Nevertheless, to calibrate the

model, this challenge was solved by using a low absorption rate (efficiency rate) in the material property and experiment as many authors reported similar absorption rates in the SLM process (4, 154, 156, 157). This study equipped a thermal model to simulate a 5-layer scanning job on a substrate plate of 1.2 x 4 x 2 mm and a 3-mm single scanning track was performed on each layer, as schematically represented in Figure 24.

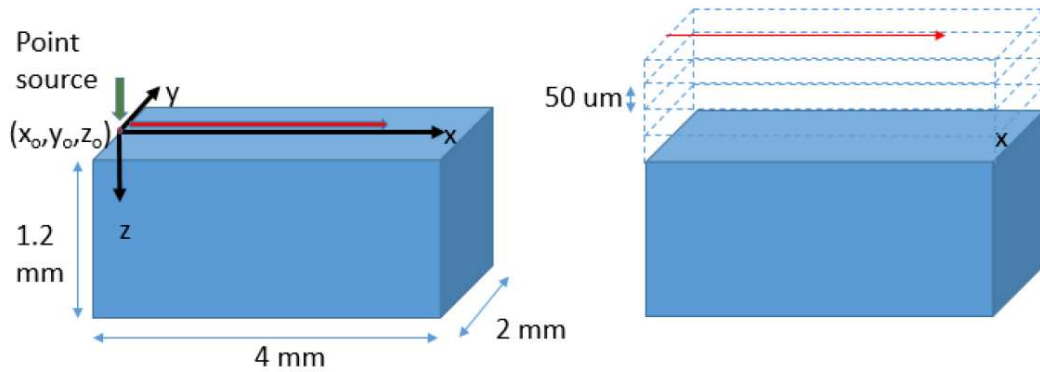


Figure 24. Schematic of the simulation model of a) the one-layer scan and b) the five-layer scan

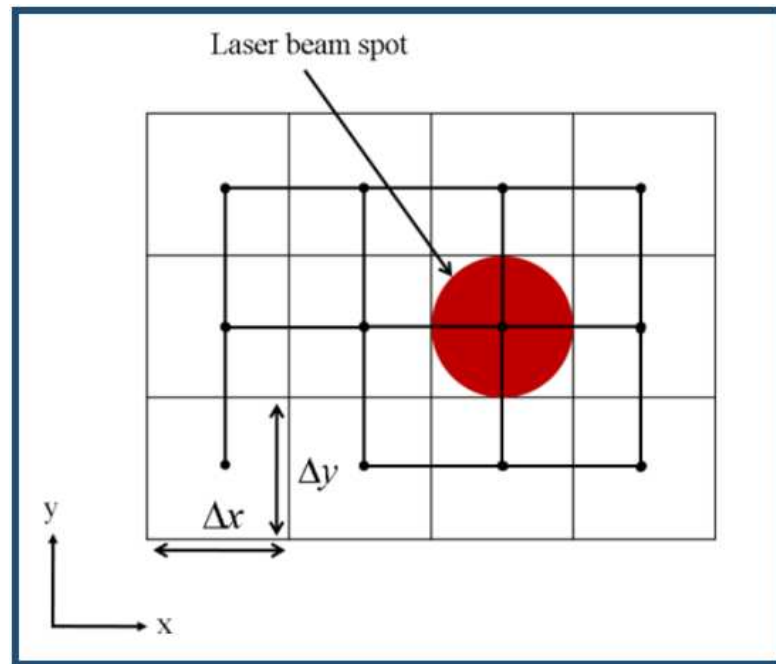


Figure 25. Heat point source as laser beam on mesh

The heat source point was assigned by an infinite value, moving on the substrate plate with the scanning speed  $V$ , the resulted temperature field on each mesh node, as shown in Figure 25, was calculated by the following equation:

$$T = T_0 + \frac{\lambda P}{2\pi kR} \exp\left[\frac{V(\xi + R)}{2\alpha}\right] \quad (\text{Equation 11})$$

in which  $\xi = x - Vt$ , is the replacement of  $x$  in (Equation 10) as the laser moves along the x-axis leading the moving coordinate in the distance of  $Vt$ . Since the Rosenthal analytical solution does not account for any temperature-dependent materials properties, the properties of SLM Ti-6Al-4V, as shown in Table 12, were applied. Besides, the boundary model is semi-infinite relatively to the size of the laser beam and the temperatures were calculated based on the spatial distance to the laser point source, there is absolutely no geometry factor accounted in this method.

Table 12. Standard parameters for thermal modelling of SLM Ti-6Al-4V

Thermal modelling parameters	
Laser Power (W)	120
Scanning speed (mm s <sup>-1</sup> )	400
Layer thickness (μm)	50
Beam diameter (μm)	70
Initial temperature (K)	473
Thermal conductivity (W m <sup>-1</sup> K <sup>-1</sup> )	15.75
Thermal diffusivity (m <sup>2</sup> s <sup>-1</sup> )	5.79 × 10 <sup>-6</sup>
Absorption rate	0.85

A delay time was taken after the scanning finished on each layer to represent the recoating time in the experiment. During this recoating time, the cooling process takes place that was simulated by replacing the point with the average finite temperature of the surrounding temperature points. Constant temperature is maintained at 200 °C at substrate plate edges as the boundary condition. Based on the initial assumption that the heat was conducted away purely by diffusion, the temperature field during the recoating time was modelled by the following diffusion equation:

$$\frac{\partial T}{\partial t} = D \left[ \frac{\partial^2 T}{\partial x^2} + \frac{\partial^2 T}{\partial y^2} + \frac{\partial^2 T}{\partial z^2} \right] \quad (\text{Equation 12})$$

in which  $D$  is the thermal diffusivity and  $t$  is the delay time.

The calculation was conducted in MATLAB using a self-developed code. It is of importance to point out that the Rosenthal solution in (Equation 11) is a direct calculation, whereas the diffusion equation was solved utilizing the finite difference method explicitly that the diffusion equation takes the form,

$$\frac{T_i^{n+1} - T_i^n}{\Delta t} = D \left[ \frac{T_{i+1}^n - 2T_i^n + T_{i-1}^n}{\Delta x^2} + \frac{T_{i+1}^n - 2T_i^n + T_{i-1}^n}{\Delta y^2} + \frac{T_{i+1}^n - 2T_i^n + T_{i-1}^n}{\Delta z^2} \right] \quad (\text{Equation 13})$$



in which  $\Delta t$  is the time between the time steps  $n+1$  and  $n$ , and  $i$  is the grid number of the finite difference mesh, and  $\Delta x$ ,  $\Delta y$  and  $\Delta z$  are the grid distance in  $x$ ,  $y$  and  $z$  respectively. The temperature at grid point  $i$  for the time step  $n+1$  results in:

$$T_i^{n+1} = T_i^n + D\Delta t \left[ \frac{T_{i+1}^n - 2T_i^n + T_{i-1}^n}{\Delta x^2} + \frac{T_{i+1}^n - 2T_i^n + T_{i-1}^n}{\Delta y^2} + \frac{T_{i+1}^n - 2T_i^n + T_{i-1}^n}{\Delta z^2} \right] \quad (\text{Equation 14})$$

As the temperature field is known at the time step  $n$  based on the Rosenthal solution in (Equation 11), the explicit time marching scheme enables the direct solution of (Equation 14).

#### 4.2.2 – Predicted melt pool profile and solidification condition

Figure 26 displays temperature isotherm contours predicted in transverse (along  $yz$ ), top view (along  $xy$ ), and longitudinal cross-sections side views (along  $xz$ ) of the standard processing condition in which the red and orange colour fields depicted the liquidus and  $\beta$ -transus isotherms. It is worth pointing out that due to the infinite value of the laser point source, the temperatures of the melt pool were calculated far above the liquidus temperature, 1650°C, and therefore in order to define the geometry of the molten pool, any temperatures above the liquidus temperature were cut off, that resulted in the white melt pool appearance in Figure 26.

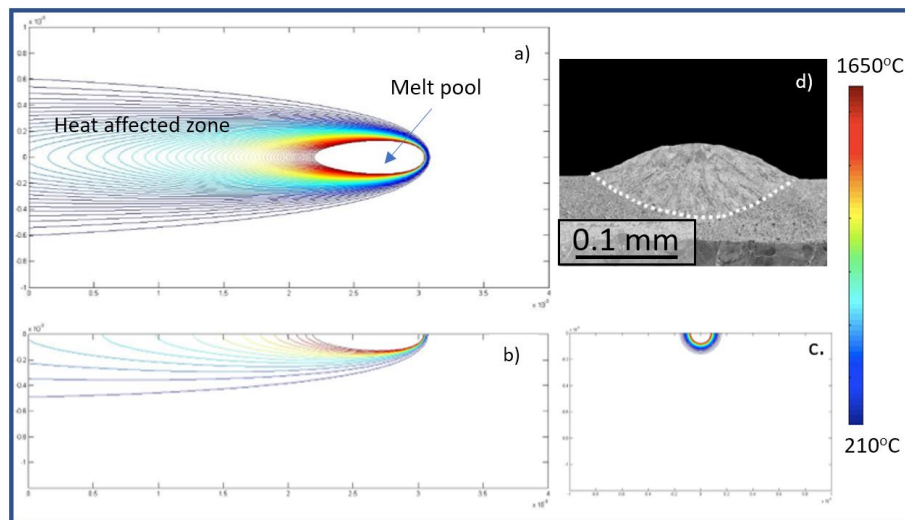


Figure 26. The predicted isotherm profile in the a) XY plane, b) XZ plane, c) YZ plane and d) the experimental melt pool profile on the substrate plate for comparison

The melt pool of the SLM Ti-6Al-4V was formed as a ‘tear drop’ shape with a size of 0.16 mm wide and 0.85mm long. The depth of the melt pool was measured as about 90  $\mu\text{m}$ , which is approximately two-layer thickness in the SLM process, indicating that the optimal processing parameters of Ti-6Al-4V created good fusion in the interlayers of the part.

The shape and size of the predicted melt pool agrees with other studies within the similar conditions. Besides, Verhaeghe, Craeghs (156) reported that the size of the melt pool, for 60 W power, was 60  $\mu\text{m}$  deep and, 110  $\mu\text{m}$  wide which is in good agreement with the results predicted in the model in this study using the same operating conditions. In addition, the predicted melt pool of the SLM process in this study is smaller than that of the EBM process studied by Al-Bermani, Blackmore (155) owing to the smaller spot size and lower absorption rate in the SLM compared to EBM process.

The temperature isotherms during cool down are shown at three intervals from end of scanning to end of the delay time (recoating time) in Figure 27. It is observable that during cool down, the heat diffusion took hold in enlarging the heat affected zone (HAZ).

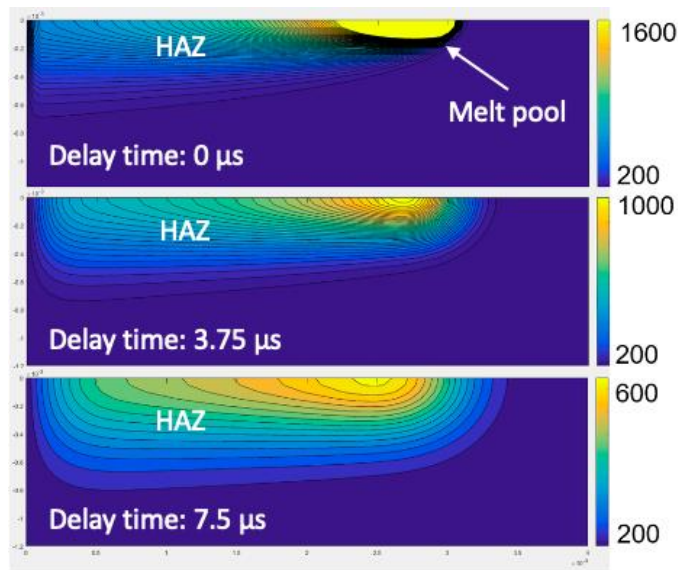


Figure 27. Isotherm profiles during cool down (Unit:  $^{\circ}\text{C}$ )

The final microstructure of a solidifying melt pool in AM is controlled by the thermal gradient ( $G$ ), the cooling rate ( $\dot{T}$ ) and the solidification growth rate ( $R$ ) which can also be derived based on the Rosenthal analytical solution in (Equation 10). The following equations represent the thermal gradient in the x- and z-directions, which were derived for the melt pool cross-section in the xz plane at  $y=0$ . The cooling rate and solidification growth rate can be found from (Equation 15)(Equation 18

$$\frac{\partial T}{\partial x} = \left[ 1 + \frac{\xi}{\sqrt{\xi^2 + z^2}} + \frac{2\alpha\xi}{V(\xi^2 + z^2)} \right] \left( -\frac{\lambda P}{2\pi k} \frac{V}{2\alpha} \frac{1}{\sqrt{\xi^2 + z^2}} \right) \exp \left[ -\frac{V}{2\alpha} (\xi + \sqrt{\xi^2 + z^2}) \right] \quad (\text{Equation 15})$$

$$\frac{\partial T}{\partial z} = \left( 1 + \frac{2\alpha}{V\sqrt{\xi^2 + z^2}} \right) \left( -\frac{\lambda P}{2\pi k} \frac{V}{2\alpha} \frac{z}{\sqrt{\xi^2 + z^2}} \right) \exp \left[ -\frac{V}{2\alpha} (\xi + \sqrt{\xi^2 + z^2}) \right] \quad (\text{Equation 16})$$

$$\frac{\partial T}{\partial t} = \left[ 1 + \frac{\xi}{\sqrt{\xi^2 + z^2}} + \frac{2\alpha\xi}{V(\xi^2 + z^2)} \right] \left( \frac{\lambda P}{2\pi k} \frac{V}{2\alpha} \frac{1}{\sqrt{\xi^2 + z^2}} \right) \exp \left[ -\frac{V}{2\alpha} (\xi + \sqrt{\xi^2 + z^2}) \right] \quad (\text{Equation 17})$$

$$R = \frac{1}{G} \frac{\partial T}{\partial t} = \frac{1}{\sqrt{\left(\frac{\partial T}{\partial x}\right)^2 + \left(\frac{\partial T}{\partial z}\right)^2}} \frac{\partial T}{\partial t} \quad (\text{Equation 18})$$

The thermal gradient and growth rate along the melt pool are plotted on the solidification diagram in Figure 28. In the SLM process, the thermal gradient in the melt pool at the solidification front was predictively very high, in the range  $[0.435 - 7.395] \times 10^6 \text{ K m}^{-1}$ , with the highest on the solidification front and decreasing towards the tail of melt pool, which agrees with results from other modelling in the reference (158, 159). The growth rate  $R$  was estimated as nearly zero at the bottom and gradually increased to the maximum value of  $0.65 \text{ m s}^{-1}$  at the tail point.

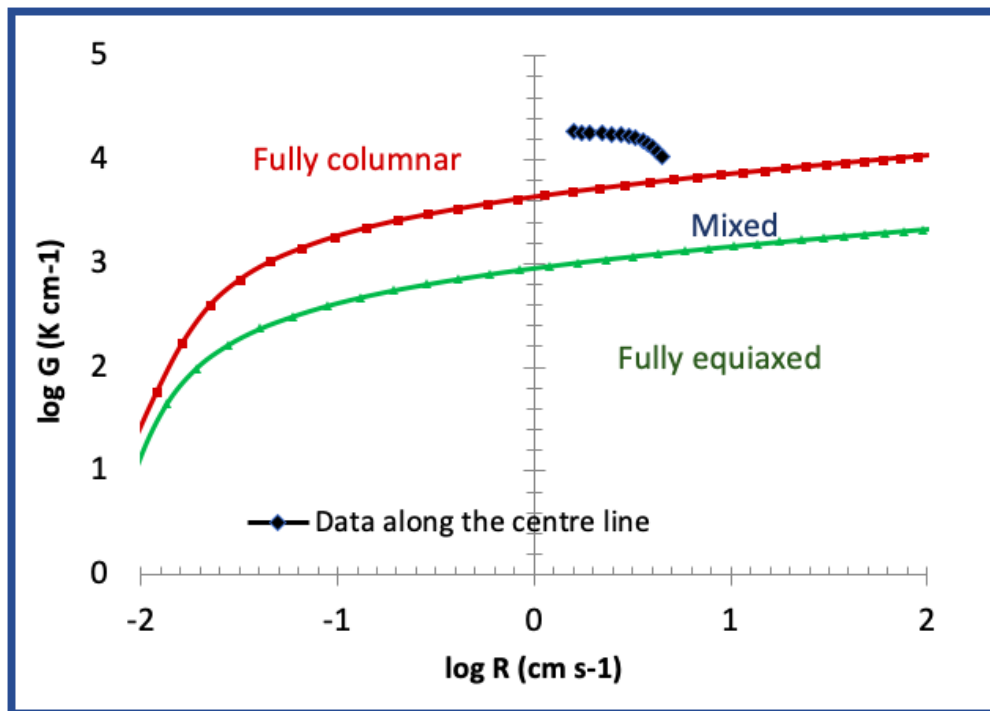


Figure 28. Solidification map showing predicted the thermal gradient  $G$  and the growth rate  $R$  along the centre line of the melt pool

Another ability of the thermal simulation that is worth mentioning is to predict the microstructure morphology via solidification rate and cooling rate. Many studies have simulated that the SLM associates with steep thermal gradients in the melt pool due to a locally fast cooling of a small volume of materials, that results in a columnar microstructure via repeatedly epitaxial growth upon deposited layers (154, 155, 157, 160).

In this analysis, high cooling rates of  $[1.072 - 2.958] \times 10^5 \text{ K s}^{-1}$  were predicted during the SLM processing of Ti-6Al-4V, with the slowest cooling rate in the middle of melt pool, as also supported in the study by Qian, Mei (158). Worth pointing out that a ratio of thermal gradient to growth rate (G/R) is the important parameter indicating the degree of constitutional super-cooling at the solidification front as a result of the instability of planar solidification(161). The super cooling determines either a cellular or a dendritic (columnar and equiaxed) growth occurs in the microstructure evolution under a particular set of condition (162). The criterion for this condition has been defined as the G/R value be smaller than  $5 \times 10^9 \text{ K s m}^{-2}$ . In this study, a minimum G/R value of  $2.38 \times 10^7 \text{ K s m}^{-2}$  and the maximum of  $1.17 \times 10^8 \text{ K s m}^{-2}$  were reckoned at respectively the tail and the solidification front of melt pool that fulfils the condition of planar solidification instability. Furthermore, the solidification diagram in Figure 28 indicates that the SLM condition promoted a fully columnar growth of solidification of Ti-6Al-4V, which favours a columnar  $\beta$  microstructure, and the predicted fast cooling also suggests a followed martensitic  $\alpha'$  microstructure.

#### **4.2.3 – Heat history**

The heat history of the modelled job in Figure 29 indicates 5 thermal cycles associated with 5 layers of scanning in the SLM job. A thermal cycle consists of two stages: laser scanning, appearing as the peak-point increase of temperature; and cool down, representing the decrease in temperature during recovery time.

The first cycle in the heat history indicates the total heat exposure directly from the laser source and the other cycles unveils the heat gained from the subsequent built layers, resulting in a decreasing trend of peak temperatures. To be more specific, the peak temperature dropped from: (Cycle 1 & 2) above the  $T_L$  (liquidus temperature), (Cycle 3)  $T_s$  (solidus temperature) –  $T_\beta$  ( $\beta$  transus temperature), (Cycle 4)  $T_\beta - T_{MS}$  (martensite temperature), and (Cycle 5) below  $T_{MS}$ . Each thermal cycle influenced the phase transformation in the microstructure of SLM Ti-6Al-4V until the peak temperature fell below the  $T_{MS}$ . In other words, the Cycle 5 is predicted to have neglectable impact on the microstructure evolution in the SLM process. Moreover, the ambient temperature of the part steadily grew as the number of thermal cycles increased.

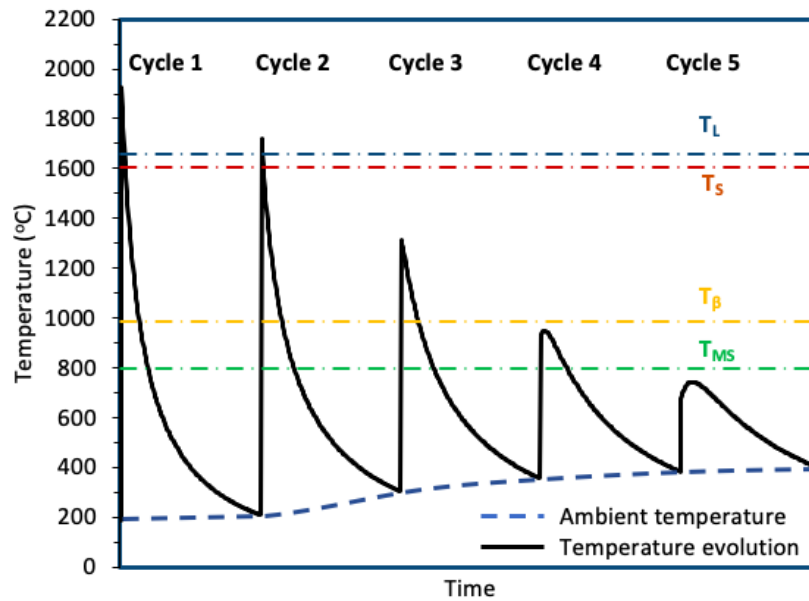


Figure 29. Diagram of the predicted heat history in the SLM process of Ti-6Al-4V

### 4.3 – Microstructure and texture evolution

#### 4.3.1 – Columnar $\beta$

As discussed, the solidification condition in the SLM process promoted the columnar growth at the solidification front of the melt pool, resulting in the evolution of columnar  $\beta$  grains, followed by the martensitic transformation. Figure 30 shows the EBSD orientation map of the martensite laths and the corresponding reconstructed columnar  $\beta$  grains by the Burger's relationship using the method introduced by Humbert, Wagner (163) and Glavicic, Kobryn (164).

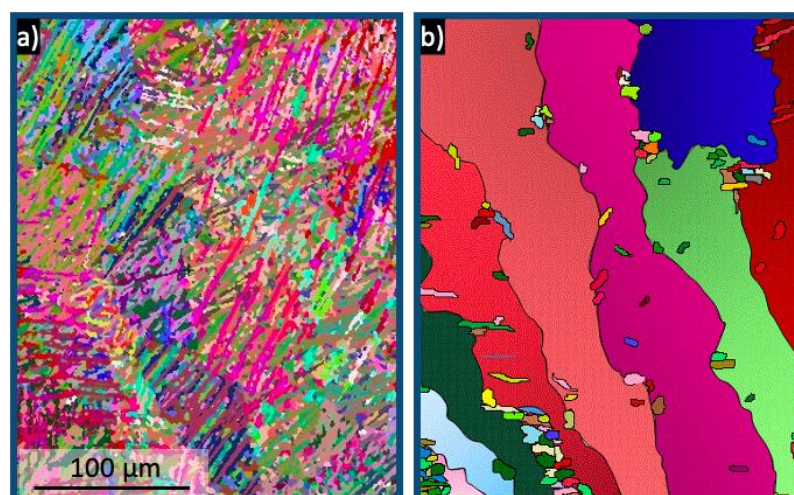


Figure 30. EBSD orientation map of a) the  $\alpha'$  martensite grains and b) the reconstructed  $\beta$  grains

In this study, a MATLAB script was developed using MTEX open source codes and employed to carry out the automatic reconstruction of the  $\beta$  phase. The reconstruction of the  $\beta$  phase was performed

considering every triplet of neighbouring  $\alpha$  grains in the EBSD data set (step size of  $0.3\mu\text{m}$ ). The orientation of each  $\alpha$  grain was represented by the Euler angles ( $\phi_1, \Phi, \phi_2$ ) in the measured dataset as discussed in section 3.6. However, due to the symmetry of the crystal, multiple rotations can result in an equivalent orientation for a particular crystal. As a result, the rotational symmetry elements of  $\alpha$  and  $\beta$  phases had to be considered in order to distinguish independent orientations. In the present approach the rotational symmetry elements of the  $\alpha$  and  $\beta$  phases (12 and 24 respectively) were described using the Burgers orientation relationship,  $\{0001\}_\alpha // \{110\}_\beta \mid \langle 11\bar{2}0 \rangle_\alpha // \langle 111 \rangle_\beta$ , which is equivalent to a Bunge's rotation expressed by the matrix  $D (135^\circ, 90^\circ, 325^\circ)$ . The solution common to the  $\alpha$  triplet was considered as orientation of the parent  $\beta$  phase. It is noteworthy that solutions exceeding a misorientation of  $8^\circ$  were discarded from the original dataset to reconstruct the parent  $\beta$  phase with the accuracy of  $8^\circ$  orientation spread and thus also enabling the generation of an orientation map from a representative number of data points.

The columnar  $\beta$  structures formed by AM of Ti-6Al-4V are known to be coarse and highly directional, resulting from high thermal gradient taking place during SLM process (4, 8, 155, 157, 165). There are, however, contradictory findings in several studies on  $\beta$ -grain morphology as affected by laser energy density, as well as little work on evaluating the texture evolution of SLM Ti-6Al-4V (166-168). Thijs, Verhaeghe (8) noticed that prior  $\beta$  grains appears as elongated columnar structure, growing epitaxial and discontinuously parallel to the build direction, which can be explained by the great vertical thermal gradient as heat flow to the base plate (169). By contrast, Simonelli, Tse (168) figured out the columnar  $\beta$  grains grow continuously along the entire height of sample with some slanted grains due to thermal gradient in the  $x$  direction. In addition, Murr, Quinones (170) suggested that the resulting microstructure evolves depending on the sample height. Vilaro, Colin (34) also reported the coarse columnar grain morphology,  $150\mu\text{m}$  wide, which is similar to the applied hatch spacing and independent on the height of the samples.

Figure 31 displays a morphological diagram and OM photographs of prior columnar  $\beta$  gains produced by standard processing parameters. The observation reveals that prior  $\beta$  grains developed epitaxially and continuously heading outward the centre line of the sample at the angle of  $10\text{-}30^\circ$ . The inclination of growing direction of columnar grains can be explained by the complicated applied scanning strategy that adapted the local scanning vector stripes to solidified alternative parts in one layer may cause the thermal gradient heading towards the centre of the built solid part.

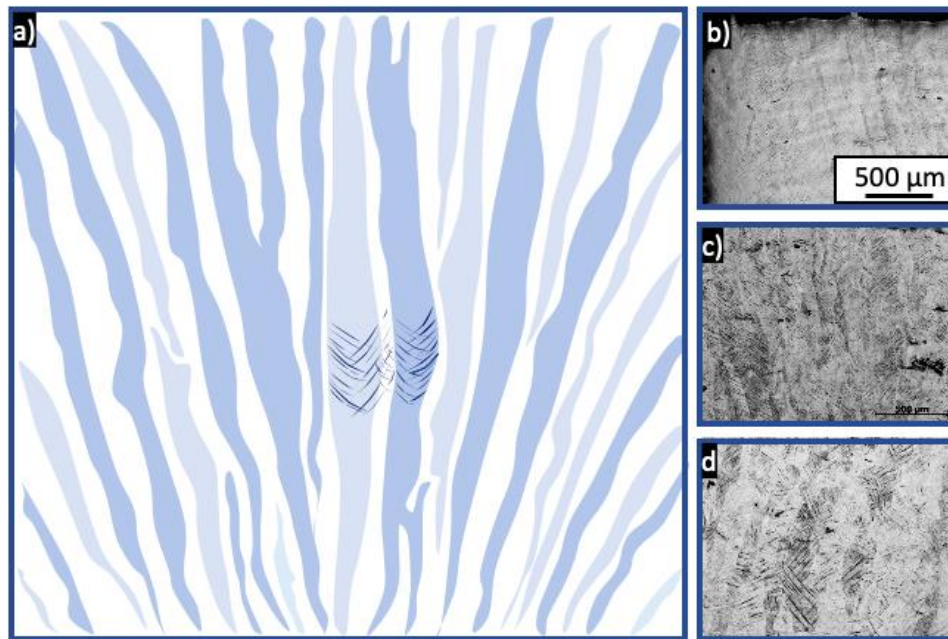


Figure 31. Illustration of columnar  $\beta$  microstructure in a) schematic graph of the sample, OM images in the b) top left corner, c) central and d) bottom right areas of the sample

It should be mentioned that columnar grains in the middle part were coarser than in other regions, on average  $181\ \mu\text{m}$  diameter, compared to  $111\ \mu\text{m}$  and  $93\ \mu\text{m}$  in the top and bottom corners respectively (see Figure 31). The bottom of the printed part was affected by the base plate which functions as a heat sink, leading to fine columnar grains. Whereas the columnar grains in the top layers could not expand due to fewer effective thermal cycles, as well as more radiation heat loss could be permitted. Furthermore, thermal simulation showed that heat was conducted slower in the centre of the melt pool and by that, if the entire area were integrated, slower cooling rate occurred in the middle of the specimen would lead to coarser grains.

#### **4.3.2 – $\alpha'$ martensite**

At room temperature, SLM Ti-6Al-4V consists of nearly fully  $\alpha'$  martensitic microstructure due to the exceptionally high cooling rate in the SLM fabrication, calculated as  $1.072 - 2.958 \times 10^5\ \text{K s}^{-1}$ , far above the criteria of martensitic transformation. The  $\alpha'$  martensites appeared as needle-like structures crossing one another inside the prior columnar  $\beta$  grain as shown in Figure 32. The columnar  $\beta$  grain boundaries acted as nucleation sites from which the  $\alpha'$  martensite grew towards the interior of the parent phase. The high aspect ratio of the  $\alpha'$  martensite was clearly observable as the width and length of the martensite laths are in the range of several of nanometre and tens of micrometre, respectively.



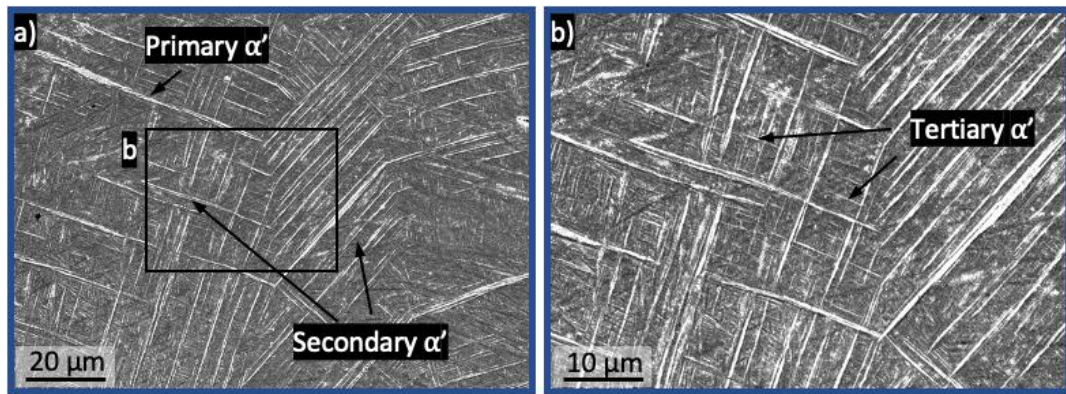


Figure 32. SEM images showing the hierarchical structure of  $\alpha'$  martensite at a) lower magnification: primary and secondary  $\alpha'$  and b) at higher magnification: tertiary  $\alpha'$

The  $\alpha'$  martensite morphology formed a hierarchy of three different types of martensitic structures based on their size and appearance as observable in Figure 32. Primary  $\alpha'$  martensites appeared as groups of coarse parallel grains precipitating across the thickness of prior columnar  $\beta$  phase, with the length of 50-70  $\mu\text{m}$  and the width of several micrometres. Great amount of secondary  $\alpha'$  martensites were finer laths with the length of 15-18  $\mu\text{m}$  and the width of hundreds of nanometres, growing in parallel and perpendicular to the primary  $\alpha'$  grains. On the finest scale, tertiary  $\alpha'$  martensites of 1-3  $\mu\text{m}$  long and tens of nanometres wide laths, appearing in the gap of secondary and primary  $\alpha'$  martensites. The coarse size of primary and secondary  $\alpha'$  martensite laths indicates that they were likely to develop in the early stages and further grew in the subsequent thermal cycles in the heat history. By contrast, the fine tertiary  $\alpha'$  martensite is believed to nucleate and grow in the later stages in the heat history, and thus was hindered by the lack of heat and existed boundaries.

The formation of the hierarchical structures was closely related to the thermal profile of the SLM process. The heat history in Figure 29 unveils that upon thermal cycle 1, the columnar  $\beta$  and  $\alpha'$  martensite grains initially formed as the temperature dropped to below the  $T_{\beta}$  and  $T_{M_S}$  respectively. However, at cycle 2 the microstructure in the previous cycle was totally abolished due to the peak temperature exceeding the liquidus temperature,  $T_L$ . Upon the cool down at Cycle 2, new columnar  $\beta$  grains were transformed from the liquid state below the  $T_{\beta}$ , followed by the nucleation of the primary  $\alpha'$  laths at the prior  $\beta$  boundaries as the temperature furtherly dropped to the  $T_{M_S}$ . Besides, dislocations and twins were also generated during  $\beta \rightarrow \alpha'$  transformation to release the stress and overcome the accommodation strain (171). The resulted microstructure of SLM Ti-6Al-4V at ambient temperature consisted of coarse primary  $\alpha'$  grains, residual prior  $\beta$  grains, and dislocations and twins inside the  $\alpha'$  grains.



As the subsequent layers were deposited, the microstructure of SLM Ti-6Al-4V further evolved by the subsequent cyclic thermal loadings. Cycle 3 observed the peaked temperature in the range of  $T_{\beta} - T_s$ , which decomposed the primary  $\alpha'$  into  $\beta$  phase, but the endured dislocations helped re-nucleate the primary  $\alpha'$  upon the cooling temperature below the  $T_{MS}$ . Moreover, the secondary  $\alpha'$  martensite laths as well as the new dislocations were precipitated. Similarly, cycle 4 experienced the peak temperature in the  $T_{MS} - T_{\beta}$  range, a proportion of  $\alpha'$  martensite grains were transformed back into the  $\beta$  phase retaining the dislocations. On the other hand, the untransformed primary and secondary  $\alpha'$  laths continued to grow coarser in the volume. Upon cooling, the fine tertiary  $\alpha'$  laths were transformed together with new dislocations. At cycle 5, the peak temperature was below the  $T_{MS}$ , which could not further affect the microstructure apart from the grain coarsening upon heating. The final microstructure of SLM Ti-6Al-4V, therefore, consisted of the primary, secondary, and tertiary  $\alpha'$  grains as indicated in Figure 33.

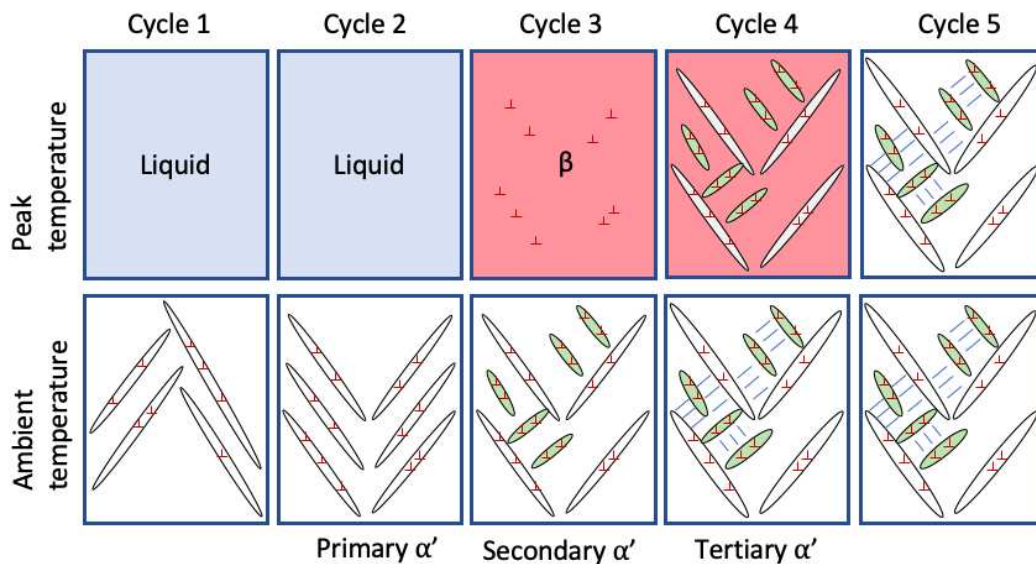


Figure 33. Schematic illustration of the martensite evolution during the heat history of SLM process

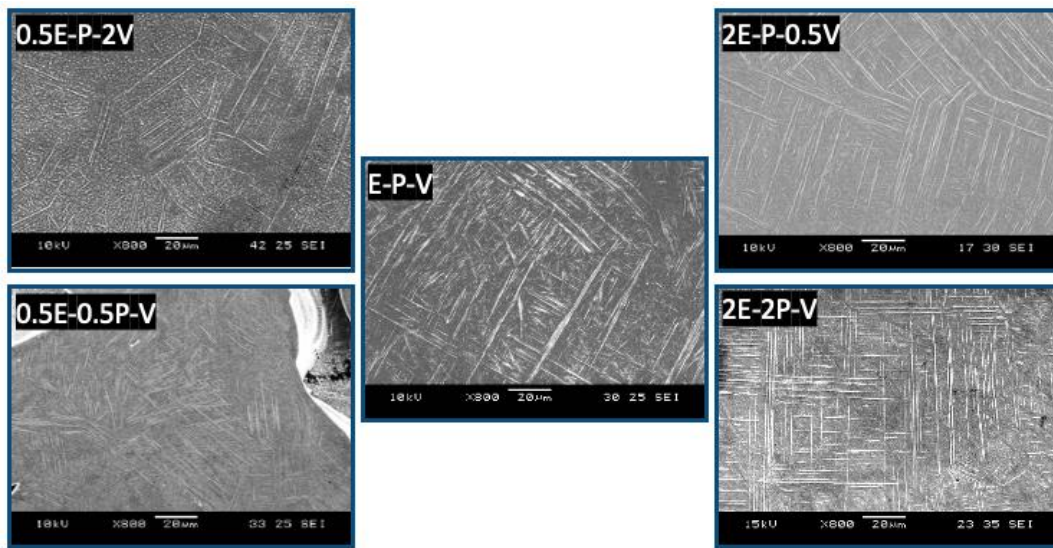
#### 4.4 – Effect of the laser energy density on the microstructure evolution

In this section, a range of laser energy density was designed by varying laser power and scanning speed based on the optimal processing window of SLM Ti-6Al-4V. The optimal parameters of SLM Ti-6Al-4V, as discussed in section 4.1, was designated as **E-P-V**; whereas the other parameter sets were defined as half (0.5E) or double (2E) the energy density by using either half or double the laser power or scanning speed as tabulated in Table 13. The low energy density 0.5E comprises of 2 parameters, **0.5E-P-2V** and **0.5E-0.5P-V**, and the high energy density (2E) consists **2E-P-0.5V** and **2E-2P-V**.

Table 13. Groups of processing parameters to analyse the effect of laser energy density

Nomenclature	0.5E-		E-	2E-	
	P-2V	0.5P-V	P-V	P-0.5V	2P-V
Laser energy density ( $\text{J mm}^{-3}$ )	37.5	37.5	75	150	150
Laser power (W)	120	60	120	120	240
Scanning speed ( $\text{mm s}^{-1}$ )	800	400	400	200	400

The analysis was conducted in the central areas of specimens in which the  $\alpha'$  martensite grain size was the median value of primary and secondary  $\alpha'$  lath size. The typical images of  $\alpha'$  martensite laths of each processing condition can be seen on Figure 34.

Figure 34. SEM images showing the  $\alpha'$  martensite grains in different conditions

The influence of laser energy density on the size of  $\alpha'$  martensite grains is significant. It is observable in Figure 35 that the average columnar grain size increases from 28.9 to 213.4  $\mu\text{m}$ , and martensitic lath size from 17.8 to 53.6  $\mu\text{m}$  when increasing the laser energy density from 37.5  $\text{J mm}^{-3}$  (0.5E) to 150  $\text{J mm}^{-3}$  (2E). The effect of processing parameters on the microstructure evolution in the SLM process was studied in the work of Kobryn and Semiatin (166) studied that pointed out a higher cooling rate would result in a finer grain size. In this study, the low energy density (0.5E) was achieved by either the low power or the high scanning speed, thus resulted in a higher cooling rate, and consequently a finer grain size. By contrast, a combination of high power and low scanning speed would result in a lower cooling rate and a larger grain size in the high energy density (2E) conditions.

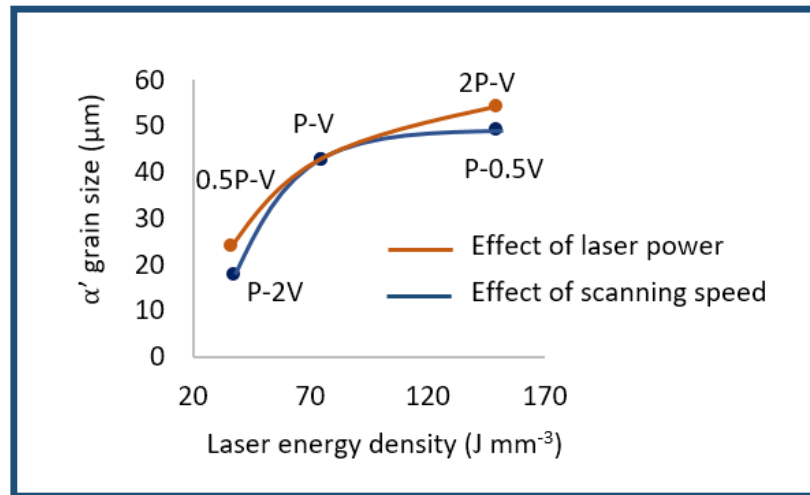


Figure 35. Relationship between processing parameters and a) columnar  $\beta$  grain size and b)  $\alpha'$  martensite grain size

On the contrary, the influence of laser energy density on the tertiary  $\alpha'$  grain size was marginal. As discussed, the primary and secondary  $\alpha'$  grains were justified to precipitate in the early thermal cycles, while the finer tertiary  $\alpha'$  grains were formed in the later phase of the heat history. Increasing laser energy density would increase primary and secondary  $\alpha'$  martensites grain size, as evident in Figure 34 and Figure 35. But the evolution of tertiary  $\alpha'$  martensite was hindered by the borders of previously formed  $\alpha'$  martensites, and thus no noticeable growth was noticed in tertiary  $\alpha'$  grains relative to that in lower energy density conditions.

In fact, increasing laser energy intensity resulted in increasing the grain density of tertiary  $\alpha'$  martensites. As calculated by the number of tertiary  $\alpha'$  grains in the investigated regions of  $20 \times 20 \mu\text{m}^2$ , tertiary  $\alpha'$  grain density steadily increased with higher laser energy input (see Figure 36). The formation mechanism of tertiary  $\alpha'$  grains was highly dependent on the later heat history process, and it is suggested in Figure 37 that a high energy input would result in a higher number of effective thermal cycles. In these subsequent cycles, although no quartic  $\alpha'$  was observed, several studies have shown that these thermal cycles perform as an auto-tempering effect whereby the previously formed (primary and secondary)  $\alpha'$  martensites experience a tempering-like treatment to become softened (172, 173), and thus a small fraction of these martensites were decomposed and precipitated into newly formed (tertiary)  $\alpha'$  grains upon cooling, which increased the tertiary  $\alpha'$  grain density.

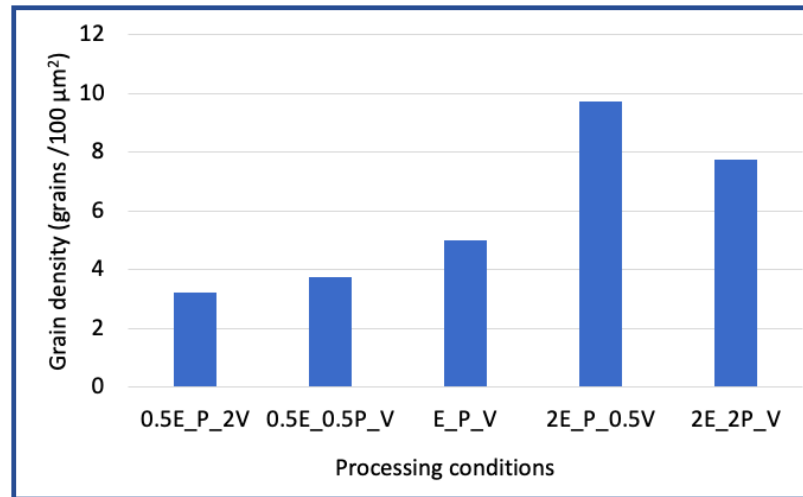


Figure 36. Grain density of the tertiary  $\alpha'$  martensites in different processing conditions

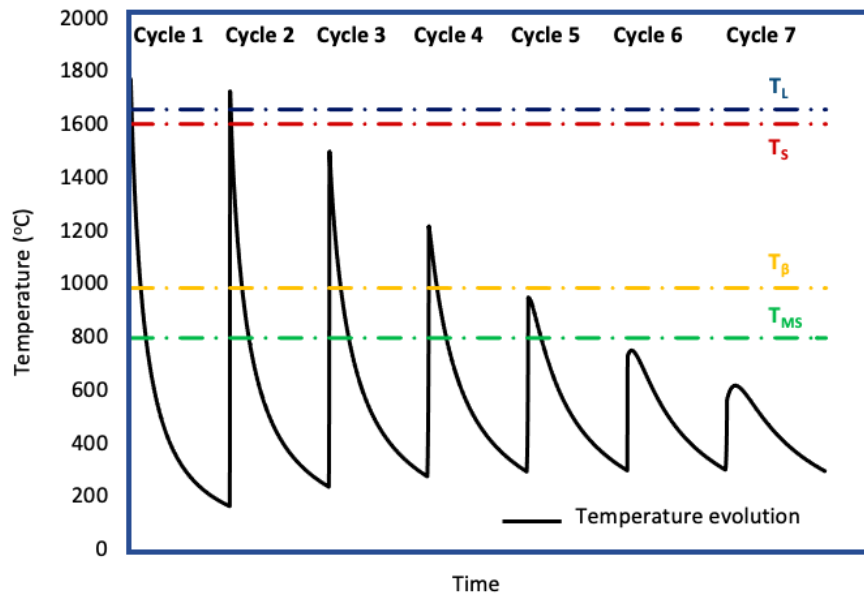


Figure 37. Diagram of heat history in SLM process of Ti-6Al-4V using high laser energy density condition (2E-P-0.5V)

Figure 38 shows the thermal isotherm of different processing parameters from the top and side view. It can be seen that the length of the melt pool increased when increasing the laser power, whereas the depth and width of the melt pool observed similar trend with scanning speed. This indicates both laser power and scanning speed controlled the melt pool shape and effectively thermal behaviour of the materials, thus consequently had a similar effect on the martensitic lath size as observed in Figure 35.

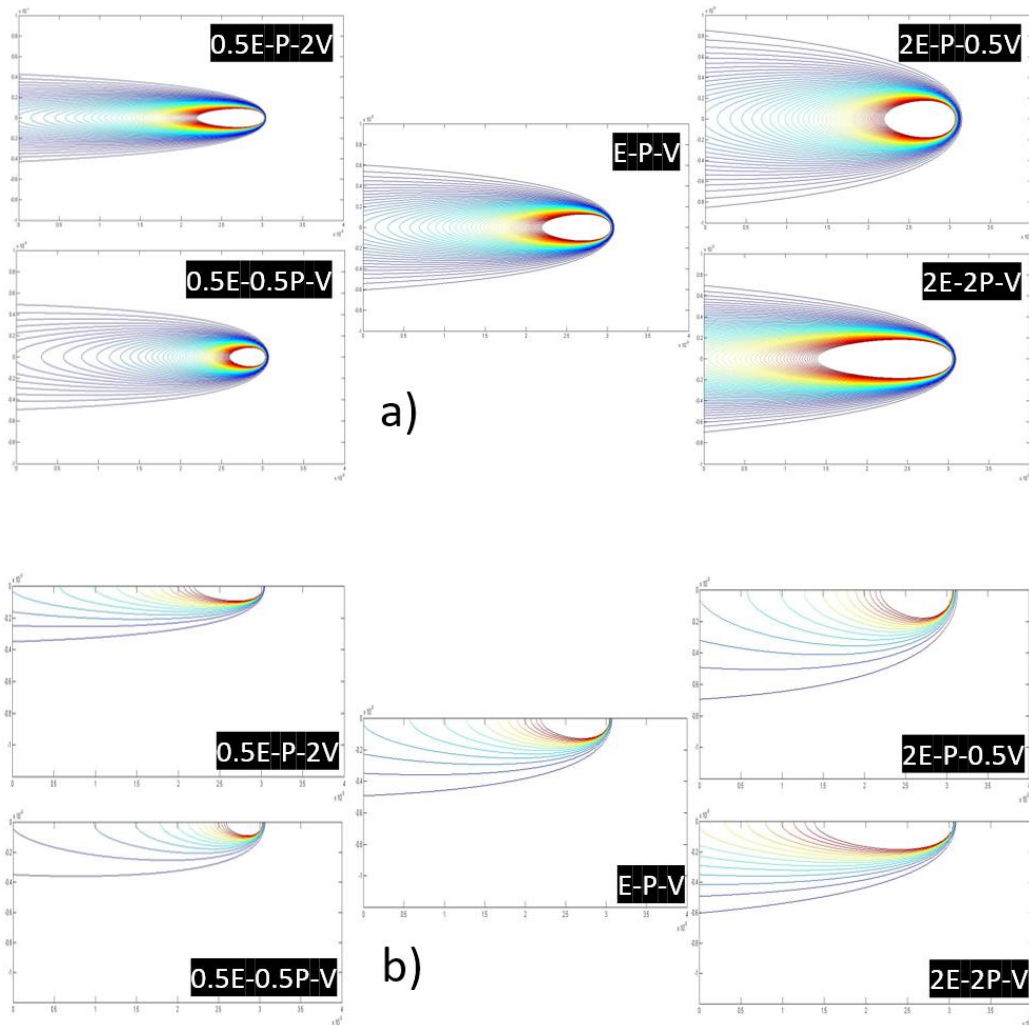


Figure 38. The predicted temperature isotherms in different processing conditions in the a) XY plane and b) XZ plane

## **4.5 – Effect of the laser energy density on mechanical properties**

### **4.5.1 – The hardness and quasi-static tensile properties**

Mechanical properties, such as tensile strength, fatigue life and micro hardness, are essential in industrial applications and also in the materials development for the SLM Ti-6Al-4V. It is therefore of importance to analyse the mechanical properties of SLM Ti-6Al-4V associated with the microstructure evolution influenced by the laser energy density. The key microstructural factors strongly affecting mechanical properties of ( $\alpha+\beta$ ) titanium alloys have been studied, which are the  $\beta$ -grain size, the  $\alpha$ -colony size, the thickness of lamellar  $\alpha$ , the size and shape of the primary  $\alpha$ -grains, and the volume fraction of  $\alpha$  and  $\beta$  (7, 174). In this section, the micro-hardness and tensile properties will be analysed to understand the effect of laser energy density on mechanical properties under quasi-static

conditions, which are highly influenced by the heterogeneity in the microstructure of columnar  $\beta$  and  $\alpha'$  martensite structures.

The averaged micro-hardness properties in each processing conditions of SLM Ti-6Al-4V are shown in Figure 39. To evaluate the tensile properties, a set of 4 dog-bone ASTM E8 standard specimens for each of 5 different processing conditions, totally 20 specimens, were employed in this section. Figure 40 illustrates the typical stress-strain curves in 5 processing conditions. The tensile properties were analysed as the 0.2% proof Yield Strength (YS), the Ultimate Tensile Strength (UTS) and the Elongation which are summarised in Figure 41 and Figure 42. All the mechanical properties of SLM Ti-6Al-4V are illustrated together with the ISO 5832 – 3 standard data of Ti-6Al-4V manufactured by conventional methods what can be found in reference (175) for comparison.

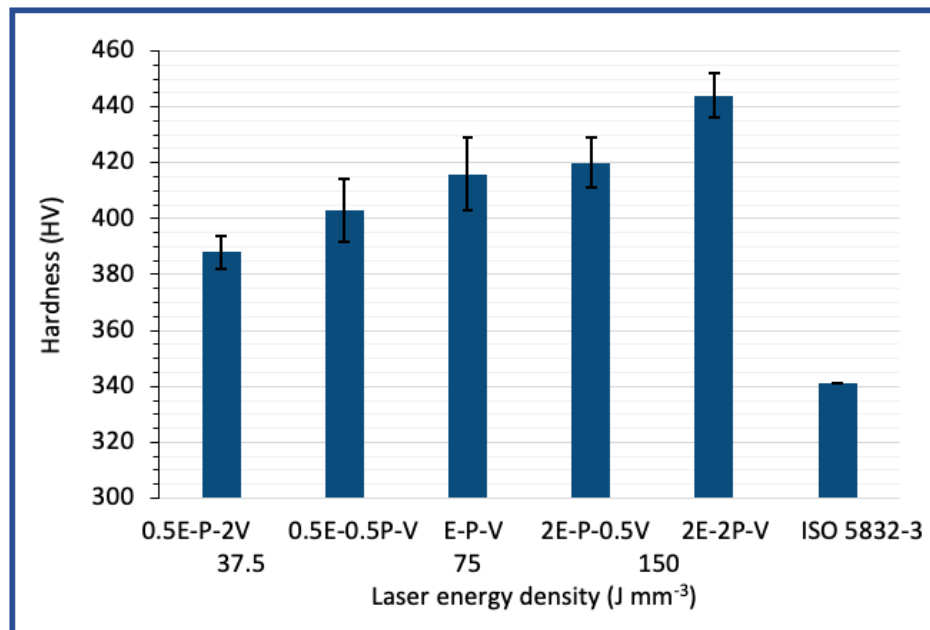


Figure 39. Relationship between hardness and laser energy density



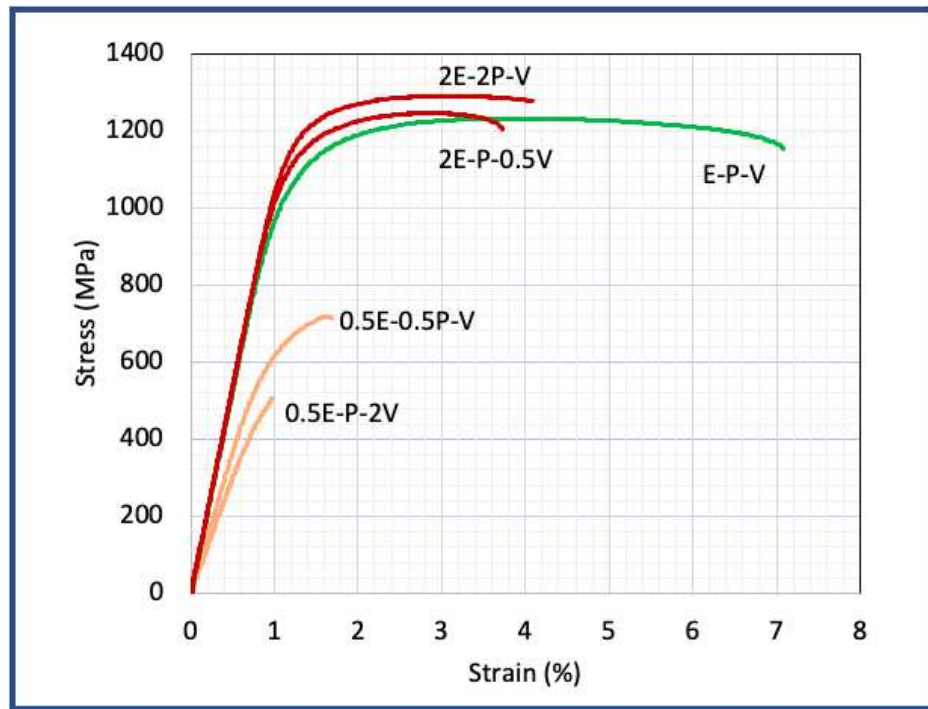


Figure 40. Tensile curves of SLM Ti-6Al-4V in different processing conditions

The poor hardness and ductility of the specimens produced by inadequate energy density—0.5E—conditions are noticeable. This is because of the high porosity and lack of fusion within the interlayers of the specimens leading to premature material failure. The findings reassure the value of adequate laser energy densities in Ti-6Al-4V's SLM processing to manufacture high-quality components.

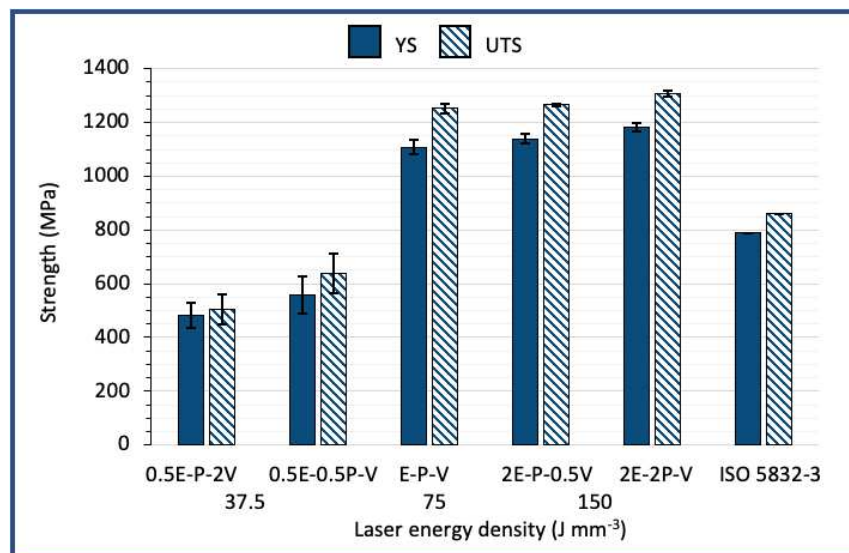


Figure 41. Relationship between tensile strength and laser energy density

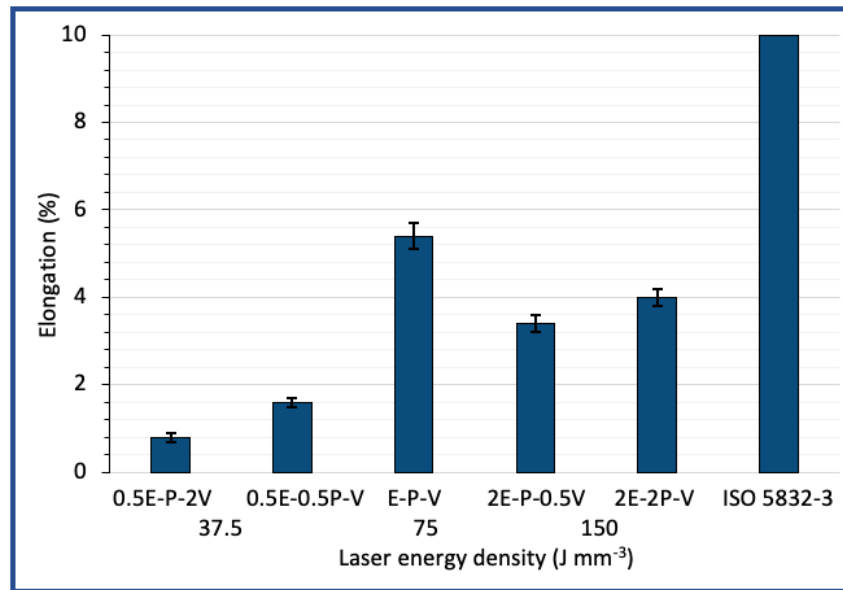


Figure 42. Relationship between elongation and laser energy density

As regard to the specimens manufactured by the standard and high energy density conditions, it is observable that both the strength and hardness are significantly improved, as 45 - 52% superior than that by the ISO 5832-3 standard. However, the superior mechanical strength came at the cost of ductility, with the maximum elongation of  $5.4 \pm 0.3\%$  achieved by the standard energy densities compared to 10% by the ISO 5832-3. This finding suggests that the hierarchical martensite microstructure in the SLM Ti-6Al-4V played a key role in improving the hardness and tensile strength, while, on the other hand, deteriorating the ductility compared to the wrought and annealed Ti-6Al-4V with the conventional  $\alpha+\beta$  microstructure.

The hardness and tensile strength of SLM Ti-6Al-4V are observed to increase with the increase in laser energy density. Interesting is that a higher energy density would result in a coarser martensite grain morphology as it has been discussed, which should have reduced the tensile strength according to the Hall-Petch's relationship. To be more specific, the Hall-Petch's relationship states that a higher strength can be achieved by reducing the grain size (176). It can be concluded that the mechanical properties of SLM Ti-6Al-4V did not follow the Hall-Petch's relationship due to the highly dislocation and the heterogeneity in the martensitic microstructure which will be discussed more in details in section 4.5.3.

#### **4.5.2 – Fracture behaviours**

Fractography of the tensile specimens were carried out by SEM to understand the fracture behaviours of SLM Ti-6Al-4V. The fracture surface profiles of all the processing conditions are observed to have a flat crack opening region perpendicular to the axial loading (see Figure 43). Furthermore, the fracture surfaces have the terrace-like feature, revealing the dominant fracture behaviour was inter-granular.



This is reasoned as the samples were built horizontally on the substrate plate, the columnar  $\beta$  grains grew along the cross section of the samples, and the crack easily propagated along the columnar  $\beta$  boundaries perpendicular to the tensile loading. In addition, high porosity and unmelted spherical particles are found at the fracture surfaces of low energy density specimens (see Figure 44) which evidently confirm the poor mechanical properties of these conditions.

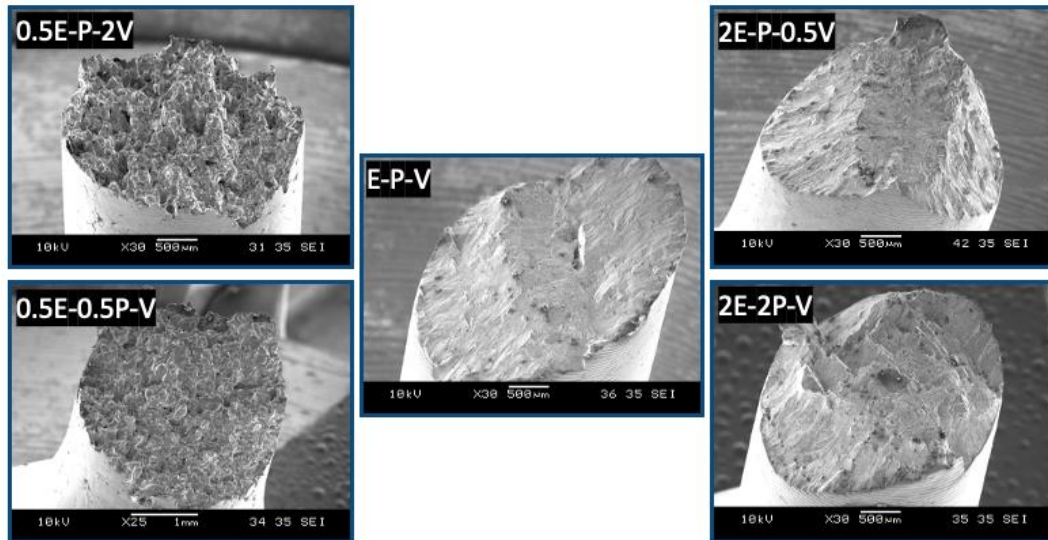


Figure 43. SEM images of fracture surfaces in different processing conditions

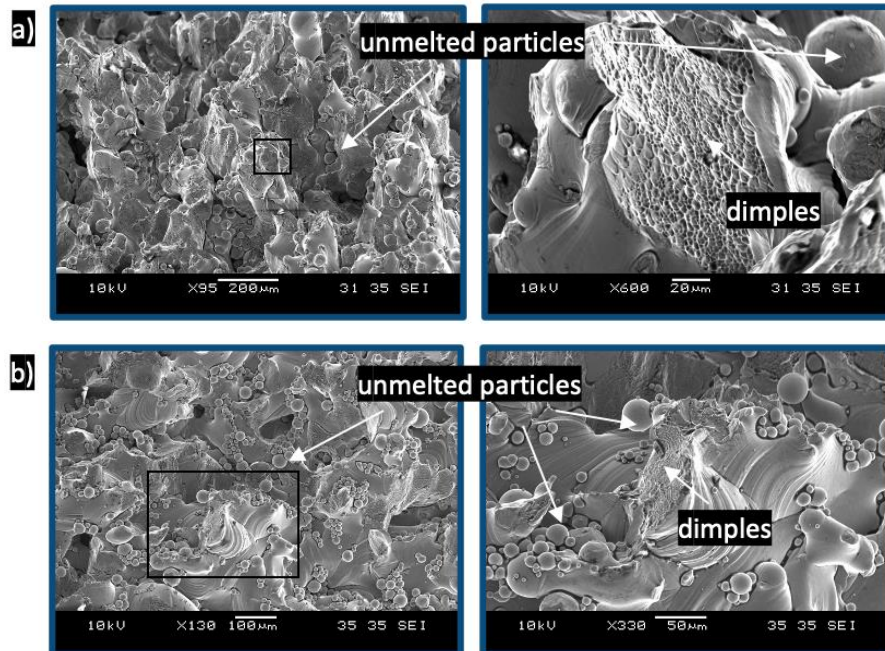


Figure 44. SEM images of fracture surfaces revealing lack of consolidation in the conditions a) 0.5E-P-2V and b) 0.5E-0.5P-V.

Dimples were found on all the conditions, showing no clear directional marks, so the crack propagation direction is unlikely to be figured out. However, in the standard condition, the propagation path could

be predicted by the alignment of micro cracks existed on the fracture surfaces (see Figure 45). It is noteworthy slip bands are only present in the high laser energy density specimens (see Figure 46, Figure 47), suggesting the local plastic deformation occurred. Whereas the stair marks revealed the effect of twinning in the martensites on the plastic deformation of SLM Ti-6Al-4V. These twinings were created due to the formation of martensites which were controlled by the thermal loadings during processing conditions, thus it can be concluded that the processing parameters also influences the deformation of SLM Ti-6Al-4V.

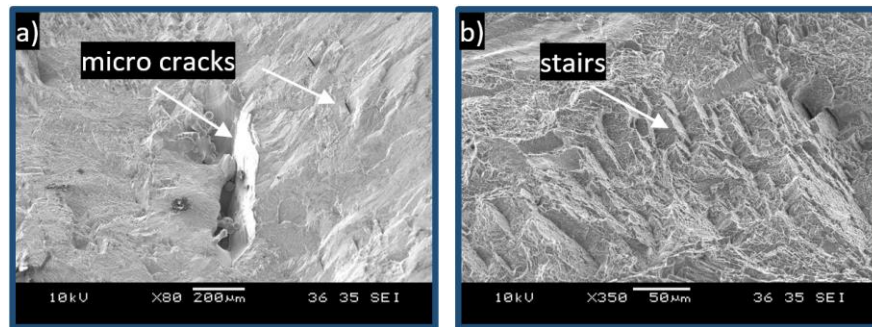


Figure 45. SEM images showing a) micro cracks and b) stairs on the fracture surfaces of the E-P-V condition

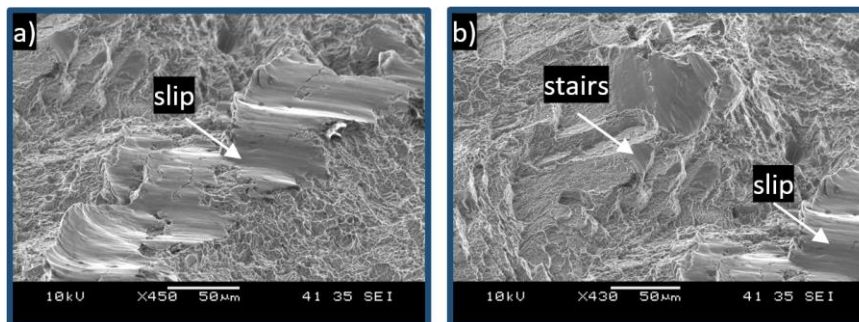


Figure 46. SEM images showing a) slip sign and b) stairs on the fracture surfaces of the 2E-P-0.5V condition

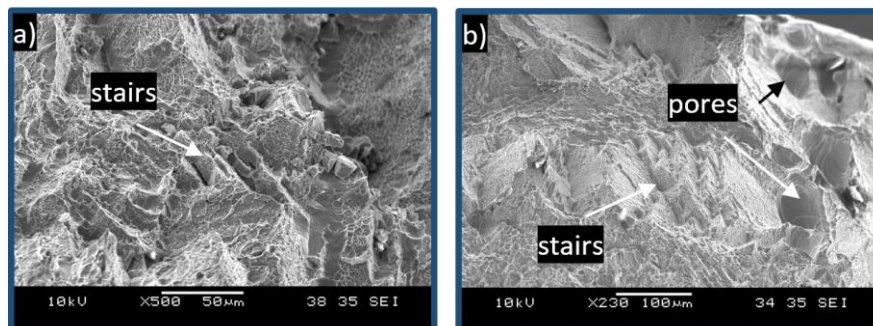


Figure 47. SEM images showing a) stairs and b) stairs and pores on the fractures surfaces of the 2E-2P-V condition

### **4.5.3 – The relationship of the $\alpha'$ martensite and the mechanical properties**

Martensite grains are formed by a finite volume shift in shape by shear from a high cooling rate and thermal cyclic loading during the SLM process. Since the martensite plate is directly coherent with the prior  $\beta$  matrix, the martensite plate and parent matrix establish an accommodation strain at their boundaries. This accommodation strain can be either elastic or plastic, or a mixture of both, depended on the SLM processing condition. Whether or not the strain is accommodated in the parent elastically or with a sizeable amount of plastic deformation is an important consideration. If the strain in the matrix is elastic, the  $\alpha'$  martensite and the parent  $\beta$  phase can move easily at the boundaries, resulting in a more ductile property. By contrast, if plastic strain is induced during the SLM process, the boundaries between  $\alpha'$  martensite plates and the parent  $\beta$  matrix tend to be locked in place by the dislocations which result in a high strength and low ductility property.

This phenomenon on thermoelasticity was originally studied and expressed by Kurdjumov and Maksimova (177). They suggested that the thermoelastic transformation processes an equilibrium between the chemical and non-chemical forces when the martensite plates grow. The thermodynamics of the martensite transformation from the parent phase at equilibrium condition, based on the study of Ortín and Planes (178), is expressed as the following equation:

$$\Delta G^{P-M} = -\Delta G_{ch}^{P-M} + \Delta G_{el}^{P-M} + E_{fr}^{P-M} = 0 \quad (\text{Equation 19})$$

where  $\Delta G^{P-M}$  is the delta Gibbs free energy per mole,  $\Delta G_{ch}^{P-M}$  is the component of the delta Gibbs free energy from the difference of chemical equilibrium state between the parent and martensite phase,  $\Delta G_{el}^{P-M}$  is the component from the elastic energy, and  $E_{fr}^{P-M}$  is the work done by frictional forces.

The elastic part of the free energy is primary due to the energy stored in the interfaces between the  $\alpha'$  martensite and the parent  $\beta$ , and to the elastic strain due to the creation of the martensite. In turn, work done by frictional losses include the moving the martensite interfaces, the energy losses associated with the creation of dislocations, and the partial plastic accommodation strain associated with the transformation. In general, at low laser energy density, the main part of work by frictional forces is for moving the martensite plates whilst at high energy density conditions, the work done by frictional forces favors the creation of dislocations.

Upon the subsequent thermal cycle, where the  $\alpha'$  martensite is reverted to the  $\beta$  phase, the stored elastic energy is recovered and aids the reverse transformation. It will now be assumed that the temperature during the reversed transformation is above the  $T_{MS}$ , the equilibrium temperature

between the  $\beta$  phase and the martensite. The equilibrium condition for the transformation, assuming that  $T > T_{MS}$  may now be written as:

$$-\Delta G_{ch}^{P-M} - \Delta G_{el}^{P-M} + E_{fr}^{P-M} = 0 \quad (\text{Equation 20})$$

Note that in the (Equation 20), both the chemical and elastic free energies are negative while the frictional loss due to dislocations is positive. This means that in the reverse transformation, both the chemical and elastic forces act to overcome the frictional forces. This can be understood that during the reverse transformation, the dislocations remain in materials, and over the course of subsequent thermal loadings, the total dislocations increase. Since the high energy density would increase the number of thermal cycles with the peak temperature above the  $T_{MS}$ , hence results in more dislocations in the materials and leads to higher strength and lower ductility, as proved by the resulted tensile properties.

Noteworthy is that during the following thermal cycles of  $T_{peak}$  near  $T_{MS}$ , earlier precipitated  $\alpha'$  grains often exposed themselves to auto-tempering processes, and were hence less dislocated and softer than the newly formed microstructures that were un-tempered (173, 179). The level of auto-tempering depends largely on the order of martensite development (180). Primary  $\alpha'$  martensites, which were transformed in the early phase of the heat history and grew across the prior  $\beta$  grains, were more auto tempered and less dislocated. In comparison, the tertiary  $\alpha'$  grains were less subject to auto-tempering because of the absence of following thermal cycles and were thus more dislocated and harder. That is to say, the ability to accommodate strain increases from tertiary to primary  $\alpha'$  martensites, which contributes to a heterogeneous microstructure and incompatibility in deformation. As the tensile loading is carried out on this heterogeneous microstructure, the softer and comparatively more ductile primary  $\alpha'$  grains would undergo deformation with higher strain, and independently from the harder and more brittle tertiary  $\alpha'$  grains, causing localised plasticity (180). This phenomenon has been documented in several studies in martensitic steel as the effect of auto-tempering (179, 181, 182).

Increasing the laser energy input often promotes more strain accommodation incompatibility and a more heterogeneous microstructure due to more auto-tempering on primary  $\alpha'$  grains and more precipitation of tertiary  $\alpha'$  grains. Fractography in these high-energy input conditions in Figure 46 indicates that localised plasticity occurs at primary  $\alpha'$  martensite boundaries resulting in slip bands. This effect of interface localised plasticity on the deformation of SLM Ti-6Al-4V has yet to be studied (180).

It is shown here that martensite boundaries of SLM built Ti-6Al-4V parts are extremely vulnerable to localised plasticity and highly accumulated dislocations to tolerate the strain incompatibility, and more dislocated tertiary  $\alpha'$  microstructure, which results in an overall brittle characteristics that does not follow the Hall-Petch's relationship.

#### **4.6 – Chapter summary**

Laser energy density is the important parameter that requires careful consideration in order to produce high quality parts. An insufficient or excessive energy density would result in many undesirable defects, such as porosity, interlayer cracks, balling and keyhole effect, as well as bad surface quality. The standard processing window for SLM Ti-6Al-4V as tabulated in Table 11 was successfully chosen within the optimal range of laser energy density, based on the capability of producing nearly fully dense parts with the highest surface quality.

The thermal simulation based on the Rosenthal point source was successfully applied to predict and compare the influence of laser energy density on the size and shape of melt pool as well as the solidification condition and the heat history in the SLM process. The predicted melt pool geometry had the “tear drop” shape, of which the laser power affected the length and the scanning speed influenced the width and the depth. In addition, the thermal simulation gave correct predictions on the solidification condition and cooling rates in the melt pool on which a fully columnar  $\beta$  and  $\alpha'$  martensite microstructure thrived.

The final microstructure of SLM Ti-6Al-4V at room temperature consists nearly fully of martensite  $\alpha'$  and a minor of prior  $\beta$  phase. During the manufacturing process, columnar  $\beta$  grains grew epitaxially up through each melted layer to form continuous columnar grains due to high growth rate and cooling rate. A hierarchical structure of  $\alpha'$  martensite including primary, secondary and tertiary  $\alpha'$ , appeared as acicular grains crossing one another at different length scale inside the columnar  $\beta$  grains. The formation of primary, secondary and tertiary  $\alpha'$  martensite in the SLM Ti-6Al-4V was proposed based on the predicted heat history by the thermal simulation in which the primary, secondary and tertiary  $\alpha'$  is respectively formed in Cycle 2 ( $T_L < T_{peak}$ ), Cycle 3 ( $T_\beta < T_{peak} < T_S$ ) and Cycle 4 ( $T_{MS} < T_{peak} < T_\beta$ ).

Due to the cyclic thermal loadings in the layer-by-layer technique of SLM, the thermoelasticity and auto-tempering process on the formation of  $\alpha'$  martensite resulted in the heterogeneous microstructure. The thermoelasticity formed dislocations in the evolution of  $\alpha'$  whereas the auto-tempering released them but resulted in the strain accommodation incompatibility among the  $\alpha'$  structures, causing the localised plasticity in the deformation of SLM Ti-6Al-4V.

Increasing laser energy density further facilitated the heterogeneity in the microstructure and mechanical properties of SLM Ti-6Al-4V. A high laser energy density increased the size of softer, less dislocated primary and secondary  $\alpha'$  grains while precipitated more harder, more dislocated tertiary  $\alpha'$  martensites. Also, the increase in laser energy density induced more plastic accommodation strain and more piled-up dislocations in  $\alpha'$  martensites, which improved the hardness and tensile strength but also significantly reduced the ductility.

## Chapter 5 – Dynamic behaviours of SLM Ti-6Al-4V

In the previous chapter, the mechanical properties of SLM Ti-6Al-4V were analysed under quasi-static condition. In comparison, dynamic condition also plays a critical role in the operating conditions of Ti-6Al-4V and a large variety of Ti-6Al-4V applications that are serviced under high strain rates in aerospace and many other industries, such as landing gears, turbine blades and ballistic impact uses. However, the dynamic behaviours of Ti-6Al-4V and, more importantly, SLM Ti-6Al-4V are poorly understood. This chapter will focus on the relationship between the dynamic compressive responses and the microstructure evolution as subject to a wide range of laser energy densities in order to have a better understanding of the performance and behaviours of SLM Ti-6Al-4V under dynamic conditions. The mechanism and kinetics of dynamic recrystallization will also be investigated.

### 5.1 – Dynamic compression properties

In this study, dynamic properties of SLM Ti-6Al-4V were investigated by conducting SHPB tests at a strain rate of  $3000 \text{ s}^{-1}$  until the specimens were completely compressed. In addition, the laser energy density range was selected for evaluation based on the results of the previous chapter, with further extension to the higher end of the range by applying the 4E condition for further comparison as shown in Table 14.

Table 14. Processing conditions of SLM Ti-6Al-4V for dynamic properties analysis

Laser energy density ( $\text{J mm}^{-3}$ )	37.5	75	150	150	300
Laser power (W)	120	120	120	240	240
Scanning speed ( $\text{mm s}^{-1}$ )	800	400	200	400	200
Designation	0.5E-P-2V	E-P-V	2E-P-0.5V	2E-2P-V	4E-2P-0.5V

The standard dynamic stress-strain response of SLM Ti-6Al-4V is depicted in Figure 48. In literature, Zheng, Zeng (104) also examined the dynamic response of Ti-6Al-4V at the same strain rate of  $3000 \text{ s}^{-1}$ , claiming that the stress-strain response consists four regimes: elastic deformation, homogenous plastic deformation, adiabatic shear banding, and the specimen failure. Nevertheless, as the initiation of adiabatic shear bands leads to the substantial drop of dynamic strength, marking the beginning of catastrophic material failure (10, 108, 109), this study hence suggests classifying the dynamic response of SLM Ti-6Al-4V into 3 distinct regions: (i) elastic deformation, (ii) plastic deformation and (iii) material failure, as can be seen in Figure 48.

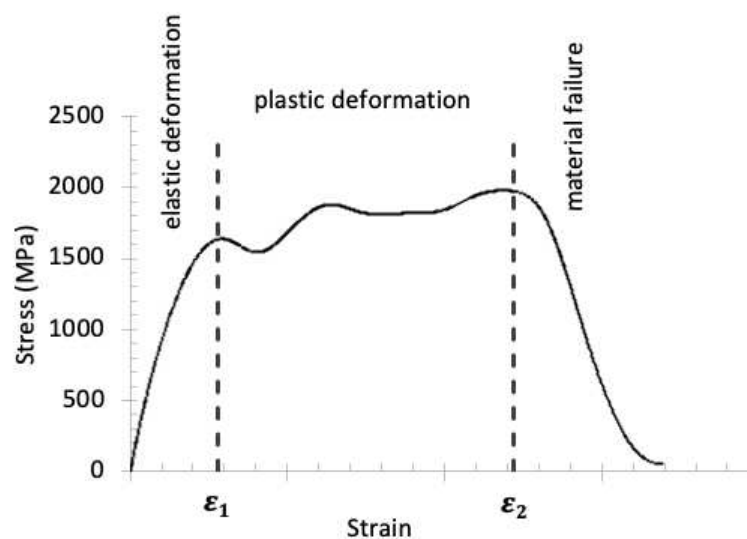


Figure 48. The dynamic mechanical response of SLM Ti-6Al-4V



The dynamic properties of SLM Ti-6Al-4V can be represented in the elastic and plastic deformation before failure. In the elastic deformation, a sharp linear increase in stress was observed as the strain increases until the first inflexion point ( $\epsilon_1$ ) marking the end of the first level, followed by the first stress drop in the plastic deformation. This kind of early stress drop was mentioned in other studies caused by the low plasticity at room temperature (104) or the discontinuous yielding behaviours (183). During the plastic deformation segment, the strength loss due to grains softening effect, caused by the local temperature rise, was balanced by the strength gained from the strain hardening effect. The competition of these two effects became unstable when the strain reached the second reflection point ( $\epsilon_2$ ), at which the thermal softening outweighed the strain hardening, and initiated localised shear bands which sharply reduced the stress bearing capacity of the specimens. As such, the stress drops revealed the instability in the thermo-viscoplasticity of SLM Ti-6Al-4V which is the beginning of the material failure with the initiation of adiabatic shear bands (ASBs) and the crack propagation (108, 130, 137).

More importantly, the ASB can be technically regarded as the key sign of disastrous material failure. To minimise its formation and effect, the initiation criteria for shear bands have attracted attention and been found to be linked to the critical strain (184), which was first proposed Bai (185) and verified by experimental studies for titanium alloys by Xu, Liu (186). In this study, the critical strain prior to the initiation of ASB is the second inflection point ( $\epsilon_2$ ) as can be seen in Figure 48. The critical strains ( $\epsilon_2$ ) of different SLM processing conditions were carefully examined together with the other two quantities—yield stress (YS) and first inflection point ( $\epsilon_1$ )—as tabulated in Table 15. Besides, the dynamic responses as subject to different processing conditions are illustrated in Figure 49-Figure 53, presenting the stress-strain curves of all the tested samples.

*Table 15. The mechanical properties under dynamic conditions of SLM Ti-6Al-4V*

Processing condition			YS (MPa)	$\epsilon_1$	$\epsilon_2$
0.5E-	P-	2V	931 ± 109	0.023 ± 0.004	0.165 ± 0.021
E-	P-	V	1652 ± 82	0.028 ± 0.002	0.125 ± 0.014
2E-	2P-	V	1611 ± 62	0.028 ± 0.001	0.111 ± 0.009
2E-	P-	0.5V	1820 ± 54	0.027 ± 0.000	0.105 ± 0.010
4E-	2P-	0.5V	1954 ± 10	0.03 ± 0.000	0.118 ± 0.008

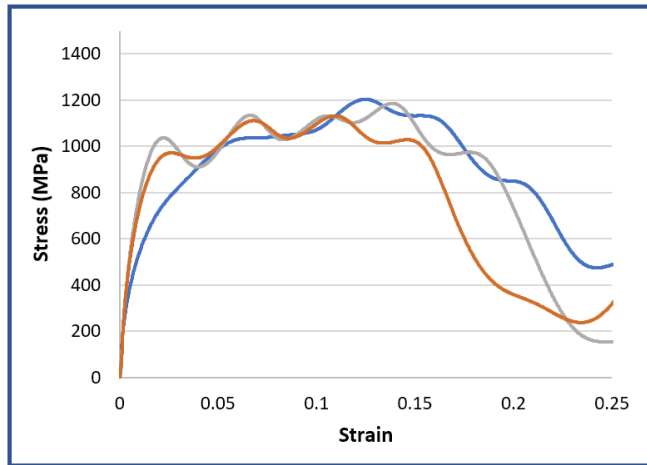


Figure 49. Dynamic stress and strain curves of 0.5E-P-2V samples

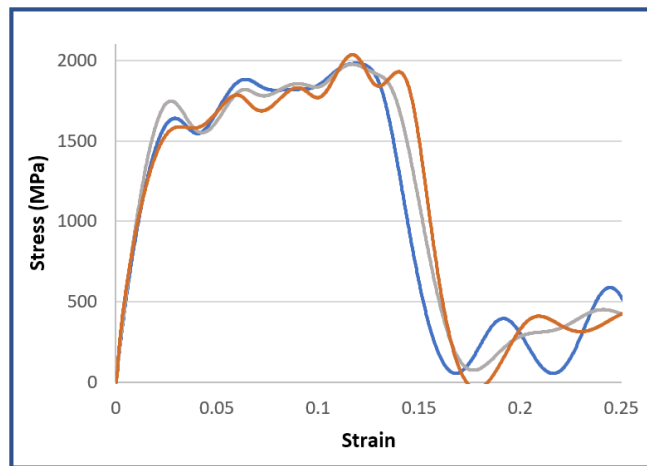


Figure 50. Dynamic stress and strain curves of E-P-V samples

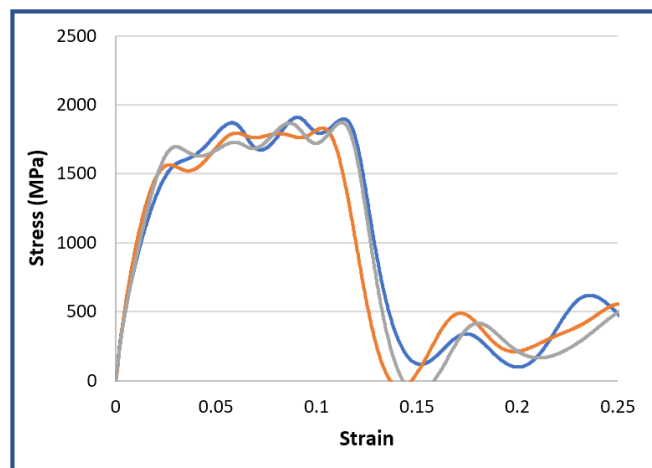


Figure 51. Dynamic stress and strain curves of 2E-2P-V samples

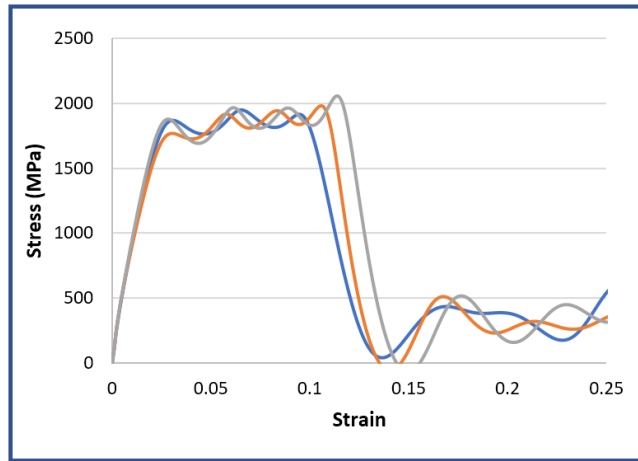


Figure 52. Dynamic stress and strain curves of 2E-P-0.5V samples

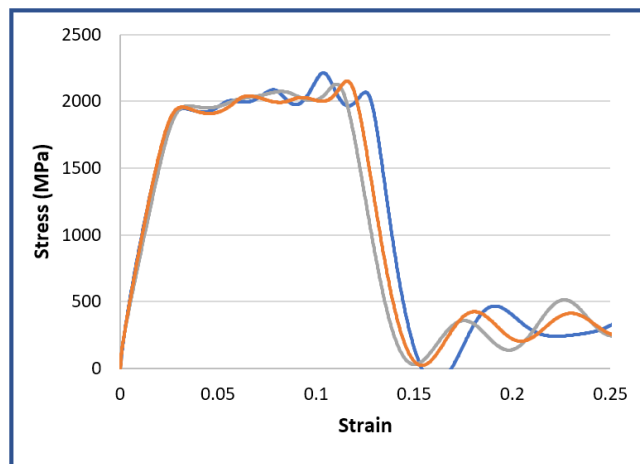


Figure 53. Dynamic stress and strain curves of 4E-2P-0.5V samples

The laser energy input has a significant effect on the dynamic behaviours of SLM Ti-6Al-4V. It can be seen from Table 15 that increasing the energy density observes a spectacular rise in the YS at an expense the critical strain  $\epsilon_2$ . These patterns are expected as it has been pointed out in the previous chapter that the laser energy input has the significant influence on the densification degree of materials. Increasing the energy density would improve the hardness and the relative density as well as result in higher level of dislocations, which account for the resistance to plastic deformation and for the detrimental effect to the strain accommodation and elongation.

## **5.2 – Adiabatic shear bands**

The formation of ASB, which appears as narrow regions of severe localised plastic deformation, degrades the mechanical properties and leads to the service life limit of materials by fatal failure under high strain rate conditions. Hence, understand the characteristics of the ASBs helps minimise its effect on material failure. There have been a great number of studies investigating on the ASB behaviour of many different alloys: steel (98-100), Ta (101, 102), Al (103), Ti (104, 105) and Mg (106), and it is

generally accepted that the ASB occurs in the instability areas where the grain softening exceeds the grain hardening effect (97). Due to its low heat conductivity, titanium alloys and Ti-6Al-4V in particular, are intensively prone to the ASB formation and catastrophic failure.

This research examined dynamic compressed specimens on the longitudinal cutting plane. It is noted that the ASBs initiated on the maximum shear paths which also facilitated the coalescence of voids and cracks (see Figure 54-Figure 58). These shear paths shared the V-shape feature in all processing conditions, creating an about 45° diagonal angle to the loading direction. Additionally, despite the lower critical strain, high-energy density samples (2E and 4E) observed the bifurcation of ASBs at crack ends, creating a network of ASBs shown in Figure 56 and Figure 58 which was due to the complex dislocations resulted from the as-built condition. Regarding low energy density specimens, pre-existing cracks and porosity were in abundance, making it harder to discern the ASBs at the crack tips. In general, the ASBs were found to be narrower when increasing the energy density conditions (30-35 mm at 0.5E condition compared to 15-20 mm at 4E condition) as lower critical strains in high energy densities minimised the expansion of ASBs.

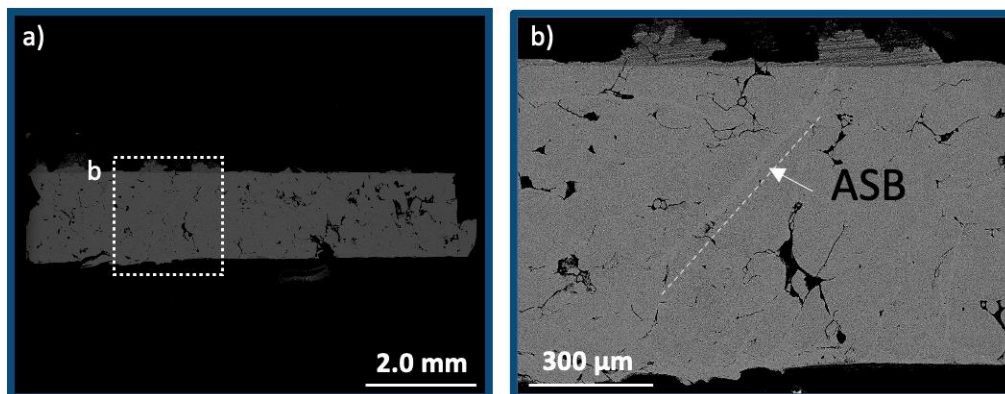


Figure 54. SEM images showing a) the 0.5E-P-2V compressed specimen and b) the local region of ASB

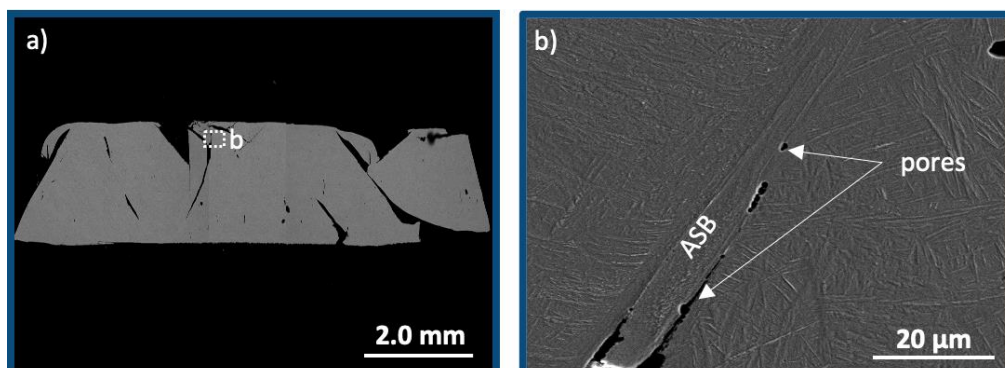


Figure 55. SEM images showing a) the E-P-V compressed specimen and b) the local region of ASB

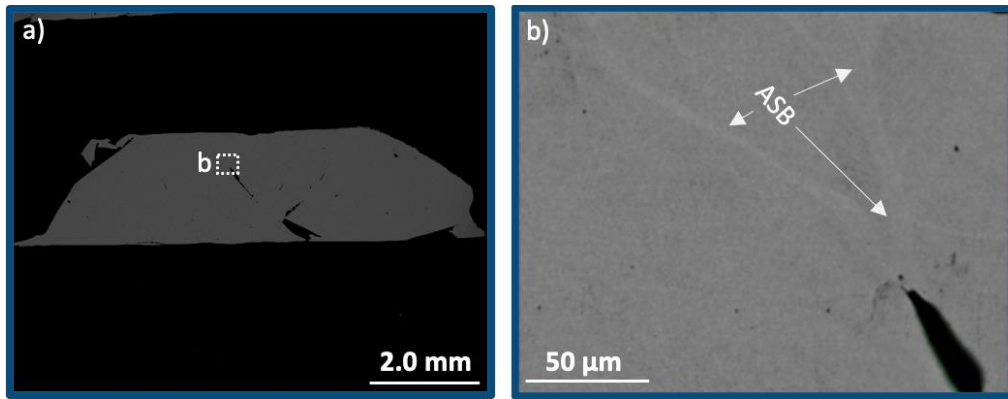


Figure 56. SEM images showing a) the 2E-P-0.5V compressed specimen and b) the local region of ASB

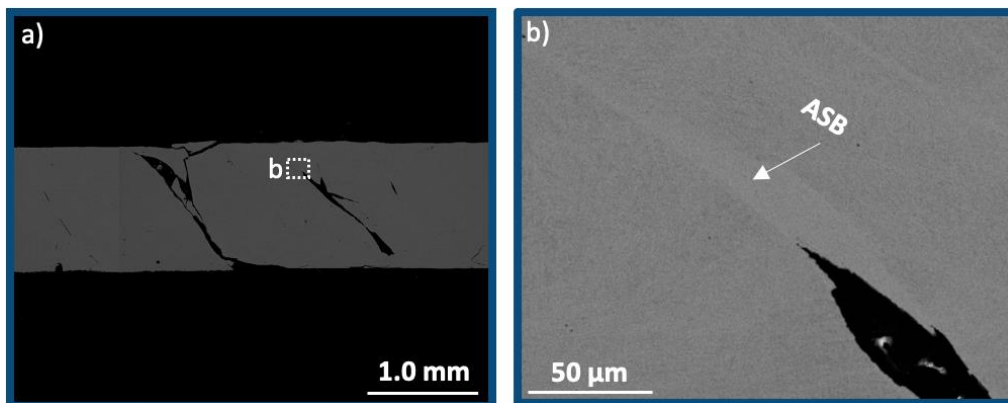


Figure 57. SEM images showing a) the 2E-2P-V compressed specimen and b) the local region of ASB

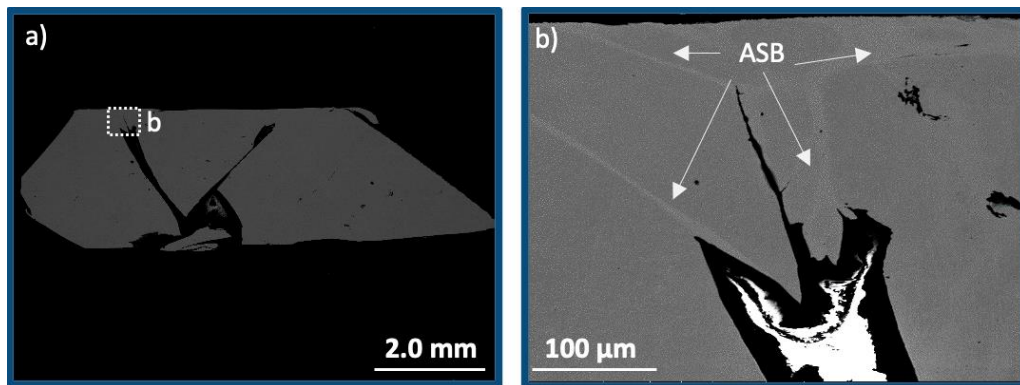


Figure 58. SEM images showing a) the 4E-2P-0.5V compressed specimen and b) the local region of ASB

For a broader view on the dynamic properties of SLM Ti-6Al-4V, a reference material, Ti-6Al-4V made by conventional wrought, was employed as a benchmark on the SHPB dynamic test. Furthermore, interrupting dynamic tests at predefined strains were conducted with the aid of stopping rings to understand the development of the ASB over deformation. It is noteworthy that these interrupting tests could only be achieved on the reference materials because the brittleness and low critical strain features of SLM Ti-6Al-4V could not meet the requirements of interrupting tests. Three different predefined strains were selected corresponding plastic deformation and material failure stages of the

deformation that were remeasured in the post-test procedure as 0.17, 0.33 and 0.5 as shown in Figure 59.

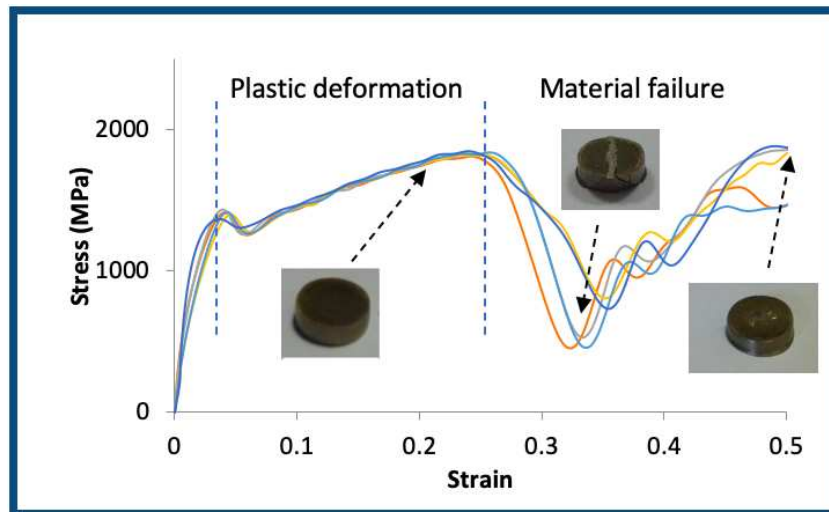


Figure 59. Dynamic mechanical responses of the reference Ti-6Al-4V with images of interrupting tested samples at different strains

Figure 60 provides a full view of the longitudinal portion of compressed reference specimens at predefined strains. It is clearly observed that the grain softening effect was compensated by the grain hardening effect that no ASBs were observed in the specimens at 0.17 strain, the plastic deformation point. The ASBs and associated cracks were not formed until the deformation reached the critical strain ( $\epsilon_2=0.26$  for the reference material). Over the course of evolution, the ASB increased its width from 10-25  $\mu\text{m}$  at 0.33 strain to 20-35  $\mu\text{m}$  at 0.5 strain. At the later stage of deformation, high density of dislocations produced in the materials led to the bifurcation effect in the ASBs resulting in a separate shear band as shown in Figure 61.

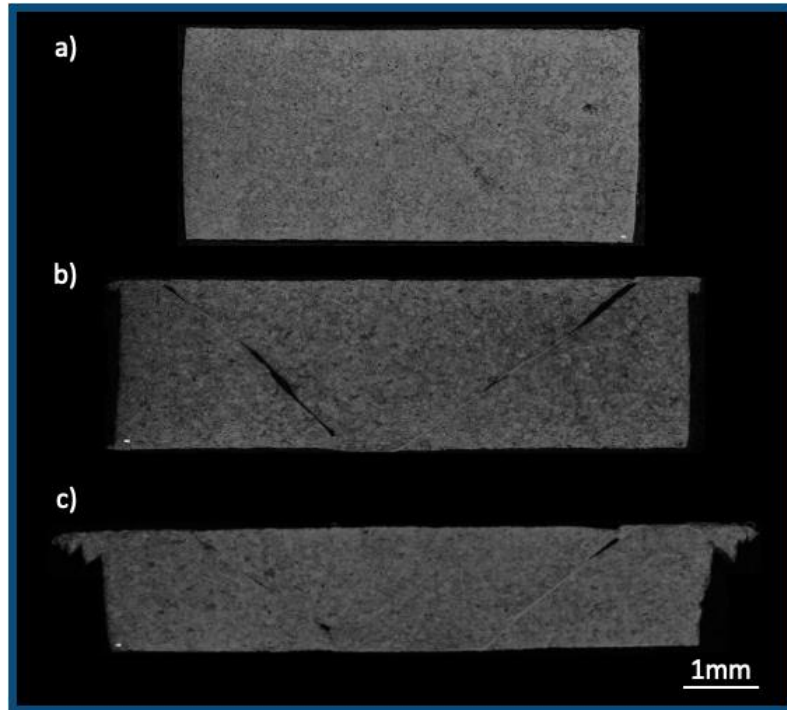


Figure 60. OM images showing the reference Ti-6Al-4V tested specimen at a) 0.17 strain, b) 0.33 strain and c) 0.5 strain

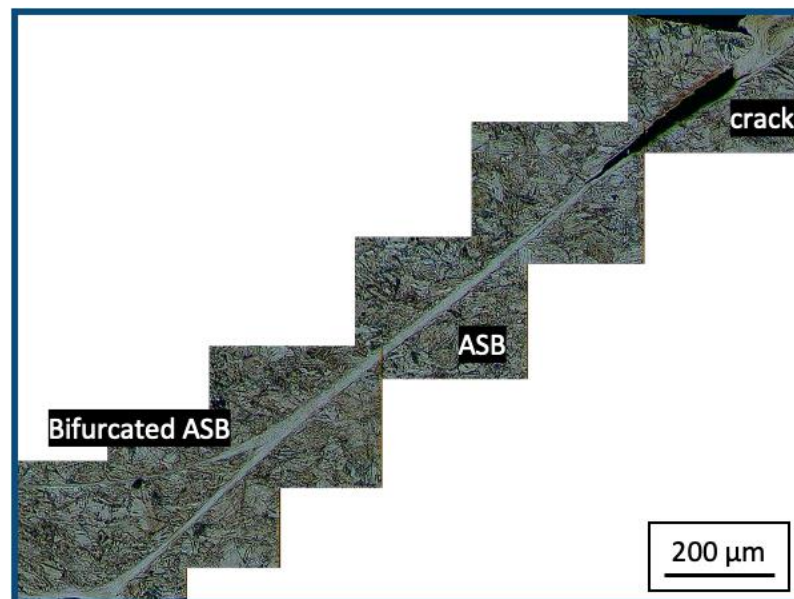


Figure 61. OM image showing the bifurcation of ASB at 0.5 strain

The ASB bifurcation was shown to occur due to the high dislocations resulted from high level of deformation (130). Whereas in SLM Ti-6Al-4V, the initial dislocations resulted from the thermal cycles during the fabrication process reduced the strain accommodation in the high strain rate conditions, leading to bifurcation at lower strain compared to traditional manufactured products. It is also suggested high laser energy densities are not advised for as-built manufacturing products in service under high strain rate conditions.

### **5.3 – The role of deformation twins**

Deformation twinning is a major deformation mode in plastic deformation of many metals with low stacking-fault energy, especially the *fcc* structure metals (187). Unlike annealing twins, deformation twins are created by the mutual shearing of the parallel lattice plane and are accompanied with dislocation related operations. In addition, the deformation twins become significant deformation structures in titanium and its alloys owing to their limited independent slip system to handle unpredictable plastic strains (63). Multiple researchers have indicated the existence of deformation twinning in the plastic deformation of titanium, where twins also serve as the primary mechanism for further deformation by adapting hard orientation into soft one (188-191). While there are no doubts about the presence of deformation twinning in titanium in a variety of strain conditions, there are many gaps in our understanding of the role of deformation twins in the dynamic response of titanium.

The key deformation modes in SLM Ti-6Al-4V with *hcp*  $\alpha'$  martensite microstructure include the prismatic  $\langle a \rangle$  slip, the tensile twins  $\{10-12\}$  and  $\{11-21\}$ , and the compressive twins  $\{11-22\}$  and  $\{10-11\}$ , as schematically shown in Figure 62. The tensile and compressive twins are categorised for their ability to accommodate strain during the *c*-axis deformation. The four twinning modes of have been reported in other studies and summarised in Table 16 in which  $K_1$  is twinning plane,  $\eta_1$  is the twinning shear direction, and the shearing magnitude and the shuffling parameter for each mode, as referred to the study of Yoo (192). Among these, the  $\{10-12\}$  tensile and  $\{11-22\}$  compressive twins are reported as the most active twins induced by deformation at ambient temperature (192, 193). More importantly, it was concluded by Qin, Jonas (194) that the critical strain for the activation of twinning in titanium is responsive to strain rate. Similarly, Chichili, Ramesh (195) and Gurao, Kapoor (196) found that the twinning fraction in titanium can increase under the high strain rate conditions. Both of these studies also had an important finding on the effect of deformation twinning on intensifying specific texture in the sample. Nevertheless, the development and effect of deformation twins on the other microstructure features, such as dynamic recrystallization or texture, require more comprehensive understanding.



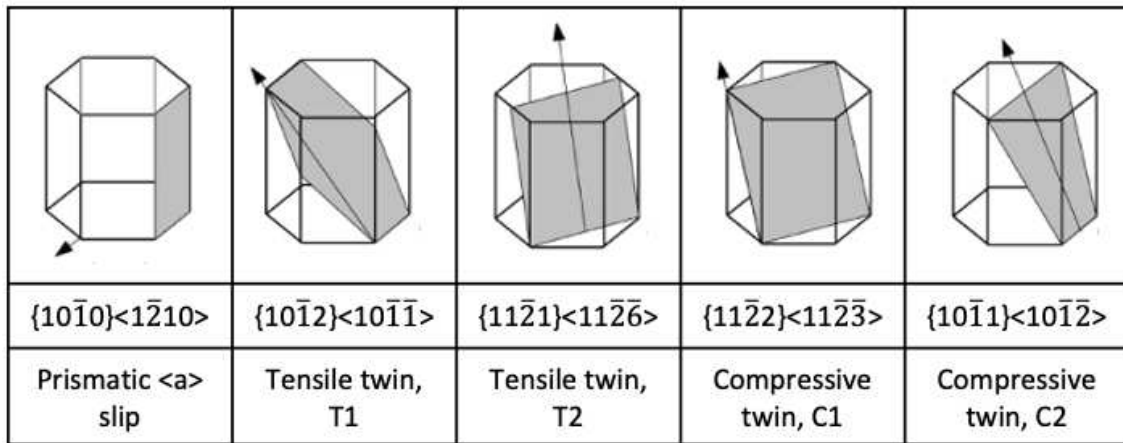


Figure 62. Crystallography of key deformation modes in Ti-6Al-4V

Table 16. Deformation twinning modes in titanium and its alloys

Twin	Type	K1	$\eta_1$	Shearing Magnitude	Shuffling Parameter	Misorientation Relationship
{10-12}	Tensile	(10-12)	[10-1-1]	0.174	4	85.03° [11-20]
{11-21}	Tensile	(11-21)	[11-2-6]	0.63	2	34.96° [10-10]
{11-22}	Compressive	(11-22)	[11-2-3]	0.219	6	64.40° [10-10]
{10-11}	Compressive	(10-11)	[10-1-2]	0.099	8	57.22° [11-20]

The categories and analysis of deformation twinning can be quantitatively defined by the misorientation relationship obtained from EBSD data. The twinning was determined by calculating the misorientation angle of the grain boundary to the rotation axis (189). More precisely, the {10-12} and {10-11} twins are of 85.03° and 57.22° respectively misoriented to the [11-20] axis, whereas the {11-21} and {11-22} twins are of 34.96° and 64.40° misoriented to the [10-10] axis, as shown in Table 16. The twinning fraction was calculated by the area fraction of twinned grains in each twinning mode over the total EBSD scanned areas in the reference and the SLM Ti-6Al-4V samples, which are summarised in Table 17 and Table 18 respectively.

Table 17. Twinning fraction in the reference material at different strains (Unit: %)

Twin	$\varepsilon = 0.17$	$\varepsilon = 0.33$	$\varepsilon = 0.5$
{10-12}	21.92	36.2	34.06
{11-21}	6.58	14.41	20.68
{11-22}	0.24	0.31	11.76
{10-11}	29.06	22.61	31.69
Total	<u>57.8</u>	<u>73.53</u>	<u>98.19</u>

Table 18. Twinning fraction in SLM Ti-6Al-4V samples in different processing conditions (Unit: %)

<b>Twinning</b>	<b>0.5E- P-2V</b>	<b>E- P-V</b>	<b>2E- 2P-V</b>	<b>2E- P-0.5V</b>	<b>4E- 2P-0.5V</b>
{10-12}	4.59	7.76	8.09	12.84	15.32
{11-21}	1.27	0.26	1.68	2.33	3.42
{11-22}	0.52	0.14	0.12	0.1	0.09
{10-11}	8.35	7.64	5.50	1.79	1.52
<i>Total</i>	<u>14.73</u>	<u>15.80</u>	<u>15.39</u>	<u>17.06</u>	<u>20.35</u>

EBSO orientation maps of the reference specimens at different strains are shown in Figure 63. The deformation twins were observed as parallel as well as intersected lenticular structures across the equiaxed grains. Besides, twinning fraction is shown to increase progressively as the deformation degree increases. A total of 73.53% twinning area was captured at 0.33 strain in which the {10-12} and {10-11} twinning modes dominated the total twinning fraction (see Table 17). As the deformation reached 0.50 strain, the twinning was activated throughout the specimens with twinning fraction was almost 100%. In other words, a complete twinning morphology was reached after the materials failure and the ASBs were fully developed.

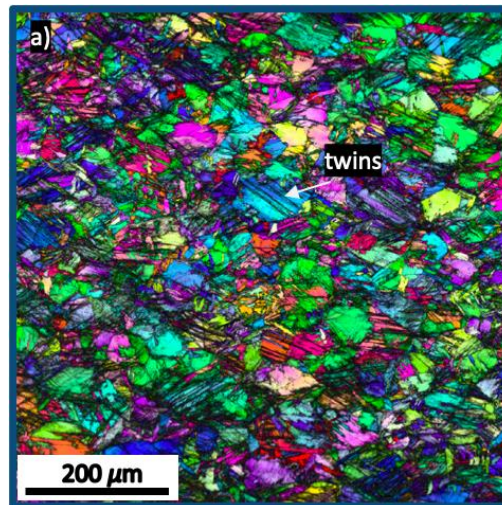


Figure 63. (Continued)

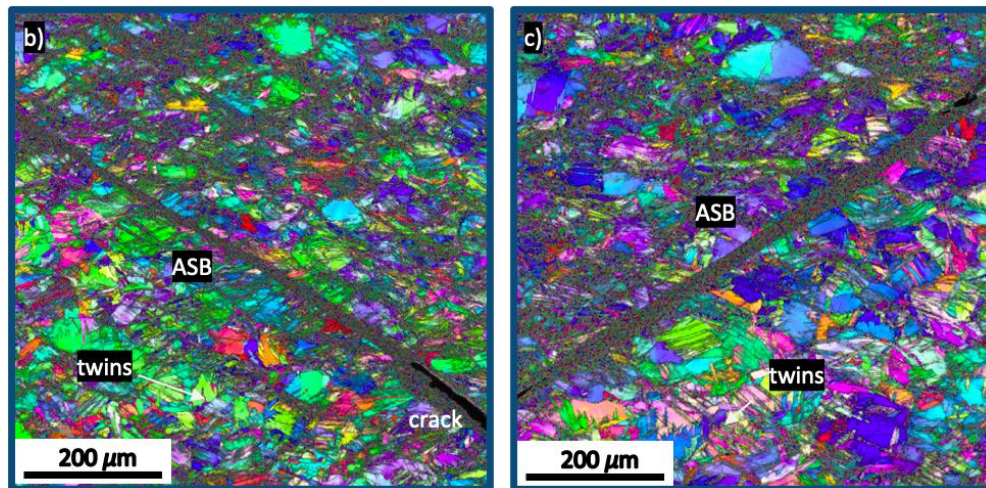


Figure 63. EBSD map of the reference Ti-6Al-4V at a) 0.17 strain, b) 0.33 strain and c) 0.5 strain

It is shown that the  $\{10-12\}$  tensile and the  $\{10-11\}$  compressive twinning appeared to be the most omnipresent modes due to the low twin shearing strain and a simple shuffle mechanism at room temperature (197, 198). By contrast, only at the later stage of deformation did the less favoured  $\{11-21\}$  and  $\{11-22\}$  twinning activate. It is worth pointing out that the activation of the  $\{11-21\}$  twinning led to the formation of fine secondary twins in the interior of  $\{11-21\}$  twins as shown in Figure 64. The secondary twins were determined to be mainly the  $\{10-12\}$  tensile twins, and also the  $\{11-22\}$  compressive twins, developing inside the  $\{11-21\}$  twins due to the low critical shear stress of the parent twins.

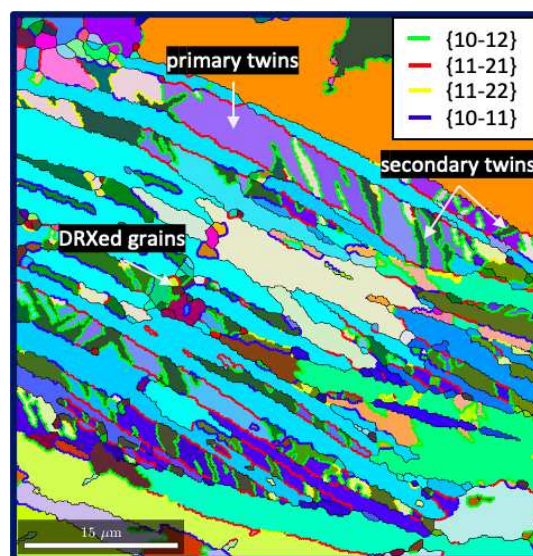


Figure 64. EBSD map showing secondary twins in the reference Ti-6Al-4V specimen

Regarding the SLM components, Figure 65-Figure 69 display the EBSD orientation maps of ASB areas under all laser energy density conditions. The deformation twins in these conditions appeared solely as parallel structures across the  $\alpha'$  martensite grains. As similar to the reference materials, the



quantitative analysis revealed that  $\{10\text{-}12\}$  twins were the most dominant twinning mode in the SLM materials due to the low twin shear and a simple shuffle mechanism, as can be seen in Table 18. No secondary twins were observed in the SLM Ti-6Al-4V due to the low fraction of  $\{11\text{-}21\}$  twins as well as the low critical strain in the SLM built components.

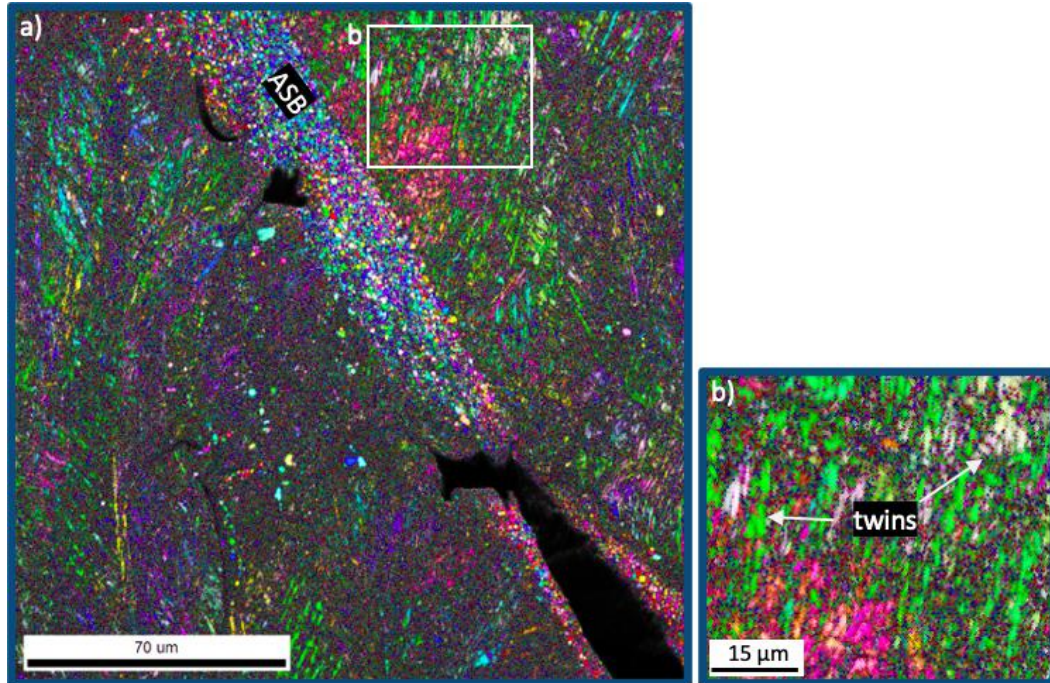


Figure 65. EBSD map showing a) the scanned area and b) deformation twins in 0.5E-P-2V condition

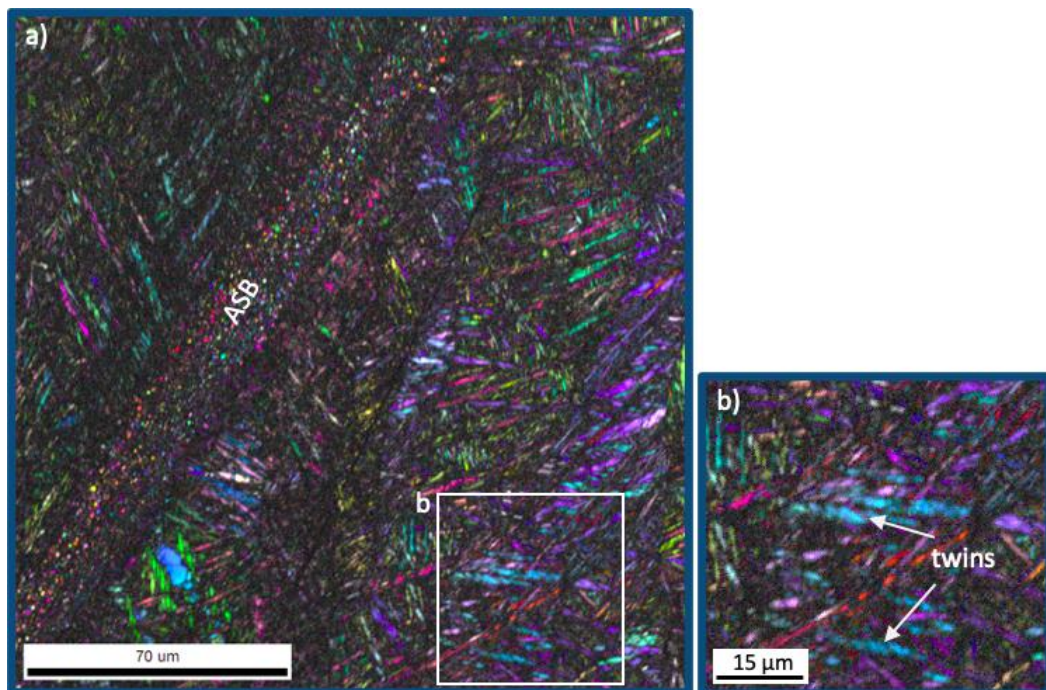


Figure 66. EBSD map showing a) the scanned area and b) deformation twins in E-P-V condition



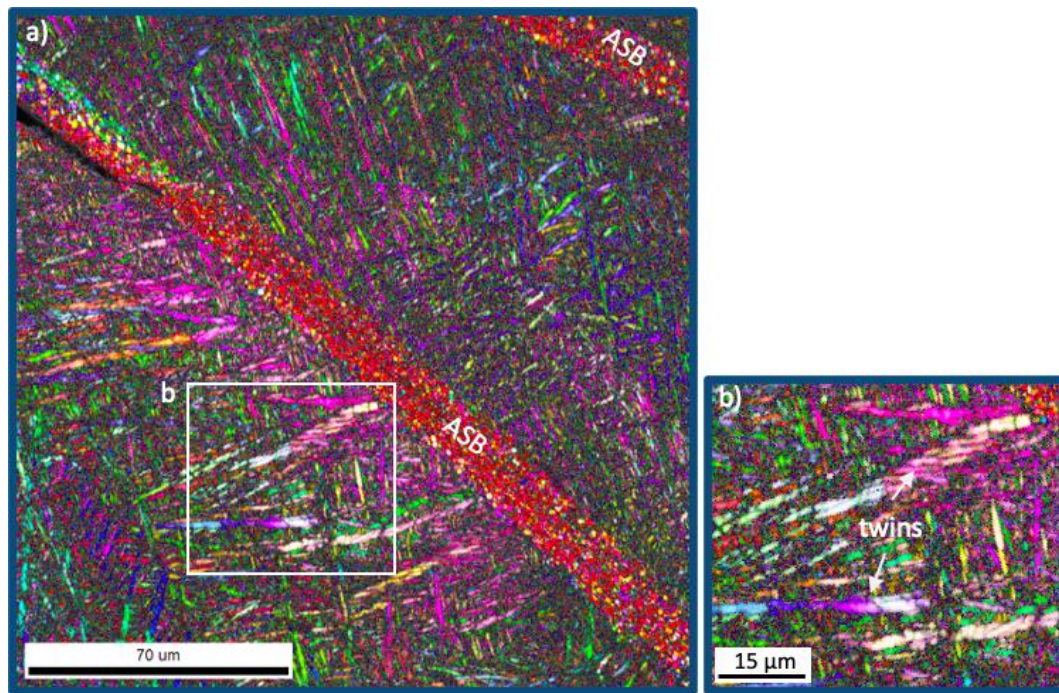


Figure 67. EBSD map showing a) the scanned area and b) deformation twins in 2E-P-0.5V condition

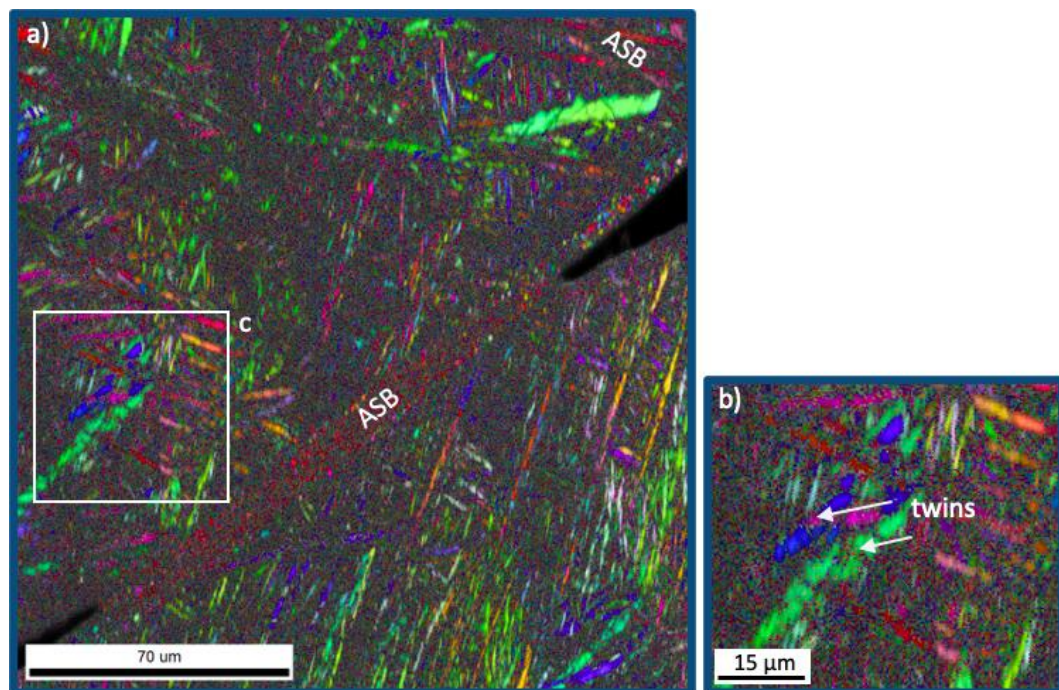


Figure 68. EBSD map showing a) the scanned area and b) deformation twins in 2E-2P-V condition

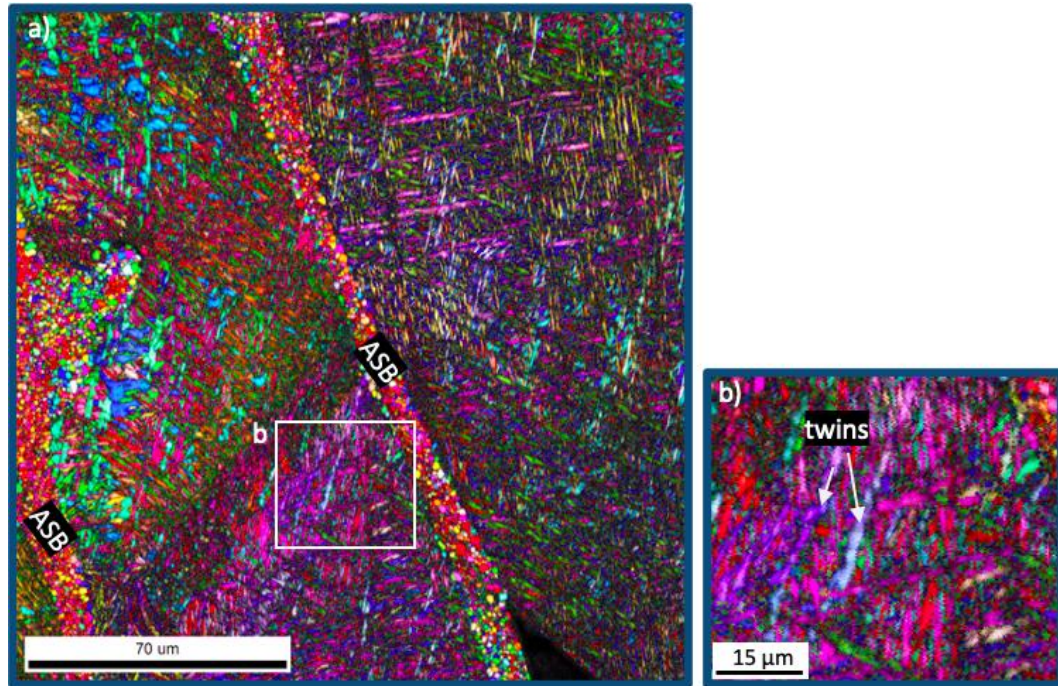


Figure 69. EBSD map showing a) the scanned area and b) deformation twins in 4E-2P-0.5V condition

It is discovered that the  $\{10-12\}$  twins substantially increased their fraction over the increase of applied laser energy density, from 4.59 % at 0.5E condition to 15.32% at 4E condition. This growing trend, however, came at an expense of the  $\{10-11\}$  compressive twins, which fell dramatically from 8.35% at 0.5E condition to 1.52 % at 4E energy density. Still, higher energy density would increase the total twin fraction, with the maximum of 20.35% at the 4E energy density. As it has been discussed in the previous chapter, the high energy density resulted in more plastic-type accommodation strain and thermal dislocations on the boundaries of tertiary  $\alpha'$  martensites, which significantly reduced the dislocation mobility and therefore increased the overall twinning fraction.

The grain orientation is of importance in how deformation strain is accommodated and also in activating twins. The tensile strain was caused perpendicular to the loading direction from a compressive loading point of view; and as such, grains with their c-axis close to perpendicular with the compression direction could accommodate this deformation by introducing  $\{10-12\}$  twins. It has been pointed out in chapter 4 that a major part of the columnar grains had their c-axis aligned along the build direction which was perpendicular with the compression direction. Furthermore, the activation of  $\{10-12\}$  twins flipped the c-axis  $85^\circ$ , to the orientation close to parallel with the compression direction (198). All the  $\{10-12\}$  twinned grains possessed this typical orientation relation, and in fact, it is the main orientation relation in all the high laser energy density specimens. In other words, the  $\{10-12\}$  twinning enabled the tensile strain to be accommodated in the direction of the parent grain's c-axis and the compressive strain perpendicular to it. In a similar light, the  $\{10-11\}$  twins steered the c-axis by  $57.2^\circ$  (198) which resulted in a high intensity at  $\Phi \sim 57^\circ$  in the Orientation Distribution Function



(ODF) of all the tested specimens, as shown in Figure 70. This is also evident in the EBSD orientation maps of ASB regions (see Figure 65-Figure 69) where the grains in the areas close to the ASBs were reoriented by the  $\{10\text{-}11\}$  compressive twins towards the  $(10\text{-}11)$  pole (purple colour).

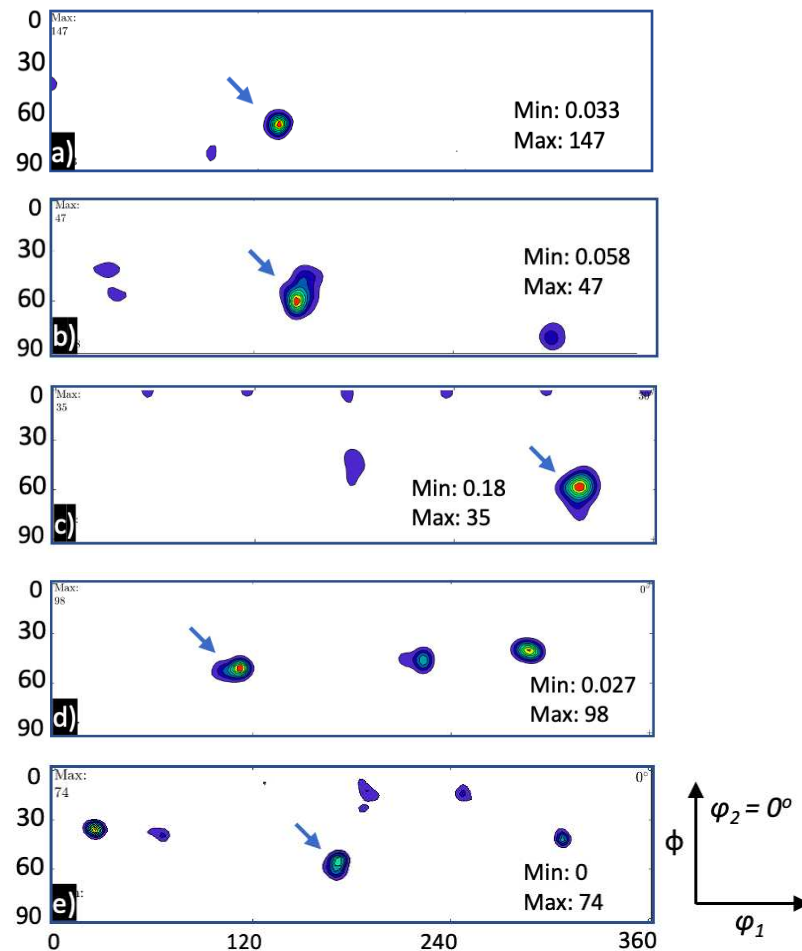


Figure 70. ODF of the SLM Ti-6Al-4V dynamic specimen showing high intensity at  $\phi = 57.2^\circ$  (marked as arrows) in the a) 0.5E-P-2V, b) E-P-V, c) 2E-P-0.5V, d) 2E-2P-V and e) 4E-2P-0.5V condition

In addition, it can be pointed out that the accommodating strain capability of  $\{10\text{-}12\}$  and  $\{10\text{-}11\}$  twinning modes was relatively inefficient since the twinning fraction increased in the high laser energy input samples but the critical strain  $\varepsilon_2$  reduced (see Table 15). Indeed, their major effect was contributing to the hardening behaviour of SLM built specimens via the reorientation effect. Microstructure was reoriented from a soft orientation into a hard one. The  $\{10\text{-}12\}$  twins allowed materials to tolerate compression along the loading direction and tension in a perpendicular direction, while the  $\{10\text{-}11\}$  enabled materials to withstand the maximum shear stress in the diagonal direction.

#### **5.4 – Dynamic recrystallized grains**

Characterizing the microstructure within ASBs provides useful information for comprehending the ASB formation mechanism and development process. Generally, the ASB microstructures in many alloys have been reported to share a lot of features in common, such as fine equiaxed grain morphology with the average grain size of less than 1  $\mu\text{m}$  and high angle grain boundaries (HAGBs), which are the key signs of the dynamic recrystallization (DRX) occurring within the ASBs (98-103, 105, 106). In addition, Yang, Xu (199) discovered that the dynamic recrystallized (DRXed) grains show elongation along the shear direction, and claimed that nucleation and growth process of DRXed grains follow the preferentially direction along the shear. On the other hand, many other studies have reported that the DRXed microstructure in titanium appears as distortionless grains with a random texture, indicating the DRX does not possess any preferred texture (104, 200). Despite many attempts have been made to understand the DRX inside the ASBs in terms of texture as well as mechanisms, the findings are limited and still a matter of debate, let alone those specifically on SLM built materials, particularly SLM Ti-6Al-4V.

This study is confident to be the first to investigate the texture evolution and the mechanism of DRX inside the ASBs of Ti-6Al-4V components built by SLM as subject to a wide range of laser energy input. To completely demonstrate the features of the DRXed microstructure, a high-resolution EBSD with small indexing steps of 0.02  $\mu\text{m}$  was applied to scan and investigate the microstructure in the shear band regions. EBSD orientation maps, pole figures as well as orientation distribution function methods were employed to represent the microstructure and the texture inside the ASBs of the reference and SLM built components.

Firstly, as regards the reference materials, it is observed that the DRX occurred within ASBs with no preferred orientation. Distortionless ultrafine equiaxed grains with a random texture were found in the ASBs at 0.33 and 0.5 strains as shown in Figure 71 and Figure 72, that consisted of a total of 65-75% HAGBs, confirming the occurrence of DRX in the shear band. Besides, the DRXed grains reached their maximum size of 0.4  $\mu\text{m}$  at 0.33 strain which did not grow any further when increasing the strain to 0.5.



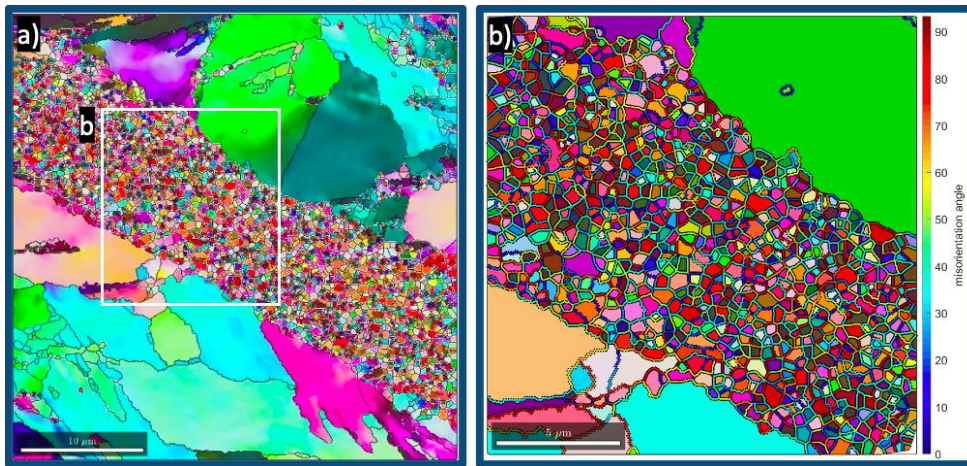


Figure 71. EBSD map of the ASB region and b) high- magnification of DRXed grains with misorientation angle boundary in the reference Ti-6Al-4V at 0.33 strain

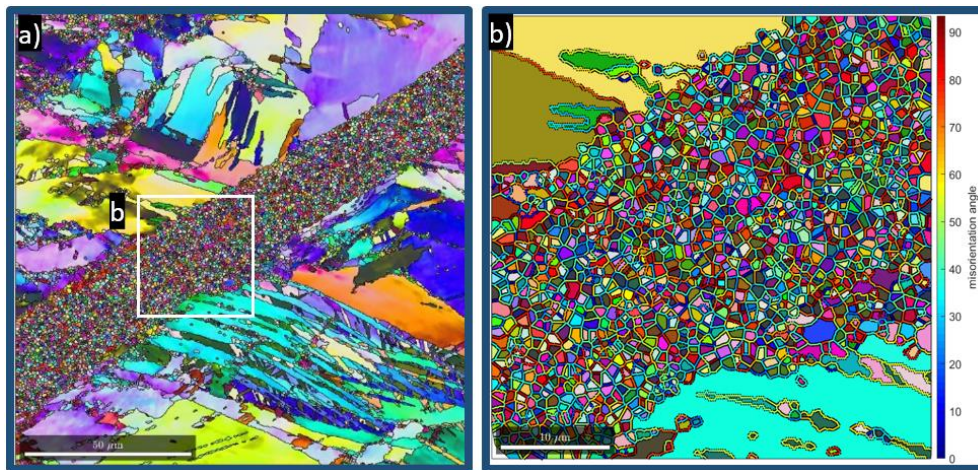


Figure 72. a) EBSD map of the ASB region and b) high- magnification of DRXed grains with misorientation angle boundary in the reference Ti-6Al-4V at 0.5 strain

The ASB microstructures in SLM materials, as shown in Figure 73-Figure 77, underwent substantially grain refinement. Ultrafine equiaxed grains, as the results of the DRX, with the grain size of 60 nm – 500 nm can be easily distinguished. It is important to recognise that the DRX also partially occurred in highly deformed areas outside the ASBs, which appeared as the small number of equiaxed grains amid the parent  $\alpha'$  martensites. These areas, consisting of the mixture of DRXed grains and parent grains, created a transition from non-DRXed areas to fully DRXed areas (the ASBs), and were denoted as the transition zones. However, the only DRXed grains inside ASBs were considered fully developed as the nucleation-and-growth of the new grains completely replaced the parent microstructure.

The SLM specimens observed a more complicated scenario compared to the reference materials that whether DRXed grains evolved in the preferred orientation is subject to laser energy density levels. More precisely, all the specimens from high energy density (2E and 4E) conditions recrystallized in the

favoured [0001] orientation, shown as red colour in the EBSD orientation maps and the intensity in the centre of the (0001) pole in Figure 75-Figure 77. This preferred orientation curtailed and ceased its influence when the applied energy density decreased to the normal and low (E and 0.5E) conditions. The (0001) component in 4E and 2E made up nearly 90% of the DRXed grains texture, while the figures for the standard and low conditions were approximately 16% and 0% respectively.

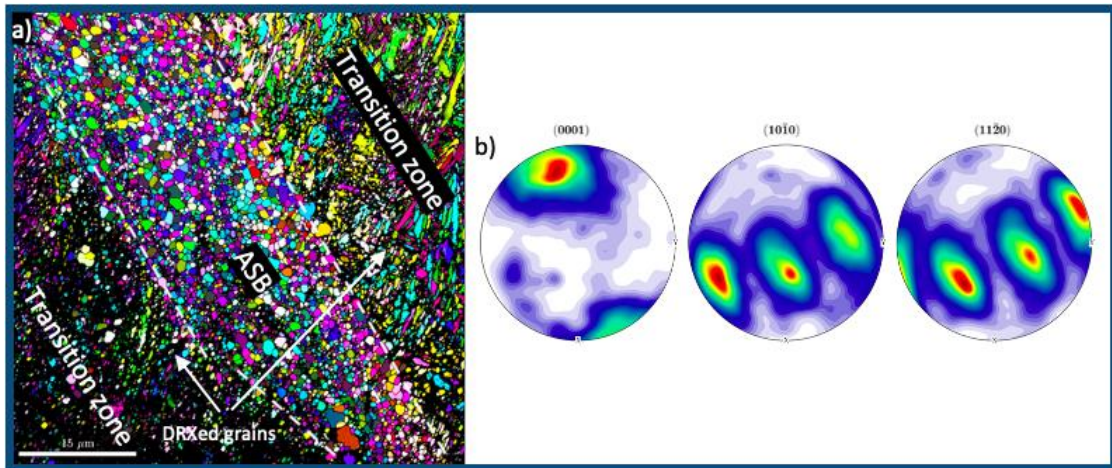


Figure 73. a) EBSD map of the ASB regions and b) Pole figure of the DRXed grains in 0.5E-P-2V condition

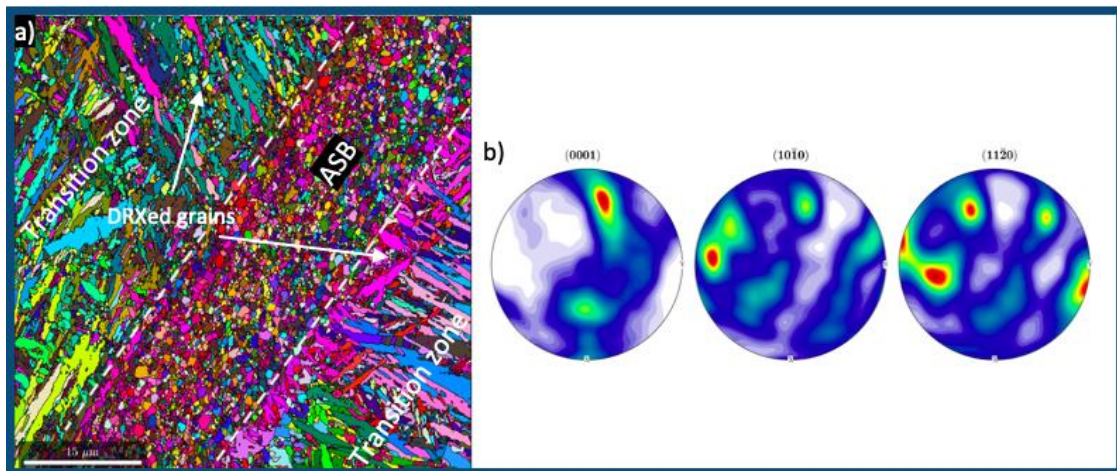


Figure 74. a) EBSD map of the ASB regions and b) Pole figure of the DRXed grains in E-P-V condition



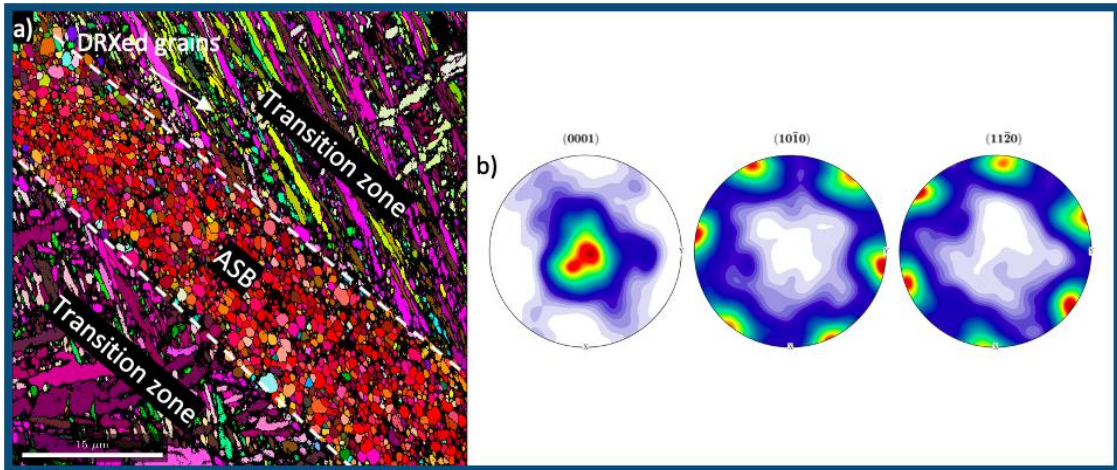


Figure 75. a) EBSD map of the ASB regions and b) Pole figure of the DRXed grains in 2E-P-0.5V condition

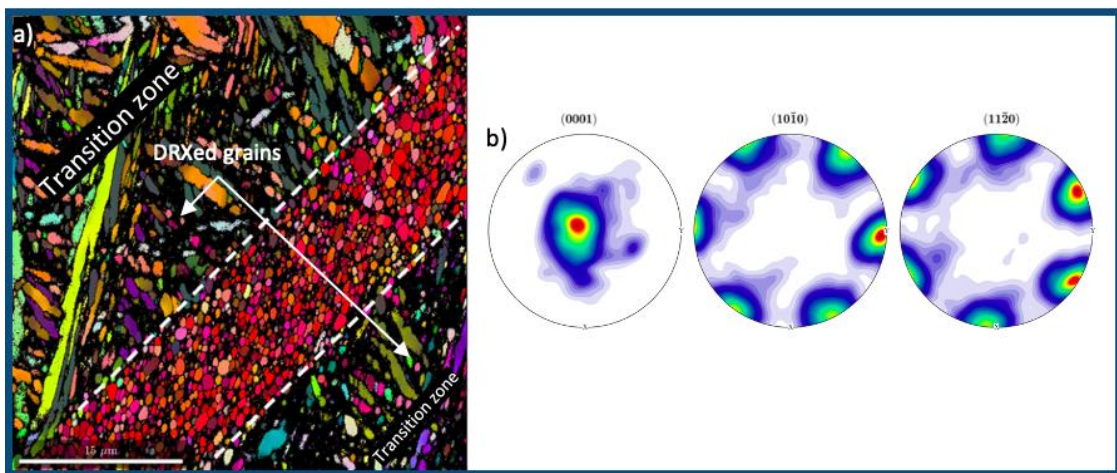


Figure 76. a) EBSD map of the ASB regions and b) Pole figure of the DRXed grains in 2E-2P-V condition

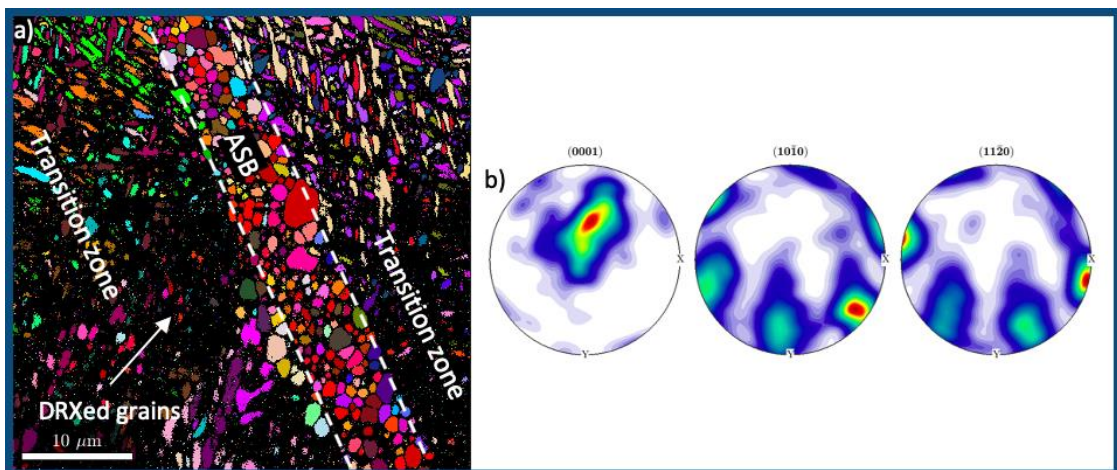


Figure 77. a) EBSD map of the ASB regions and b) Pole figure of the DRXed grains in 4E-2P-0.5V condition

More details on the preferred  $[0001]$  direction could be seen in the ODF of DRXed grains in all the applied energy density conditions in Figure 78. The DRXed grains of the 4E condition possessed a strong  $\{0001\} \langle 10\bar{1}0 \rangle$  texture. Similarly, the ODFs of the 2E conditions show a strong  $\{0001\} \langle 11\bar{2}0 \rangle$ . Both the  $\{0001\} \langle 10\bar{1}0 \rangle$  and  $\{0001\} \langle 11\bar{2}0 \rangle$  are two components of the fibre  $\{0001\}$  texture, appearing as 6 intensities on the  $[0001]$  direction ( $\Phi=0^\circ$ ). A weak component of  $\{0001\} \langle 10\bar{1}0 \rangle$  texture can be found in the ODF of the E condition (see Figure 78b), whilst none of the  $\{0001\}$  texture appeared in the 0.5E.

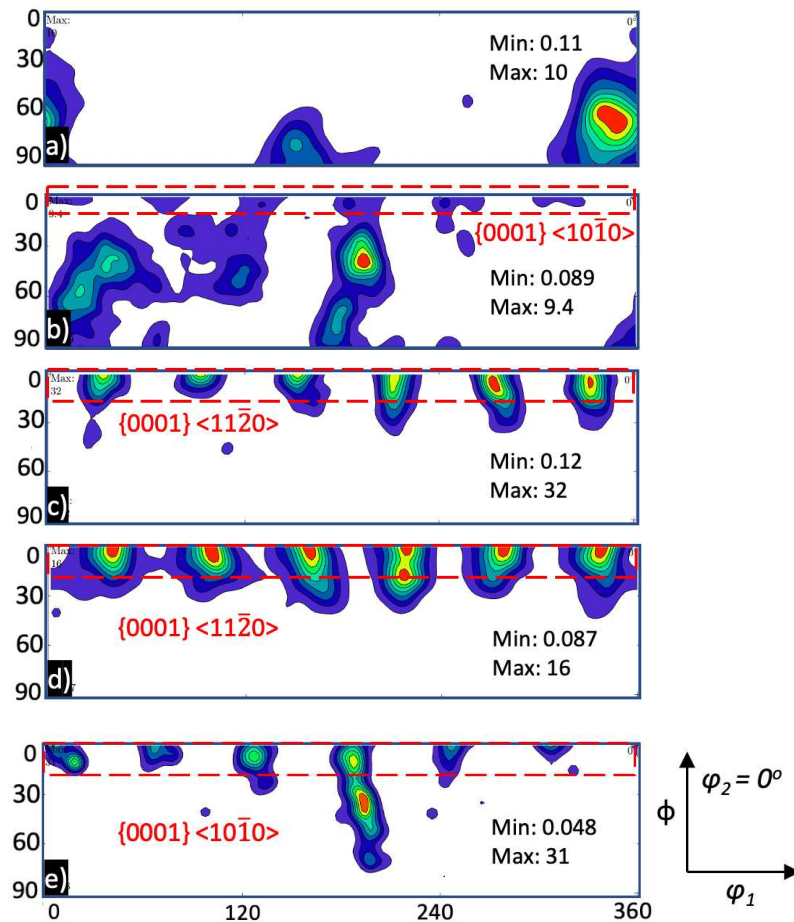


Figure 78. ODF figures of the DRXed grains in the condition a) 0.5E-P-2V, b) E-P-V, c) 2E-P-0.5V, d) 2E-2P-V, and e) 4E-2P-0.5V

DRX is well-established to be achieved under extreme deformation that is regulated by the accumulation of dislocations and the initiation of slips and twins (102, 109, 201). However, given that the DRX in the reference Ti-6Al-4V, under the identical levels of deformation twins, did not undergo preferred orientation development as compared to that in SLM Ti-6Al-4V. Furthermore, the activation of slip would not be of significance for the DRX in this analysis, due to its slight presence as opposed to deformation twins. Therefore, the formation of dislocations was the main influence in the evolution of DRXed grains in SLM Ti-6Al-4V.



Dislocations were resulted from both the fabrication and the deformation. Compared to the reference Ti-6Al-4V, the SLM samples were initially dislocated by thermal cyclic loadings during the production. It is of importance that the accumulation of dislocations from the thermal cycles also induced the strain energy stored in the grains deformed by the thermal dislocations (202). And since the strain energy is actually the driving force for the occurrence and development of DRX (116), it could be reasoned that the initial thermal dislocation promoted the preferred texture of the DRX grains in SLM Ti-6Al-4V.

To analyse and quantify the initial dislocations, this work measured the kernel average misorientation (KAM) in the EBSD scan data of SLM Ti-6Al-4V as-built and dynamic tested samples using MTEX open codes for MATLAB. The KAM reflects the density of geometrically necessary dislocations at a measuring point for a given set of nearest neighbouring points (203), and as such, a high KAM value represents the high-density dislocations piling up in the studied area (204, 205). To quantify the KAM, MTEX denoted the orientations at the position  $(i, j)$  by  $o_{i,j}$ , and then KAM value at the position  $(i, j)$ ,  $kam_{i,j}$ , was determined by the following equation:

$$kam_{i,j} = \frac{1}{|N(i,j)|} \sum_{(k,l) \in N(i,j)} \omega(o_{i,j}, o_{k,l}) \quad (\text{Equation 21})$$

in which  $N(i, j)$  was the domain of all neighbouring data points examined, and  $\omega(o_{i,j}, o_{k,l})$  was the misorientation angle between the orientation  $o_{i,j}$  and the neighbouring orientation  $o_{k,l}$ .

Figure 79-Figure 81 show the KAM-represented thermal dislocations in the as-built specimens as subject to laser energy. It is revealed that the initial dislocations in the as-built conditions occurred in the  $\alpha'$  martensite grains and with a high density piled up along the cooling directions creating [0001] dislocation lines.

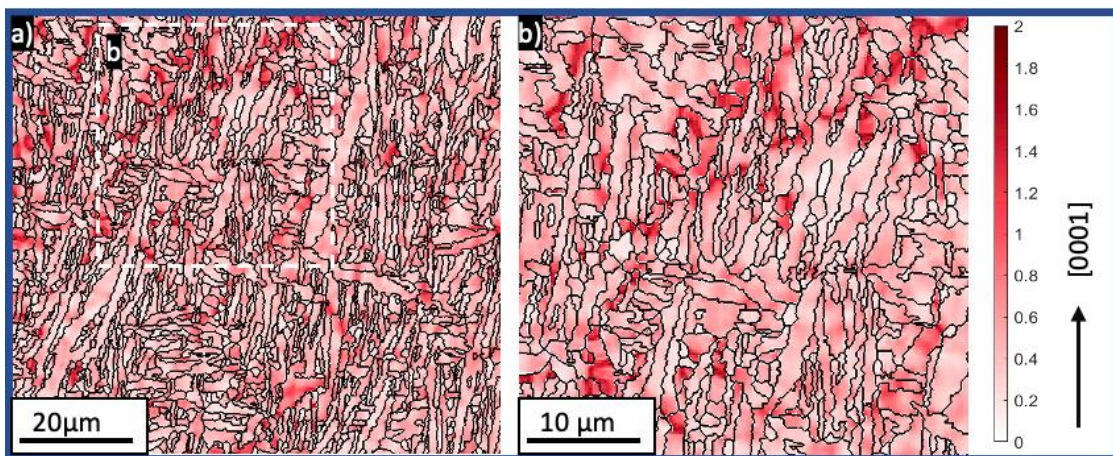


Figure 79. KAM map showing thermal dislocations in the as-built condition of 0.5E-P-2V at a) lower and b) higher magnification

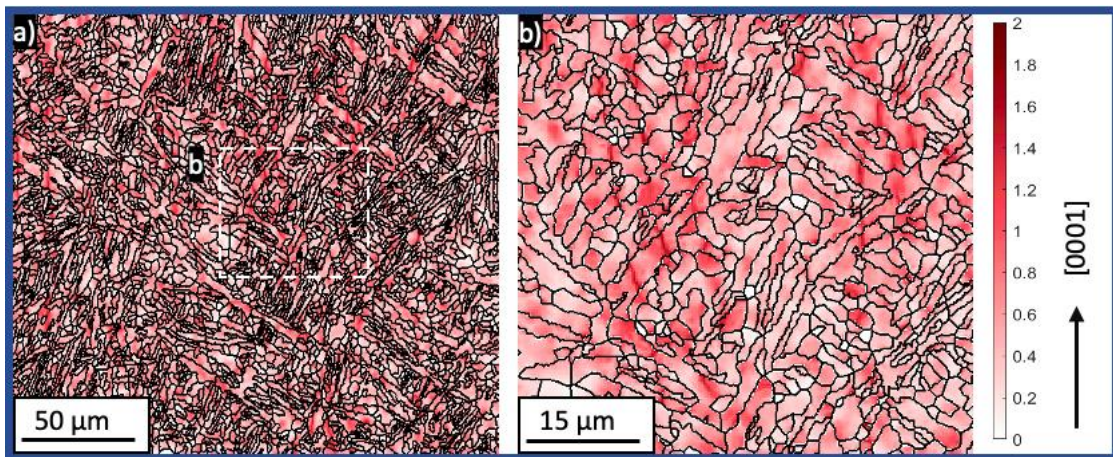


Figure 80. KAM map showing thermal dislocations in the as-built condition of E-P-V at a) lower and b) higher magnification

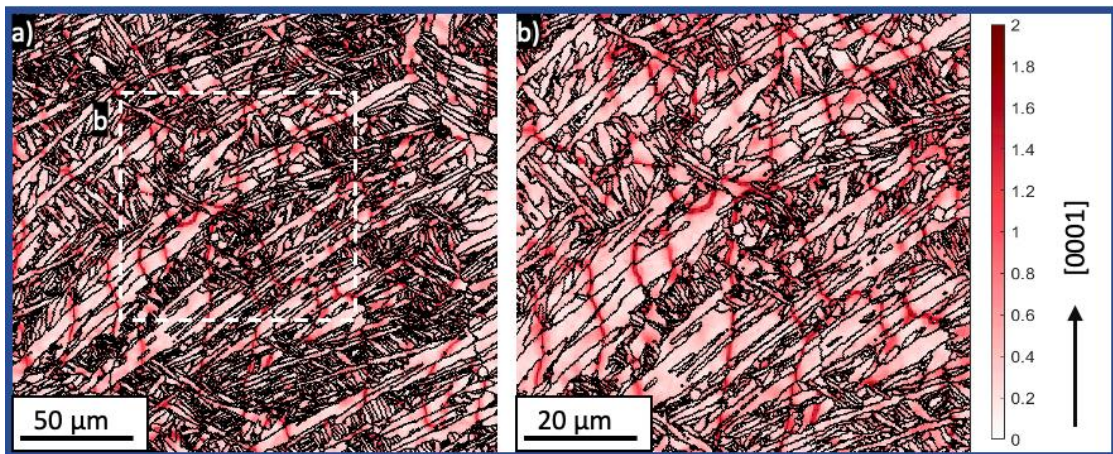


Figure 81. KAM map showing thermal dislocations in the as-built condition of 2E-P-0.5V at a) lower and b) higher magnification

The formation of [0001] dislocation lines was in association with the thermo-plasticity of martensite and the heat history of the SLM process. As stated, the  $\beta \rightarrow \alpha'$  transformation reduced the dislocation mobility and thus resulted in more sessile dislocations. These sessile dislocations piled up at the boundaries of between the  $\alpha'$  and the prior  $\beta$  as well as along the thermal cooling directions inside the martensite grains (206). A high laser energy density causes more effective thermal cycles, and consequently accumulated more piled-up dislocations that were along the [0001] cooling direction, as shown in Figure 81. Primary and secondary martensites were shown to be less dislocated than tertiary grains were due to the auto-tempering process as mentioned in the previous chapter. The KAM method also confirms that, despite the higher auto-tempering levels, the overall intensity of dislocation increases in high laser energy density, as the average KAM value is 0.86 in 2E in comparison with 0.72 in 0.5E, owing to more sessile dislocations piling up.



As regards SLM dynamic tested samples, KAM map clearly distinguishes the ASBs owing to the high-density dislocations accumulated in the transition regions as shown in Figure 82-Figure 86. These dislocations, which were resulted from both the initial built process and from the dynamic test, were found to be highly concentrated at the deformation twins in the  $\alpha'$  martensites. Additionally, at high energy density conditions—4E and 2E—the dislocations piled up at both deformation twins as well as at the substructures in the  $\alpha'$  grains (see Figure 86). The substructures were observed as equiaxed shapes whose size matched with the size of the DRXed grains, indicating that they were in the initial stage of DRX (207). The interaction between dislocations and substructures decreased as the laser energy density reduces to E and 0.5E. Instead, dislocations were accumulated more homogeneously in the transition regions at low energy density condition, shown as dark red colour in the KAM analysis (see Figure 82).

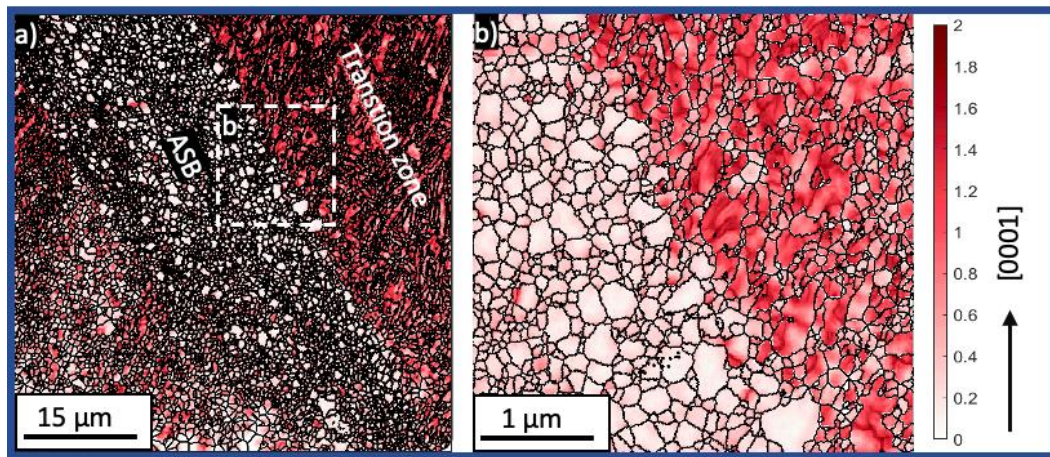


Figure 82. KAM map showing dislocations in a) the ASB region and b) high magnification inside the ASB of the 0.5E-P-2V condition

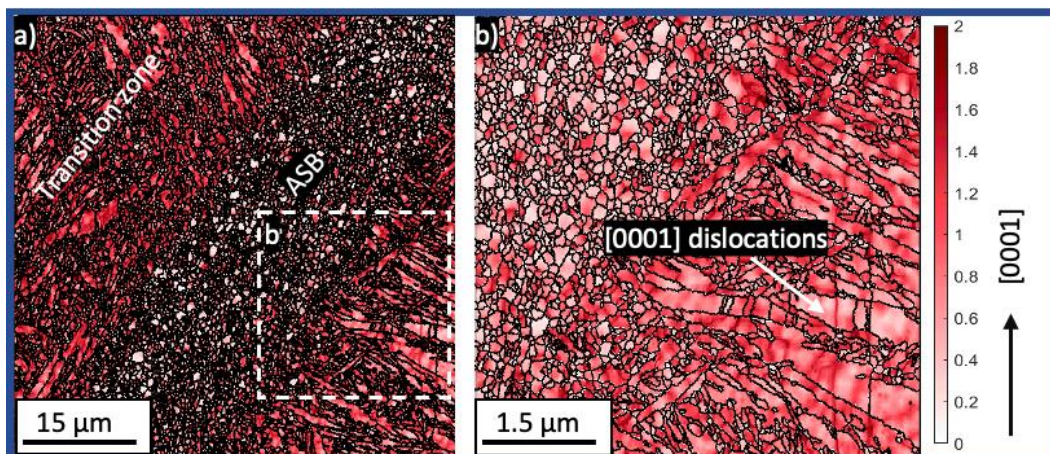


Figure 83. KAM map showing dislocations in a) the ASB region and b) high magnification inside the ASB of the E-P-V condition



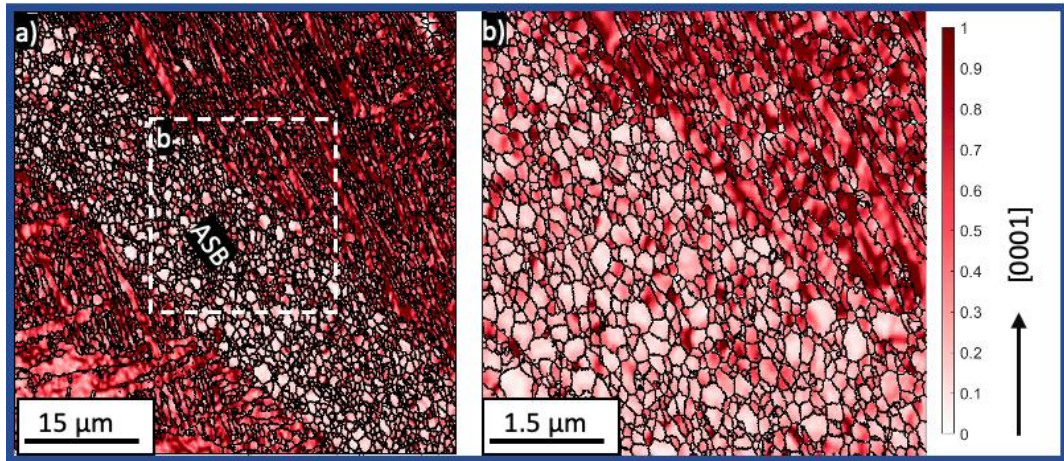


Figure 84. KAM map showing dislocations in a) the ASB region and b) high magnification inside the ASB of the 2E-P-0.5V condition

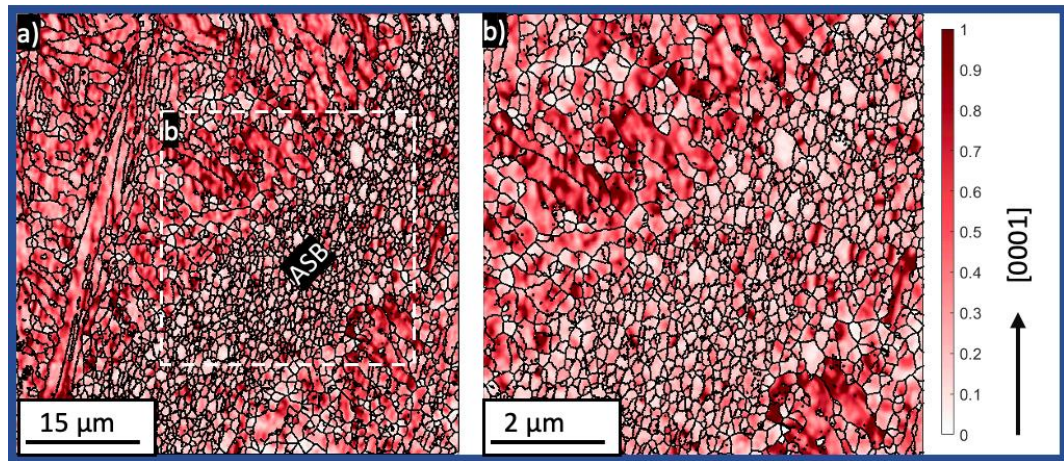


Figure 85. KAM map showing dislocations in a) the ASB region and b) high magnification inside the ASB of the 2E-2P-V condition.

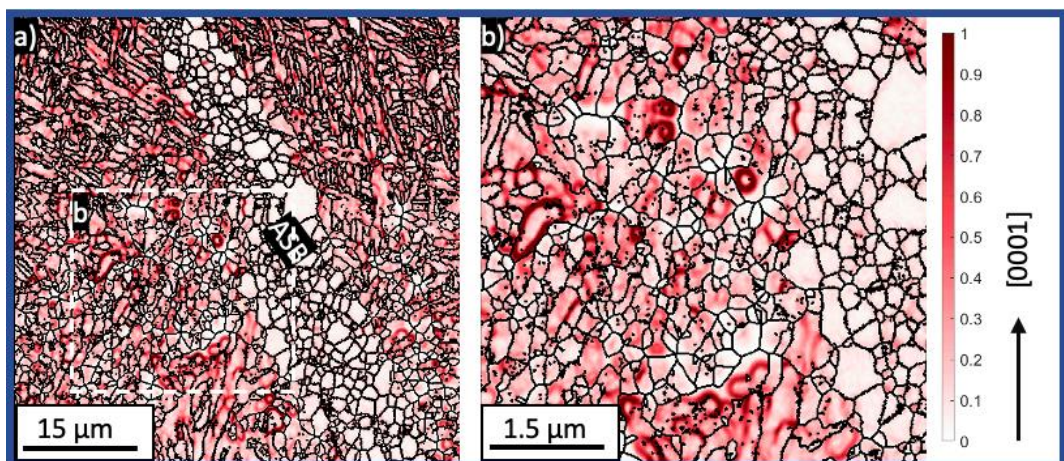


Figure 86. KAM map showing dislocations in a) the ASB region and b) high magnification inside the ASB of the 4E-2P-0.5V condition



The heterogeneity of SLM Ti-6Al-4V in DRX lies in the intensity of [0001] thermal dislocation lines and the accumulation of dislocations in deformation twins. The DRX process has been reported to be predominantly promoted by the interactions of twins and dislocations for providing sufficient strain energy and preferred nucleation sites (208, 209). As such, DRX in high energy density conditions could be activated at low critical strain and evolve in the preferred orientation, as influenced by the [0001] thermal dislocations and the dislocations accumulated in the deformation twins. By contrast, the low density of thermal dislocations in the 0.5E energy density condition halted the dislocation-twin interactions, and hence DRX mechanism was proceeded largely by twin boundaries, resulting in a random texture of DRXed grains.

### **5.5 – Mechanisms of the dynamic recrystallization in SLM built Ti-6Al-4V**

The final microstructure inside the ASBs of SLM Ti-6Al-4V, appearing as ultrafine equiaxed grains with a large fraction of high-angle grain boundaries (HAGBs), is closely related to DRX process. It has been recently studied that the DRX mechanisms are generally classified into continuous DRX (CDRX) (115-117), discontinuous DRX (DDRX) (115, 118, 119), and twinning-induced DRX (TDRX) (120, 121). As summarised, CDRX mechanism increases the misorientation of grain boundaries from low angles into high angles within highly deformed grains before new grains are progressively formed (115). In comparison, DDRX shapes new grains by breaking down the low-angle grain boundaries which separate the new grains from the parent grains (122). Lastly, TDRX uses the activated twins as preferred sites for the nucleation-and-growth the new grains (121).

In this analysis, the DRX was shown to take place partially in the regions next to the ASBs forming the transition zones and eventually leading to the expansion or bifurcation of the existing ASBs during deformation. Thus, when analysing the DRX process in SLM materials, these transition regions can be considered as the *early stage* of the DRX when the DRX first occurs, compared to the *complete stage* as in the ASBs.

#### **5.5.1 – The early stage of DRX**

Deformation twins are essential in the early stage nucleation of DRXed grains. In this research, twins were mainly observed to be in parallel morphology, and the quantitative analysis showed that about 90% of the DRXed grains in the transition regions — the early stage of DRX — were localised in the interior or at the boundaries of these parallel twins. Various twin morphologies, parallel or intersectional, were identified as a nucleation site for the DRX mechanism.(210, 211). Yan, Feng (207) examined the effect of pre-existing twins to the DRX mechanism in titanium and claimed that TDRX occurs on intersectional {10-12} and {11-22} twins, and on parallel {11-21} twins, whereas DDRX occurs

on the boundaries of slipped {11-21} twins and the untwinned grains. In the contrary, only a minor fraction of DRX grains were formed in the untwinned grains, making up about 10%.

The details of DRX mechanisms in the early stage occurring in the martensite in this study were analysed in EBSD data and KAM map (as illustrated in Figure 87) based on the effect of dislocations and twinning boundaries. It was found that DRXed grains associated with deformation twins were fully or partially bounded by twin boundaries, suggesting that the DRX mechanism occurring in the twinned regions did not adjust totally the twinning relationship in the new grains.

More details on the DRX mechanism for different twinning types are discussed as below:

- (1) **The {10-12} twins**: DRXed grains were located at the boundaries and within the {10-12} twins. Worth pointing out was that such DRXed grains remained on their boundaries a fraction of {10-12} twin as indexed by the EBSD technique. This finding was resulted from the TDRX mechanism as suggested in the study of Yan, Feng (207). The correlated KAM map in Figure 87b also suggested an early-stage high dislocation density in the grains. As discussed, {10-12} activation allowed parent grains to accommodate both the perpendicular tensile strain and the compressive strain along the c-axis. Therefore, the strain energy and dislocations in the twins {10-12} (including boundaries and twin interiors) were greater than in other twins, facilitating nucleation of DRXed grains in twinned grains.
- (2) **The {10-11} twins**: Similar to the {10-12} tensile twins, the {10-11} compressive twins were parallel, and the DRXed grains were observed to appear in the interior of the {10-11} twins. The boundaries of these DRX grains remain a fraction of the parent twin boundaries, indicating that the TDRX mechanism took hold in the interior of {10-11} twins.
- (3) **The {11-22} twins**: Different from other densely distributed DRX grains, the DRXed grains nucleating on the {11-22} twin boundaries appeared disjointedly as to the minor fraction of {11-22} twins. Such DRXed grains partly shared their boundaries with the {11-22} twins, and hence the DRX mechanism was defined as TDRX.
- (4) **The {11-21} twins**: The fine DRXed grains nucleated along the bulged parts in the {11-21} twins that appeared partly as HAGBs on the twins (see Figure 87c). The new DRXed grains had no connection with the parent twins (boundaries and orientation), implying the DDRX mechanism as similarly suggested in the study of Azarbarmas, Aghaie-Khafri (212)

On the other hand, the DRX only occurred in a small fraction of untwinned grains via the both CDRX and DDRX mechanisms. Dislocations accumulated in the interior of the untwinned grains, forming the

system of subgrains as shown in the KAM map (see Figure 87b and Figure 87c). These subgrains would progressively turned into HAGBs over increasing strain to finally transform into DRXed grains at the later stage, which is classified as the CDRX mechanism as also reported in the analysis of Jiang, Xu (213). In comparison, DRX nuclei developed at bulged grain boundaries, as revealed in the EBSD and KAM, leading to the heterogeneous distribution of new DRXed grains owing to the DDRX mechanism (212).

In the early stage, the DRXed grains in all processing conditions shared the same pattern of misorientation angle distribution (see Figure 88). The highest peak at 85° - 90° misorientation angle represents a total of 28 - 35% of the boundaries, followed by other peaks of around 10% at 30° and 65° misorientation angles. Finally, a small portion of low-angle grain boundaries (LAGBs) accounts for 5% total boundaries. The largest proportion of boundaries with 85-90° misorientation is associated with the TDRX on the {10-12} twins, which highlights the critical role of the {10-12} tensile twins as nucleation sites for the TDRX. Besides, the small fraction of (LAGBs) in the misorientation diagrams indicates that the small amount of DRXed grains by the CDRX mechanism in the untwinned grains as compared to those in the twinned grain

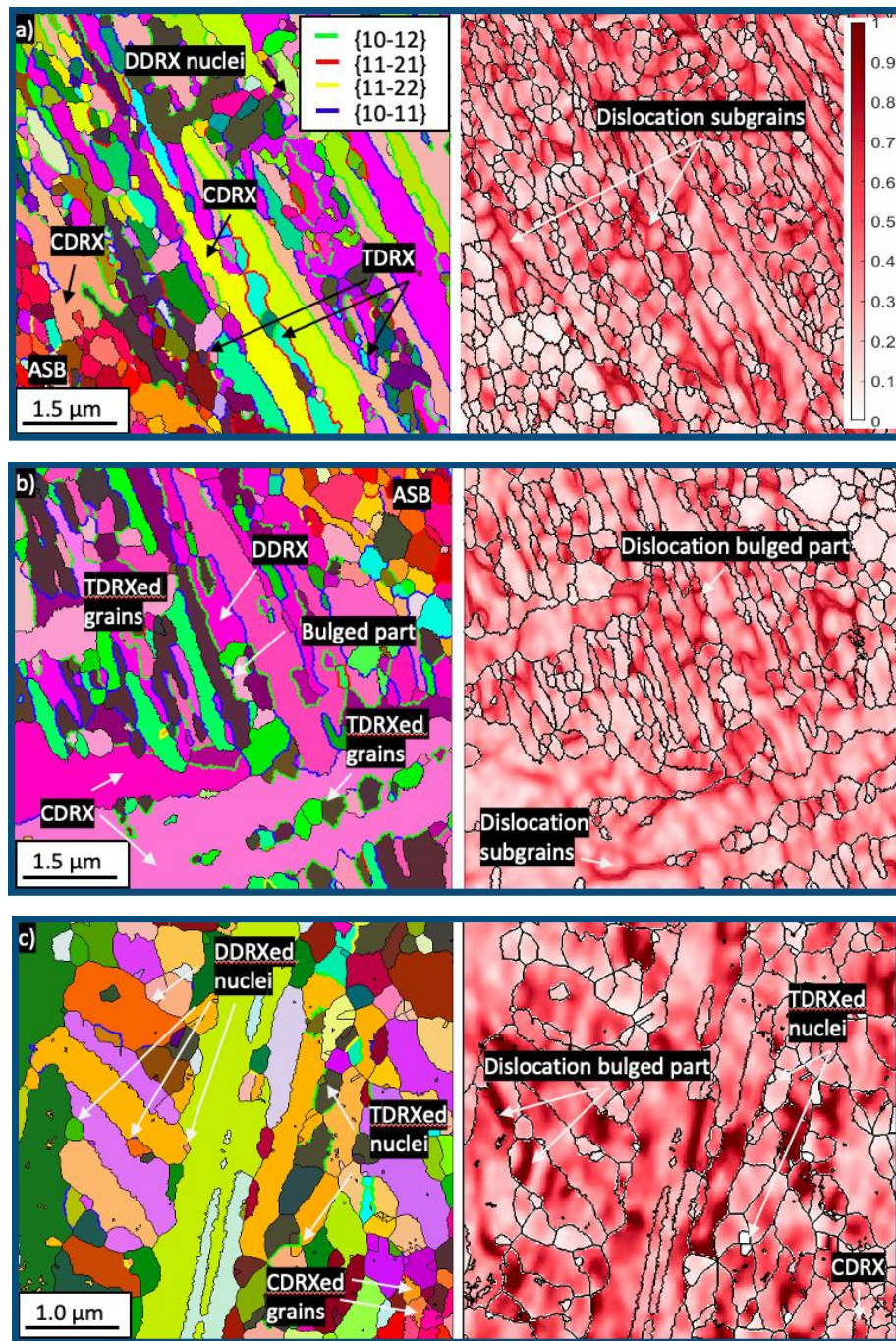


Figure 87. EBSD and KAM maps showing the DRXed grains at the early stage (in the transition zones) at a) 0.5E-P-2V, b) 2E-P-0.5V and c) 2E-2P-V condition

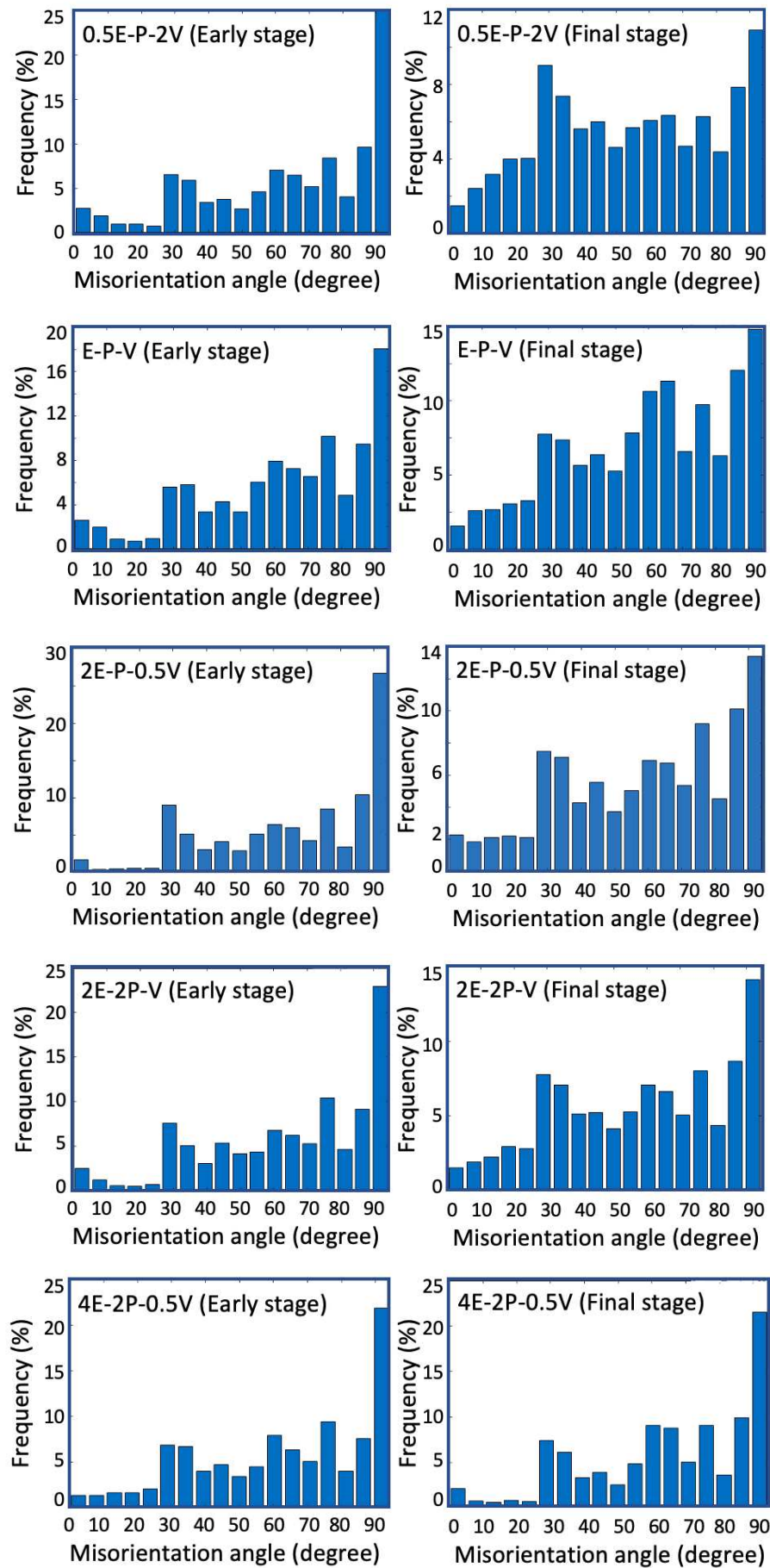


Figure 88. Misorientation angle distribution the DRXed grains in different conditions



### **5.5.2 – The final stage of DRX**

The final forms of DRXed grains appeared as fully equiaxed grains in the ASBs. As it has been mentioned that only a proportion of the  $\alpha'$  martensite grains were initially DRXed in the early stage. Thus, the non-DRXed material, in both twinned and untwinned grains, was actively DRXed in the final stage. As it has been pointed out the DRX did not completely change the twinning relationship, and the DRXed grains partly possessed the boundaries from the parent twins. Therefore, it is possible to use the boundary misorientation angle distribution diagrams as shown in Figure 88 to analyse the mechanisms that occurred in the DRX.

Firstly, the increase of LAGBs, which indicates a progressive rotation of substructures in untwinned grains to form new DRXed grains, is the significant sign of CDRX mechanism occurring in the final stage. The increase of LAGBs, or other words the CDRX process, was observed in the untwinned grains owing to the interaction between plastic deformation strain with the prismatic  $\langle a \rangle$  slip dislocations that were activated more readily in the untwinned grains to promote the cross-slip dislocations (214). KAM map confirms that such dislocation operation sites in the high energy density conditions were related with high misorientation, giving rise to the progressive rotation of subgrains from the initial orientation, and therefore aided the progression of CDRX (213).

Furthermore, lowering the energy density is likely to promote the transition from CDRX to DDRX mechanism in the untwinned grains as noticeable by the gradual reduce in the HAGBs' frequency in Figure 88. The DDRX mechanism was claimed in the study of Fatemi, Moradipour (215) to be significantly suppressed by the solute drag effect that is caused by the element segregation at grain boundaries. Low energy density applied in the SLM process resulted in less plastic accommodation strain between the  $\alpha'$  martensites and the prior  $\beta$  matrix, which increased the mobility of dislocations and grain boundaries to become high enough to overcome of any solute drag effect, thus promoting the DDRX mechanism.

The TDRX rate associated with  $\{10-12\}$  twins reduced as the DRX further progressed to the final stage. This phenomenon can be recognised by the drop in the frequency of  $90^\circ$  boundaries as compared to that the early stage, which implied the proportion of new  $\{10-12\}$  twinning boundaries greatly reduced in the final stage. Besides, this kind of drop is more apparent in lower energy density conditions, which means that the TDRX in the  $\{10-12\}$  twins was less favourable in the low the laser energy density condition.

As reported, the  $[0001]$  preferred texture in DRXed grains was significant in high energy density conditions (4E and 2E) and weakened in the standard condition (E) until it totally disappeared in the

low energy input condition (0.5E). It is noteworthy that the final recrystallized texture depends either on the oriented nucleation of new grains or the subsequent oriented growth of grains with specific orientations, or the combination of both (216). Since a large part of DRXed grains were nucleated by the TDRX, whose nucleus was investigated to have the same orientation with the matrix, the subsequent oriented growth played a more critical role in their final favourable texture. The growth of the DRXed grains is a process of migration of boundaries to the outside of the grains (217), and this study suggests that the final DRXed grains tend to possess the preferred selection of [0001] basal orientation due to movement of DRXed grain boundaries along the [0001] thermal dislocations from the SLM process.

Finally, the type of accommodation strain in the parent materials highly influenced the DRX's progression. The plastic accommodation strain between the boundaries of martensites and the prior  $\beta$  matrix, which largely appeared under high energy density conditions, decreased the interfacial mobility due to extreme locked-down dislocations at grain boundaries, which was likely to encourage the CDRX and alter the subsequent grain growth behaviour following the [0001] direction of the thermal dislocations. On the other hand, low energy densities resulted in more elastic accommodation strain, which homogenised dislocation mobility within grains, hence reducing the preferred selection of the [0001] texture and providing a more equal opportunity for other orientations to thrive.

### **5.6 – Chapter summary**

The dynamic stress-strain response can be divided into three regions: elastic deformation, plastic deformation and material failure. During plastic deformation, the strength loss from the thermal softening effect is offset by the grain hardening effect until the loss of strength outweighs the hardening effect, when shaping the ASBs, leading to material failure. The ASBs initiate on the maximum shear paths that also facilitate the coalescence of voids and cracks. The microstructure inside the ASBs consists of as fine equiaxed grains with the size of 60 – 500 nm, resulting from the DRX in the local shear paths. The DRXed grains inside the ASBs have a preferred texture of [0001] direction, which is significant under high energy densities and weakened under lower energy input conditions until it completely disappears under 0.5E laser energy input.

Using interrupting tests on reference materials, it is found that over the course of deformation, DRX further occurs in the highly deformed areas outside the ASBs, making the transition zones between non-DRXed areas and fully DRXed areas (the ASBs), until the DRXed grains totally replace the parent martensites, leading to the expansion/bifurcation of the ASBs. These transition zones in SLM built materials are thus treated as the early stage of the DRX whereas the ASBs as the final stage for investigation of the DRX mechanism.

Twinning is the major deformation mode in Ti-6Al-4V in which the {10-12} and {10-11} twinning modes are the two most dominant and important in dynamic deformation of SLM Ti-6Al-4V due to their low twin shear and simple shuffle mechanism. The {10-12} twins enable the tensile strain to be accommodated in the direction of the parent grain's c-axis and the compressive grain perpendicular to it. The {10-11} twins steer the c-axis by  $57.2^\circ$  to accommodate the shear strain. In the early stage, 90% of the DRXed grains are achieved in association with deformation twins in which TDRX occurs in the {10-12}, {10-11} and {11-22} twins, and DDRX takes place in {11-21} twins. However, the TDRX associated with {10-12} twins reduced, appearing in the drop of  $90^\circ$  boundaries in the misorientation distribution diagram, as the DRX further progressed to the final stage, which is more apparent the low the laser energy density condition.

DRX is achieved via CDRX and DDRX in the untwinned martensites. There exists a transition from CDRX to DDRX when reducing the laser energy densities. The cross-slip dislocations whose operation sites in the untwinned grains under high energy density conditions were related with high misorientation, giving rise to the progressive rotation of subgrains, and therefore aided the CDRX. By contrast, low energy density increased the mobility of dislocations and grain boundaries to overcome of any solute drag effect, consequently promoting the DDRX mechanism.

The growth of the DRXed grains is a process of migrating boundaries outside of the grains and the final DRXed grains tend to possess the preferred texture of [0001] orientation under high energy densities due to movement of DRXed grain boundaries along the [0001] thermal dislocations from the SLM fabrication process. By contrast, low energy densities, resulting in increased dislocation mobility, provide a more opportunity for other orientations to thrive.



## Chapter 6 – Heat treatment of SLM Ti-6Al-4V

SLM Ti-6Al-4V parts in the as-built condition may find it hard to compete with the conventionally built counterparts in terms of mechanical performance. Since mechanical properties are strongly influenced by the microstructure, the appearance of  $\alpha'$  martensite and columnar  $\beta$  morphology greatly reduces the ductility and the critical strain under quasi-static and dynamic conditions. Therefore, an appropriate post-process heat treatment is critical for improving ductility as well as achieving the desirable properties. In this chapter, it is found that heat treatments have promising results and should be a mandatory part of the AM process to achieve desirable properties of SLM Ti-6Al-4V. Furthermore, the evolution of microstructures during heat treatment is analysed in detail using experimental and numerical methods to elaborate the influence of anneal temperature and holding time on the decomposition and the globularization of  $\alpha'$  martensites, which contribute to controlling the microstructure and mechanical properties of SLM Ti-6Al-4V.

## **6.1 – Heat treatment design**

The microstructure of the as-constructed SLM Ti-6Al-4V, as presented in Chapter 4, consists of columnar prior  $\beta$  grains and fine acicular  $\alpha'$  martensites owing to the extremely high cooling rate of  $10^4$ – $10^6$  K s<sup>-1</sup>. Such microstructure is harmful to the ductility and thus also to the critical strain of (under dynamic conditions) as compared to that in conventionally developed Ti-6Al-4V. It is well established that the grain morphology, the grain size, and the  $\alpha/\beta$  phase structure significantly affect the plastic deformation, the mechanical strength and the ductility of Ti-6Al-4V (7, 62, 63). Moreover, Ti-6Al-4V developed by traditional methods such as casting or wrought is often subsequently treated thermo-mechanically to possess either a complete lamellar or a fully equiaxed morphology, or a bimodal morphology of both (218). In aerospace and many other industries, the bimodal morphology of equiaxed and lamellar grains is favoured for its balance of high strength (from fine lamellas) and high ductility (from equiaxed grains).

In a bimodal morphology, the equiaxed grains (primary  $\alpha$ ) are formed by the grain fragmentation and globularization aided by the thermo-mechanical process, whereas the lamellar grains (secondary  $\alpha$ ) are initiated by a rapid cooling, usually by water or air quenching, to form the  $\alpha'$  martensite followed by another anneal to decompose the  $\alpha'$  into the  $\alpha+\beta$  lamellas (15, 79, 219). Nevertheless, it leaves a challenging issue to the SLM Ti-6Al-4V, since the main use of AM is the fabrication of near-net-shape products that could not be thermo-mechanically processed to maintain the complex geometry. Other heat treatment designs involving water quenching are also unsuitable due to component oxidation. Viable heat treatment must be planned to take advantage of the grain globularization during annealing so that the equiaxed grains can thrive. Yet the emergence of equiaxed grains must be well controlled to avoid coarse lamellar morphology, which results in a penalty on the strength of the material. The optimised annealing strategy, therefore, must transform the initial martensitic microstructure into the desirable bimodal morphology that balances the advantage of fine lamellar and equiaxed microstructure.

The globularization process has been studied and well accepted to comprise two main mechanisms: the boundary spitting and the termination migration (220-223). At early stage, the boundary splitting occurs at the intraphase boundaries and develops across the thickness of the lamellae. The intraphase boundaries may appear as the recovered substructures which cause instability at the triple junctions between intraphase and interphase boundaries (224). The diffusion flux from the intraphase boundaries into the interphase counterparts, which is driven to reduce the surface tension at the instable junctions, results in the fragmentation the lamellar grain. At later stage, the termination migration mechanism transfers the mass from the outer curved edges to the flat surface of the

lamellae, gradually causing the grain coarsening and the globularization (222, 225). The globularization process strongly depends on the free energy and diffusion of solute contents at the interface boundaries (226). The free energy is usually enhanced during the thermo-mechanical process, whereas the diffusion of solute contents is controlled by the annealing temperature and time.

The annealing temperature was thus chosen within the solid solution treatment range to facilitate globularization. The solid solution treatment temperatures start from the dissolution point, above which the  $\alpha'$  decomposes into the dual  $\alpha+\beta$  phases and the  $\beta$  phase increases its volume significantly by dissolving a part the  $\alpha$  phase into it, that has been determined as 705°C for Ti-Al systems (227), to the transus temperature  $T_{\beta}$ . By contrast, the  $\beta$  annealing was passed since the microstructure recrystallization in this procedure, which contributes to colony lamellar morphology, would result in undesirable mechanical properties. Besides, the annealing of Ti-6Al-4V must be conducted in a vacuum atmosphere to prevent part oxidation, and thus followed by a furnace cooling. The designed heat treatment strategies for SLM Ti-6Al-4V are shown in Figure 89, underlining the effect of annealing temperature and holding time. Moreover, since this chapter aims at the heat treatments for near-net-shape products, the SLM Ti-6Al-4V dog-bone specimens were fabricated directly on the print platform for investigation. All the specimens employed in this chapter were produced from the same batch using the standard processing conditions (E-P-V) as discussed in Chapter 4.

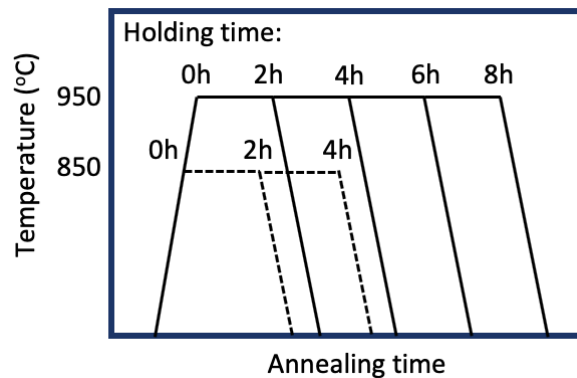


Figure 89. Diagram showing the heat treatment strategies

## **6.2 – Microstructure evolution**

The heat treatment in the solid solution temperatures observes the transformation of  $\alpha'$  into the lamellar  $\alpha+\beta$  phase. Since annealing in the  $\alpha+\beta$  temperature did not alter the prior  $\beta$  grains, the columnar structures appeared intact, and in fact, the prior  $\beta$  grains are more distinguishable after the heat treatment due to the formation of Grain Boundary  $\alpha$  ( $\alpha_{GB}$ ) as shown in Figure 90. Besides, the newly transformed  $\beta$  appeared as a thin layer on the boundaries of  $\alpha$  platelets. The equilibrium volume fraction of  $\beta$  phase is higher for higher annealing temperature, evaluated as 12% in 850 °C – 2h

compared to 21% in 950 °C – 2h. In a different aspect, the  $\alpha$  phase was transformed as lamellar grains as shown in the EBSD maps in Figure 92 and Figure 93. The hierarchical structure from the initial  $\alpha'$  phase —the primary, secondary and tertiary  $\alpha'$ — persisted but transformed into the so-called Class-I, Class-II and Class-III  $\alpha$  (see Figure 93). Furthermore, it is observable that the  $\alpha$  grains are notably coarser under higher annealing temperature. The median grain width ranges from 1 – 2  $\mu\text{m}$  at 850 °C – 2h to 3.5 – 4  $\mu\text{m}$  at 950 °C – 2h. More details on the grain area and the volume fraction of  $\alpha$  phase in each heat treatment condition can be found in Figure 94 and Table 19.

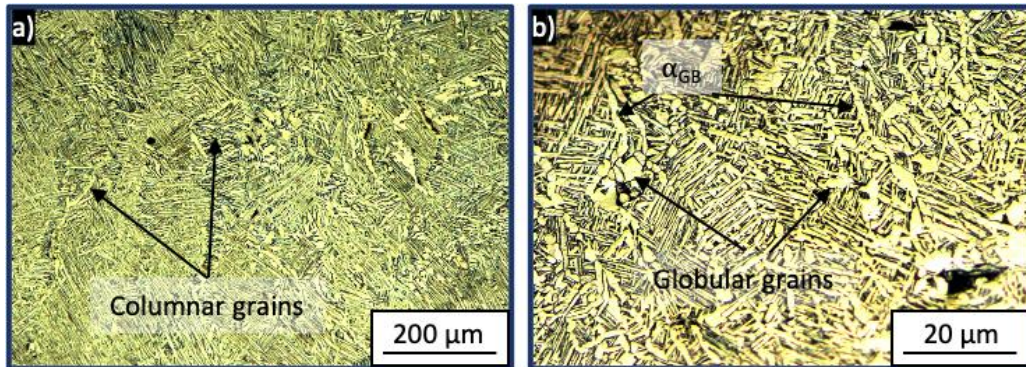


Figure 90. OM images of the microstructure after heat treated at a) 850 °C – 4h showing columnar grains and b) 950 °C – 4h showing  $\alpha_{GB}$  and globular grains

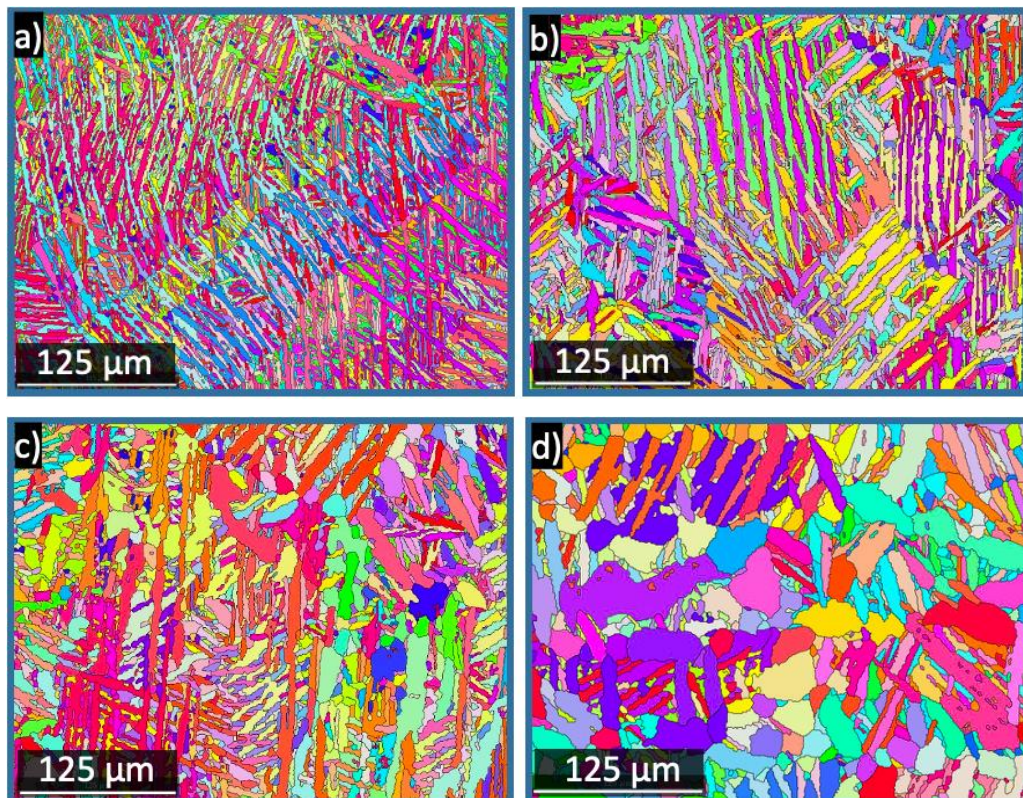


Figure 91. EBSD maps showing the microstructure in the annealing conditions of a) 850 °C – 2h, b) 950 °C – 2h, c) 950 °C – 4h and d) 950 °C – 8h



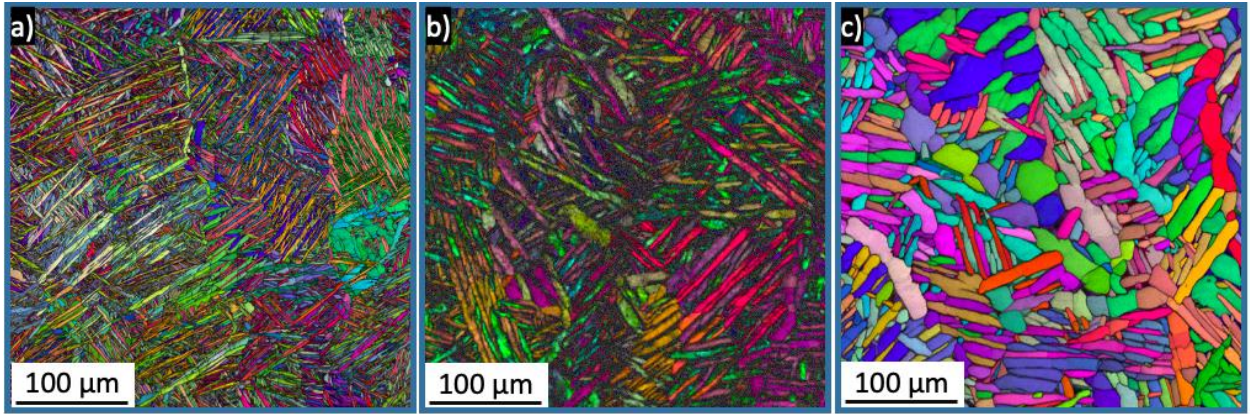


Figure 92. EBSD maps showing the microstructure in the annealing conditions of a) 850 °C – 4h, b) 950 °C – 2h and c) 950 °C – 6h

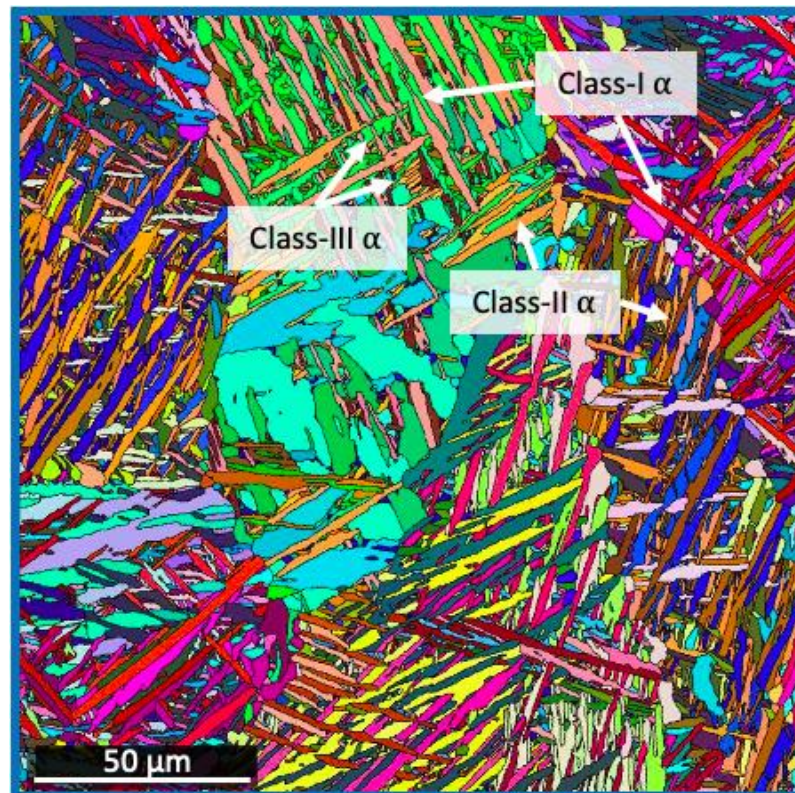
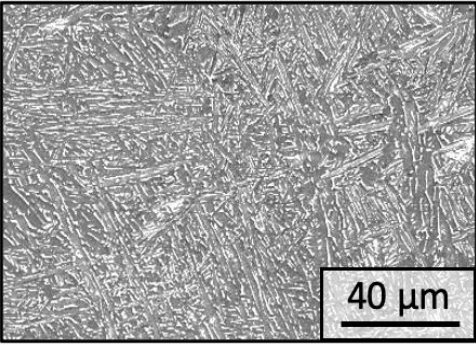
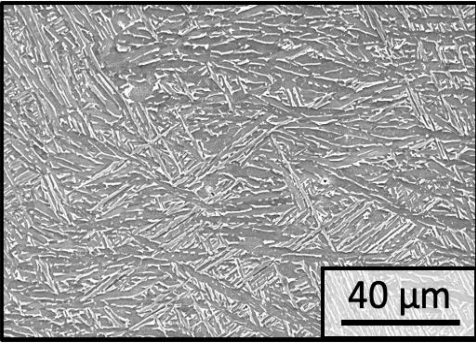
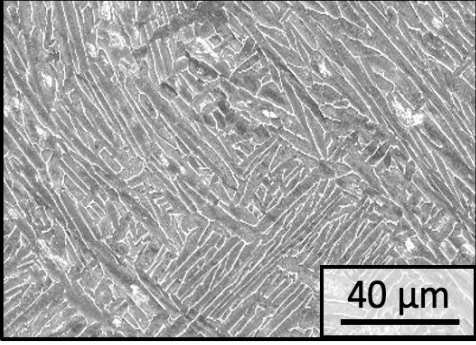
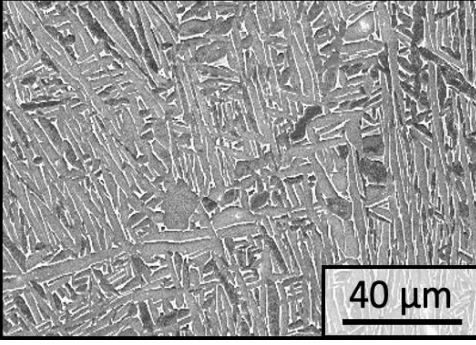
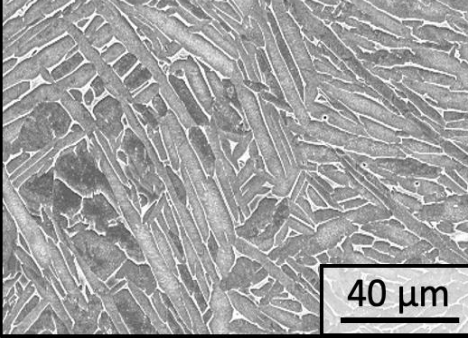
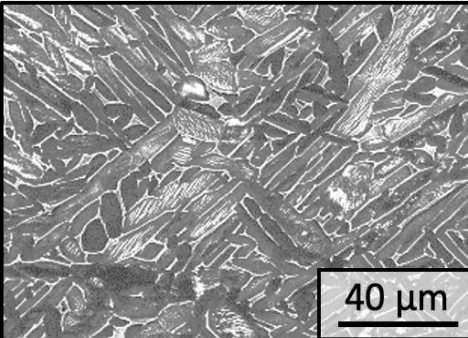


Figure 93. EBSD map showing the hierarchical structures at 850 °C – 4h

Table 19. SEM images and the phase fraction analysis in each annealing condition

SEM micrograph	Annealing condition	$\alpha/\beta$ phase fraction
	850 °C – 2h	0.88
	850 °C – 4h	0.81
	950 °C – 2h	0.79
	950 °C – 4h	0.69

	950 °C – 6h	0.66
	950 °C – 8h	0.65

In addition, Figure 94 breaks down the grain size of the  $\alpha'$  in the as-built condition and the  $\alpha$  in the heat-treated conditions, in each hierarchical class of  $\alpha'$  martensites and  $\alpha$  lamellas. It is shown that the effect of time on the grain coarsening was greater at higher annealing temperatures. At the lower temperature (850 °C) the grain coarsening occurred on both the  $\alpha$  and the  $\beta$  phases which competed and hindered one another, consequently restricting the grain growth (15). Nevertheless, at the higher temperature, the  $\alpha$  decreased its volume fraction, thus increased the influence of holding time on the grain growth. Besides, the coarsening effect was observed to have a greater impact on the larger grains (Class I > Class II > Class III). It is reasoned that the grain coarsening was achieved via the continuous process of termination migration and Ostwald ripening over prolonged annealing (226, 228). Of the two mechanisms, the Ostwald ripening dissolved the small grains and redeposited onto larger grains (229), which further increased the size gap between the large Class I- $\alpha$  and the fine Class-III  $\alpha$  grains.

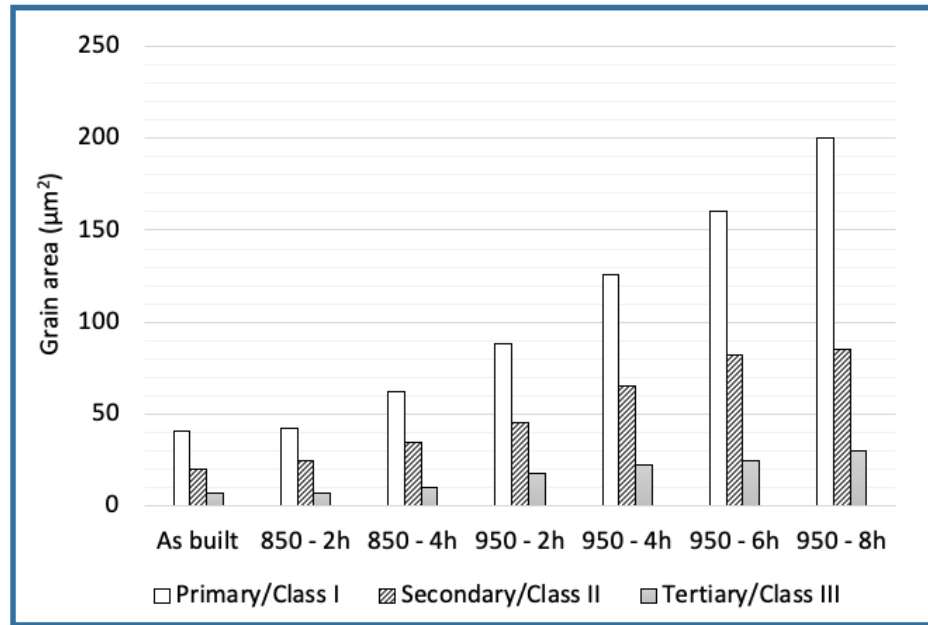


Figure 94. Diagram showing the coarsening effect in the hierarchical structure by heat treatment

A critical change occurred in prolonged heat treatment conditions which was the appearance of globular grains, noticeable after 4 hours of 950 °C annealing. The globular grains were observed in large numbers on the prior  $\beta$  columnar boundaries, in line with the  $\alpha_{GB}$  as shown in Figure 90b. When the annealing time was up to 6 and 8 hours, the globularization effect occurred more on the  $\alpha$  grains within the prior columnar structures.

The globularization generally is driven either by a static or a dynamic process. A critical strain is necessary for dynamic globularization to occur, and the degree of globularization is highly influenced by deformation strain (230-232). For static globularization, Stefansson, Semiatin (223) found that globularization kinetics is dependent on the deformation prior to the heat treatment and the heat treatment temperature, which significantly impedes static globularization process by decreasing the annealing temperature. Besides, Shell and Semiatin (233) investigated the effect of initial microstructure on globularization and found that the globularization rate of Ti-6Al-4V is faster on fine acicular  $\alpha$  grains than it is on a coarse colony morphology as the boundary splitting mechanism on thin grains is easier and faster. For Ti-6Al-4V with an initial fully lamellar morphology, the globularization rate was reported to be achieved up to 40-50% by hot working followed by an isothermal annealing (234). It is worth pointing out that up to the current knowledge, there has been no research quantifying the static globularization effect on heat treatments of Ti-6Al-4V with the initial  $\alpha'$  martensite microstructure.

In order to quantify globularization effect in the heat treatments of SLM Ti-6Al-4V, it is necessary to investigate the geometry parameters of microstructures via aspect ratio and shape factor as shown in



Figure 95. The aspect ratio is defined as the length over width ratio of a grain, and a low aspect ratio could distinguish a fragmented grain from the lamellar grains. The shape factor represents the curvature of a grain, which is determined by the ratio of grain perimeter over the perimeter of a circle having the equal area. Simply put, a low shape factor indicates the grain is globularized. In this study, a globular grain is considered fully globularized when its aspect ratio and shape factor are not larger than 2 and 1.12, respectively. And finally, the globularized fraction was quantified by the fraction of fully globular grains over the total grains.

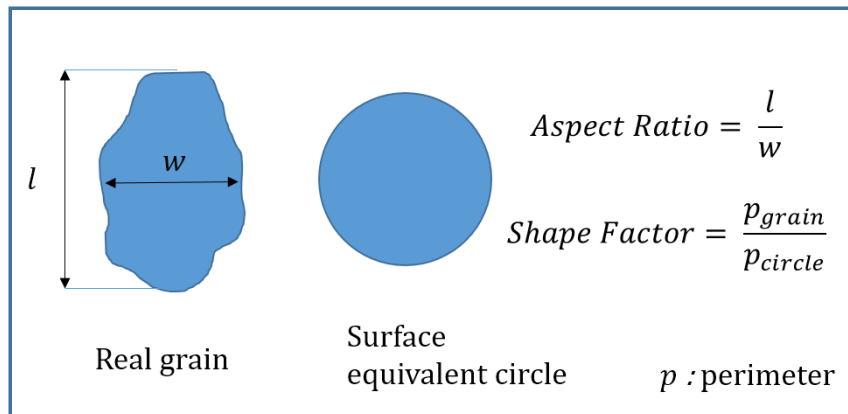


Figure 95. Schematics definition of grain aspect ratio and shape factor

Figure 96-Figure 98 illustrate average aspect ratios, shape factors and globularized fraction calculated in the as built as well as in all heat treatment conditions. Despite the transformation of the  $\alpha'$  into lamellar  $\alpha+\beta$  after 2-hour annealing at 850 °C, the grain aspect ratio and the shape factor did not experience any significant change, remaining as acicular shapes as compared to the initial acicular  $\alpha'$  morphology. Annealing at 850 °C – 4h and 950 °C – 2h observed a slight decrease in the grain aspect ratio, indicating the occurrence of boundary splitting which began to fragmentise the lamellar grains.

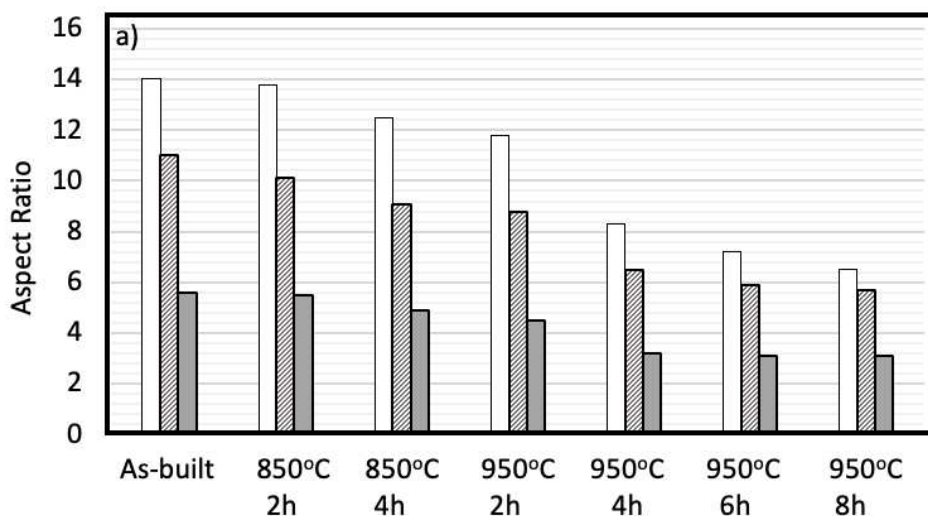


Figure 96. Diagram showing grain aspect ratio in the as built and heat treatment conditions

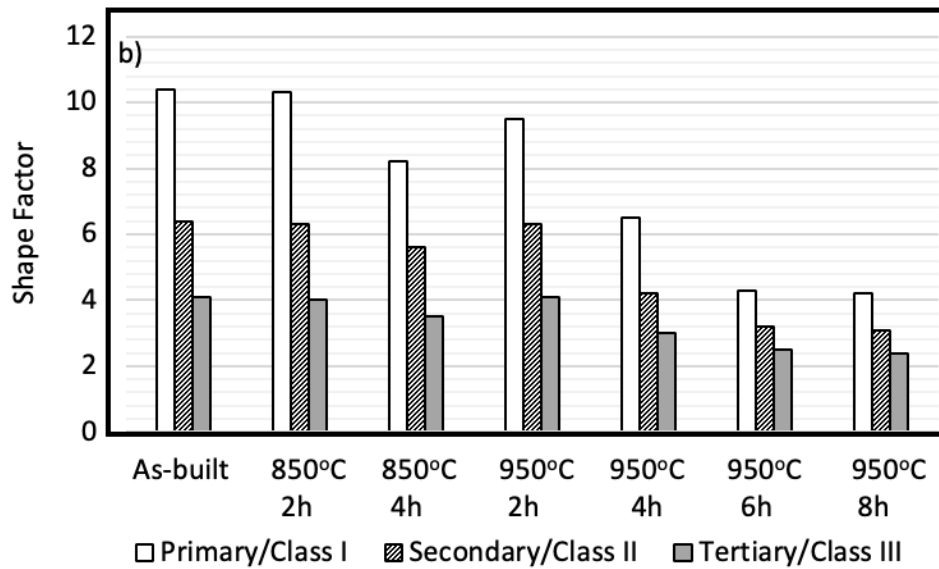


Figure 97. Diagram showing grain shape factor in the as built and heat treatment conditions

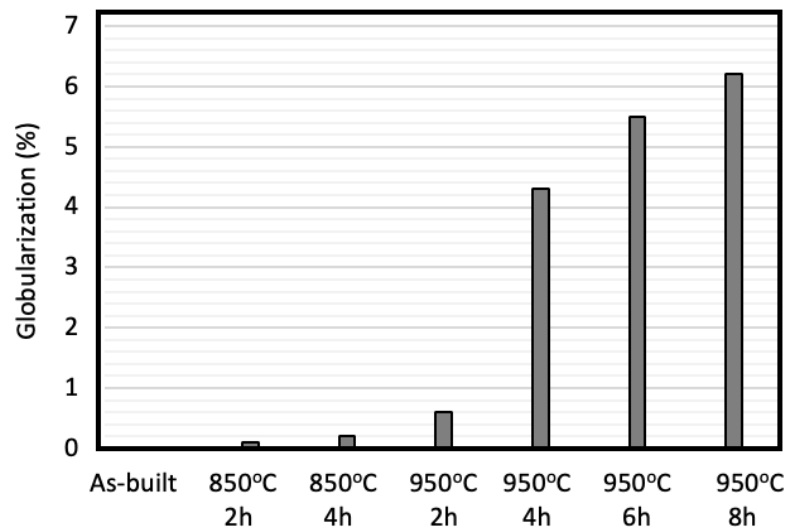


Figure 98. Diagram showing the globularized fraction in the as built and heat treatment conditions

The globularization effect significantly increased from 2 to 4 hours of annealing at 950 °C as it is seen in Figure 96 and Figure 97. Both the aspect ratio and the shape factor in all the hierarchical classes of the  $\alpha$  grains fell sharply during this time. Additionally, the globularized fraction significantly increased after 4 hours, as 4.3% then gradually increased to 5.5% and 6.2% as holding time is up to 6 and 8 hours respectively (see Figure 98). Besides, the aspect ratio and the shape factor had their largest drop on Class-I  $\alpha$  grains as compared to that on Class-II and Class-III counterparts. This indicates a greater degree of globularization on larger grains.

### 6.3 – The decomposition of $\alpha'$ martensite

Phase transformation of  $\alpha'$  into  $\alpha+\beta$  acted as the foundation for the globularization process to take hold during annealing of SLM Ti-6Al-4V. Thus, a detailed analysis on the decomposition of  $\alpha'$  is an essential requirement for better understanding the globularization and, therefore, better controlling the mechanical properties.

The decomposition of  $\alpha'$  martensite microstructure in Ti-6Al-4V is an allotropic displacive transformation, which is a competition between two rivalry processes: nucleation-and-growth and spinodal decomposition, depending on the thermodynamics and stability of the phases (235-237). Many studies have determined the mechanism of allotropic displacive transformation by using the thermodynamic graphical approach which was developed by Soffa and Laughlin (238). The approach employs the free energy diagram and the thermodynamic phase stability to analyse the coaction between the clustering and the ordering process in many alloy systems, such as Fe-Cr (239), Cu-Ni-Sn (240), Ni-Cr-W (241), Co-Al-W (242), Cu-Ti (243). Similarly, the decomposition of  $\alpha'$  martensite in titanium alloys has been theoretically analysed based on this regard (236, 244-246).

In the thermodynamic graphical approach, the Gibbs free energy characterises the thermodynamics of the phase as a function of different parameters, such as the alloying element composition and the crystalline structure order (238). Heo, Shih (247) used this approach to analyse the kinetic pathways of the  $\beta \rightarrow \alpha' \rightarrow (\alpha+\beta)$  in a Ti-M binary system. They used a double-well type energy curve for the  $\alpha$  phase and a single-well type for the  $\beta$  phase. By contrast, in the recent work of Ji, Heo (248), the free energy for Ti-6Al-4V was formed by combining three single-well type curves of the  $\alpha$ , the  $\beta$  and the intermetallic phase ( $\text{Ti}_3\text{Al}$ ). In this study the free energy was constructed by the composition of alloying elements and the structure-order parameters of the  $\alpha$  and the  $\beta$  phases as the intermetallic precipitation was neglected. By this expression, the total free energy density of the system was expressed as the double-well type curve, in which the  $\alpha$  and the  $\beta$  phases were each presented by a single-well type curve, as illustrated in Figure 99.

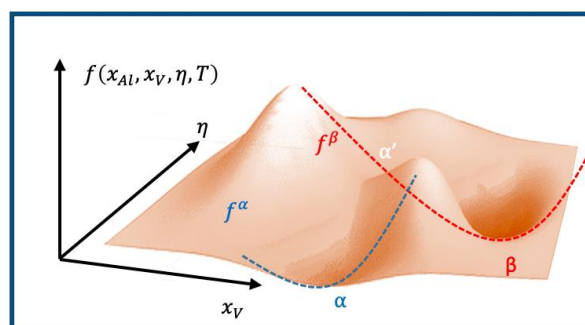


Figure 99. Illustration of the total free energy of the Ti-Al-V system on the  $\eta - x_V$  space

The free energy of the  $\alpha$  and  $\beta$  phase were calculated using the CALPHAD (CALculation of PHase Diagrams) method, which is a new approach for treating multi-component phase using temperature and composition dependent thermodynamic Gibbs Energy (249). The alloying elements were represented by Al and V, and their composition were expressed as  $(x_{Al}, x_V)$ . As the phase transformation started from the  $\alpha'$  (*hcp*) into the final phases of the  $\alpha$  (*hcp*) and the  $\beta$  (*bcc*), the structure-order parameter  $\eta$  was hence defined as  $\eta = 0$  for the *hcp* ( $\alpha$ ) structure and  $\eta = 1$  for the *bcc* ( $\beta$ ) one. The homogeneous free energy density of a phase  $i$  ( $i = \alpha, \beta$ ) at a given temperature  $T$  is denoted as  $f^i(x_{Al}, x_V, T)$ , and the total free energy density of the system is expressed as the following:

$$f(x_{Al}, x_V, \eta, T) = [1 - h(\eta)]. f^\alpha(x_{Al}, x_V, T) + h(\eta). f^\beta(x_{Al}, x_V, T) + W. g(\eta) \quad (\text{Equation 22})$$

in which  $h(\eta) = 3\eta^2 - 2\eta^3$  is the function that captures the interphase between the *hcp* structure ( $\eta = 0$ ) and the *bcc* structure ( $\eta = 1$ ),  $g(\eta) = 3\eta^2(1 - \eta)^2$  is the Landau-type double-well potential, and  $W$  is the height of the potential.

The stability of a phase at given particular thermodynamic parameters depends directly on the topological properties of the Gibbs free energy (238). More specifically, a phase is stable when the relative value of the free energy is minimum, and its second derivatives are positive. The most possible pathway of a phase transformation, thus, is the route connecting the most stable phases, and has the minimum energy barriers on the Gibbs free energy function (236). Figure 100a shows the separated metastable and unstable regions of the Gibbs free energy based on the secondary derivatives with respect to V composition. The metastable regions are determined as the  $\frac{\partial^2 f}{\partial x_V^2} > 0$ , whereas the unstable phase region is where the  $\frac{\partial^2 f}{\partial x_V^2} < 0$ . In addition, the phase transformation occurs through the nucleation-and-growth mechanism in the metastable regions and through the spinodal decomposition mechanism in the unstable region (see Figure 100a).

The  $\beta \rightarrow \alpha'$  displacive transformation is indicated by a dash arrow on free energy curves in Figure 100b defined by the V composition of the  $\alpha'$  phase in the SLM Ti-6Al-4V printed samples. The formation  $\alpha'$  phase stays in the instability regime on the free energy curve, and the decomposition of  $\alpha'$  must follow the kinetic pathway of the spinodal decomposition, forming solute-rich and solute-lean phases before reaching the equilibrium  $\alpha + \beta$  phases. The decomposition pathway could be simply expressed as  $\alpha' \rightarrow$  solute-rich + solute-lean  $\rightarrow \alpha + \beta$ , which was also theoretically confirmed by the thermographic approach in the study of Heo, Shih (247).

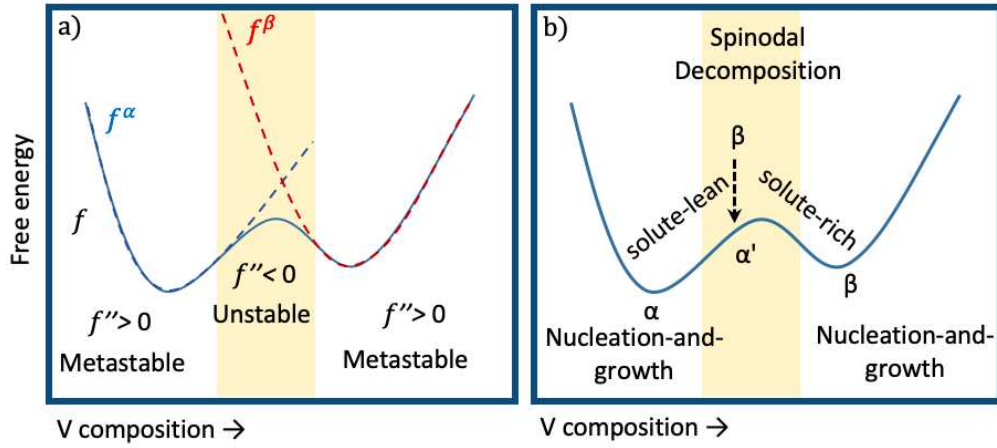


Figure 100. The total free energy diagram showing (a) phase stability and (b) transformation pathway of SLM Ti-6Al-4V

The evolution of the phase field variables was modelled by a set of Cahn-Hilliard equations as the following

$$\frac{\partial \eta}{\partial t} = \vec{\nabla} \cdot M \vec{\nabla} \left[ \frac{\partial f(x_{Al}, x_V, \eta, T)}{\partial \eta} - \epsilon \nabla^2 \eta \right] \quad (\text{Equation 23})$$

$$\frac{1}{V_m} \frac{\partial x_i}{\partial t} = \vec{\nabla} \cdot M \vec{\nabla} \left[ \frac{\partial f(x_{Al}, x_V, \eta, T)}{\partial x_i} - \epsilon \nabla^2 x_i \right], (i = Al, V) \quad (\text{Equation 24})$$

in which  $V_m$  is the molar volume,  $\epsilon$  is the gradient energy coefficient and  $M$  is the mobility of the system. The mobility of the system is constructed based on the mobility of each element as shown in (Equation 25) in which the mobility of each element can be calculated by (Equation 26), using atomic diffusion  $D_i$  database, gas constant  $R$ , temperature  $T$ , concentration  $x_i$  and molar volume  $V_m$ .

$$M = V_m^{-1} \{-x_{Al}x_V M_V - x_V[(1 - x_{Al})x_{Al}(M_{Al} - M_{Ti}) - x_{Al}x_V(M_V - M_{Ti})]\} \quad (\text{Equation 25})$$

$$M_{i=Al,V,Ti} = \frac{D_i x_i V_m}{RT} \quad (\text{Equation 26})$$

The numerical solution of the phase field equations was implemented in MATLAB using the source codes from the work of Biner (250) that employed the semi-implicit Fourier-spectral method (251). The evolution of the two phases over the calculation iterations as presented in Figure 101. The spinodal decomposition started from the homogeneous  $\alpha'$  ( $\eta = 0.5$ ) and evolved towards the equilibrium  $\alpha + \beta$ . Nevertheless, the equilibrium could not be achieved in the spinodal decomposition. It is revealed that

at 850 °C, the homogeneous  $\alpha'$  evolved into the solute-lean phase, at  $\eta = 0.33$ , and the solute-rich phase, at  $\eta = 0.65$ . The model also revealed that higher temperatures aided the decomposition: at 950 °C the solute-lean phase reached  $\eta = 0.17$  and the solute-rich phase at  $\eta = 0.72$ , closer to the equilibrium  $\alpha+\beta$  as compared to 850 °C.

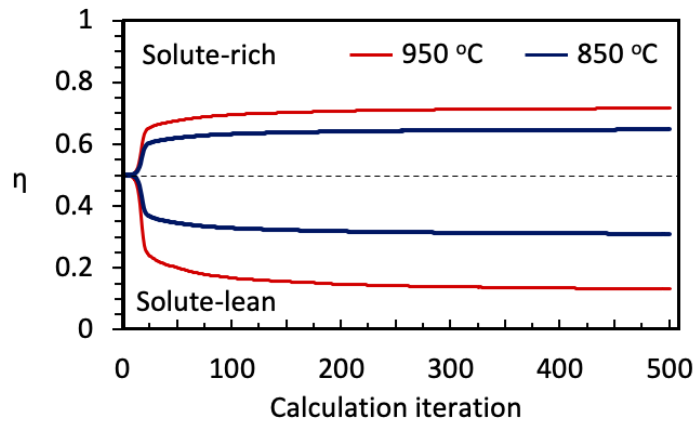


Figure 101. Diagram showing the evolution of  $\eta$  over simulation iteration at different temperatures

Figure 102 successfully emulated the partitioning of solute elements into the two distinct phases represented as blue (solute-lean) and red (solute-rich) colour. The solute-rich phase was enriched in V (and leaned in Al), and by contrast the solute-lean phase was leaned in V (and enriched in Al). The simulated morphology appeared as the lamellar solute-rich and solute-lean grains successively coupling one another due to the phase separation.

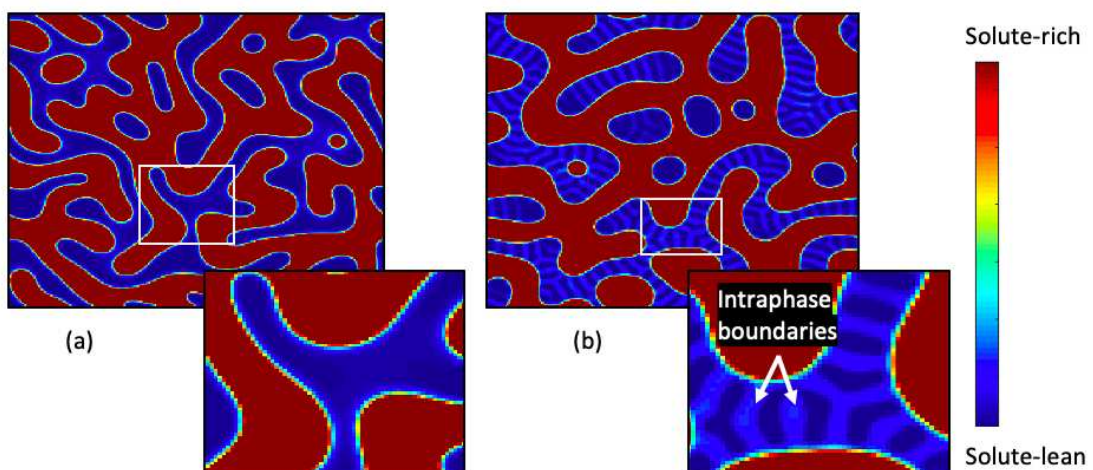


Figure 102. The Phase Field simulated microstructure at a) 850 °C and b) 950 °C

In the experiments the equilibrium state was achieved as observed in Figure 90 and Table 19, yet it is possible to discern and analyse the solute-rich phase and solute-lean phases via the etching effect and EDS analysis on the final  $\alpha$  grains. To be more specific, the  $\alpha$  grains developed from the solute-lean phase consisted of higher V concentration than those from the solute-rich phase, by 4.03 wt. to 1.45



wt. % of V as reckoned in the EDS. This disparity in V concentration between these two  $\alpha$  types resulted in different etching response, as the solute-lean  $\alpha$  lamellas were whiter shade than the solute-rich  $\alpha$  lamellas as shown in Figure 103. The solute-rich and solute-lean phases appeared one after another, distinguished by the  $\beta$  acting as interphase boundaries, confirming the morphology results by the Phase Field model.

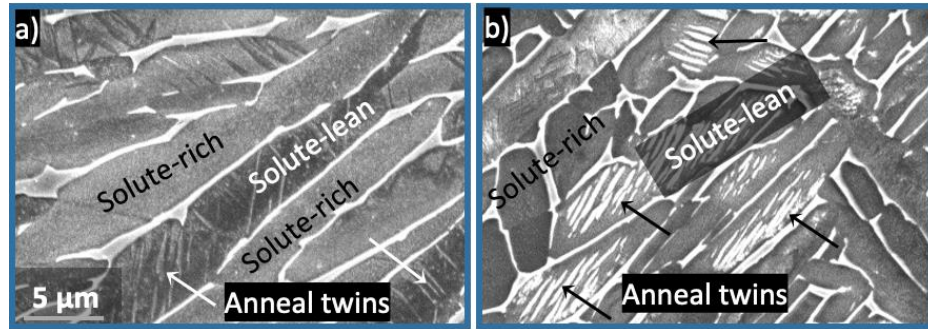


Figure 103. SEM images showing solute-rich and solute-lean phases with the appearance of anneal twins marked by arrows in a) 950 °C – 4 hours and b) – 8 hours

The occurrence of anneal twins in the solute-lean grains was also observed as fine acicular structures across or partially across the parent grain (see Figure 103). This phenomenon was documented to initiate due to low stacking fault, especially in the *fcc* structure metals such as Cu, Al, Ni (252, 253). As higher concentration of Al in the solute-lean phase would decrease the stacking fault, thus initiating the anneal twins during phase evolution. More importantly, as anneal twins only occurred in the solute-lean phase, they could be taken as a sign to discern the two phases.

In addition, it can be seen in Figure 102 the simulation also successfully expressed the formation of anneal twins at 950 °C, appearing as the intra-boundaries in the solute-lean phase. As higher temperature aided the phase evolution toward the equilibrium phases, it also increased the interfacial energy gap of the two phases, as seen in Figure 104. This finding indicates that V was diffused from the interphase into the solute-lean phase in order to minimise the interfacial energy gap, which initiated the anneal twins in the solute-lean phase.

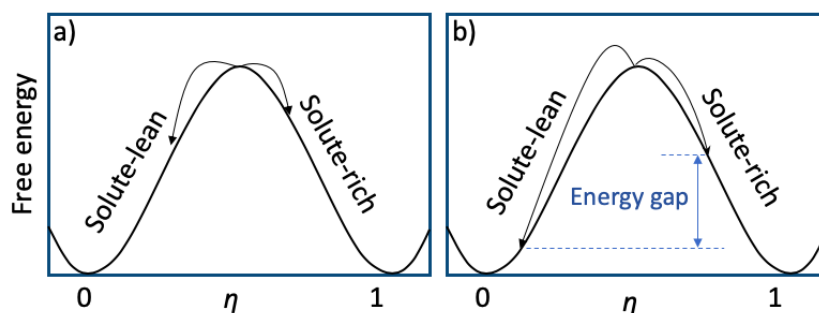


Figure 104. The evolution of  $\eta$  in the free energy diagram at a) 850 °C and b) 950 °C

There existed several limitations in the current framework that are necessary to be highlighted. Firstly, the model employed only the homogeneous bulk thermodynamic database without taking the heterogeneity of the as-built microstructure into account, which resulted in no spatial reference in the simulated morphology. Secondly, there was no correlation between the calculation iterations and the real time, hence the effect of holding time on the microstructure evolution could not be analysed precisely. As the current model aimed at determining the thermodynamics and the kinetic pathways of the phase transformation, the mentioned limitations did not alter the final results and conclusions, however. On the other hand, these issues left some room for tackling for future work.

#### **6.4 – The kinetic pathways of the $\alpha'$ decomposition**

In the spinodal decomposition, the  $\alpha'$  martensite started the phase separation via the solute element partitioning. The formation of the solute-lean phase by the enrichment of Al, the  $\alpha$ -stabilizer, which helped maintain the *hcp* structure of from the initial phase. On the other hand, the high concentration of V, the  $\beta$ -stabilizer, partitioned into the solute-rich phase would lead to the *hcp*  $\rightarrow$  *bcc* transformation, consequently resulting in a different final morphology.

In the event that the *hcp*  $\rightarrow$  *bcc* transformation occurred in the solute-rich phase due to the V enrichment, the  $\alpha'$  phase would be separated into the solute-lean  $\alpha$  and the solute-rich  $\beta$  phase, which was aided by high anneal temperature and longer holding time. The solute-rich  $\beta$  phase was observed dispersedly in the 950 °C - 6h and 8h as equiaxed  $\beta$  grains that possessed ultrafine secondary alpha ( $\alpha_s$ ) laths in their matrix as seen in Figure 105. The equiaxed  $\beta$  grains stood out from the other typical  $\beta$  phase, which appeared as thin layers on the boundaries of  $\alpha$  grains. It is also observed that the equiaxed  $\beta$  grains were in pairs with an identical size solute-lean  $\alpha$  lamellae as the result from the spinodal decomposition. Besides, these *bcc* solute-rich phase appeared equivalently to the Class-III  $\alpha$  grains, indicating that the *hcp*  $\rightarrow$  *bcc* transformation was more likely to occur in the fine tertiary  $\alpha'$  as also supported by the studies of Semiatin, Lehner (254) and Semiatin, Knisley (255).

Since solute-lean and solute-rich are the non-equilibrium phases, it is thus required a second progress following the spinodal decomposition to reach the equilibrium states. The equilibrium could be achieved by long-range solute element diffusion, as reported in the work of Liu, Lu (256), and the second progress did so by precipitating the solute contents in the phase to reduce its concentration in the matrix.

The crystal structure of the solute phase strongly influenced the precipitation mechanism in the second stage to reach the equilibrium  $\alpha+\beta$ . More precisely, the *hcp* solute-lean and solute-rich phases resulted in the  $\beta$  layer at boundaries by precipitating V from their matrix. The deficit of V concentration in the

matrix gradually formed the equilibrium  $\alpha$ , as shown in the microstructure in Figure 103. By contrast, the  $bcc$  solute-rich phase reached the equilibrium  $\beta$  state by precipitating Al from its matrix, resulting in the  $\alpha_s$  laths, as evidenced in Figure 105.

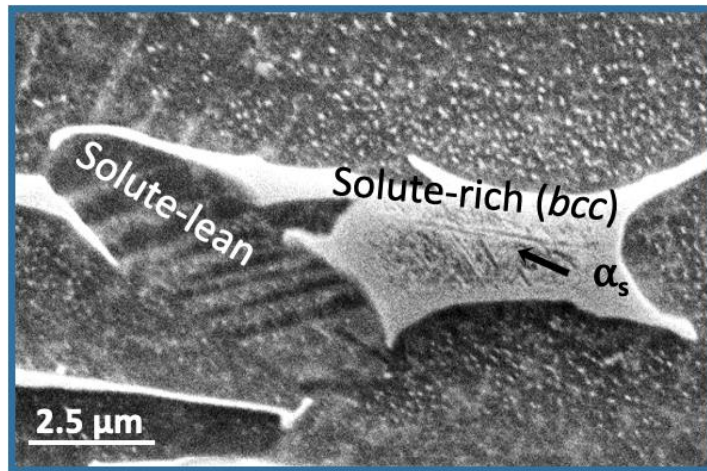


Figure 105. SEM image showing the  $\alpha_s$  laths in the equiaxed  $\beta$  grain in 950 °C – 6h

Since the crystallisation transformation in the solute-rich phase critically changes the mechanism in the decomposition of  $\alpha'$  during the heat treatment, there are two possible kinetic pathways as via either the  $hcp$  or the  $bcc$  solute-rich phase. The first kinetic pathway,  $\alpha' \rightarrow hcp$  solute-lean +  $hcp$  solute-rich  $\rightarrow$  equilibrium  $\alpha+\beta$ , is represented in Figure 106. Whereas the second pathway,  $\alpha' \rightarrow hcp$  solute lean +  $bcc$  solute-rich  $\rightarrow$  equilibrium  $\alpha+\beta$ , is shown in Figure 107. The schematic illustration presents the microstructure at each step in the transformation with the associated  $\eta$  progression in the thermodynamic diagram.

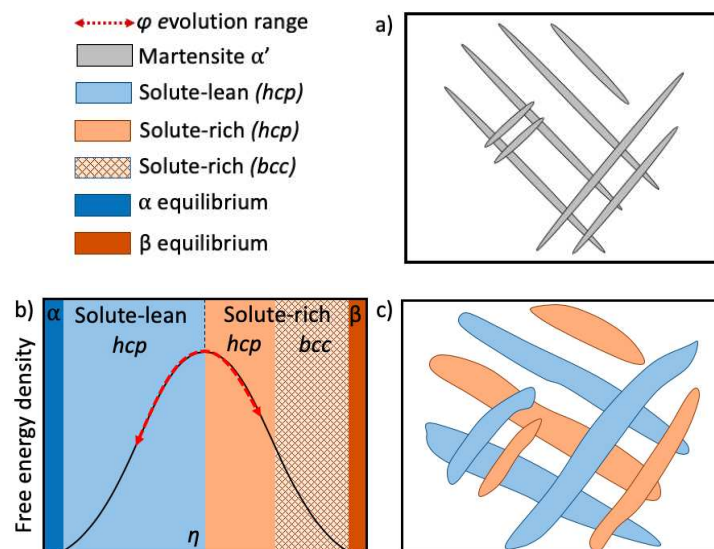


Figure 106. (Continued)

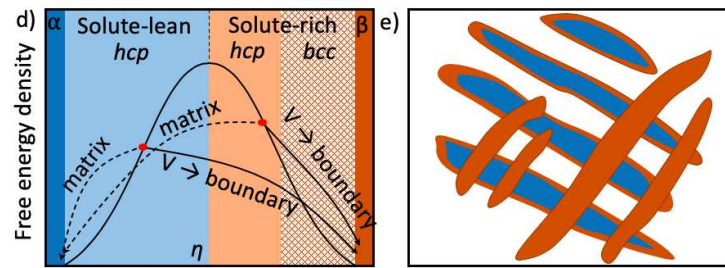


Figure 106. Thermodynamic diagrams and schematic illustrations showing the kinetic pathway of SLM Ti-6Al-4V from a) initial  $\alpha'$  martensites, b,c) spinodal decomposition into hcp solute-lean and hcp solute-rich phases and d,e) precipitation into equilibrium  $\alpha+\beta$

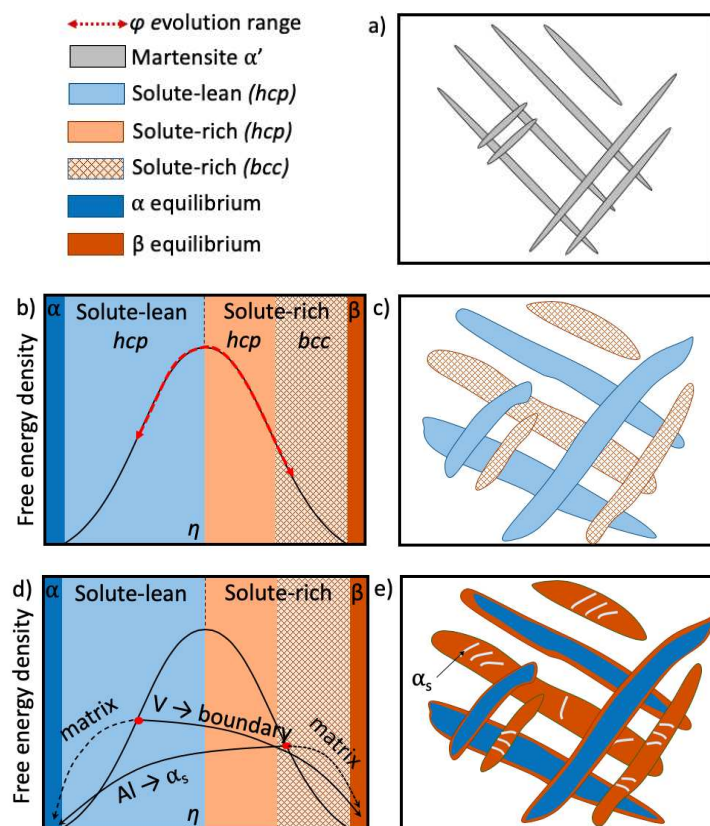


Figure 107. Thermodynamic diagrams and schematic illustrations showing the kinetic pathway of SLM Ti-6Al-4V from a) initial  $\alpha'$  martensites, b,c) spinodal decomposition into hcp solute-lean and bcc solute-rich phases and d,e) precipitation into equilibrium  $\alpha+\beta$

Annealing at 850 °C only experienced the decomposition of  $\alpha'$  via the first kinetic pathway, in which both the solute-lean and solute-rich possessed the hcp structure as unveiled by the Phase Field model, and finally transformed into the lamellar morphology of  $\alpha$  grains with the thin  $\beta$  phase at boundaries. On the other hand, both kinetic pathways were observed when annealing at 950 °C. The fraction of the

$hcp \rightarrow bcc$  transformation increased over time as the  $bcc$  solute-rich phase only accounted for a small number of grains in 950 °C – 4h and increased its fraction over prolonged annealing to 6 and 8 hours.

Nevertheless, this left the question of at which value of  $\eta$  the solute-rich phase initiated the  $hcp \rightarrow bcc$  transformation. As discussed, the crystalline transformation started to occur at 950 °C, which was claimed by the formation of the equilibrium  $\beta$  grains with precipitated  $\alpha_s$  laths. Hence, based on evolution of  $\eta$  for the solute-rich phase in the Phase Field model at 950 °C this analysis proposes the critical value  $\eta = 0.72$  at which the  $hcp \rightarrow bcc$  transformation occurs in the solute-rich phase due to V enrichment.

### **6.5 – The static globularization process.**

The static globularization in the lamellar microstructure involves two mechanisms, namely boundary splitting and termination migration. Both these mechanisms have been used widely to analyse the coarsening effect and the globularization in titanium alloys during heat treatment (221, 225, 226, 257, 258) which are schematically illustrated in Figure 108.

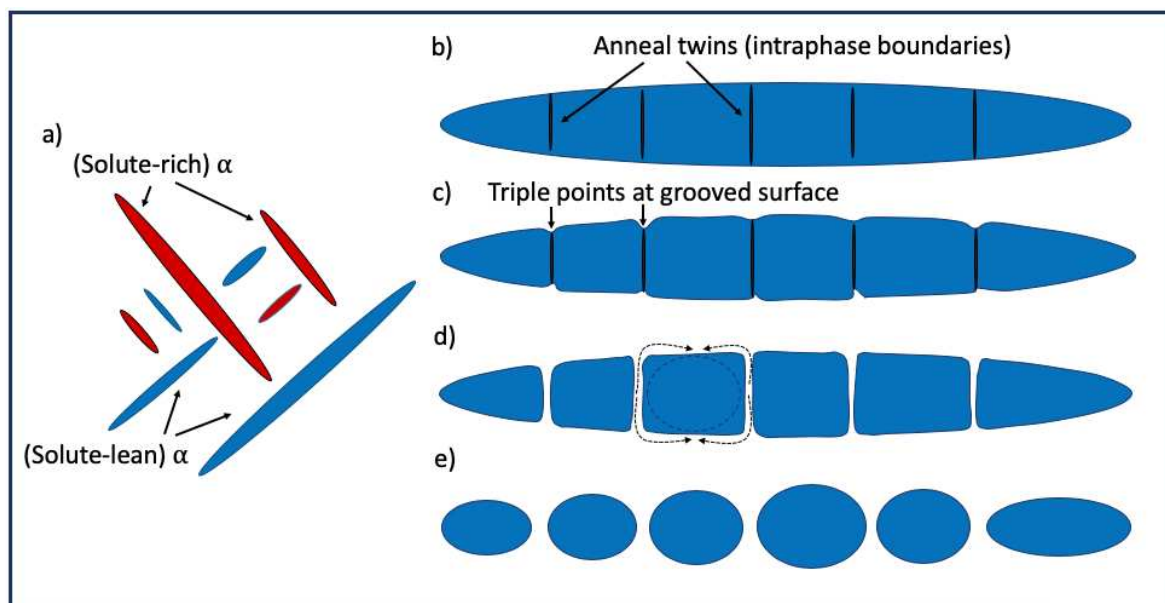


*Figure 108. Schematic of the globularization process: a) initial morphology of solute-rich and solute-lean phases, b) initial solute-lean  $\alpha$  grain with anneal twins, c) boundary splitting mechanism at the triple points, d) termination migration mechanism on fragmented grains and e) final globular grains*

The boundary splitting mechanism is associated with the instability of 180° dihedral angles between the  $\alpha/\beta$  interphase boundaries and the  $\alpha$  intraphase boundaries, which gives rise of the grooves at the triple points between the interphase and intraphase boundaries. Equilibrium between the different surface tension at the triple points causes a mass transfer from the grooves to the interphase surface



which deepens the grooves—from either or both sides of the lamellae—and thereby eventually fragmentises the  $\alpha$  grain. The kinetics of the boundary splitting is thus based on the deepening rate of the triple points.

After the boundary splitting progress, the lamellar  $\alpha$  grain greatly reduces its aspect ratio, but only when the following mechanism of termination migration takes hold could the globularization be complete. The termination migration causes a diffusional flux from the grain' edges to the flat surfaces, resulting in the recession of the grain edges and the completion of the globularization.

At 950 °C, anneal twins appeared in the  $\alpha$  grains that evolved from the solute-lean phase, and only these  $\alpha$  grains were influenced by the boundary splitting mechanism as observed in the EBSD analysis (see Figure 109). For this reason, the static globularization was not capable to transform the lamellar into the fully equiaxed morphology. In fact, Chao, Hodgson (259) studied the thermo-mechanical processing of the martensitic microstructure, and reported that the globularization only occurs locally in the microstructure.

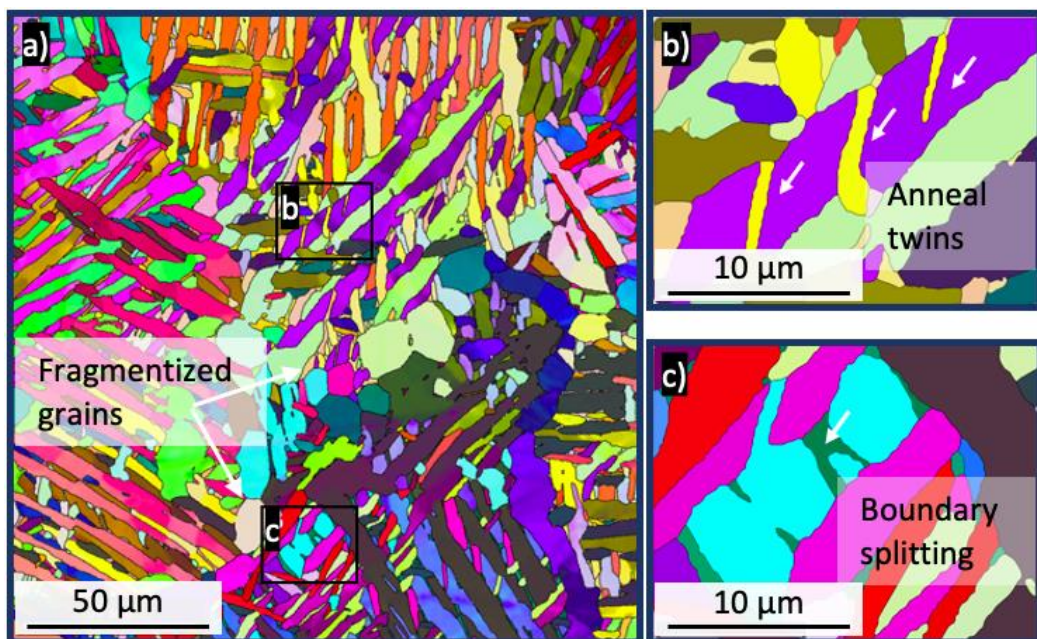


Figure 109. a) EBSD map the globularized microstructure showing fragmentised grains, b) anneal twins and c) thermal grooving process in the solute-lean  $\alpha$  grain at 950 °C

The lack of anneal twins in the  $\alpha$  grains evolving from the solute-rich phase as well as in the microstructure annealed at 850 °C halted the boundary splitting. The globularization in these  $\alpha$  grains thus only occurred via the termination migration mechanism. However, since the initial aspect ratio was very high, the termination migration in these  $\alpha$  grains mainly resulted as the coarsening effect. This explains for the low globularized fraction in the annealing conditions of 850 °C, as shown in Figure 98.



The grain analysis revealed that after 2 hours of annealing at 950 °C, the aspect ratio and the shape factor reduced due to the boundary splitting occurring at the early stage. And after 4 hours annealing, the aspect ratio and shape factor significantly decreased, and the globularized fraction started to increase, indicating that a great amount of  $\alpha$  grains finished the boundary splitting and initiated the termination migration. The boundary splitting played a significant role in the early hours of annealing due to its short duration time, which is justified as the short diffusion length and the small amount of mass transfer. By contrast, the longer diffusion length and larger amount of mass transfer, requiring longer time to complete, were the key reasons that the termination migration was dominant in the prolonged annealing

The duration time of the boundary splitting mechanism can be estimated by determining the time to break down the lamellae via the thermal grooving process. The approach was proposed from the Mullins grooving analysis (260) by calculating the movement time of the triple points to meet one another (each triple point needs to move a distance of half the grain thickness).

The position of the triple point  $Y_0$ , after the diffusion time  $t$ , is given by the following equations:

$$Y_0 = -0.86m(A't)^n \quad (\text{Equation 27})$$

$$A' = \frac{C_\beta \gamma_{\alpha\beta} V_m D_\beta}{RT} \quad (\text{Equation 28})$$

in which  $m = \tan(\theta)$  is the average slope at the root of the triple point,  $C_\beta$  is the equilibrium concentration of alpha stabilizers (Al) in the  $\beta$  phase,  $\gamma_{\alpha\beta}$  is the interface energy ( $\text{J m}^{-2}$ ),  $V_m$  is the molar volume of titanium ( $\text{m}^3 \text{mol}^{-1}$ ),  $D_\beta$  is the diffusivity of vanadium in the  $\beta$  phase ( $\text{m}^2 \text{s}^{-1}$ ),  $R$  is the universal gas constant ( $\text{mol}^{-1} \text{K}^{-1}$ ),  $T$  is the annealing temperature (K) (261).

Nevertheless, the quantity  $A'$  can be determined more conveniently from the coarsening behaviour as shown by its relationship with the average particle diameter  $d_\alpha$  and the diffusion time  $t$  in the following equation:

$$d_\alpha = Kt^n = \left\{ \frac{8C_\beta \gamma_{\alpha\beta} V_m D t}{9RT} \right\}^n \quad (\text{Equation 29})$$

By simplifying  $(8/9)^n = 1$ , the particle diameter  $d_\alpha$  can be expressed by the following:

$$d_\alpha = Kt^n = (A't)^n \quad (\text{Equation 30})$$

Thus, it can be deduced from (Equation 30) that  $A'^n = K$ . The values of  $K$  and  $n$  can be determined by a regression model using lamellar grain data in the EBSD analysis, which were obtained as  $K = 4.02$  and  $n = 0.41$ .

The time required for boundary splitting mechanism can be calculated by assimilating the value of triple point distant  $Y_0$  as half the average lamellar thickness ( $Y_0 = 2.67 \mu\text{m}$ ) into (Equation 31).

$$t = \left( \frac{Y_0}{0.86mK} \right)^{1/n} \quad (\text{Equation 31})$$

The duration time of the boundary splitting was predicted to be 2.2 hours at 950 °C. Adding the prior time required for the  $\alpha'$  decomposition, the boundary splitting finished after 2.2 hours of annealing at 950 °C. This explains for the significant reduction of the shape factor and the aspect ratio in the microstructure when increasing the anneal time from 2 hours to 4 hours at 950°C, as discussed previously.

The completion time of the termination migration  $\tau_g$  was estimated using the following equations, as proposed by Semiatin, Stefansson (258)

$$\frac{\tau_g}{t'} = \frac{\eta^3 - \left[ 0.328\eta^{7/3} \left( 1 + \sqrt{1 - 0.763\eta^{-4/3}} \right)^2 \right]}{4 \left[ \frac{2(1 + \eta)}{3(0.5 - 0.573\eta^{-1/3})} + \frac{0.5\eta^{1/3} + 0.665\eta^{2/3}}{3(0.143 + 0.934\eta^{-1/3})} \right]} \quad (\text{Equation 32})$$

$$\eta = \frac{w}{l} + 0.5 \quad (\text{Equation 33})$$

$$\tau' = \frac{l^3 RT}{C_\beta \gamma_{\alpha\beta} V_m D_\beta} \quad (\text{Equation 34})$$

$$D_\beta = 77 \times 10^3 \exp\left(\frac{-17460}{T}\right) \quad (\text{Equation 35})$$

in which  $\eta$  and  $\tau'$  are respectively the geometric and time normalization factor,  $w$  is the grain width,  $l$  is the grain length,  $V_m = 1.044 \times 10^5 \text{mol}^{-1}$  is the molar volume,  $D_\beta$  is the diffusivity of V in the  $\beta$  phase (262),  $R = 8.314 \text{mol}^{-1} \text{K}^{-1}$  is the universal gas constant and  $T$  is the absolute temperature,  $\gamma_{\alpha\beta} = 0.26 \text{Jm}^{-2}$  is the  $\alpha/\beta$  interface energy (221, 261).

In (Equation 34),  $C_\beta$  is the equilibrium concentration of the rate-limiting solute i.e., V in the  $\beta$  phase. However, the term  $C_\beta$  should be modified by the composition factor  $C_F$  since both the  $\alpha$  and  $\beta$  phases are not the terminal solid solution.

$$C_F = \frac{C_\beta(1 - C_\beta)}{(C_\alpha - C_\beta)^2(1 + \partial \ln r / \partial \ln C_\beta)} \quad (\text{Equation 36})$$

in which  $C_\alpha$  are the equilibrium concentration of Al in the  $\alpha$  phase, and the quantity  $1 + \partial \ln r / \partial \ln C_\beta = 0.75$  and  $r$  is the activity coefficient of the solute in the  $\beta$  phase (257).

The calculated duration time of the termination migration was 10.6 hours at 950 °C for the fragmented grains after the boundary splitting mechanism. This finding suggests that the microstructure of the 950 °C – 6h and 8h was still the process of the termination migration.

## **6.6 – Mechanical properties**

Mechanical properties of annealed SLM Ti-6Al-4V were performed and analysed in both quasi-static and dynamic test conditions to emphasise the effect of heat treatment on mechanical properties compared to as-built properties discussed in Chapters 4 and 5. Furthermore, it should be noted that specimens used in this chapter were specifically produced as net-shape specimens to imitate the properties of net-shape functional parts manufactured for industrial applications.

Figure 110 shows the quasi-static stress strain curves of SLM Ti-6Al-4V in the as-built and heat treatment conditions, and the bar graph in Figure 111 provides more details on tensile strength and elongation. The as-made dog-bone specimens, vertically constructed from the SLM base, had lower ductility compared to the horizontally built and machined specimens as described in chapter 4 by 2.8% to 5.3%. The difference in ductility was mainly caused by the vertically built samples requiring higher printing layers to be made, which in turn resulted in more interlayer porosity and microcracks in the samples, and consequently lower ductility.

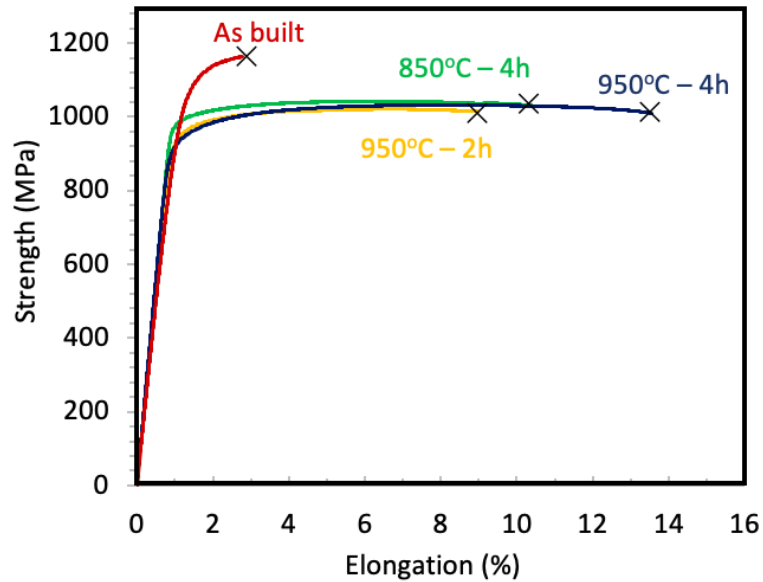


Figure 110. Diagram showing the stress-strain curves of the as built and exemplary annealing conditions

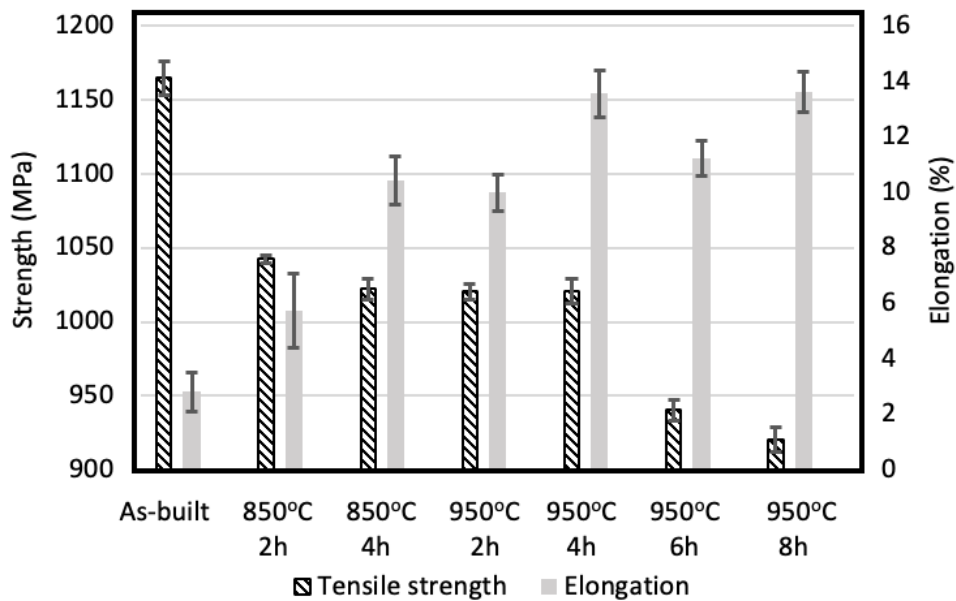


Figure 111. Diagram showing the strength and elongation of the as built and annealing conditions

It is shown that the applied heat treatment conditions significantly improved the quasi-static properties of SLM Ti-6Al-4V, resulting in a great balance of high ductility and good tensile strength. The relatively fine lamellar microstructure achieved by annealing at 850 °C vastly increased the average ductility to 9.99% and 10.42% after 2 hours and 4 hours respectively, while it still remained very high strength of approximately 1050 MPa. Annealing at 950°C in 4 hours, with the formation of globular grains, proved to be the best heat treatment for its enormous improvement on the ductility to 13.55% with the high tensile strength of 1020.61 MPa. The globularization occurred in this condition greatly gave the advantage of SLM Ti-6Al-4V as having the comparable tensile properties with the wrought

products. Furthermore, continuously increasing the holding time to 6 hours and 8 hours slightly improved the ductility of SLM Ti-6Al-4V, owing to more globular grains in the microstructure, but at a greater expense of tensile strength, which was reduced to approximately 940 MPa and 920 MPa respectively. This large reduction of tensile strength in the prolonged annealing at high temperature was due to the coarse lamellar grain morphology, reckoned by many similar studies (15, 219, 263, 264), and therefore is not advisable for industrial applications.

Based on the heat treatment findings on the microstructure and the quasi-static tensile properties, the three annealing strategies of 850 °C – 4h, 950 °C – 2h and – 4h were narrowed down to optimise the dynamic mechanical properties of SLM Ti-6Al-4V. The dynamic stress-strain curves and compressive properties of the three annealing conditions are shown in Figure 112 and Figure 113. It is clearly noticeable that the heat treatment greatly improved the critical strain  $\varepsilon_2$  without any severe reduction in the compressive strength. The yield strength (YS) remained as high as 1550 – 1630 MPa, whereas the  $\varepsilon_2$  was increased up to 0.23 strain under 950 °C – 4h, as compared to 0.125 strain of the as-built condition.

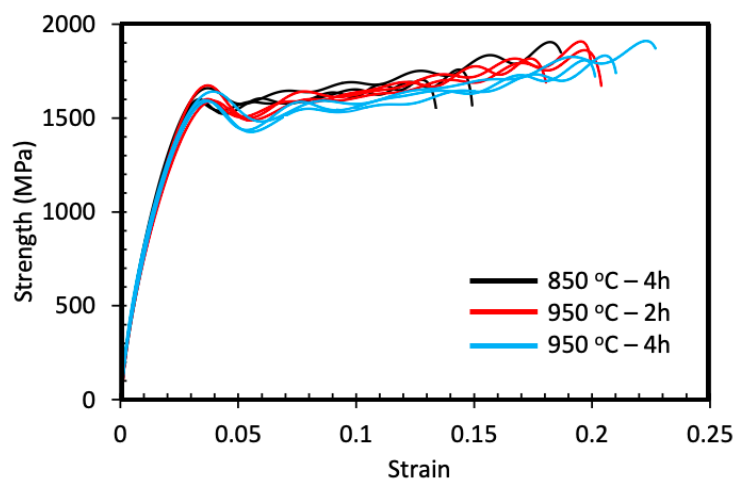


Figure 112. Diagram showing dynamic stress-strain curves of the three annealing conditions

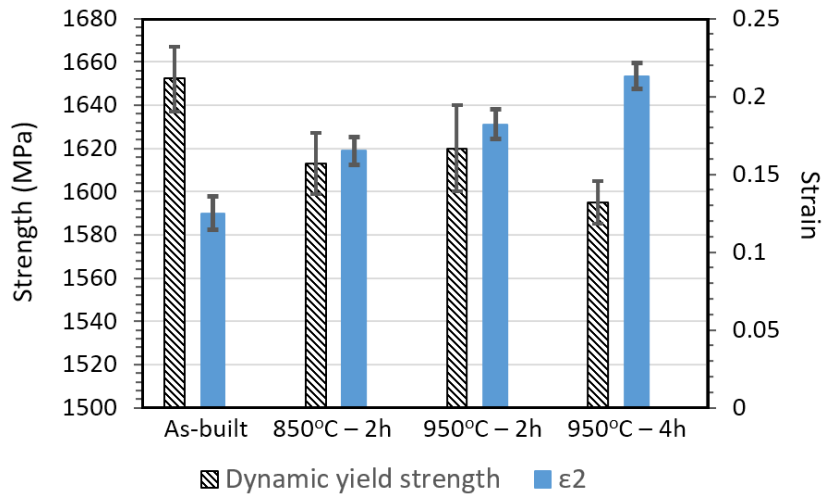


Figure 113. Dynamic mechanical properties of the as built and three annealing conditions

It is highlighted that the globularization effect occurring in the 950 °C – 4h was the key factor that greatly improved the dynamic mechanical properties, as comparable to that of the reference wrought material (see Figure 59). Besides, the lamellar microstructure with the hierarchical morphology, inherited from the  $\alpha'$  decomposition under 950 °C – 2h and 850 °C – 4h, also had the positive effect on the mechanical properties, suitable for the applications favouring higher strength over ductility. Annealing longer than 4 hours at 950 °C significantly reduced the tensile strength and thus is not advisable for general purposes.

## 6.7 – Chapter summary

In order to transform the acicular  $\alpha'$  into the  $\alpha+\beta$  with a bimodal morphology, which is desirable for the combination of high strength and good ductility, heat treatment strategies using the solid solution temperatures at 850 °C and 950 °C were designed. By these strategies, the acicular  $\alpha'$  decomposes into the lamellar  $\alpha+\beta$ , followed by the globularization to form globular grains.

The resulted  $\alpha$  phase appeared as lamellar grains with the hierarchical structure inherited from the initial microstructure, denoted as Class-I, Class-II and Class-III  $\alpha$ . It is found that higher annealing temperature would result in a coarser grain morphology and promote the globularization. In addition, increasing the holding time would gradually reduce the grain aspect ratio and shape factor, leading a significant increase of globular grains after 4 hours of annealing at 950 °C.

The thermodynamic graphical approach determined that the  $\alpha'$  decomposed into the solute-rich and solute-lean phases via spinodal decomposition before reaching the equilibrium  $\alpha+\beta$  phase by long-range solute element diffusion. The solute-rich is enriched in V (and leaned in Al), while the solute-lean is leaned in V (and enriched in Al). The solute-rich and solute-lean phases were observed as lamellar



grains coupling one another, which was also successfully expressed by the Phase Field model. At 950 °C, the solute-lean phase precipitated annealing twins to reduce the interface energy gap, which can be taken as a sign to discern the two phases in the experiments.

During the spinodal decomposition, the solute-lean remained the *hcp* structure, whereas the solute-rich may experience the *hcp* → *bcc* transformation due to the enrichment of  $\beta$  stabilizers. To reach the equilibrium state, the *hcp* solute phase precipitated V at the boundaries, leading to the equilibrium  $\alpha$  in the matrix and the equilibrium  $\beta$  at boundaries. Whereas the *bcc* solute phase precipitated Al to form the  $\alpha_s$  and resulted in the equilibrium  $\beta$  in the matrix. Therefore, the kinetic pathway of the phase transformation of  $\alpha'$  depended on the *hcp* → *bcc* transformation in the solute-rich phase.

The static globularization involves two mechanisms, namely boundary splitting and termination migration. The boundary splitting is the mass transfer from the grooves at triple points to the interphase boundaries until the lamellar grain is finally fragmented, whose duration time was calculated as 2.2 hours. This mechanism occurred at 950 °C in the solute-lean  $\alpha$  grains, which possessed the anneal twins acting as intraphase boundaries to aid the boundary splitting mechanism. The termination migration moves the solutes from the curved edges to the flat surfaces on the same grains or the adjacent grains. This second mechanism occurs on the fragmented grains after the boundary splitting to form the final globular grains, which was calculated to complete in 10.6 hours (at 950 °C). In other  $\alpha$  grains, the termination migration only resulted as the coarsening effect due to the high initial aspect ratio of the grains.

The heat treatment strategies had a direct positive impact on the mechanical properties, in both quasi-static and dynamic conditions. More importantly, the formation of bimodal microstructure at 950 °C – 4h resulted in the best mechanical properties. Further increasing the holding time was not optimised as the ductility gain would not compensate for the strength loss.

## **Chapter 7 – Conclusions and Future work**

This chapter ties together all the work and highlights the primary contributions to this thesis. Besides, potential research for future investigation is also proposed.

## **7.1 – Conclusions and contributions of the thesis**

Research into the microstructure characterization and mechanical properties of Ti-6Al-4V materials developed by SLM is best summarised in two sections. Firstly, the study of the microstructure and the mechanical properties of SLM Ti-6Al-4V in as built conditions, discussed in Chapters 4 and 5, provides insights into the heterogeneity in microstructural evolution that occurs during the layer-by-layer melting and rapid solidification process as well as when it is exposed to the high strain rate condition. This study is the first to investigate the dynamic texture evolution as subject to laser energy density to enrich the knowledge on martensite in titanium alloys. Secondly, the study of the microstructure subjected to heat treatment conditions, discussed in Chapter 6, includes information on the decomposition and the globularization process of the initial martensitic microstructure and its effect on mechanical properties.

The key contributions of the thesis are elaborated in the following sections.

### **7.1.1 – Evolution of SLM Ti-6Al-4V microstructures as subject to laser energy density**

#### *Optimised processing parameters for Ti-6Al-4V.*

SLM has shown the ability to produce quality parts with high density and low surface roughness in their as-built state. A macrostructural analysis based on the effect of laser energy density is used to achieve a processing window of optimised parameters for Ti-6Al-4V.

#### *Characterised heterogeneous microstructure of Ti-6Al-4V by SLM.*

The work demonstrates that acicular  $\alpha'$  martensite is formed in the SLM processing of Ti-6Al-4V. Thermal simulation also finds that the temperature profiles and cooling rates are favourable for the formation of prior columnar  $\beta$  phase. Thermal history of the SLM reveals the evolution of a hierarchical structure of primary, secondary and tertiary  $\alpha'$  martensite upon subsequent thermal cycles with different length scale. These martensitic structures are differently subject to auto-tempering process during cyclic thermal loadings and resulted in heterogeneity in softness, dislocation mobility and the ability to accommodate strain among these structures. This provides the possibility to improve the mechanical properties of SLM-built Ti-6Al-4V parts via regulating the evolution of the hierarchical structures during fabrication process.

#### *Novel preferred orientation of recrystallized grains under dynamic condition – The first study to investigate texture evolution under dynamic loading state.*

In the fabrication, increasing the laser energy density promotes more auto-tempering on primary  $\alpha'$  grains and more precipitation of tertiary  $\alpha'$  grains, which consequently causes more strain accommodation incompatibility between softer, less dislocated primary  $\alpha'$  and harder, more dislocated tertiary  $\alpha'$ . The localised plasticity resulting from the strain incompatibility leads to an overall brittle characteristic and decreases the ductility of SLM built Ti-6Al-4V parts. In addition, high laser energy density reduces the dislocation mobility in  $\alpha'$  martensite, resulting more piled-up dislocations along the [0001] directions. These [0001] dislocations promote the preferred texture of [0001] orientation in the DRX grains within ASBs formed under dynamic conditions, which could not be found in the samples produced by low energy densities.

*Enhanced mechanical properties of SLM Ti-6Al-4V due to the martensitic microstructure.*

The  $\alpha'$  martensite significantly improves the strength of Ti-6Al-4V under both quasi-static and dynamic conditions, but at a great expense of ductility. Under dynamic deformation, the  $\alpha'$  martensite activates {10-12} twins to accommodate the tensile strain along its c-axis and the compressive strain perpendicular to it, and also {10-11} twins to tolerate the shear strain in its 57.2°. The deformation twins play an important role in the DRX of  $\alpha'$  martensite to form the ASBs. 90% of the DRXed grains are obtained in the early stage in association with deformation twins in which TDRX mechanism occurs in the {10-12}, {10-11} and {11-22} twins, and DDRX takes place in {11-21} twins. In the untwinned grains, the  $\alpha'$  martensite recrystallizes via both DDRX and CDRX.

**7.1.2 – Decomposition and globularization of  $\alpha'$  martensite in SLM Ti-6Al-4V**

*The heat treatment design for SLM Ti-6Al-4V to obtain a bimodal microstructure.*

The heat treatment of SLM Ti-6Al-4V is designed to facilitate the decomposition of  $\alpha'$  martensite into a bimodal microstructure to achieve desirable mechanical properties. The annealing temperatures are defined to be in the solid solution range. This study shows that the final microstructure is strongly influenced by temperature and time, and the globular grains significantly increase substantially after 4 hours of annealing at 950 °C which is proven to be the best annealing strategy based on the significant enhancement on ductility while remaining high strength.

*Phase Field modelling and kinetic pathways of the decomposition of  $\alpha'$  martensite.*

The  $\alpha'$  is defined by the thermodynamic graphical technique to decompose into solute-rich and solute-lean phases via spinodal decomposition, and then transforms into equilibrium  $\alpha+\beta$  phase by long-range solute element diffusion. Phase Field model shows that high annealing temperature increases the interface energy gap between the solute-rich and solute-lean, thus initiating anneal twins in the solute-

lean phase. The solute-lean phase—which is enriched in Al,  $\alpha$  stabilizer—remains the hcp structure, whereas the solute-rich phase may experience the  $hcp \rightarrow bcc$  transformation due to the enrichment of V as a  $\beta$  stabilizer. The solute phase that is in hcp structure precipitates V to form equilibrium  $\alpha$  in the matrix and the equilibrium  $\beta$  at boundaries. By contrast, the bcc solute-rich phase precipitates Al as  $\alpha_s$  to form equilibrium  $\beta$  in the matrix.

#### Globularization process to form $\alpha$ globular grains.

In the globularization, anneal twins acts as intraphase boundaries which enable the boundary splitting mechanism to fragmentise  $\alpha$  grains via thermal grooving on boundaries along anneal twins. The fragmentised grains further evolve into globular grains by the termination migration mechanism. Duration time for the boundary splitting at 950 °C is 2.2 hours whereas the termination migration requires 10.6 hours to finish, which makes boundary splitting is more important in short annealing time.

## **7.2 – Future work**

### **7.2.1 – Controlling the heterogeneity of SLM Ti-6Al-4V microstructure for superior properties**

The heterogeneity of SLM Ti-6Al-4V microstructure is mainly caused by the thermo-plasticity and auto-tempering in the formation of  $\alpha'$  hierarchy structures, which causes undesirable properties and are needed to be minimised. However, the heterogeneity could be exploited to in a way to result superior properties by in situ decomposition of unfavourable  $\alpha'$  into lamellar  $\alpha+\beta$  phase, or by controlling the volume fraction and size of each  $\alpha'$  hierarchy structures to reduce the strain incompatibility. The key point in this hypothesis is to properly control the processing routes that can be used to modify the thermal profile of the solidified layers. If the effective thermal cycles are maintained sufficiently enough, the auto-tempering can in situ decompose the early-formed  $\alpha'$  martensites. Or can it be done by raising the temperature on the strategic cycles to control the volume fraction and grain size of certain  $\alpha'$  martensites. Besides, a following heat treatment could be further designed to achieve the target.

### **7.2.2 – Phase Field modelling on martensite evolution during Selective Laser Melting**

In this study, the Phase Field model has proven its capacity in validating the physical phenomenon and observation of  $\alpha'$  decomposition in order to aid the investigation. A new model to simulate the evolution of hierarchy structures of  $\alpha'$  martensites during the manufacturing process therefore is of importance to enrich the knowledge on martensite as well as to control the heterogeneity in the SLM Ti-6Al-4V. Furthermore, the formation-decomposition of  $\alpha'$  when being successfully simulated could

be used to precisely predict the final morphology in the heat treatment process. Thus, further investigation on Phase Field modelling is highly encouraged.

### **7.2.3 – Study on machinability of SLM Ti-6Al-4V**

It is shown that although the optimised processing window is obtained, the surface quality can only be improved to a certain degree which is not enough for aerospace industry or other high value applications. In many cases, SLM parts are often designed with a tolerance for machining to achieve the required surface finish or to optimise fitting structures. Titanium alloys is generally difficult to machine, and it becomes more so for SLM Ti-6Al-4V due to the hard and brittle  $\alpha'$  microstructure with high residual stress. This thesis provides fundamental understandings on dynamic behaviours of SLM Ti-6Al-4V as subject to different processing parameters, which could also be further extended to study the machinability the SLM built part with focuses on cutting forces, chip morphology and shear band formation in machining.

### **7.3 – Journal publication**

Do DK, Li P. The effect of laser energy input on the microstructure, physical and mechanical properties of Ti-6Al-4V alloys by selective laser melting. Virtual and Physical Prototyping. 2016 Jan 2;11(1):41-7.



---

## References

1. Attaran M. The rise of 3-D printing: The advantages of additive manufacturing over traditional manufacturing. *Business Horizons*. 2017;60(5):677-88.
2. Gisario A, Kazarian M, Martina F, Mehrpouya M. Metal additive manufacturing in the commercial aviation industry: A review. *Journal of Manufacturing Systems*. 2019;53:124-49.
3. Larrañeta E, Dominguez-Robles J, Lamprou DA. Additive Manufacturing Can Assist in the Fight Against COVID-19 and Other Pandemics and Impact on the Global Supply Chain. *3D Printing and Additive Manufacturing*. 2020.
4. Kelly SM, Kampe SL. Microstructural evolution in laser-deposited multilayer Ti-6Al-4V builds: Part II. Thermal modeling. *Metallurgical and Materials Transactions A*. 2004;35(6):1869-79.
5. Pelleg J. Chapter Three - Testing: Comparison of AM data with traditionally fabricated. In: Pelleg J, editor. *Additive and Traditionally Manufactured Components*: Elsevier; 2020. p. 49-176.
6. Wu M-W, Lai P-H, Chen J-K. Anisotropy in the impact toughness of selective laser melted Ti-6Al-4V alloy. *Materials Science and Engineering: A*. 2016;650:295-9.
7. Donachie MJ. *Titanium: a technical guide*: ASM international; 2000.
8. Thijs L, Verhaeghe F, Craeghs T, Humbeeck JV, Kruth J-P. A study of the microstructural evolution during selective laser melting of Ti-6Al-4V. *Acta Materialia*. 2010;58(9):3303-12.
9. Ouellet S, Cronin D, Worswick M. Compressive response of polymeric foams under quasi-static, medium and high strain rate conditions. *Polymer Testing*. 2006;25(6):731-43.
10. Sassi S, Tarfaoui M, Nachtane M, Ben Yahia H. Strain rate effects on the dynamic compressive response and the failure behavior of polyester matrix. *Composites Part B: Engineering*. 2019;174:107040.
11. Li Q, Xu YB, Bassim MN. Dynamic mechanical behavior of pure titanium. *Journal of Materials Processing Technology*. 2004;155-156:1889-92.
12. Odeshi AG, Bassim MN, Al-Ameeri S. Effect of heat treatment on adiabatic shear bands in a high-strength low alloy steel. *Materials Science and Engineering: A*. 2006;419(1):69-75.
13. Khan AS, Kazmi R, Farrokh B. Multiaxial and non-proportional loading responses, anisotropy and modeling of Ti-6Al-4V titanium alloy over wide ranges of strain rates and temperatures. *International Journal of Plasticity*. 2007;23(6):931-50.
14. Simonelli M, Tse YY, Tuck C. Effect of the build orientation on the mechanical properties and fracture modes of SLM Ti-6Al-4V. *Materials Science and Engineering: A*. 2014;616:1-11.

15. Vrancken B, Thijs L, Kruth J-P, Van Humbeeck J. Heat treatment of Ti6Al4V produced by Selective Laser Melting: Microstructure and mechanical properties. *Journal of Alloys and Compounds*. 2012;541:177-85.
16. Mouzakis DE. *Advanced Technologies in Manufacturing 3D-Layered Structures for Defense and Aerospace. Lamination: Theory and Application*. 2018:89.
17. Astm I. *ASTM F2792-10: standard terminology for additive manufacturing technologies*. ASTM International. 2010.
18. Shapiro AA, Borgonia J, Chen Q, Dillon R, McEnerney B, Polit-Casillas R, et al. Additive manufacturing for aerospace flight applications. *Journal of Spacecraft and Rockets*. 2016:952-9.
19. Brandt M. The role of lasers in additive manufacturing. *Laser Additive Manufacturing*. 2017:1-18.
20. Kruth J-P, Leu M-C, Nakagawa T. Progress in additive manufacturing and rapid prototyping. *CIRP Annals-Manufacturing Technology*. 1998;47(2):525-40.
21. Wysocki B, Maj P, Sitek R, Buhagiar J, Kurzydłowski KJ, Świążzkowski W. Laser and electron beam additive manufacturing methods of fabricating titanium bone implants. *Applied Sciences*. 2017;7(7):657.
22. Kruth J- P, Mercelis P, Van Vaerenbergh J, Froyen L, Rombouts M. Binding mechanisms in selective laser sintering and selective laser melting. *Rapid Prototyping Journal*. 2005;11(1):26-36.
23. Kruth J-P, Badrossamay M, Yasa E, Deckers J, Thijs L, Van Humbeeck J, editors. *Part and material properties in selective laser melting of metals. Proceedings of the 16th International Symposium on Electromachining (ISEM XVI); 2010: SHANGHAI JIAO TONG UNIV PRESS*.
24. Murr LE, Esquivel EV, Quinones SA, Gaytan SM, Lopez MI, Martinez EY, et al. Microstructures and mechanical properties of electron beam-rapid manufactured Ti–6Al–4V biomedical prototypes compared to wrought Ti–6Al–4V. *Materials Characterization*. 2009;60(2):96-105.
25. Wang C, Tan XP, Du Z, Chandra S, Sun Z, Lim CWJ, et al. Additive manufacturing of NiTi shape memory alloys using pre-mixed powders. *Journal of Materials Processing Technology*. 2019;271:152-61.
26. Vandenbroucke B, Kruth JP. Selective laser melting of biocompatible metals for rapid manufacturing of medical parts. *Rapid Prototyping Journal*. 2007.
27. Yadroitsev I, Bertrand P, Smurov I. Parametric analysis of the selective laser melting process. *Applied Surface Science*. 2007;253(19):8064-9.
28. Liu B, Li B-Q, Li Z. Selective laser remelting of an additive layer manufacturing process on AlSi10Mg. *Results in Physics*. 2019;12:982-8.
29. Kruth JP, Levy G, Klocke F, Childs THC. Consolidation phenomena in laser and powder-bed based layered manufacturing. *CIRP Annals*. 2007;56(2):730-59.
30. Zhang LC, Klemm D, Eckert J, Hao YL, Sercombe TB. Manufacture by selective laser melting and mechanical behavior of a biomedical Ti–24Nb–4Zr–8Sn alloy. *Scripta Materialia*. 2011;65(1):21-4.

31. Matthews MJ, Guss G, Khairallah SA, Rubenchik AM, Depond PJ, King WE. Denudation of metal powder layers in laser powder bed fusion processes. *Acta Materialia*. 2016;114:33-42.
32. Leuders S, Thöne M, Riemer A, Niendorf T, Tröster T, Richard HA, et al. On the mechanical behaviour of titanium alloy TiAl6V4 manufactured by selective laser melting: Fatigue resistance and crack growth performance. *International Journal of Fatigue*. 2013;48:300-7.
33. Kasperovich G, Hausmann J. Improvement of fatigue resistance and ductility of TiAl6V4 processed by selective laser melting. *Journal of Materials Processing Technology*. 2015;220:202-14.
34. Vilaro T, Colin C, Bartout J-D. As-fabricated and heat-treated microstructures of the Ti-6Al-4V alloy processed by selective laser melting. *Metallurgical and materials transactions A*. 2011;42(10):3190-9.
35. Biswas N, Ding JL, Balla VK, Field DP, Bandyopadhyay A. Deformation and fracture behavior of laser processed dense and porous Ti6Al4V alloy under static and dynamic loading. *Materials Science and Engineering: A*. 2012;549:213-21.
36. Li P-H, Guo W-G, Huang W-D, Su Y, Lin X, Yuan K-B. Thermomechanical response of 3D laser-deposited Ti-6Al-4V alloy over a wide range of strain rates and temperatures. *Materials Science and Engineering: A*. 2015;647:34-42.
37. Cain V, Thijs L, Van Humbeeck J, Van Hooreweder B, Knutsen R. Crack propagation and fracture toughness of Ti6Al4V alloy produced by selective laser melting. *Additive Manufacturing*. 2015;5:68-76.
38. Leuders S, Lieneke T, Lammers S, Tröster T, Niendorf T. On the fatigue properties of metals manufactured by selective laser melting – The role of ductility. *Journal of Materials Research*. 2014;29(17):1911-9.
39. Facchini L, Magalini E, Robotti P, Molinari A, Höges S, Wissenbach K. Ductility of a Ti-6Al-4V alloy produced by selective laser melting of prealloyed powders. *Rapid Prototyping Journal*. 2010.
40. Gong H, Rafi K, Gu H, Janaki Ram GD, Starr T, Stucker B. Influence of defects on mechanical properties of Ti-6Al-4V components produced by selective laser melting and electron beam melting. *Materials & Design*. 2015;86:545-54.
41. Mertens A, Reginster S, Paydas H, Contrepolis Q, Dormal T, Lemaire O, et al. Mechanical properties of alloy Ti-6Al-4V and of stainless steel 316L processed by selective laser melting: influence of out-of-equilibrium microstructures. *Powder Metallurgy*. 2014;57(3):184-9.
42. Hollander DA, von Walter M, Wirtz T, Sellei R, Schmidt-Rohlfing B, Paar O, et al. Structural, mechanical and in vitro characterization of individually structured Ti-6Al-4V produced by direct laser forming. *Biomaterials*. 2006;27(7):955-63.
43. Qiu C, Adkins NJE, Attallah MM. Microstructure and tensile properties of selectively laser-melted and of HIPed laser-melted Ti-6Al-4V. *Materials Science and Engineering: A*. 2013;578:230-9.
44. Xu W, Lui EW, Pateras A, Qian M, Brandt M. In situ tailoring microstructure in additively manufactured Ti-6Al-4V for superior mechanical performance. *Acta Materialia*. 2017;125:390-400.
45. Xu W, Brandt M, Sun S, Elambasseril J, Liu Q, Latham K, et al. Additive manufacturing of strong and ductile Ti-6Al-4V by selective laser melting via in situ martensite decomposition. *Acta Materialia*. 2015;85:74-84.

- 
46. Galarraga H, Lados DA, Dehoff RR, Kirka MM, Nandwana P. Effects of the microstructure and porosity on properties of Ti-6Al-4V ELI alloy fabricated by electron beam melting (EBM). *Additive Manufacturing*. 2016;10:47-57.
  47. Kobryn P, Moore E, Semiatin S. The effect of laser power and traverse speed on microstructure, porosity, and build height in laser-deposited Ti-6Al-4V. *Scripta Materialia*. 2000;43(4):299-305.
  48. Yang Y, Man HC. Microstructure evolution of laser clad layers of W–C–Co alloy powders<sup>1</sup>This paper is sponsored by The Natural Science Foundation of Guangdong Province, China.1. *Surface and Coatings Technology*. 2000;132(2):130-6.
  49. Choi J, Chang Y. Characteristics of laser aided direct metal/material deposition process for tool steel. *International Journal of Machine Tools and Manufacture*. 2005;45(4):597-607.
  50. Tammas-Williams S, Zhao H, Léonard F, Derguti F, Todd I, Prangnell PB. XCT analysis of the influence of melt strategies on defect population in Ti-6Al-4V components manufactured by Selective Electron Beam Melting. *Materials Characterization*. 2015;102:47-61.
  51. Li P, Warner DH, Fatemi A, Phan N. Critical assessment of the fatigue performance of additively manufactured Ti-6Al-4V and perspective for future research. *International Journal of Fatigue*. 2016;85:130-43.
  52. Kruth JP, Froyen L, Van Vaerenbergh J, Mercelis P, Rombouts M, Lauwers B. Selective laser melting of iron-based powder. *Journal of Materials Processing Technology*. 2004;149(1):616-22.
  53. Mumtaz K, Hopkinson N. Top surface and side roughness of Inconel 625 parts processed using selective laser melting. *Rapid Prototyping Journal*. 2009.
  54. Simchi A. The role of particle size on the laser sintering of iron powder. *Metallurgical and Materials Transactions B*. 2004;35(5):937-48.
  55. Wang D, Liu Y, Yang Y, Xiao D. Theoretical and experimental study on surface roughness of 316L stainless steel metal parts obtained through selective laser melting. *Rapid Prototyping Journal*. 2016.
  56. Resch M, Alexander FHK, Dieter S, editors. Laser-assisted generating of three-dimensional parts by the blown powder process. *ProcSPIE*; 2001.
  57. Zhai Y, Galarraga H, Lados DA. Microstructure, static properties, and fatigue crack growth mechanisms in Ti-6Al-4V fabricated by additive manufacturing: LENS and EBM. *Engineering Failure Analysis*. 2016;69:3-14.
  58. Mahamood RM, Akinlabi ET, editors. Effect of laser power on surface finish during laser metal deposition process. *Proceedings of the World Congress on Engineering and Computer Science*; 2014.
  59. Kaplan A, Groboth G. Process analysis of laser beam cladding. *J Manuf Sci Eng*. 2001;123(4):609-14.
  60. Mazumder J, Dutta D, Kikuchi N, Ghosh A. Closed loop direct metal deposition: art to part. *Optics and Lasers in Engineering*. 2000;34(4):397-414.
  61. Rafi HK, Karthik NV, Gong H, Starr TL, Stucker BE. Microstructures and Mechanical Properties of Ti6Al4V Parts Fabricated by Selective Laser Melting and Electron Beam Melting. *Journal of Materials Engineering and Performance*. 2013;22(12):3872-83.

- 
62. Banerjee D, Williams JC. Perspectives on Titanium Science and Technology. *Acta Materialia*. 2013;61(3):844-79.
63. Lütjering G, Williams JC. *Titanium*: Springer Science & Business Media; 2007.
64. Balachandran S, Kumar S, Banerjee D. On recrystallization of the  $\alpha$  and  $\beta$  phases in titanium alloys. *Acta Materialia*. 2017;131:423-34.
65. Shao H, Shan D, Zhao Y, Ge P, Zeng W. Accordance between fracture toughness and strength difference in TC21 titanium alloy with equiaxed microstructure. *Materials Science and Engineering: A*. 2016;664:10-6.
66. Banerjee R, Bhattacharyya D, Collins P, Viswanathan G, Fraser H. Precipitation of grain boundary  $\alpha$  in a laser deposited compositionally graded Ti–8Al–xV alloy—an orientation microscopy study. *Acta materialia*. 2004;52(2):377-85.
67. Kelly SM. Thermal and microstructure modeling of metal deposition processes with application to Ti-6Al-4V: Virginia Tech; 2004.
68. Shi R, Ma N, Wang Y. Predicting equilibrium shape of precipitates as function of coherency state. *Acta Materialia*. 2012;60(10):4172-84.
69. Barton NR, Dawson PR. On the spatial arrangement of lattice orientations in hot-rolled multiphase titanium. *Modelling and Simulation in Materials Science and Engineering*. 2001;9(5):433-63.
70. He D, Zhu JC, Zaefferer S, Raabe D, Liu Y, Lai ZL, et al. Influences of deformation strain, strain rate and cooling rate on the Burgers orientation relationship and variants morphology during  $\beta \rightarrow \alpha$  phase transformation in a near  $\alpha$  titanium alloy. *Materials Science and Engineering: A*. 2012;549:20-9.
71. Tiley J, Searles T, Lee E, Kar S, Banerjee R, Russ JC, et al. Quantification of microstructural features in  $\alpha/\beta$  titanium alloys. *Materials Science and Engineering: A*. 2004;372(1):191-8.
72. Stefanescu D, Ruxanda R. Solidification Structure of Titanium Alloys. 92004. p. 116-26.
73. Beladi H, Chao Q, Rohrer GS. Variant selection and intervariant crystallographic planes distribution in martensite in a Ti–6Al–4V alloy. *Acta Materialia*. 2014;80:478-89.
74. Banerjee D, Williams J. Perspectives on titanium science and technology. *Acta Materialia*. 2013;61(3):844-79.
75. Furuhashi T, Takagi S, Watanabe H, Maki T. Crystallography of grain boundary  $\alpha$  precipitates in a  $\beta$  titanium alloy. *Metallurgical and Materials Transactions A*. 1996;27(6):1635-46.
76. Bhattacharyya D, Viswanathan GB, Fraser HL. Crystallographic and morphological relationships between  $\beta$  phase and the Widmanstätten and allotriomorphic  $\alpha$  phase at special  $\beta$  grain boundaries in an  $\alpha/\beta$  titanium alloy. *Acta Materialia*. 2007;55(20):6765-78.
77. Liu S, Shin YC. Additive manufacturing of Ti6Al4V alloy: A review. *Materials & Design*. 2019;164:107552.
78. Ahmed T, Rack HJ. Phase transformations during cooling in  $\alpha+\beta$  titanium alloys. *Materials Science and Engineering: A*. 1998;243(1):206-11.

- 
79. Gil Mur FX, Rodríguez D, Planell JA. Influence of tempering temperature and time on the  $\alpha'$ -Ti-6Al-4V martensite. *Journal of Alloys and Compounds*. 1996;234(2):287-9.
80. Reisgen U, Olschok S, Sharma R, Gach S. Influence on martensite-start-temperature and volume expansion of low-transformation-temperature materials used for residual stress relief in beam welding. *Materialwissenschaft und Werkstofftechnik*. 2017;48(12):1276-82.
81. Tahara M, Kim HY, Inamura T, Hosoda H, Miyazaki S. Lattice modulation and superelasticity in oxygen-added  $\beta$ -Ti alloys. *Acta Materialia*. 2011;59(16):6208-18.
82. Yano T, Murakami Y, Shindo D, Kuramoto S. Study of the nanostructure of Gum Metal using energy-filtered transmission electron microscopy. *Acta Materialia*. 2009;57(2):628-33.
83. Wang T, Zhu YY, Zhang SQ, Tang HB, Wang HM. Grain morphology evolution behavior of titanium alloy components during laser melting deposition additive manufacturing. *Journal of Alloys and Compounds*. 2015;632:505-13.
84. Wu X, Liang J, Mei J, Mitchell C, Goodwin PS, Voice W. Microstructures of laser-deposited Ti-6Al-4V. *Materials & Design*. 2004;25(2):137-44.
85. Wang F, Mei J, Jiang H, Wu X. Laser fabrication of Ti6Al4V/TiC composites using simultaneous powder and wire feed. *Materials Science and Engineering: A*. 2007;445-446:461-6.
86. Simonelli M, Tse YY, Tuck C. On the Texture Formation of Selective Laser Melted Ti-6Al-4V. *Metallurgical and Materials Transactions A*. 2014;45(6):2863-72.
87. Strantz M, Vafadari R, De Baere D, Vrancken B, Van Paepegem W, Vandendael I, et al. Fatigue of Ti6Al4V structural health monitoring systems produced by selective laser melting. *Materials*. 2016;9(2):106.
88. Grong O. *Metallurgical modelling of welding*. Institute of Materials, 1 Carlton House Terrace, London, SW 1 Y 5 DB, UK, 1997 605. 1997.
89. Parry L, Ashcroft IA, Wildman RD. Understanding the effect of laser scan strategy on residual stress in selective laser melting through thermo-mechanical simulation. *Additive Manufacturing*. 2016;12:1-15.
90. Antonysamy AA, Meyer J, Prangnell PB. Effect of build geometry on the  $\beta$ -grain structure and texture in additive manufacture of Ti6Al4V by selective electron beam melting. *Materials Characterization*. 2013;84:153-68.
91. Do DK, Li P. The effect of laser energy input on the microstructure, physical and mechanical properties of Ti-6Al-4V alloys by selective laser melting. *Virtual and Physical Prototyping*. 2016;11(1):41-7.
92. Yu J, Rombouts M, Maes G, Motmans F. Material Properties of Ti6Al4V Parts Produced by Laser Metal Deposition. *Physics Procedia*. 2012;39:416-24.
93. Ali H, Ma L, Ghadbeigi H, Mumtaz K. In-situ residual stress reduction, martensitic decomposition and mechanical properties enhancement through high temperature powder bed pre-heating of Selective Laser Melted Ti6Al4V. *Materials Science and Engineering: A*. 2017;695:211-20.
94. Yang J, Yu H, Yin J, Gao M, Wang Z, Zeng X. Formation and control of martensite in Ti-6Al-4V alloy produced by selective laser melting. *Materials & Design*. 2016;108:308-18.

95. Agius D, Kourousis KI, Wallbrink C. A review of the as-built SLM Ti-6Al-4V mechanical properties towards achieving fatigue resistant designs. *Metals*. 2018;8(1):75.
96. Verleysen P, Peirs J. Quasi-static and high strain rate fracture behaviour of Ti6Al4V. *International Journal of Impact Engineering*. 2017;108:370-88.
97. Zener C, Hollomon JH. Effect of strain rate upon plastic flow of steel. *Journal of Applied physics*. 1944;15(1):22-32.
98. Meyers MA, Xu YB, Xue Q, Pérez-Prado MT, McNelley TR. Microstructural evolution in adiabatic shear localization in stainless steel. *Acta Materialia*. 2003;51(5):1307-25.
99. Lins JFC, Sandim HRZ, Kestenbach HJ, Raabe D, Vecchio KS. A microstructural investigation of adiabatic shear bands in an interstitial free steel. *Materials Science and Engineering: A*. 2007;457(1):205-18.
100. Xue Q, Gray GT. Development of adiabatic shear bands in annealed 316L stainless steel: Part I. Correlation between evolving microstructure and mechanical behavior. *Metallurgical and Materials Transactions A*. 2006;37(8):2435-46.
101. Pérez-Prado MT, Hines JA, Vecchio KS. Microstructural evolution in adiabatic shear bands in Ta and Ta-W alloys. *Acta Materialia*. 2001;49(15):2905-17.
102. Nesterenko VF, Meyers MA, LaSalvia JC, Bondar MP, Chen YJ, Lukyanov YL. Shear localization and recrystallization in high-strain, high-strain-rate deformation of tantalum. *Materials Science and Engineering: A*. 1997;229(1):23-41.
103. Xu YB, Zhong WL, Chen YJ, Shen LT, Liu Q, Bai YL, et al. Shear localization and recrystallization in dynamic deformation of 8090 Al-Li alloy. *Materials Science and Engineering: A*. 2001;299(1):287-95.
104. Zheng Y, Zeng W, Wang Y, Zhou D, Gao X. High strain rate compression behavior of a heavily stabilized beta titanium alloy: Kink deformation and adiabatic shearing. *Journal of Alloys and Compounds*. 2017;708:84-92.
105. Li Z, Wang B, Zhao S, Valiev RZ, Vecchio KS, Meyers MA. Dynamic deformation and failure of ultrafine-grained titanium. *Acta Materialia*. 2017;125:210-8.
106. Yang Y, Jiang L, Xu Z, Wang Z. An examination of adiabatic shearing behavior in ZK60 alloy with different states of heat treatment. *Materials Science and Engineering: A*. 2017;685:57-64.
107. Ran C, Chen P, Sheng Z, Li J, Zhang W. Microstructural Evolution in High-Strain-Rate Deformation of Ti-5Al-5Mo-5V-1Cr-1Fe Alloy. *Materials*. 2018;11(5):839.
108. Rittel D, Osovski S. Dynamic failure by adiabatic shear banding. *International Journal of Fracture*. 2010;162(1):177-85.
109. Rittel D, Landau P, Venkert A. Dynamic Recrystallization as a Potential Cause for Adiabatic Shear Failure. *Physical Review Letters*. 2008;101(16):165501.
110. Xu Y, Zhang J, Bai Y, Meyers MA. Shear Localization in Dynamic Deformation: Microstructural Evolution. *Metallurgical and Materials Transactions A*. 2008;39(4):811.



111. Zhang W, He L, Lu Z, Kennedy GB, Thadhani NN, Li P. Microstructural characteristics and formation mechanism of adiabatic shear bands in Al–Zn–Mg–Cu alloy under dynamic shear loading. *Materials Science and Engineering: A*. 2020;791:139430.
112. Murr L, Pizana C. Dynamic recrystallization: the dynamic deformation regime. *Metallurgical and materials transactions A*. 2007;38(11):2611-28.
113. Yang Y, Wang B. Dynamic recrystallization in adiabatic shear band in  $\alpha$ -titanium. *Materials Letters*. 2006;60(17-18):2198-202.
114. Hines JA, Vecchio KS, Ahzi S. A model for microstructure evolution in adiabatic shear bands. *Metallurgical and Materials Transactions A*. 1998;29(1):191-203.
115. Sakai T, Belyakov A, Kaibyshev R, Miura H, Jonas JJ. Dynamic and post-dynamic recrystallization under hot, cold and severe plastic deformation conditions. *Progress in Materials Science*. 2014;60:130-207.
116. Yin X-Q, Park C-H, Li Y-F, Ye W-J, Zuo Y-T, Lee S-W, et al. Mechanism of continuous dynamic recrystallization in a 50Ti-47Ni-3Fe shape memory alloy during hot compressive deformation. *Journal of Alloys and Compounds*. 2017;693:426-31.
117. Abedi HR, Zarei Hanzaki A, Liu Z, Xin R, Haghdadi N, Hodgson PD. Continuous dynamic recrystallization in low density steel. *Materials & Design*. 2017;114:55-64.
118. Cram DG, Zurob HS, Brechet YJM, Hutchinson CR. Modelling discontinuous dynamic recrystallization using a physically based model for nucleation. *Acta Materialia*. 2009;57(17):5218-28.
119. Cram DG, Fang XY, Zurob HS, Bréchet YJM, Hutchinson CR. The effect of solute on discontinuous dynamic recrystallization. *Acta Materialia*. 2012;60(18):6390-404.
120. Peng J, Zhang Z, Li Y, Zhou W, Wu Y. Twinning-induced dynamic recrystallization and micro-plastic mechanism during hot-rolling process of a magnesium alloy. *Materials Science and Engineering: A*. 2017;699:99-105.
121. Ma Q, Li B, Marin EB, Horstemeyer SJ. Twinning-induced dynamic recrystallization in a magnesium alloy extruded at 450°C. *Scripta Materialia*. 2011;65(9):823-6.
122. Dogan E, Vaughan MW, Wang SJ, Karaman I, Proust G. Role of starting texture and deformation modes on low-temperature shear formability and shear localization of Mg–3Al–1Zn alloy. *Acta Materialia*. 2015;89:408-22.
123. Zhang HK, Xiao H, Fang XW, Zhang Q, Logé RE, Huang K. A critical assessment of experimental investigation of dynamic recrystallization of metallic materials. *Materials & Design*. 2020;193:108873.
124. Boyer RR. An overview on the use of titanium in the aerospace industry. *Materials Science and Engineering: A*. 1996;213(1):103-14.
125. Peters M, Kumpfert J, Ward CH, Leyens C. Titanium Alloys for Aerospace Applications. *Advanced Engineering Materials*. 2003;5(6):419-27.
126. Edwards P, Ramulu M. Fatigue performance evaluation of selective laser melted Ti–6Al–4V. *Materials Science and Engineering: A*. 2014;598:327-37.

127. Koike M, Greer P, Owen K, Lilly G, Murr LE, Gaytan SM, et al. Evaluation of titanium alloys fabricated using rapid prototyping technologies—electron beam melting and laser beam melting. *Materials*. 2011;4(10):1776-92.
128. Ramoso M, Booyen G, Ngonda T, Chikwanda H, editors. Mechanical properties of direct laser sintered Ti-6Al-4V. *Materials Science and Technology Conference (MS&T)*; 2011.
129. Rafi HK, Starr TL, Stucker BE. A comparison of the tensile, fatigue, and fracture behavior of Ti-6Al-4V and 15-5 PH stainless steel parts made by selective laser melting. *The International Journal of Advanced Manufacturing Technology*. 2013;69(5):1299-309.
130. Martinez F, Murr LE, Ramirez A, Lopez MI, Gaytan SM. Dynamic deformation and adiabatic shear microstructures associated with ballistic plug formation and fracture in Ti-6Al-4V targets. *Materials Science and Engineering: A*. 2007;454-455:581-9.
131. Nemat-Nasser S, Guo W-G, Nesterenko VF, Indrakanti SS, Gu Y-B. Dynamic response of conventional and hot isostatically pressed Ti-6Al-4V alloys: experiments and modeling. *Mechanics of Materials*. 2001;33(8):425-39.
132. Liao S-c, Duffy J. Adiabatic shear bands in a Ti-6Al-4V titanium alloy. *Journal of the Mechanics and Physics of Solids*. 1998;46(11):2201-31.
133. da Silva MG, Ramesh KT. The rate-dependent deformation and localization of fully dense and porous Ti-6Al-4V. *Materials Science and Engineering: A*. 1997;232(1):11-22.
134. Fadida R, Rittel D, Shirizly A. Dynamic Mechanical Behavior of Additively Manufactured Ti6Al4V With Controlled Voids. *Journal of Applied Mechanics*. 2015;82(4).
135. Ramezani M, Flores-Johnson E, Shen LM, Neitzert T. High Strain Rate Compressive Behaviour of Selective Laser Melted Ti-6Al-4V. *Materials Science Forum*. 2017;890:323-6.
136. Pang Z, Liu Y, Li M, Zhu C, Li S, Wang Y, et al. Influence of process parameter and strain rate on the dynamic compressive properties of selective laser-melted Ti-6Al-4V alloy. *Applied Physics A*. 2019;125(2):90.
137. Mohammadhosseini A, Masood S, Fraser D, Jahedi M. Dynamic compressive behaviour of Ti-6Al-4V alloy processed by electron beam melting under high strain rate loading. *Advances in Manufacturing*. 2015;3(3):232-43.
138. Ding R, Guo ZX, Wilson A. Microstructural evolution of a Ti-6Al-4V alloy during thermomechanical processing. *Materials Science and Engineering: A*. 2002;327(2):233-45.
139. Liang X, Liu Z, Wang B. Dynamic recrystallization characterization in Ti-6Al-4V machined surface layer with process-microstructure-property correlations. *Applied Surface Science*. 2020;530:147184.
140. Semiatin S. An overview of the thermomechanical processing of  $\alpha/\beta$  titanium alloys: current status and future research opportunities. *Metallurgical and Materials Transactions A*. 2020:1-33.
141. Jhabvala J, Boillat E, Antignac T, Glardon R. On the effect of scanning strategies in the selective laser melting process. *Virtual and Physical Prototyping*. 2010;5(2):99-109.
142. Engler O, Randle V. Introduction to texture analysis: macrotexture, microtexture, and orientation mapping: CRC press; 2009.

- 
143. Wang YN, Huang JC. Texture analysis in hexagonal materials. *Materials Chemistry and Physics*. 2003;81(1):11-26.
144. Zhao H, Wang F, Li Y, Xia W. Experimental and numerical analysis of gas entrapment defects in plate ADC12 die castings. *Journal of materials processing technology*. 2009;209(9):4537-42.
145. Simchi A. Direct laser sintering of metal powders: Mechanism, kinetics and microstructural features. *Materials Science and Engineering: A*. 2006;428(1):148-58.
146. Rombouts M, Kruth J-P, Froyen L, Mercelis P. Fundamentals of selective laser melting of alloyed steel powders. *CIRP Annals-Manufacturing Technology*. 2006;55(1):187-92.
147. Campanelli SL, Angelastro A, Ludovico AD, Contuzzi N. Capabilities and performances of the selective laser melting process: INTECH Open Access Publisher; 2010.
148. Kruth J-P, Badrossamay M, Yasa E, Deckers J, Thijs L, Van Humbeeck J, editors. Part and material properties in selective laser melting of metals. *Proceedings of the 16th International Symposium on Electromachining*; 2010.
149. Tolochko Nikolay K, Mozzharov Sergei E, Yadroitsev Igor A, Laoui T, Froyen L, Titov Victor I, et al. Balling processes during selective laser treatment of powders. *Rapid Prototyping Journal*. 2004;10(2):78-87.
150. Kruth J-P, Mercelis P, Vaerenbergh JV, Froyen L, Rombouts M. Binding mechanisms in selective laser sintering and selective laser melting. *Rapid prototyping journal*. 2005;11(1):26-36.
151. Taha M, Yousef A, Gany K, Sabour H. On selective laser melting of ultra high carbon steel: Effect of scan speed and post heat treatment. *Materialwissenschaft und Werkstofftechnik*. 2012;43(11):913-23.
152. Thijs L, Verhaeghe F, Craeghs T, Van Humbeeck J, Kruth J-P. A study of the microstructural evolution during selective laser melting of Ti-6Al-4V. *Acta Materialia*. 2010;58(9):3303-12.
153. Yasa E, Deckers J, Kruth J-P. The investigation of the influence of laser re-melting on density, surface quality and microstructure of selective laser melting parts. *Rapid Prototyping Journal*. 2011;17(5):312-27.
154. Bontha S, Klingbeil NW, Kobryn PA, Fraser HL. Thermal process maps for predicting solidification microstructure in laser fabrication of thin-wall structures. *Journal of Materials Processing Technology*. 2006;178(1):135-42.
155. Al-Bermani SS, Blackmore ML, Zhang W, Todd I. The Origin of Microstructural Diversity, Texture, and Mechanical Properties in Electron Beam Melted Ti-6Al-4V. *Metallurgical and Materials Transactions A*. 2010;41(13):3422-34.
156. Verhaeghe F, Craeghs T, Heulens J, Pandelaers L. A pragmatic model for selective laser melting with evaporation. *Acta Materialia*. 2009;57(20):6006-12.
157. Kobryn PA, Semiatin SL. Microstructure and texture evolution during solidification processing of Ti-6Al-4V. *Journal of Materials Processing Technology*. 2003;135(2):330-9.
158. Qian L, Mei J, Liang J, Wu X. Influence of position and laser power on thermal history and microstructure of direct laser fabricated Ti-6Al-4V samples. *Materials science and technology*. 2005;21(5):597-605.

- 
159. Mazumder J, Schifferer A, Choi J. Direct materials deposition: designed macro and microstructure. *Material Research Innovations*. 1999;3(3):118-31.
160. Bontha S, Klingbeil NW, Kobryn PA, Fraser HL. Effects of process variables and size-scale on solidification microstructure in beam-based fabrication of bulky 3D structures. *Materials Science and Engineering: A*. 2009;513-514:311-8.
161. Kou S. *Welding metallurgy*. New Jersey, USA. 2003:431-46.
162. David SA, Vitek JM. Correlation between solidification parameters and weld microstructures. *International Materials Reviews*. 1989;34(1):213-45.
163. Humbert M, Wagner F, Moustahfid H, Esling C. Determination of the orientation of a parent  $\beta$  grain from the orientations of the inherited  $\alpha$  plates in the phase transformation from body-centred cubic to hexagonal close packed. *Journal of applied crystallography*. 1995;28(5):571-6.
164. Glavicic M, Kobryn P, Bieler T, Semiatin S. An automated method to determine the orientation of the high-temperature beta phase from measured EBSD data for the low-temperature alpha-phase in Ti-6Al-4V. *Materials Science and Engineering: A*. 2003;351(1):258-64.
165. Zhao X, Li S, Zhang M, Liu Y, Sercombe TB, Wang S, et al. Comparison of the microstructures and mechanical properties of Ti-6Al-4V fabricated by selective laser melting and electron beam melting. *Materials & Design*. 2016;95:21-31.
166. Kobryn P, Semiatin S. Microstructure and texture evolution during solidification processing of Ti-6Al-4V. *Journal of Materials Processing Technology*. 2003;135(2):330-9.
167. Al-Bermani S, Blackmore M, Zhang W, Todd I. The origin of microstructural diversity, texture, and mechanical properties in electron beam melted Ti-6Al-4V. *Metallurgical and materials transactions a*. 2010;41(13):3422-34.
168. Simonelli M, Tse Y, Tuck C, editors. *Further Understanding of Ti6Al4V Selective Laser Melting Using Texture Analysis*. Proceedings of 23rd Annual International Solid Freeform Fabrication Symposium, Austin, TX; 2012.
169. Roberts I, Wang C, Esterlein R, Stanford M, Mynors D. A three-dimensional finite element analysis of the temperature field during laser melting of metal powders in additive layer manufacturing. *International Journal of Machine Tools and Manufacture*. 2009;49(12):916-23.
170. Murr L, Quinones S, Gaytan S, Lopez M, Rodela A, Martinez E, et al. Microstructure and mechanical behavior of Ti-6Al-4V produced by rapid-layer manufacturing, for biomedical applications. *Journal of the mechanical behavior of biomedical materials*. 2009;2(1):20-32.
171. Podzorov V, Kim BG, Kiryukhin V, Gershenson ME, Cheong SW. Martensitic accommodation strain and the metal-insulator transition in manganites. *Physical Review B*. 2001;64(14):140406.
172. Matsuda H, Mizuno R, Funakawa Y, Seto K, Matsuoka S, Tanaka Y. Effects of auto-tempering behaviour of martensite on mechanical properties of ultra high strength steel sheets. *Journal of Alloys and Compounds*. 2013;577:S661-S7.
173. Ramesh Babu S, Nyysönen T, Jaskari M, Järvenpää A, Davis TP, Pallaspuro S, et al. Observations on the Relationship between Crystal Orientation and the Level of Auto-Tempering in an As-Quenched Martensitic Steel. *Metals*. 2019;9(12):1255.

- 
174. Lütjering G, Williams JC. Titanium: Springer; 2003.
175. Facchini L, Magalini E, Robotti P, Molinari A, Höges S, Wissenbach K. Ductility of a Ti-6Al-4V alloy produced by selective laser melting of prealloyed powders. *Rapid Prototyping Journal*. 2010;16(6):450-9.
176. Whang SH. Introduction. In: Whang SH, editor. *Nanostructured Metals and Alloys*: Woodhead Publishing; 2011. p. xxi-xxxv.
177. Kurdjumov G, Maksimova OJDANS. Kinetics of austenite to martensite transformation at low temperatures. 1948;61(1):83-6.
178. Ortín J, Planes A. Thermodynamics of thermoelastic martensitic transformations. *Acta Metallurgica*. 1989;37(5):1433-41.
179. Li C-n, Yuan G, Ji F-q, Ren D-s, Wang G-d. Effects of auto-tempering on microstructure and mechanical properties in hot rolled plain C-Mn dual phase steels. *Materials Science and Engineering: A*. 2016;665:98-107.
180. Moridi A, Demir AG, Caprio L, Hart AJ, Previtali B, Colosimo BM. Deformation and failure mechanisms of Ti-6Al-4V as built by selective laser melting. *Materials Science and Engineering: A*. 2019;768:138456.
181. Nishibata T, Kojima N. Effect of quenching rate on hardness and microstructure of hot-stamped steel. *Journal of Alloys and Compounds*. 2013;577:S549-S54.
182. Chang ZY, Li YJ, Wu D. Enhanced ductility and toughness in 2000 MPa grade press hardening steels by auto-tempering. *Materials Science and Engineering: A*. 2020;784:139342.
183. Philippart I, Rack HJ. High temperature dynamic yielding in metastable Ti-6.8Mo-4.5F-1.5Al. *Materials Science and Engineering: A*. 1998;243(1):196-200.
184. Staker MR. The relation between adiabatic shear instability strain and material properties. *Acta Metallurgica*. 1981;29(4):683-9.
185. Bai YL. Thermo-plastic instability in simple shear. *Journal of the Mechanics and Physics of Solids*. 1982;30(4):195-207.
186. Xu YB, Liu L, Yu JQ, Shen LT, Bai YL. Thermoplastic shear localisation in titanium alloys during dynamic deformation. *Materials Science and Technology*. 2000;16(6):609-11.
187. Hattar K. 8 - Deformation structures including twins in nanograined pure metals. In: Whang SH, editor. *Nanostructured Metals and Alloys*: Woodhead Publishing; 2011. p. 213-42.
188. Salem AA, Kalidindi SR, Doherty RD. Strain hardening of titanium: role of deformation twinning. *Acta Materialia*. 2003;51(14):4225-37.
189. Wang T, Li B, Li M, Li Y, Wang Z, Nie Z. Effects of strain rates on deformation twinning behavior in  $\alpha$ -titanium. *Materials Characterization*. 2015;106:218-25.
190. Salem AA, Kalidindi SR, Semiatin SL. Strain hardening due to deformation twinning in  $\alpha$ -titanium: Constitutive relations and crystal-plasticity modeling. *Acta Materialia*. 2005;53(12):3495-502.

191. Chun YB, Yu SH, Semiatin SL, Hwang SK. Effect of deformation twinning on microstructure and texture evolution during cold rolling of CP-titanium. *Materials Science and Engineering: A*. 2005;398(1):209-19.
192. Yoo MH. Slip, twinning, and fracture in hexagonal close-packed metals. *Metallurgical Transactions A*. 1981;12(3):409-18.
193. Wang L, Barabash R, Bieler T, Liu W, Eisenlohr P. Study of  $\{11\bar{2}1\}$  twinning in  $\alpha$ -Ti by EBSD and Laue Microdiffraction. *Metallurgical and Materials Transactions A*. 2013;44(8):3664-74.
194. Qin H, Jonas JJ, Yu H, Brodusch N, Gauvin R, Zhang X. Initiation and accommodation of primary twins in high-purity titanium. *Acta Materialia*. 2014;71:293-305.
195. Chichili DR, Ramesh KT, Hemker KJ. The high-strain-rate response of alpha-titanium: experiments, deformation mechanisms and modeling. *Acta Materialia*. 1998;46(3):1025-43.
196. Gurao NP, Kapoor R, Suwas S. Deformation behaviour of commercially pure titanium at extreme strain rates. *Acta Materialia*. 2011;59(9):3431-46.
197. Song S, Gray III G. Structural interpretation of the nucleation and growth of deformation twins in Zr and Ti—II. Tem study of twin morphology and defect reactions during twinning. *Acta metallurgica et materialia*. 1995;43(6):2339-50.
198. Chun Y, Yu S, Semiatin S, Hwang S. Effect of deformation twinning on microstructure and texture evolution during cold rolling of CP-titanium. *Materials Science and Engineering: A*. 2005;398(1-2):209-19.
199. Yang H, Xu Y, Seki Y, Nesterenko VF, Meyers MA. Analysis and characterization by electron backscatter diffraction of microstructural evolution in the adiabatic shear bands in Fe–Cr–Ni alloys. *Journal of Materials Research*. 2009;24(8):2617-27.
200. Jiang Y, Chen Z, Zhan C, Chen T, Wang R, Liu C. Adiabatic shear localization in pure titanium deformed by dynamic loading: Microstructure and microtexture characteristic. *Materials Science and Engineering: A*. 2015;640:436-42.
201. Rogers HC. Adiabatic plastic deformation. *Annual Review of Materials Science*. 1979;9(1):283-311.
202. Surendar A, Samavatian V, Maselena A, Ibatova AZ, Samavatian M. Effect of solder layer thickness on thermo-mechanical reliability of a power electronic system. *Journal of Materials Science: Materials in Electronics*. 2018;29(17):15249-58.
203. Calcagnotto M, Ponge D, Demir E, Raabe D. Orientation gradients and geometrically necessary dislocations in ultrafine grained dual-phase steels studied by 2D and 3D EBSD. *Materials Science and Engineering: A*. 2010;527(10):2738-46.
204. Wei D-X, Koizumi Y, Nagasako M, Chiba A. Refinement of lamellar structures in Ti-Al alloy. *Acta Materialia*. 2017;125:81-97.
205. Chen Y-W, Tsai Y-T, Tung P-Y, Tsai S-P, Chen C-Y, Wang S-H, et al. Phase quantification in low carbon Nb-Mo bearing steel by electron backscatter diffraction technique coupled with kernel average misorientation. *Materials Characterization*. 2018;139:49-58.

- 
206. Liu L, Ding Q, Zhong Y, Zou J, Wu J, Chiu Y-L, et al. Dislocation network in additive manufactured steel breaks strength–ductility trade-off. *Materials Today*. 2018;21(4):354-61.
207. Yan CK, Feng AH, Qu SJ, Cao GJ, Sun JL, Shen J, et al. Dynamic recrystallization of titanium: Effect of pre-activated twinning at cryogenic temperature. *Acta Materialia*. 2018;154:311-24.
208. Guan D, Rainforth WM, Ma L, Wynne B, Gao J. Twin recrystallization mechanisms and exceptional contribution to texture evolution during annealing in a magnesium alloy. *Acta Materialia*. 2017;126:132-44.
209. Bozzolo N, Bernacki M. Viewpoint on the Formation and Evolution of Annealing Twins During Thermomechanical Processing of FCC Metals and Alloys. *Metallurgical and Materials Transactions A*. 2020;51(6):2665-84.
210. Xin Y, Zhou H, Wu G, Yu H, Chapuis A, Liu Q. A twin size effect on thermally activated twin boundary migration in a Mg–3Al–1Zn alloy. *Materials Science and Engineering: A*. 2015;639:534-9.
211. Jiang MG, Yan H, Chen RS. Twinning, recrystallization and texture development during multi-directional impact forging in an AZ61 Mg alloy. *Journal of Alloys and Compounds*. 2015;650:399-409.
212. Azarbarmas M, Aghaie-Khafri M, Cabrera JM, Calvo J. Dynamic recrystallization mechanisms and twinning evolution during hot deformation of Inconel 718. *Materials Science and Engineering: A*. 2016;678:137-52.
213. Jiang MG, Xu C, Yan H, Lu SH, Nakata T, Lao CS, et al. Correlation between dynamic recrystallization and formation of rare earth texture in a Mg–Zn–Gd magnesium alloy during extrusion. *Scientific Reports*. 2018;8(1):16800.
214. Oren E, Yahel E, Makov G. Kinetics of dislocation cross-slip: A molecular dynamics study. *Computational Materials Science*. 2017;138:246-54.
215. Fatemi SM, Moradipour Y, Hajian M. Deformation Mechanisms and Evolution of Second Phase Particles of Mg–Y–Nd–Gd–Zr Alloy During Plane Strain Compression. *Metals and Materials International*. 2020.
216. Bhattacharyya JJ, Agnew SR, Muralidharan G. Texture enhancement during grain growth of magnesium alloy AZ31B. *Acta Materialia*. 2015;86:80-94.
217. Mosayebi M, Zarei-Hanzaki A, Abedi HR, Barabi A, Jalali MS, Ghaderi A, et al. The correlation between the recrystallization texture and subsequent isothermal grain growth in a friction stir processed rare earth containing magnesium alloy. *Materials Characterization*. 2020;163:110236.
218. Kang L, Yang C. A Review on High-Strength Titanium Alloys: Microstructure, Strengthening, and Properties. *Advanced Engineering Materials*. 2019;21(8):1801359.
219. Ter Haar GM, Becker TH. Selective laser melting produced Ti-6Al-4V: post-process heat treatments to achieve superior tensile properties. *Materials*. 2018;11(1):146.
220. Weiss I, Froes FH, Eylon D, Welsch GE. Modification of alpha morphology in Ti-6Al-4V by thermomechanical processing. *Metallurgical Transactions A*. 1986;17(11):1935-47.
221. Zherebtsov S, Murzinova M, Salishchev G, Semiatin SL. Spheroidization of the lamellar microstructure in Ti–6Al–4V alloy during warm deformation and annealing. *Acta Materialia*. 2011;59(10):4138-50.



222. Stefansson N, Semiatin SL. Mechanisms of globularization of Ti-6Al-4V during static heat treatment. *Metallurgical and Materials Transactions A*. 2003;34(3):691-8.
223. Stefansson N, Semiatin SL, Eylon D. The kinetics of static globularization of Ti-6Al-4V. *Metallurgical and Materials Transactions A*. 2002;33(11):3527-34.
224. Fan XG, Yang H, Yan SL, Gao PF, Zhou JH. Mechanism and kinetics of static globularization in TA15 titanium alloy with transformed structure. *Journal of Alloys and Compounds*. 2012;533:1-8.
225. Semiatin S, Furrer D. Modeling of microstructure evolution during the thermomechanical processing of titanium alloys. *ASM Handbook*. 2009;22:522-35.
226. Stefansson N, Semiatin S. Mechanisms of globularization of Ti-6Al-4V during static heat treatment. *Metallurgical and Materials Transactions A*. 2003;34(3):691-8.
227. Sharma G, Ramanujan RV, Tiwari GP. Instability mechanisms in lamellar microstructures. *Acta Materialia*. 2000;48(4):875-89.
228. MacKay RA, Nathal MV.  $\gamma'$  coarsening in high volume fraction nickel-base alloys. *Acta Metallurgica et Materialia*. 1990;38(6):993-1005.
229. Liu B, Hu X. Chapter 1 - Hollow Micro- and Nanomaterials: Synthesis and Applications. In: Zhao Q, editor. *Advanced Nanomaterials for Pollutant Sensing and Environmental Catalysis*: Elsevier; 2020. p. 1-38.
230. Song H-W, Zhang S-H, Cheng M. Dynamic globularization kinetics during hot working of a two phase titanium alloy with a colony alpha microstructure. *Journal of Alloys and Compounds*. 2009;480(2):922-7.
231. Wang K, Zeng W, Zhao Y, Lai Y, Zhou Y. Dynamic globularization kinetics during hot working of Ti-17 alloy with initial lamellar microstructure. *Materials Science and Engineering: A*. 2010;527(10):2559-66.
232. Semiatin SL, Kobryn PA, Roush ED, Furrer DJ, Howson TE, Boyer RR, et al. Plastic flow and microstructure evolution during thermomechanical processing of laser-deposited Ti-6Al-4V preforms. *Metallurgical and Materials Transactions A*. 2001;32(7):1801-11.
233. Shell EB, Semiatin SL. Effect of initial microstructure on plastic flow and dynamic globularization during hot working of Ti-6Al-4V. *Metallurgical and Materials Transactions A*. 1999;30(12):3219-29.
234. Ma X, Zeng W, Tian F, Zhou Y. The kinetics of dynamic globularization during hot working of a two phase titanium alloy with starting lamellar microstructure. *Materials Science and Engineering: A*. 2012;548:6-11.
235. Davis R, Flower HM, West DRF. The decomposition of Ti-Mo alloy martensites by nucleation and growth and spinodal mechanisms. *Acta Metallurgica*. 1979;27(6):1041-52.
236. Bönisch M, Calin M, Waitz T, Panigrahi A, Zehetbauer M, Gebert A, et al. Thermal stability and phase transformations of martensitic Ti-Nb alloys. *Science and Technology of Advanced Materials*. 2013;14(5):055004.

237. Sato K, Matsumoto H, Kodaira K, Konno TJ, Chiba A. Phase transformation and age-hardening of hexagonal  $\alpha'$  martensite in Ti–12mass%V–2mass%Al alloys studied by transmission electron microscopy. *Journal of Alloys and Compounds*. 2010;506(2):607-14.
238. Soffa WA, Laughlin DE. DECOMPOSITION AND ORDERING PROCESSES INVOLVING THERMODYNAMICALLY 1ST-ORDER ORDER- DISORDER TRANSFORMATIONS. *Acta Metallurgica*. 1989;37(11):3019-28.
239. Xu X, Westraadt JE, Odqvist J, Youngs TGA, King SM, Hedstrom P. Effect of heat treatment above the miscibility gap on nanostructure formation due to spinodal decomposition in Fe-52.85 at.%Cr. *Acta Materialia*. 2018;145:347-58.
240. Kondo S-i, Nakashima H, Morimura T. Spinodal decomposition in a melt-spun Cu-15Ni-8Sn alloy. *Physica B-Condensed Matter*. 2019;560:244-54.
241. Gao X, Hu R, Zhang T, Li J, Yuan L, Kong J. Precipitation of coherent Ni-2(Cr, W) superlattice in an Ni-Cr-W superalloy. *Materials Characterization*. 2016;111:86-92.
242. Azzam A, Philippe T, Hauet A, Danoix F, Locq D, Caron P, et al. Kinetics pathway of precipitation in model Co-Al-W superalloy. *Acta Materialia*. 2018;145:377-87.
243. Semboshi S, Kaneno Y, Takasugi T, Masahashi N. High Strength and High Electrical Conductivity Cu-Ti Alloy Wires Fabricated by Aging and Severe Drawing. *Metallurgical and Materials Transactions a-Physical Metallurgy and Materials Science*. 2018;49A(10):4956-65.
244. Boyne A, Wang D, Shi RP, Zheng Y, Behera A, Nag S, et al. Pseudospinodal mechanism for fine  $\alpha/\beta$  microstructures in  $\beta$ -Ti alloys. *Acta Materialia*. 2014;64:188-97.
245. Wang D, Shi R, Zheng Y, Banerjee R, Fraser HL, Wang Y. Integrated Computational Materials Engineering (ICME) Approach to Design of Novel Microstructures for Ti-Alloys. *Jom*. 2014;66(7):1287-98.
246. Barriobero-Vila P, Biancardi Oliveira V, Schwarz S, Buslaps T, Requena G. Tracking the  $\alpha''$  martensite decomposition during continuous heating of a Ti-6Al-6V-2Sn alloy. *Acta Materialia*. 2017;135:132-43.
247. Heo TW, Shih DS, Chen L-Q. Kinetic Pathways of Phase Transformations in Two-Phase Ti Alloys. *Metallurgical and Materials Transactions a-Physical Metallurgy and Materials Science*. 2014;45A(8):3438-45.
248. Ji Y, Heo TW, Zhang F, Chen L-Q. Theoretical Assessment on the Phase Transformation Kinetic Pathways of Multi-component Ti Alloys: Application to Ti-6Al-4V. *Journal of Phase Equilibria and Diffusion*. 2016;37(1):53-64.
249. Shi R, Luo AA. Applications of CALPHAD modeling and databases in advanced lightweight metallic materials. *Calphad-Computer Coupling of Phase Diagrams and Thermochemistry*. 2018;62:1-17.
250. Biner SB. *Programming phase-field modeling*: Springer; 2017.
251. Lee HG, Lee J-Y. A semi-analytical Fourier spectral method for the Allen-Cahn equation. *Computers & Mathematics with Applications*. 2014;68(3):174-84.

- 
252. Choudhuri D, Gwalani B, Gorsse S, Komarasamy M, Mantri SA, Srinivasan SG, et al. Enhancing strength and strain hardenability via deformation twinning in fcc-based high entropy alloys reinforced with intermetallic compounds. *Acta Materialia*. 2019;165:420-30.
253. Mahajan S, Pande CS, Imam MA, Rath BB. Formation of annealing twins in f.c.c. crystals. *Acta Materialia*. 1997;45(6):2633-8.
254. Semiatin SL, Lehner TM, Miller JD, Doherty RD, Furrer DU. Alpha/Beta heat treatment of a titanium alloy with a nonuniform microstructure. *Metallurgical and Materials Transactions a-Physical Metallurgy and Materials Science*. 2007;38A(4):910-21.
255. Semiatin SL, Knisley SL, Fagin PN, Zhang F, Barker DR. Microstructure evolution during alpha-beta heat treatment of Ti-6Al-4V. *Metallurgical and Materials Transactions a-Physical Metallurgy and Materials Science*. 2003;34A(10):2377-86.
256. Liu Z, Lu SL, Tang HP, Qian M, Zhan L. Characterization and decomposition crystallography of the massive phase grains in an additively-manufactured Ti-6Al-4V alloy. *Materials Characterization*. 2017;127:146-52.
257. Semiatin S, Lehner T, Miller J, Doherty R, Furrer D. Alpha/beta heat treatment of a titanium alloy with a nonuniform microstructure. *Metallurgical and Materials Transactions A*. 2007;38(4):910-21.
258. Semiatin S, Stefansson N, Doherty R. Prediction of the kinetics of static globularization of Ti-6Al-4V. *Metallurgical and Materials Transactions A*. 2005;36(5):1372-6.
259. Chao Q, Hodgson PD, Beladi H. Ultrafine grain formation in a Ti-6Al-4V alloy by thermomechanical processing of a martensitic microstructure. *Metallurgical and Materials Transactions A*. 2014;45(5):2659-71.
260. Mullins W. Grain boundary grooving by volume diffusion. *Transactions of the American Institute of Mining and Metallurgical Engineers*. 1960;218(2):354-61.
261. Fan X, Yang H, Yan S, Gao P, Zhou J. Mechanism and kinetics of static globularization in TA15 titanium alloy with transformed structure. *Journal of Alloys and Compounds*. 2012;533:1-8.
262. Zherebtsov S, Murzinova M, Salishchev G, Semiatin S. Spheroidization of the lamellar microstructure in Ti-6Al-4V alloy during warm deformation and annealing. *Acta Materialia*. 2011;59(10):4138-50.
263. Sun X, Guo Y, Wei Q, Li Y, Zhang S. A comparative study on the microstructure and mechanical behavior of titanium: Ultrafine grain vs. coarse grain. *Materials Science and Engineering: A*. 2016;669:226-45.
264. Chong Y, Bhattacharjee T, Tsuji N. Bi-lamellar microstructure in Ti-6Al-4V: Microstructure evolution and mechanical properties. *Materials Science and Engineering: A*. 2019;762:138077.